# BAYESIAN APPROACHES TO INFER THE PHYSICAL PROPERTIES OF STAR-FORMING GALAXIES AT COSMIC DAWN

A Dissertation

by

BRETT WESTON KILLEBREW SALMON

Submitted to the Office of Graduate and Professional Studies of
Texas A&M University
in partial fulfillment of the requirements for the degree of

DOCTOR OF PHILOSOPHY

| | |
|---|---|
| Chair of Committee, | Casey Papovich |
| Committee Members, | Kim-Vy Tran |
| | Lucas Macri |
| | James Long |
| Head of Department, | Peter McIntyre |

August 2016

Major Subject: Physics

# ABSTRACT

In this dissertation, I seek to advance our understanding of galaxy formation and evolution in the early universe. Using the largest single project ever conducted by the *Hubble Space Telescope* (the Cosmic Assembly Near-infrared Deep Extragalactic Legacy Survey, CANDELS) I use deep and wide broadband photometric imaging to infer the physical properties of galaxies from $z = 8.5$ to $z = 1.5$. First, I will present a study that extends the relationship between the star-formation rates (SFRs) and stellar masses ($M_\star$) of galaxies to $3.5 < z < 6.5$, improves the constraints on the distant star-formation histories, and resolves an outstanding puzzle in the redshift evolution of the specific SFR (sSFR $\equiv$ SFR/$M_\star$).

To improve determinations of distant galaxy SFRs, I then place new constraints on how dust is attenuated in galaxies. I calculate the Bayesian evidence for galaxies under different assumptions of their underlying dust-attenuation law. By modeling galaxy ultraviolet-to-near-IR broadband CANDELS data I produce Bayesian evidence towards the dust law in individual galaxies that is confirmed by their observed IR luminosities. Moreover, I find a tight correlation between the strength of attenuation in galaxies and their dust law, a relation reinforced by the results from radiative transfer simulations.

Finally, I use the Bayesian methods developed in this dissertation to study the number density of SFR in galaxies from $z = 8$ to $z = 4$, and resolve the current disconnect between its evolution and that of the stellar mass function. In doing so, I place the first constraints on the dust law of $z > 4$ galaxies, finding it obeys a similar relation as found at $z \sim 2$. I find a clear excess in number density at high SFRs. This new SFR function is in better agreement with the observed stellar mass

functions, the few to-date infrared detections at high redshifts, and the connection to the observed distribution of lower redshift infrared sources. Together, these studies greatly improve our understanding of the galaxy star-formation histories, the nature of their dust attenuation, and the distribution of SFR among some of the most distant galaxies in the universe.

DEDICATION

To Mom, who taught me to follow my dreams,

To Dad, who taught me to never be too serious,

and To Will, who taught me that it's okay to be weird.

When I heard the learn'd astronomer,

When the proofs, the figures, were ranged in columns before me,

When I was shown the charts and diagrams, to add, divide, and measure them,

When I sitting heard the astronomer where he lectured

with much applause in the lecture-room,

How soon unaccountable I became tired and sick,

Till rising and gliding out I wanderd off by myself,

In the mystical moist night-air, and from time to time,

Look'd up in perfect silence at the stars.

– *Leaves of Grass (1867)*, Walt Whitman (1819-1892)

# ACKNOWLEDGEMENTS

Foremost, I extend my sincere gratitude to my graduate advisor, Casey Papovich, for his careful attention and guidance over these many years. You have made an astronomer out of a bumbling undergrad, and taught me invaluable lessons in advising, teaching, writing, and research. I forgive you for teaching me IDL. I also thank my unofficial co-advisor, Steven Finkelstein, who has been my mentor for my entire graduate career. Your faith in my competence was not unrecognized. I also thank my committee members Kim-Vy Tran and Lucas Macri for their diverse guidance throughout graduate school, and James Long for correcting my astronomer's understanding of statistics.

I thank the postdocs at Texas A&M that have taught me a great deal, especially answering the questions that I would not or could not ask from a professor, Vithal Tilvi, Nicola Mehrtens, and Ryan Quadri. I also thank those that have offered me opportunities for teaching and outreach activities, which have given me great fulfillment: Tatiana Erukhimova, Jennifer Marshall, Keely Finkelstein, and Ryan Quadri. Of course, I thank my undergraduate advisors Chuck Keeton and Andrew Baker for their patience during the nascent years of my astronomy career and their sound advice about my prospects for graduate school.

I acknowledge the CANDELS collaboration for their hard work to provide a robust and valuable dataset. I especially thank Harry Ferguson and Sandy Faber for their organization of the team and their prioritization of junior scientist careers. I also thank the Mitchell family and the late George P. Mitchell for starting a world-class astronomy department through their commitment to science and philanthropy.

My work is based on observations taken by the CANDELS Multi-Cycle Trea-

sury Program with the NASA/ESA *HST*, which is operated by the Association of Universities for Research in Astronomy, Inc., under NASA contract NAS5-26555. This work is supported by *HST* program No. GO-12060. Support for Program No. GO-12060 was provided by NASA through a grant from the Space Telescope Science Institute, which is operated by the Association of Universities for Research in Astronomy, Incorporated, under NASA contract NAS5-26555. This work is based on observations made with the *Spitzer Space Telescope*, which is operated by the Jet Propulsion Laboratory, California Institute of Technology under contract with the National Aeronautics and Space Administration (NASA). I also acknowledge the Texas A&M University Brazos HPC cluster that contributed to the research reported here.

Finally, I thank my family for supporting me through stressful times. Thank you, Julia, for your reassurance and keeping my head on my shoulders. I cannot thank enough my incredibly loyal friends for flying across the country to Texas so often to visit with me, some of you multiple times: Drew, Fahim, Ticchio, Joanna, Dave, Stephen, Kyle, Mark, Joe, Vinay, and Anthony. I also thank my grad friends for the truly unique academic and social support network that we have grown, especially as some of the first astronomy students at A&M, a legacy that I hope continues. Thank you Adam, Jimmy, Ryan, and Mike, for making a far away place feel like home.

# NOMENCLATURE

| | |
|---|---|
| Å | Angstroms |
| $\Omega_\lambda$ | Energy Density of the Universe |
| $\Omega_{\rm M}$ | Matter Density of the Universe |
| $\Psi$ | Star Formation Rate |
| $\lambda$ | Wavelength |
| $\delta$ | Power-Law Slope of Parameterized Dust Law |
| $\tau$ | $e$-folding Time of Star-Formation History |
| $\sigma_{\rm NMAD}$ | Median Absolute Deviation |
| $\mu$m | Micron/Micrometer |
| AB | Absolute Bolometric |
| ACS | Advanced Camera for Surveys |
| AGN | Active Galactic Nucleus |
| $A_{\rm V}$ | Total Extinction/Attenuation at the V band |
| CANDELS | Cosmic Assembly Near-IR Deep Extragalactic Legacy Survey |
| $D$ | Data |
| $D_{\rm L}$ | Luminosity Distance |
| $E(B-V)$ | Selective Extinction, or Color Excess |
| $f_{\rm esc}$ | Escape Fraction |
| GOODS-S | Great Observatories Origins Deep Survey - South |
| Gyr | Gigayear |
| $H_0$ | Hubble Constant |
| H I | Neutral Atomic Hydrogen |
| H II | Ionized Atomic Hydrogen |

| | |
|---|---|
| HST | Hubble Space Telescope |
| IGM | Intergalactic Medium |
| IMF | Initial Mass Function |
| IR | Infrared |
| IRAC | Infrared Array Camera |
| IRX | Infrared Excess |
| ISM | Inter-Stellar Medium |
| JASA | Journal of the American Statistical Association |
| JRSS | Journal of the Royal Statistical Society |
| $L_\odot$ | Solar Luminosity |
| Ly$\alpha$ | Lyman Alpha |
| $L_{\rm TIR}$ | Total Infrared Luminosity |
| $M_\odot$ | Solar Mass |
| $M_\star$ | Stellar Mass |
| $M_{1500}$ | UV Magnitude |
| mag | Magnitude |
| MIPS | Multiband Imaging Photometer for Spitzer |
| Mpc | Megaparsec |
| $N_{\rm LyC}$ | Number of Lyman Continuum Photons |
| PACS | Photodetecting Array Camera and Spectrometer |
| PAH | Polycyclic Aromatic Hydrocarbon |
| PDF | Probability Density Function |
| PSF | Point Spread Function |
| $R_{\rm V}$ | Total-to-selective Extinction/Attenuation at the V band |
| S/N | Signal-to-Noise |

| | |
|---|---|
| SAM | Semi-Analytic Model |
| SED | Spectral Energy Distribution |
| SExtractor | Source Extracter |
| SFH | Star-Formation History |
| SFR | Star-Formation Rate |
| SMC | Small Magellanic Cloud |
| SMF | Stellar Mass Function |
| SMMR | Statistical Methods in Medical Research |
| sSFR | Specific Star-Formation Rate |
| UDS | Ultra Deep Survey |
| UV | Ultraviolet |
| $Z$ | Metallicity |
| $z$ | Redshift |
| $z_{\rm phot}$ | Photometric Redshift |
| $z_{\rm spec}$ | Spectroscopic Redshift |

TABLE OF CONTENTS

Page

ABSTRACT . . . . . ii

DEDICATION . . . . . iv

ACKNOWLEDGEMENTS . . . . . v

NOMENCLATURE . . . . . vii

TABLE OF CONTENTS . . . . . x

LIST OF FIGURES . . . . . xiv

LIST OF TABLES . . . . . xvii

1. INTRODUCTION . . . . . 1

1.1 Searching for the First Galaxies . . . . . 1
1.2 The Star-Formation Activity of Galaxies . . . . . 3
1.2.1 The Star Formation Rate and Stellar Mass Relation . . . . . 3
1.2.2 The Star-Formation Histories of Galaxies . . . . . 4
1.2.3 The Specific Star-Formation Rate Evolution . . . . . 5
1.3 The Enigma of Dust Attenuation . . . . . 6
1.4 Reionization and the Distribution of SFR . . . . . 7

2. THE RELATION BETWEEN STAR FORMATION RATE AND STELLAR MASS FOR GALAXIES AT $3.5 \leq z \leq 6.5$ IN CANDELS . . . . . 10

2.1 Synopsis . . . . . 10
2.2 Background Information . . . . . 11
2.3 Observational Data and Simulations . . . . . 15
2.3.1 CANDELS GOODS-S Multi-wavelength Data . . . . . 15
2.3.2 CANDELS GOODS-S Redshifts . . . . . 17
2.3.3 Sample Selection . . . . . 19
2.3.4 Galaxy Photometry from Models and Simulations . . . . . 19
2.4 Stellar Population Synthesis Fitting: Methods . . . . . 23
2.4.1 Star Formation History . . . . . 26
2.4.2 Nebular Emission . . . . . 29

2.4.3 Dust Attenuation Prescriptions . . . . . 34
2.5 A Bayesian Approach to Determine Physical Parameters . . . . . 36
2.5.1 Probability Density Functions: Methods . . . . . 36
2.5.2 Probability Density Functions: Results . . . . . 40
2.5.3 Impact of SED Fitting Assumptions on Marginalized Values . 45
2.5.4 Tests of Derived SFR and Stellar Masses Using Semi-Analytic Models . . . . . 46
2.6 Evolution of SFR and Stellar Mass at $3.5 < z < 6.5$ . . . . . 50
2.6.1 $M_{1500}$–Stellar Mass Relation . . . . . 52
2.6.2 SFR–Stellar Mass Relation . . . . . 54
2.7 Discussion . . . . . 61
2.7.1 Implications of the SFR–Stellar Mass Relation . . . . . 61
2.7.2 Evolution of the SFR . . . . . 62
2.7.3 Evolution of the sSFR . . . . . 67

3. BREAKING THE CURVE WITH CANDELS: A BAYESIAN APPROACH TO REVEAL THE NON-UNIVERSALITY OF THE DUST-ATTENUATION LAW AT HIGH REDSHIFT . . . . . 72

3.1 Synopsis . . . . . 72
3.2 Background Information . . . . . 73
3.3 Data, Redshifts, and Sample Selection . . . . . 77
3.3.1 Photometry: CANDELS GOODS Multi-Wavelength Data . . 77
3.3.2 IR Photometry: Spitzer and Herschel . . . . . 78
3.3.3 Redshifts . . . . . 78
3.3.4 Sample Selection . . . . . 80
3.3.5 Calculation of Total Infrared Luminosities . . . . . 82
3.3.6 Calculation of the UV Luminosity . . . . . 84
3.3.7 Calculation of the UV Spectral Slope $\beta$ . . . . . 84
3.4 Modeling Stellar Populations . . . . . 87
3.4.1 Bayesian Methods . . . . . 87
3.4.2 Stellar Population Models . . . . . 88
3.4.3 Known Dust Attenuation Curves . . . . . 90
3.5 Distinguishing Between Dust Laws with Bayes Factors . . . . . 94
3.6 Parameterizing the Dust Law . . . . . 96
3.7 The Non-Universality of Dust Laws at $z \sim 2$ . . . . . 99
3.7.1 Relevant Spectral Features . . . . . 99
3.7.2 Results from the Spectroscopic Redshift Sample . . . . . 101
3.7.3 Results from the Photometric Redshift Sample . . . . . 106
3.8 Discussion . . . . . 110
3.8.1 Origins of the Relation Between $E(B-V)$ and $\delta$ . . . . . 110
3.8.2 Physical Origins of Non-Universal Attenuation . . . . . 111
3.8.3 Comparison with Dust Theory . . . . . 115

3.8.4 Comparisons with Recent Literature . . . 116
3.8.5 Implications for SED-Derived Properties of Galaxies . . . 117

4. THE SFR FUNCTION FROM $4 < Z < 8$ AND THE NON-UNIVERSALITY OF THE HIGH-REDSHIFT DUST LAW . . . 120

4.1 Synopsis . . . 120
4.2 Background Information . . . 120
4.3 Data, Redshifts, and Sample Selection . . . 121
4.3.1 Photometry: CANDELS Multi-wavelength Data . . . 121
4.3.2 Photometric Redshifts . . . 123
4.4 Sample Selection . . . 123
4.4.1 Galaxy Samples for Analysis of the Dust Law . . . 124
4.4.2 Galaxy Samples for Derivation of the SFR Function . . . 125
4.5 SED Fitting and SFRs . . . 126
4.6 Results . . . 128
4.6.1 The Evolution of the High-Redshift Dust Law . . . 128
4.6.2 The Evolution of the SFR Function . . . 130
4.7 Discussion . . . 133
4.7.1 On the Differences in Results in the Literature . . . 133
4.7.2 Implications for SFR Efficiency . . . 135

5. SUMMARY AND CONCLUSIONS . . . 138

5.1 The Relation Between SFR and Stellar Mass at High Redshift . . . 138
5.2 The Non-Universality of the $z = 2$ Extragalactic Dust Law . . . 140
5.3 The Dust Law and SFR Functions at $z > 4$ . . . 141
5.4 Future Work . . . 142
5.4.1 The Physics of Dust in the Distant Universe . . . 143
5.4.2 Using ALMA to Find Dusty Star-Forming Galaxies at High Redshift . . . 144
5.4.3 The Correlation of Nebular Emission with Galaxy Properties . . . 146
5.4.4 A Bayesian Approach to the SFRF . . . 148

REFERENCES . . . 149

APPENDIX A. APPENDICES OF SECTION 2 . . . 164

A.1 Changing the Assumed Star Formation History . . . 164
A.2 Stellar Population Synthesis Fitting: Comparing Best-Fit Results . . . 167
A.2.1 Effect of Including Nebular Emission . . . 167
A.2.2 Dependence on Attenuation Prescription . . . 169
A.2.3 Difference of Marginalized SFR Compared to Traditional Methods . . . 172

A.3 Derivation of Prior . . . . . 174

APPENDIX B. APPENDICES OF SECTION 3 . . . . . 180

B.1 Testing the Relationship Between $E(B-V)$ and $\delta$ . . . . . 180
B.2 Using Herschel to Calculate the Total Infrared Luminosities . . . . . 183
B.3 Changing the UV Slope, $\beta$ . . . . . 185
B.4 Changing the Assumed Star-Formation History . . . . . 185

LIST OF FIGURES

FIGURE Page

2.1 Redshift Accuracy and Sample Distribution. . . . . 16
2.2 Example SEDs with and Without Nebular Emission. . . . . 27
2.3 Flux Excess from Nebular Emission. . . . . 30
2.4 Examples of SEDs Assuming Different Dust Laws. . . . . 32
2.5 Examples of Marginalized Posteriors. . . . . 35
2.6 Example 2D Posterior in $M_{1500}$ and Stellar Mass. . . . . 37
2.7 Example 2D Posterior in Stellar Mass and SFR. . . . . 39
2.8 Impact of Nebular/Dust Treatment on Marginalized Values. . . . . 41
2.9 Testing Our Results with Semi-Analytic Models. . . . . 43
2.10 The Relation Between Stellar Mass and $M_{1500}$. . . . . 47
2.11 The Relation Between SFR and Stellar Mass. . . . . 49
2.12 Comparison of SFR and Stellar Mass Relation to Models. . . . . 55
2.13 Cumulative Stellar Mass Functions. . . . . 63
2.14 Tracking Galaxy Evolution by Number Density. . . . . 64
2.15 The SFR History. . . . . 65
2.16 A Rising SFH on the Relation Between SFR and Stellar Mass. . . . . 68
2.17 The Evolution of sSFR at Constant Stellar Mass. . . . . 69
2.18 The Evolution of sSFR Selected by Number Density. . . . . 71
3.1 Redshift Accuracy of $z \sim 2$ Sample. . . . . 79

3.2 Total Infrared Luminosities. . . . . 81
3.3 Common Dust Laws. . . . . 91
3.4 Dust Laws on $IRX - \beta$. . . . . 93
3.5 Example SEDs That Favor a Starburst Dust Law. . . . . 98
3.6 Example SEDs That Favor an SMC Dust Law. . . . . 100
3.7 Bayes-Factor Evidence on $IRX - \beta$. . . . . 103
3.8 Posteriors of the Parameterized Dust Law, $\delta$. . . . . 104
3.9 The Relation Between $\delta$ and $E(B-V)$ in the Spec-$z$ Sample. . . . . 105
3.10 Bayes Factors on $IRX - \beta$ with the Phot-$z$ Sample. . . . . 107
3.11 The Relation Between $\delta$ and $E(B-V)$ in the Phot-$z$ Sample. . . . . 109
3.12 Lack of Correlation with Morphologies. . . . . 111
3.13 Comparison with Dust Theory. . . . . 114
3.14 Dust Laws on the UVJ Diagram. . . . . 118
4.1 The Evolution of the Dust Law from $z = 6$ to $z = 4$. . . . . 129
4.2 $E(B-V)$ on the SFR and Stellar Mass Relation. . . . . 131
4.3 $\delta$ on the SFR and Stellar Mass Relation. . . . . 132
4.4 The SFR Function of Galaxies from $z_{\rm phot} = 6$ to $z_{\rm phot} = 4$. . . . . 134
4.5 The Relation Between UV Magnitude and $\beta$ at $z = 5$. . . . . 136
5.1 Better Determinations of the Dust Law Using SHARDS. . . . . 145
5.2 *ALMA* Can Reveal Dusty Galaxies at Very High Redshifts. . . . . 147
A.1 Changing the Assumed Star-Formation History . . . . . 165
A.2 Influence of Nebular Emission on Stellar Mass . . . . . 168
A.3 The Affects of Changing the Dust Law on Stellar Mass and SFR . . . 170
A.4 Other SFR Methods . . . . . 173

A.5 The Shape of the Assumed Priors . . . . . 175

A.6 Changing the Assumed Prior . . . . . 176

B.1 Testing Different Relations Between $E(B-V)$ and $\delta$. . . . . 182

B.16 $L_{\rm TIR}$ Comparison. . . . . 184

B.17 The $IRX-\beta$ Relation After Changing $\beta$. . . . . 187

B.18 The $IRX-\beta$ Relation Assuming Different SFHs. . . . . 188

LIST OF TABLES

TABLE Page

2.1 SED Fitting Parameters. . . . . 25

2.2 $M_{1500}$ – Stellar Mass Relation Median Values. . . . . 48

2.3 SFR – Stellar Mass Relation Median Values. . . . . 51

2.4 SFR–Stellar Mass Best-Fit Parameters. . . . . 56

3.1 SED Fitting Parameters . . . . . 86

4.1 Dust Law and SFRF Samples. . . . . 126

4.2 $M_{\rm UV} - \beta$ Relation at $z = 5$ . . . . . 136

# 1. INTRODUCTION

## 1.1 Searching for the First Galaxies

The universe was busy in its youthful years. At less than a quarter of its current age, the universe was forming stars faster than any other time in history, eventually forming half its mass in stars by 35% its current age (Madau & Dickinson, 2014). This tumultuous and active era of the universe has much to offer in describing the cosmic origins of galaxies like our Milky Way, and even earlier times can help reveal how the first galaxies formed and evolved. The star-formation histories of the first galaxies, the nature of the cosmic dust particles that enshroud them, and the physics that regulate their star formation activity are just a few of the outstanding conundrums that burden the field of high-redshift science.

Observational searches for galaxies in the early universe are non-trivial. The biggest challenge is to avoid the contamination of foreground galaxies by obtaining accurate estimates of the galaxy cosmological redshift $z$. Spectroscopic measurements are ideal, as the sharp spectral absorption and emission lines can be used to pinpoint the redshift at high confidence (Huchra et al., 1983; Colless et al., 2001; Strauss et al., 2002). However, the samples of these galaxies drop significantly as we explore the "redshift desert" beyond $z = 1.4$ where galaxies become both observationally and intrinsically faint (Steidel et al., 2004). For example, the apparent characteristic magnitude ($M^*_{\rm UV}$) of a galaxy at $z \approx 6$ is as faint as a single Cepheid variable star in a galaxy 50 million light years away (in M100; Freedman et al., 1994).

In the absence of spectroscopy, we must then turn to broadband photometric data to obtain the brightness of a galaxy integrated over a wider range in wavelength. Although broadband imaging can take deeper images faster than spectroscopy, we

forfeit wavelength resolution in the spectral energy distribution (SED). Thankfully, galaxies naturally provide a few strong spectral features including the drop in flux at wavelengths shorter than 912 Å due to the hydrogen ionization edge in massive stars and the further absorption by neutral gas in the interstellar medium (ISM). Additionally, line-of-sight neutral hydrogen gas throughout the intergalactic medium (IGM) readily absorbs Lyman-$\alpha$ (Ly$\alpha$ ) emission at the rest-frame 1216 Å of the gas, corresponding to rest-frame ultraviolet (UV) wavelengths between 912 Å and 1216 Å of the background source (the Lyman-$\alpha$ forest; Lynds, 1971; McDonald et al., 2006).

The resulting sharp Lyman break at 1216 Å has proven useful to photometrically select galaxies at $z > 3$ (Lyman Break Galaxies, LBGs; Steidel & Hamilton, 1993; Steidel et al., 1999; Giavalisco, 2002). More sophisticated redshift techniques employ all available galaxy colors in a photometric redshift fitting code, assigning a $P(z)$ probability density as a function of redshift for each galaxy (photometric redshifts; Bolzonella et al., 2000; Rudnick et al., 2003; Brammer et al., 2008). With galaxy redshifts in hand, we can then use broadband photometry to infer the physical properties of distant galaxies. SED fitting is one powerful tool to derive star-formation rates (SFRs) and stellar masses of galaxies (Sawicki & Yee, 1998; Papovich et al., 2001; Förster Schreiber et al., 2004; Drory et al., 2004; Walcher et al., 2011). In its simplest form, SED fitting matches the observed galaxy colors to libraries of stellar population synthesis models of known properties. For example, the mass-to-light ratio of a galaxy scales with its rest-frame optical to near infrared (near-IR) colors, enabling accurate estimates of its stellar mass. In addition, the rest-frame UV light cues off of the emission from young and short-lived O and B stars to provide an estimate of the star-formation rate (averaged over the $\approx$100 Myr timescales of these stars). Data that span these wavelengths are crucial for inferring the physical properties of distant galaxies (Madau et al., 1998; Bell & de Jong, 2001; Banerji et al.,

2013).

The Cosmic Assembly Near-infrared Deep Extragalactic Legacy Survey (CANDELS, PIs Faber and Ferguson; Grogin et al., 2011; Koekemoer et al., 2011), the largest single program ever conducted by the *Hubble Space Telescope* (*HST*), obtained 902 orbits covering five legacy fields to image some of the most distant galaxies in large quantity. The survey took imaging with the Advanced Camera for Surveys (ACS) and the Wide Field Camera 3 (WFC3), with supporting data from the *Spitzer* Extended Deep Survey (SEDS), together covering the rest-frame UV to optical SEDs of $z > 3$ galaxies. This deep and wide survey has allowed for great strides in our understanding of the early universe. In the following sections, I describe several areas of high-redshift science that can be explored with data from the CANDELS project, subjects that are the focus of this thesis.

## 1.2 The Star-Formation Activity of Galaxies

### *1.2.1 The Star Formation Rate and Stellar Mass Relation*

Since the Hubble tuning fork (Hubble, 1926; Sandage, 1961; Kormendy & Bender, 1996), there have been several methods to broadly classify different types of galaxies, either by color or by morphology. For example, a galaxy color-magnitude diagram shows that there are generally two distinct populations: blue star-forming and red ("and dead") quiescent galaxies (Bell et al., 2003). Similarly, the rest-frame colors (UVJ) of galaxies have been used successfully to distinguish between star-forming and quiescent galaxies (Williams et al., 2009). As advanced methods to infer the underlying stellar populations became more commonplace, stellar masses and star formation rates were quickly used as more direct metrics of star-formation activity in galaxies (Wuyts et al., 2007; Daddi et al., 2007; Noeske et al., 2007). Now, one of the most pervasive classifiers of galaxies is the relation between their star-formation

rate (SFR) and stellar mass (Williams et al., 2009; Ilbert et al., 2010; Speagle et al., 2014).

This relation is fundamental; a one-to-one correlation implies that the rate of its current star formation is connected to the resulting mass in stars from all previous star formation. The conventional explanation is that galaxies with larger stellar masses reside in dark matter halos with higher gravitational potentials, allowing the galaxy to more easily accrete gas to fuel star formation. However this is not necessarily the case for all galaxies at all times. Galaxies that either merge or accrete gas can undergo a burst phase of star formation at a given stelar mass, or similarly shut down their star-formation due to a variety of known quenching mechanisms. The relation between SFR and stellar mass, especially taken over many epochs, can therefore provide snapshots of the star-formation history of galaxies. The multi-wavelength coverage of CANDELS provides an opportunity to extend the relation between SFR and stellar mass out to $z = 6$, allowing us to study the star-formation histories of these early galaxies.

### *1.2.2 The Star-Formation Histories of Galaxies*

Another way to monitor the star-formation activity of galaxies over cosmic time is to select galaxies by their co-moving number densities. This method assumes that the number of bright objects per slice of co-moving volume does not change with redshift, meaning that the stellar-mass rank order of galaxies is conserved (van Dokkum et al., 2010; Papovich et al., 2011). Behroozi et al. (2013c) refined this method by suggesting a number density that evolves slightly with redshift in order to better track galaxy progenitor-to-descendent evolution.

This method carries two significant assumptions. First, it assumes that the identity of galaxies evolves little within their assigned number density (e.g., the most

massive galaxies at one epoch become the most massive in the next). This assumption was supported by simulations which showed that the number density of dark matter haloes evolves very little with redshift (Krumholz & Dekel, 2012; Behroozi et al., 2013c). Second, it assumes the effect of mergers does not bias the number density selection, also supported by simulations (although some simulations show a weak bias; Leja et al., 2013a,b). In any case, the number density technique is an improvement over other current selection methods (e.g., at fixed stellar mass or luminosity) to track the evolution of a galaxy population. The deep imaging from CANDELS allows for a diverse sampling of stellar masses which will enable number density selections to track new progenitor-to-descendent evolution at high redshifts.

### *1.2.3 The Specific Star-Formation Rate Evolution*

The specific SFR (sSFR $\equiv$ SFR/$M_\star$) is the frequency for a galaxy to double its current stellar mass, and has therefore been used as metric for stellar mass buildup. The evolution of sSFR with redshift is often compared to cosmological accretion models as a way to infer if the gas accretion rates coincide with the growth of galaxies of a given stellar mass. The sSFR was first found to steadily decrease with redshift from $z \sim 2$ to present day (Noeske et al., 2007; Daddi et al., 2007; Dunne et al., 2009; Oliver et al., 2010; Rodighiero et al., 2010). These results also showed that this evolution begins to break down at times earlier than the peak SFR density of the Universe ($z > 2$, see Weinmann et al., 2011, for a detailed discussion). Historically, the initial observations showed that the sSFR at a fixed stellar mass did not evolve from $z = 2$ to $z = 7$ (Stark et al., 2009; González et al., 2010; Labbé et al., 2010; Reddy et al., 2012b).

This constant sSFR "plateau" raised a number of concerns. On the observational side, if galaxies have low sSFR at high redshift then they will be unable to reproduce

the massive end of the luminosity function at later times (Maraston et al., 2010). On the theoretical side, attempts were introduced to ameliorate models such that they match the observed sSFR plateau, often by tuning SFR feedback and efficiency as a function of redshift (Weinmann et al., 2011; Neistein & Weinmann, 2010). It was also a motivation for the Bouché et al. (2010) and the Krumholz & Dekel (2012) halo quenching models, but these have potential difficulties with matching the gas masses at low redshift and the LBG abundances at high redshift. The problem is that the observed sSFR plateau implies galaxy growth is decoupled from halo growth because the specific growth rate of halos has to evolve differently from the specific growth rate of galaxies.

In summary, there are no simple models that can both match the sSFR plateau while preserving agreement with many other existing observations (see Finlator et al., 2011; Davé et al., 2011a). The answer may reside in improved estimates of sSFR in distant galaxies through more advanced methods of stellar population modeling and/or increased sample sizes of high-redshift galaxies with CANDELS data.

## 1.3 The Enigma of Dust Attenuation

Any study of distant galaxy star-formation must mind the amount of UV light lost due to dust. Cosmic particles of dust are primarily made of either carbon (similar to soot) and/or silicate (similar to sand) compounds. Dust scatters and absorbs light preferentially at shorter, rest-UV wavelengths, causing a reddening of galaxy SEDs, and then re-radiates isotropically in the far-IR. Ideally, a combination of far-IR and UV measurements would provide a complete estimate of the SFR, but the current detector sensitivities, obstructing emission from atmospheric water vapor, and source confusion make rest-frame far-IR detections serendipitous for galaxies at $z > 2$.

Fortunately, local starburst galaxies have been used to parameterize the wave-

length dependence of dust attenuation (Calzetti et al., 1994, 2000). This "dust law" for attenuation in starburst galaxies has been used for over a decade to redden the SEDs of stellar population models (scaled by the color excess, $E(B-V)$) in order to match observations. However, recent observations of the IR-to-UV luminosity ratios (IRX $\equiv L_{\rm IR}/L_{\rm UV}$) have shown that the reddening of some galaxies exhibit a different wavelength dependence (more akin to dust in the Small Magellanic Cloud, SMC) than the previously assumed starburst dust law (Siana et al., 2009; Reddy et al., 2006, 2010; Buat et al., 2012; Sklias et al., 2014). This has broad implications for galaxy studies at high redshift that rely on an assumed dust law when deriving UV-based SFRs. The potential impact of the dust law on all of the high-redshift results of this thesis served as motivation for a chapter devoted to quantifying the dust law.

## 1.4 Reionization and the Distribution of SFR

One of the great mysteries in astronomy over the last decade is understanding how the gas between galaxies (the IGM) throughout the universe went from being primarily cool and neutral to hot and ionized, a process called reionization. Evidence of this process was reinforced by the observed sharp decline in the rest-frame far-UV light of distant galaxies, implying significant absorption due to neutral gas along the line of sight. Specifically, the observed Ly$\alpha$ forest and Gunn-Peterson trough (Gunn & Peterson, 1965) at redshifts $z > 6$ indicated an increase in the neutral fraction of hydrogen gas (H I; Becker et al., 2001). Stars, galaxies, quasars, and active galactic nuclei (AGN) were initially proposed as the likely culprits that powered reionization (see Fan et al., 2006, for a review), and thus they have been intensely surveyed at high redshift. We now know that the abundances of AGN and quasars drop significantly at higher redshifts (Fan et al., 2001; Richards et al., 2006), leaving low-luminosity

galaxies to be the leading candidates for the source of reionization (Bouwens et al., 2012; Robertson et al., 2013; Finkelstein et al., 2015). However, this is only a piece of the picture, as we still do not know the manner in which these galaxies produced and released their ionizing power, nor the lower stellar mass limit of the galaxies responsible.

Understanding reionization is therefore intimately tied with the study of distant galaxy evolution and the abundance of star formation. The ionizing capability and the number density evolution of distant galaxies speaks to the ancestry of present-day galaxies and the history of their star-formation activity. Until recent years, little was known about how the first galaxies accrued their mass in stars nor the mechanisms that regulated their star formation such as stellar winds and supernovae (Behroozi et al., 2010). In an average sense, we know that the star-formation density of galaxies slowly ramped up until about 2-3 billion years after the big bang ($z = 2 - 3$), after which it declined, producing the passive galaxies we see locally (Madau & Dickinson, 2014). Comparing this observed evolution to theoretical simulations and models of dark matter haloes gives constraints on the physics that hinder star formation (Somerville & Davé, 2015).

The star-formation activity of these early galaxies also gives clues to the history of how they accreted their gas (Katz et al., 1996; Schaye et al., 2010), given that the timescale for gas to turn into stars is comparatively small (Dutton et al., 2010; Forbes et al., 2014). Star-formation theory predicts and necessitates a steady supply of gas that is sufficiently cold to be subject to the Jeans instability for star formation (Dekel & Birnboim, 2006; Krumholz et al., 2012) and accretes in small enough lumps so as to not greatly disrupt galaxy structure (Somerville & Davé, 2015). It is currently impossible to detect cold gas accretion responsible for fueling high-redshift star formation due its very low temperature and small covering fraction (Stewart

et al., 2011; Faucher-Giguère & Kereš, 2011), although some indirect observational progress has been made locally (Sancisi et al., 2008). Until large surveys from sub-mm arrays probe the cold gas fractions of these galaxies in greater numbers, we are left with indirect measures to study their accretion histories.

One promising method is to constrain the number density of galaxies as a function of their SFR out to high redshift. Comparison to the literature and dark matter halo functions can give insight as to whether galaxies form by *in-situ* processes or cosmological gas accretion (assuming gas accretion follows dark matter halo accretion). The distribution of SFR adds a piece to the puzzle of how galaxies pioneered the reionization of the universe. Clearly, there is much yet to learn about the histories of the first galaxies in the universe and the consequences of their SFR activity for both the phase state of the universe and the origins of our present-day extragalactic neighborhood.

The outline of this thesis is as follows. In Chapter 2 I present a study wherein I improve on current methods to derive star-formation rates and stellar masses from the SEDs of galaxies. I use these new measurements to extend the relation between the galaxy star-formation rate and stellar mass out to $z = 6$, derive a star-formation history by monitoring their progenitor-to-descendent evolution, and address the validity of the sSFR plateau. In Chapter 3 I use a Bayesian approach to find evidence for a non-universal dust-attenuation law at $z \sim 2$, improving a major assumption in the derivation of distant galaxy SFRs. Next, in Chapter 4 I combine the SED-fitting techniques of Chapter 2 and the dust-law evidence of Chapter 3 to calculate the number density of galaxies as a function of SFR from $z = 8$ to $z = 4$. Finally, in Chapter 5 I present the conclusions of these studies and discuss the direction of future work.

# 2. THE RELATION BETWEEN STAR FORMATION RATE AND STELLAR MASS FOR GALAXIES AT $3.5 \leq z \leq 6.5$ IN CANDELS*

## 2.1 Synopsis

Distant star-forming galaxies show a correlation between their star formation rates (SFR) and stellar masses, and this has deep implications for galaxy formation. In this chapter, we present a study on the evolution of the slope and scatter of the SFR–stellar mass relation for galaxies at $3.5 \leq z \leq 6.5$ using multi-wavelength photometry in GOODS-S from the Cosmic Assembly Near-infrared Deep Extragalactic Legacy Survey (CANDELS) and *Spitzer* Extended Deep Survey. We describe an updated, Bayesian spectral-energy distribution fitting method that incorporates effects of nebular line emission, star formation histories that are constant or rising with time, and different dust attenuation prescriptions (starburst and Small Magellanic Cloud). From $z$=6.5 to $z$=3.5 star-forming galaxies in CANDELS follow a nearly unevolving correlation between stellar mass and SFR that follows SFR $\sim M_{\star}^{a}$ with $a = 0.54 \pm 0.16$ at $z \sim 6$ and $0.70 \pm 0.21$ at $z \sim 4$. This evolution requires a star formation history that increases with decreasing redshift (on average, the SFRs of individual galaxies rise with time). The observed scatter in the SFR–stellar mass relation is tight, $\sigma(\log \mathrm{SFR}/\mathrm{M}_{\odot}\ \mathrm{yr}^{-1}) < 0.3 - 0.4$ dex, for galaxies with $\log M_{\star}/\mathrm{M}_{\odot} > 9$ dex. Assuming that the SFR is tied to the net gas inflow rate (SFR $\sim \dot{M}_{\mathrm{gas}}$), then the scatter in the gas inflow rate is also smaller than 0.3−0.4 dex for star-forming galaxies in these stellar mass and redshift ranges, at least when averaged over the

*Reprinted with permission from "The Relation Between Star Formation Rate and Stellar Mass for Galaxies at $3.5 \leq z \leq 6.5$ in CANDELS" by Salmon et al., 2015. The Astrophysical Journal, Volume 799, Issue 2, article id. 799, 183 pp. 27, Copyright 2015 by Brett Salmon.

timescale of star formation. We further show that the implied star formation history of objects selected on the basis of their co-moving number densities is consistent with the evolution in the SFR–stellar mass relation.

## 2.2 Background Information

Modern broadband photometric surveys (e.g. the Cosmic Assembly Near-infrared Deep Extragalactic Legacy Survey, hereafter CANDELS) now routinely identify thousands of galaxies at redshifts greater than $z \sim 4$ (e.g., Dickinson, 1998; Steidel et al., 1999; Giavalisco, 2002; Stark et al., 2013; Reddy et al., 2012b). Such projects are able to probe the high-redshift galaxy spectral energy distribution (SED) from the rest-frame UV to the optical for galaxies with redshifts out to $z > 7$. This information allows us to characterize galaxies by their physical properties such as stellar mass ($M_\star$) and star formation rate (SFR) (Sawicki & Yee, 1998; Papovich et al., 2001; Shapley et al., 2001; Giavalisco, 2002; Stark et al., 2009; Förster Schreiber et al., 2004; Drory et al., 2004; Labbé et al., 2006; Maraston et al., 2010; Walcher et al., 2011; Curtis-Lake et al., 2013; Lee et al., 2012).

A correlation between the SFRs and stellar masses of galaxies exposes interesting mechanisms of the star formation history: a high scatter in this correlation implies a stochastic star formation history with many discrete "bursts", while a tighter correlation implies a star formation history that traces stellar mass growth more smoothly (Noeske et al., 2007; Daddi et al., 2007; Renzini, 2009; Finlator et al., 2011; Lee et al., 2012). The level of scatter between the SFR–stellar mass relation can be attributed to differences in the star formation histories of galaxies, which can be caused by the variation in their gas accretion rates (SFR $\sim \dot{M}_{\rm gas}$) and feedback effects, assuming the timescale for gas to form stars is small (Dutton et al., 2010; Forbes et al., 2014).

While the SFR–stellar mass relation has been well studied out to $z \lesssim 2$ (Daddi et al., 2007; Noeske et al., 2007; Dunne et al., 2009; Oliver et al., 2010; Rodighiero et al., 2010), divergent results have been observed in the literature for higher redshift ($z > 2$) galaxies (see Speagle et al., 2014, for a detailed comparison of many recent studies). Many studies have argued that the correlation is tight (Daddi et al., 2007; Pannella et al., 2009; Magdis et al., 2010; Lee et al., 2011; Sawicki, 2012; Steinhardt et al., 2014), implying smooth gas accretion. This agrees with results from hydrodynamic simulations, which predict a tight relation between SFR and stellar mass (Finlator et al., 2006, 2007, 2011; Neistein & Dekel, 2008; Davé, 2008), due in large part to their consensus that mergers are subdominant to galaxy growth at high redshift $z > 2$ (Murali et al., 2002; Kereš et al., 2005) and the SFR tracks the gas accretion rate (Birnboim & Dekel, 2003; Katz et al., 2003; Kereš et al., 2005; Dekel et al., 2009; Bouché et al., 2010; Ceverino et al., 2010; Faucher-Giguère & Kereš, 2011). In contrast, other studies find no correlation or high scatter in the SFR–stellar mass relation (Shapley et al., 2005; Reddy et al., 2006; Mannucci et al., 2009; Lee et al., 2012; Wyithe et al., 2014), implying bursty star formation. As suggested by Lee et al. (2012), these differences may be physical or a result of systematics in the data analysis. If the latter, then the differences likely arise from biases in the methods of deriving stellar masses and SFRs or from inconsistent sample selections (i.e., UV color, stellar mass, flux, photometric redshift, or spectroscopic redshift selections). If physical, these differences may be due to stochasticity in the star formation history or a more complicated galaxy evolution that changes with halo mass and rest-frame UV luminosity (see Renzini, 2009; Lee et al., 2009; Wyithe et al., 2014).

Inferring stellar masses and SFRs from broadband photometry can be a convoluted process, and careful attention to the methods of SED fitting could be the key to resolve discrepant results in the SFR–stellar mass relation. Many studies

have already recognized the sensitivity of the SED fitting process to assumptions on metallicity, dust attenuation prescription, nebular emission, and choice of initial mass function (IMF; Papovich et al., 2001; Zackrisson et al., 2001, 2008; Wuyts et al., 2007; Conroy et al., 2009; Marchesini et al., 2009; Ilbert et al., 2010; Maraston et al., 2010; Michałowski et al., 2012; Banerji et al., 2013; Moustakas et al., 2013; Schaerer et al., 2013; Stark et al., 2013; Mitchell et al., 2013; Buat et al., 2014). In particular, much attention has been given to varying the dust attenuation prescription beyond the typically assumed "starburst"-like attenuation (Calzetti et al., 2000). For example, the starburst attenuation has been known to produce unphysically young stellar population ages for UV selected samples, with best–fit ages often at the edge of the parameter space (Fontana et al., 2004; Reddy et al., 2012b; Oesch et al., 2013; Kriek & Conroy, 2013; Chevallard et al., 2013; Buat et al., 2014).

This chapter aims to address the discord in the results on the scatter in the SFR and stellar mass relation, the redshift evolution of the SFR per unit stellar mass (the specific SFR, sSFR), and, in general, the nature of the star formation history at high redshift. The new Bayesian fitting method used in this chapter is able to recover stellar masses and SFRs of simulated galaxies with complex star formation histories, while at the same time producing realistic distributions of stellar population ages (as predicted by semi-analytic models). Thus, this work shows there is an observed relation between SFR and stellar mass with low scatter and an evolution of the sSFR that increases with redshift. Furthermore, the star formation history inferred from the progenitor-to-descendant evolution of galaxies selected by their co-moving number densities reproduces the observed SFR–mass relations over the redshift range of this chapter. This provides a self-consistent check on the derived star formation history.

This chapter is outlined as follows. In § 2.3 we describe the CANDELS survey

data, sample selection, and the simulated and mock catalogs from models used in this work. In § 2.4, we define our SED fitting assumptions, including our choices of dust–attenuation prescription, and we introduce our method to include nebular line emission to stellar population synthesis (SPS) models. In § 2.5 we discuss our Bayesian method to derive our stellar mass and SFR estimates from the full posterior of each galaxy, marginalizing over other nuisance parameters. We show that the quantities derived by fitting to synthetic photometry from models agree well with the true model values. In § 2.6 we show the inferred SFR–stellar mass relation at $z \sim 4$, 5, and 6. We compute the slope and scatter in the SFR–mass relation, and we compare it to recent theoretical simulations. In § 2.7 we discuss the implications of the SFR–stellar mass relation, use an evolving number density to track the progenitor-to-descendant evolution within our sample, and measure the redshift evolution of the sSFR. Finally, in § 5.1 we summarize our conclusions. We also provide Appendices that support assuming a constant star formation history in the SED fitting process over histories that exponentially rise (Appendix A.1), argue how results using best-fit parameters from the SED fits provide less reliable conclusions due to best-fit results being (more strongly) affected by model assumptions (including nebular emission and dust attenuation, Appendix A.2), and outline how the adopted prior does not significantly influence the results of this work (Appendix A.3). Throughout, we assume a Salpeter (1955) IMF. Switching Salpeter to a Chabrier (2003) IMF would require reducing in log scale both the SFR and stellar mass by 0.25 dex. Throughout, we assume a cosmology with parameters, $H_0 = 70$ km s$^{-1}$ Mpc$^{-1}$, $\Omega_{\rm M,0} = 0.3$ and $\Lambda_0 = 0.7$. All magnitudes quoted here are measured with respect to the AB system, $m_{\rm AB} = 31.4 - 2.5 \log(f_\nu/1 \text{ nJy})$ (Oke & Gunn, 1983).

## 2.3 Observational Data and Simulations

### *2.3.1 CANDELS GOODS-S Multi-wavelength Data*

This chapter uses multi-wavelength photometry from the CANDELS GOODS-S field (Grogin et al., 2011; Koekemoer et al., 2011). In addition to CANDELS, this chapter includes the Early Release Science (ERS), Hubble Ultra Deep Field (HUDF), and deep IRAC imaging in all four IRAC channels (3.6–8.0 $\mu$m) from the *Spitzer* Extended Deep Survey (Ashby et al., 2013) programs. Throughout, we denote magnitudes measured by *HST* passbands with the ACS F435W, F606W, F775W, F814W and F850LP as $B_{435}$, $V_{606}$, $i_{775}$, $I_{814}$, and $z_{850}$, and with the WFC3 F098M, F105W, F125W, F140W, and F160W, as $Y_{098}$, $Y_{105}$, $J_{125}$, $JH_{140}$, and $H_{160}$, respectively. Similarly, bandpasses acquired from ground-based observations include the CTIO/MOSAIC U-band; VLT/VIMOS U-band; the VLT/ISAAC $K_s$; and VLT/HAWK-I $K_s$.

We use fluxes from the catalog constructed by Guo et al. (2013). Guo et al. selected objects via SExtractor in dual-image mode with $H$-band as the detection image. As described in Guo et al., two versions of the catalog were constructed using SExtrator parameters that were (1) optimized in detection threshold and object deblending to identify faint, small galaxies (the "hot" catalog) and (2) optimized to keep large, resolved galaxies from being subdivided into multiple objects (the "cold" catalog). Both catalogs are then merged whereby any object in the "hot" catalog that falls within the isophote of a galaxy in the "cold" catalog is removed in favor of the "cold"-catalog object.

The *HST* bands were point spread function (PSF)-matched and the photometry is measured on the *HST* bands using the SExtractor double-image mode described above. For the ground-based and IRAC bands, the catalog uses TFIT (Laidler et al.,

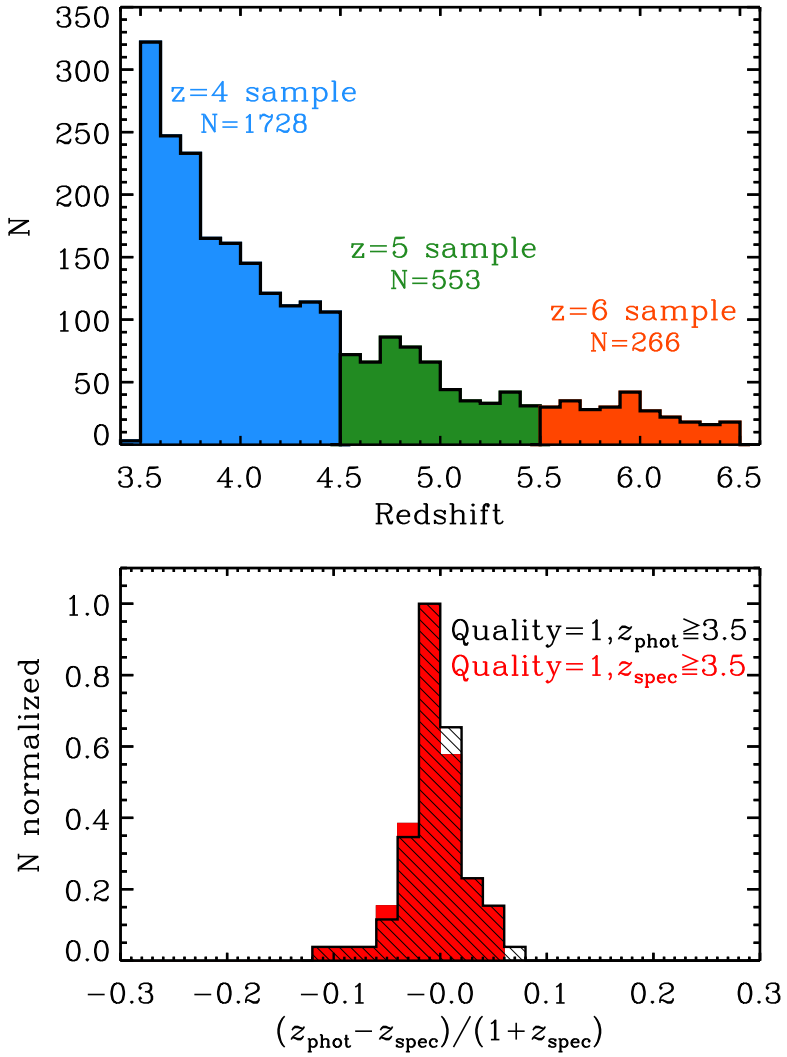


Figure 2.1: Redshift Accuracy and Sample Distribution.
*Top:* photometric redshift distributions for the objects used in this chapter. Throughout, the blue, green, and orange colors represent objects in our $z \sim 4, 5$, and 6 sample, respectively. *Bottom:* histograms of the photometric-redshift accuracy as compared to known highest quality (quality=1) spectroscopic redshifts. This figure shows that our $z_{\rm phot}$ catalog well represents the "true" best quality $z_{\rm spec}$ objects. Formally, the scatter in the photometric redshift accuracy is approximately $\sigma_{\rm MAD}/(1+z) = 0.016$ at $z \sim 4$ to 0.028 at $z \sim 6$.

2007) to measure photometry of these lower-resolution images using the *HST* WFC3 imaging as a high-resolution template for the galaxies. We use the final version of the GOODS-S TFIT catalog which includes the new $I_{814}$ (CANDELS) and $JH_{140}$ (HUDF12) photometry.

In addition to the flux densities and uncertainties provided in this catalog, we include an additional uncertainty, defined to be 10% of the flux density of each object in band. This additional uncertainty accounts for any systematic uncertainty that may be related to the source fluxes themselves. This includes, for example, flat-field variations, PSF and aperture mismatching, and local background subtraction, many of which will be (to first order) proportional to the flux itself. The value of 10% was chosen such that the distribution of reduced $\chi^2$ is $\geq 1$, and is justified based on arguments in Papovich et al. (2001). We add this uncertainty in quadrature to the measured uncertainties to estimate a total uncertainty on the flux density in each band for each object.

### *2.3.2 CANDELS GOODS-S Redshifts*

We use results from the recent CANDELS GOODS-S photometric-redshift project (Dahlen et al., 2013) which we briefly summarize here. A team of eleven investigators tested their individual photometric redshift fitting codes on blind control samples provided by the CANDELS team. A hierarchical Bayesian approach was then performed to combine the seven investigators' individual $P(z)$ distributions to a final $P(z)$ distribution for each object. The photometric-redshift ($z_{\rm phot}$) is thereafter derived as the weighted mean of this distribution. Another sample was constructed as the median $z_{\rm phot}$ of all eleven individual results. The $z_{\rm phot}$ distributions from the medians and the combined $P(z)$ methods both retained a lower scatter and outlier fraction than the results of any single investigator. Tests by Dahlen et al. (2013)

showed that the hierarchical Bayesian $z_{\rm phot}$ method produces the best (smallest) scatter between the $z_{\rm phot}$ and spectroscopic redshifts. Finally, these methods were applied to the same CANDELS TFIT catalog (Guo et al., 2013) from which our data were obtained.

Figure 2.1 compares redshifts from the combined $P(z)$ method with their highest-quality spectroscopic counterparts. The top panel exhibits a histogram of the number of objects used in our samples as a function of their photometric redshift. The bottom panel shows the ability of the photometric redshifts to recover known spectroscopic redshifts in the redshift range of this chapter.

Unless otherwise specified, we use the median absolute deviation (MAD) to compute the equivalent standard deviation, $\sigma_{\rm MAD}$, as the measure of scatter in given quantities (Beers et al., 1990), including the quoted scatter for redshift, stellar mass, and SFR. The $\sigma_{\rm MAD}$ is an analog for the 68% confidence, $\sigma$, if the error distribution were Gaussian and is therefore less sensitive to outliers (see Brammer et al., 2008). The MAD standard deviation in the photometric redshift accuracy ranges from $\sigma_{\rm MAD}/(1+z) = 0.016$ at $z \sim 4$ to 0.028 at $z \sim 6$, indicating that these photometric redshifts reliably recover known spectroscopic redshifts at high redshift.

Even in the highest quality spectroscopic redshift sample, there is a non-zero chance that some objects will have a misidentified $z_{\rm spec}$ due to a misinterpreted emission line or Lyman break (see discussion in Dahlen et al., 2013). So it is likely that some outliers are actually due to a misidentified $z_{\rm spec}$ rather than a poorly fit $z_{\rm phot}$ fit. The number of outliers where $|z_{\rm spec}-z_{\rm phot}|/(1+z_{\rm spec}) > 0.1$ are 2, 1, and 1 for $z \sim 4$, 5, and 6, respectively (only 5, 5, and 11% of each sample). For the remainder of this chapter we use the $z_{\rm phot}$ catalog derived from the combined $P(z)$ method, and substitute for high-quality ($z_{\rm qual} = 1$) spectroscopic redshifts when available.

### *2.3.3 Sample Selection*

We selected objects according to their photometric-redshift ($3.5 \leq z_{\rm phot} \leq 6.5$). This redshift range was chosen to be close to the redshift range of the traditional $B$, $V$, and $i$ -drop samples. The lower redshift bound was chosen to avoid higher photometric redshift uncertainties, which may be due to a weaker Lyman break signal at $z < 3.7$ (see Dahlen et al., 2013, their Fig. 11). Our samples have been cleaned from a total of 46 objects from X-Ray (Xue et al., 2011), IR (Donley et al., 2012), and radio (Padovani et al., 2011) detected AGN, as flagged by the Dahlen et al. (2013) photo-$z$ catalog.

Objects with a best-fit SED with $\chi^2 > 50$ are omitted from all samples. This cut removes objects with particularly poor fits, which comprise less than 4% of all objects. We interpret these objects as poor detections that do not well represent the data, and note that the removal of these objects do not impact the results of this chapter. The final sample includes 1728 objects with $3.5 < z < 4.5$, 553 objects with $4.5 < z < 5.5$, and 266 objects with $5.5 < z < 6.5$, as illustrated in Figure 2.1. We refer to these as the $z \sim 4$, 5, and 6 samples, respectively.

### *2.3.4 Galaxy Photometry from Models and Simulations*

This chapter takes advantage of recent mock catalogs with synthetic photometry for galaxies from semi-analytic models (SAMs), as well as a semi-empirical dark matter and hydrodynamic simulation. We collectively refer to these as "the models". The benefit of comparing our derived results against these model galaxies is that the models incorporate realistic star formation histories and galaxy physics. Here we use these models for two comparisons. First, in § 2.5.4 we derive stellar population parameters (SFRs and stellar masses) from the synthetic photometry for the model galaxies and compare to their "true" values as a test of our SED fitting procedures.

Second, in § 2.6.2.2 we use our derived SFRs and stellar masses from the CANDELS samples to compare to the models and interpret the SFR–mass relation and its scatter.

#### *2.3.4.1 SAMs of Somerville et al. and Lu et al.*

This chapter uses the results of two SAMs that were specifically designed for the CANDELS GOODS-S field (Somerville et al., 2008, 2012; Lu et al., 2014a,b, hereafter referred to as Somerville et al. and Lu et al. respectively), which we summarize here. Areas where the two SAMs differ are highlighted to emphasize the assumptions that lead to different SFR and stellar mass results. A more detailed comparison of the Somerville et al. and Lu et al. models can be found in Lu et al. (2014b).

The mock catalogs produced by the SAMs are based on the Bolshoi $N$-body simulation (Klypin et al., 2011) for the same field-of-view size and geometry as the CANDELS GOODS-S field. The two SAMs are applied on the halo merger trees for halos in the mock catalogs. The models adopted a cosmology favored by *WMAP7* data (Jarosik et al., 2011) and *WMAP5* data (Dunkley et al., 2009; Komatsu et al., 2009) with ΛCDM cosmology. The mass resolution of the simulation is $1.35 \times 10^8 h^{-1}\mathrm{M}_\odot$, which allows the SAMs to track halos and subhalos with mass $\sim 2.70 \times 10^9 h^{-1}\ \mathrm{M}_\odot$.

The SAMs make explicit predictions for gas cooling rates, star formation, outflows induced by star formation feedback, and galaxy-galaxy mergers for every galaxy in the mock catalog. Both models assume that gas follows dark matter to collapse into a dark matter halo. When the gas collapses into the virial radius of the halo, it is heated by accretion shocks and forms a hot gaseous halo that cools radiatively. If the cooling timescale is longer than the halo dynamical time, both models follow the treatment that the halo gas cools gradually and settles on a central disk. The central disk of cold gas in both models is assumed to have an exponential radial

profile, where stars form in regions where the surface density of the cold gas is higher than a threshold.

In the Somerville model, the SFR is predicted based on the cold gas surface density using the Schmidt–Kennicutt law (Kennicutt, 1998) explicitly. In the Lu et al. model, the star formation efficiency is assumed to be proportional to the total cold gas mass for star formation and inversely proportional to the dynamical time-scale of the disc, with an overall efficiency that matches observations (Lu et al., 2014a).

Star formation feedback is assumed in both models, but the implementations are slightly different. Both models assume that the feedback reheats a fraction of the cold gas in the galaxy and a fraction of the reheated gas leaves the host halo in a strong outflow. However, the Lu et al. model allows a fraction of the kinetic energy of supernovae (SN) to drive an additional outflow to expel a fraction of hot halo gas. Nevertheless, the mass loading of the outflow in both models is assumed to be proportional to the SFR, and inversely proportional to a certain power of the halo maximum velocity. In the Somerville model, the mass-loading factor is assumed to be inversely proportional to the second power of the halo maximum velocity, mimicking the so-called "energy driven wind." In the Lu et al. model, a much stronger power law of the halo circular velocity dependence is adopted. Both models assume a fraction of the ejected baryonic mass comes back to the halo as hot halo gas on a dynamical time-scale with different efficiencies.

The model parameters governing Star formation and feedback are tuned to match the local galaxy stellar mass function (Moustakas et al., 2013). The Lu et al. model is tuned using a Markov Chain Monte Carlo (MCMC) algorithm to find plausible models in the parameter space. The model precisely reproduces the local galaxy stellar mass function between $10^9$ and $10^{12}$ $M_\odot$, within the observational uncertainty. The Somerville model is further tuned based on a previously published model (Somerville

et al., 2008) against the new data. In spite of different parameterizations adopted by the two models, they yield qualitatively similar predictions for the assembly histories of galaxy stellar mass and SFR over cosmic time.

#### *2.3.4.2 Semi-empirical Matching of Observed Galaxies to Dark Matter Halos of Behroozi et al.*

The semi-empirical model employed by (Behroozi et al., 2013b, BWC13 hereafter) uses a flexible fitting formula for the evolution of the stellar mass–halo mass relation with redshift, ($SM(M_h, z)$; see BWC13 for further definition). This formula includes parameters for the characteristic stellar and halo masses, faint-end slope, massive-end shape, and scatter in stellar mass at fixed halo mass, as well as the redshift evolution of these quantities. Given halos from a dark matter simulation, each point in the $SM(M_h, z)$ function parameter space represents an assignment of galaxy stellar masses to every halo at every redshift; the simulation and halo catalogs used by BWC13 are detailed by Klypin et al. (2011) and Behroozi et al. (2013c,d). The abundance of halos as a function of redshift can then be used to calculate the implied stellar mass function; the buildup of stellar mass over time in halos' main progenitor branches can be used to calculate implied galaxy SFRs. BWC13 compares these predicted observables to published results from $z = 0$ to $z = 8$ and employs an MCMC algorithm to determine both the posterior distribution for $SM(M_h, z)$ and the implied $SFR(M_h, z)$. The resulting best-fits are consistent with all recent published observational results in this redshift range, including galaxy stellar mass functions, cosmic SFR, and sSFRs. Full details, including comparisons with other techniques for deriving the stellar mass–halo mass relation, are presented by BWC13.

#### *2.3.4.3 Hydrodynamic Simulation of Davé et al.*

This simulation was run with an extended version of the cosmological smooth particle hydrodynamic code Gadget-2 (Springel et al., 2005) described by Oppenheimer & Davé (2008). The simulation includes metal cooling and heating following Wiersma et al. (2009), star formation and a multi-phase interstellar medium model following Springel & Hernquist (2003), and galactic outflows assuming momentum-driven wind scalings which have been shown to be crucial for providing a reasonable match to a variety of intergalactic medium (IGM) and galaxy properties from $z \sim 0-4$ and beyond (see Davé et al., 2011b,a). The simulation employs a *WMAP-7* concordant cosmology within a co-moving cube of length 48 Mpc/h per side with $2 \times 384^3$ particles and 2.5 kpc/$h$ (co-moving) resolution. Mass growth in galaxies is resolved down to stellar masses of approximately $10^9 M_\odot$. See Davé et al. (2013) for a full description.

## 2.4 Stellar Population Synthesis Fitting: Methods

This section describes the methods and assumptions used by our SED fitting procedure to derive physical quantities. This chapter uses a custom fitting procedure, using an updated version of the methods described by Papovich et al. (2001, 2006).

We utilize the Bruzual & Charlot (2011, private communication) SPS models, which are created with an updated version of the Bruzual & Charlot (2003) source code (BC03 hereafter) modified to accept rising star formation histories, $\Psi \sim \exp(+t/\tau)$, where $\tau$ is the $e$-folding timescale. We opt to use the libraries included with the BC03 models, as recent results have suggested the alternative 2007 libraries (similar TP-AGB contribution as Maraston (2005)) overestimate the contribution from TP-AGB stars in the near infrared (NIR), and the original BC03 version is likely to be more realistic (Kriek et al., 2010; Conroy & Gunn, 2010; Mel-

bourne et al., 2012; Zibetti et al., 2013). Therefore, the remainder of this chapter uses the BC03 models. As mentioned above, we use a Salpeter (1955) IMF throughout which ranges in mass from 0.1–100 $M_{\odot}$.

Although we include the effects of H I absorption from IGM clouds along the line-of-sight to each galaxy (using the prescription of Meiksin (2006)), the true contribution of H I clouds to each galaxy will be highly stochastic. Therefore, we only include bands with wavelengths red-ward of the observed wavelength of Lyman-$\alpha$, given the galaxy redshift in our SED modeling. The redshift is fixed to the photometric redshift (or spectroscopic if available; see § 2.3.2), so fitting to bands blue-ward of Lyman-alpha offers no improvement in determining redshift.

Table 2.1 shows a list of the explored parameter space, as well as the degree to which each parameter is explored. The metallicity of all objects is fixed as 20% solar metallicity, partly due to a lack of confidence to accurately fit to this parameter given the degeneracies between fits to age and attenuation. The choice of 20% $Z_{\odot}$ is supported by recent work that suggests the metallicity of high-redshift ($z > 2$) galaxies is low (Erb et al., 2006a; Maiolino et al., 2008; Erb et al., 2010; Finkelstein et al., 2011, 2012b; Song et al., 2014, see also Mitchell et al. (2013) for a discussion on the effects of metallicity in SED fitting).

Table 2.1: SED Fitting Parameters.

| Parameter | Quantity | Prior | Relevant Sections |
|---|---|---|---|
| Redshift | fixed | photometric redshifts, $3.5 \leq z \leq 6.5$ | § 2.3.2 |
| Age | 74 | see equation A.1 [log, 10 Myr - $t_{\rm max}$] [1] | § 2.4, Appendix A.3 |
| Metallicity | fixed | 20% $Z_\odot$ ($Z = 4 \times 10^{-3}$) | § 2.4 |
| Star formation history [2] | fixed | 100 Gyr (constant) | § 2.4.1, Appendix A.1 |
| $f_{\rm esc}$ | fixed | 0 or 1 | § 2.4.2, Appendix A.2 |
| $E(B-V)$ [3] | 29 | see equation A.1 [Linear, 0.0 - 0.7] | § 2.4.3, Appendix A.3 |
| Attenuation prescription | fixed | starburst (Calzetti et al. 2000) or SMC (Pei et al. 1992) | § 2.4.3, Appendix A.2 |
| Stellar Mass | – | $M_\star > 0$, see equation A.1 | Appendix A.3 |

Objects are fit to all available ages between 10 Myr and the age of the Universe at the redshift of the object, which is at maximum 1.8 Gyr at $z = 3.5$. The age resolution of the BC03 models is quasi-logarithmic, with an average log difference in age steps of $\Delta t_{\rm age}/{\rm yr} = 0.02$ dex. We adopt a lower limit on the stellar population age of 10 Myr in order to avoid galaxies with ages younger than the minimum dynamical timescale of a galaxy at our specified redshifts (Papovich et al., 2001; Wuyts et al., 2009, 2011b). In practice, we find that this minimum age has no impact on the fully marginalized parameter distributions.

### *2.4.1 Star Formation History*

One of the aims of this chapter is to constrain the star formation history of the average population of galaxies at high redshift, $z > 3.5$. Previous works have shown that broadband SED fitting offers no statistical preference between constant, rising, or declining star formation histories, even with broadband coverage spanning to the IR (Reddy et al., 2012b). Furthermore, the star formation histories assumed in the templates can have non-negligible effects on the inferred SFRs, stellar masses, and ages (Lee et al., 2010). We addressed the shape of the star formation history as constrained by individual galaxies by running three separate fits using templates that assumed constant, declining and rising star formation history. The rising and declining star formation history templates ("$\tau$" models) included a suite of $e$-folding times. We ultimately found no obvious $\chi^2$ preference on the shape of the star formation history for individual galaxies.

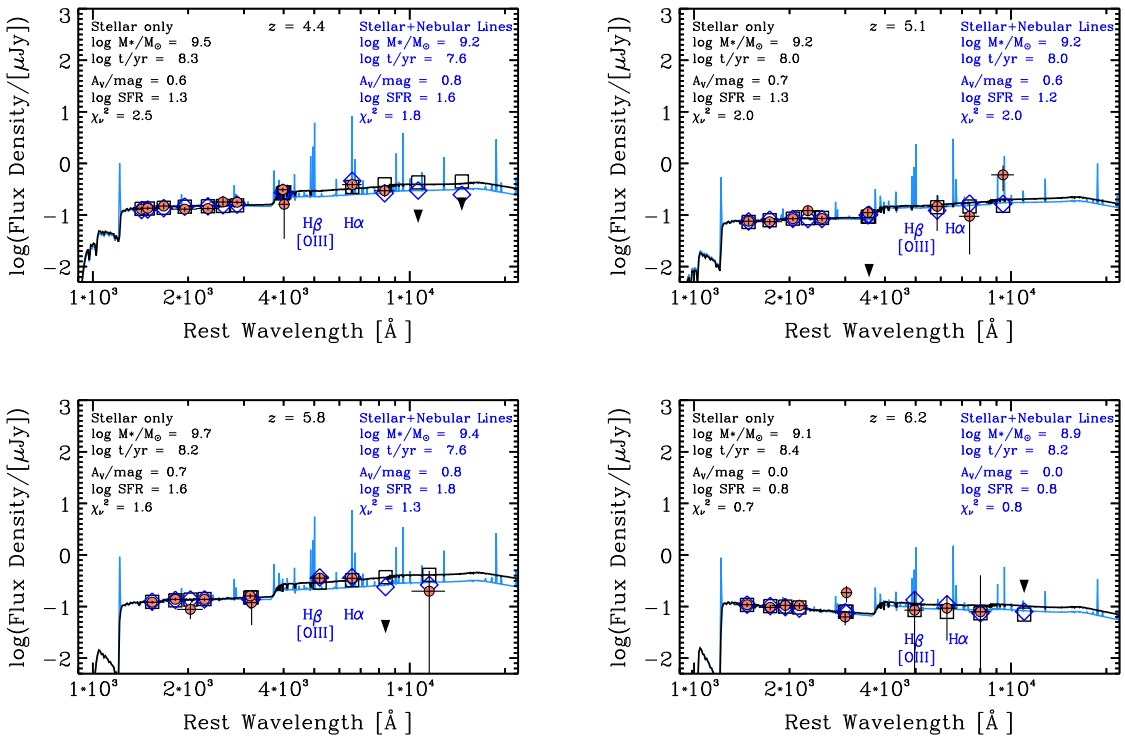


Figure 2.2: Example SEDs with and Without Nebular Emission.
Four example galaxies from our sample with SED fits that do include nebular emission lines (blue curves) and do not include emission lines (black curves). Circles are the observed photometry and diamonds (squares) are the fluxes of the best-fit SED with (without) emission lines. The legends indicate the parameters of the best-fit model for both the case where the nebular emission is excluded and included, as labeled. All objects were fit assuming a constant star formation history and starburst-like dust attenuation. At certain redshifts (including the objects with $z = 4.1$, 5.8, and 6.2), the IRAC 3.6 $\mu$m and 4.5 $\mu$m bandpasses may be enhanced by H$\beta$, [O III], or H$\alpha$ emission lines, as indicated. In contrast, the IRAC bands for the object with $z = 5.1$ do not include of these prominent emission lines.

Qualitatively, there has been some evidence to reject high-redshift star formation histories that decline with time. Previous studies have shown that high-redshift declining star formation histories would under-predict the sSFR at lower redshifts (Stark et al., 2009; González et al., 2010; Maraston et al., 2010). In addition, the

instantaneous SFRs derived when assuming a declining star formation history will be under-produced by a factor of 5-10 as compared to direct estimates based off of UV-to-mid-infrared emission (Reddy et al., 2012b). Other evidence against declining star formation histories comes independently from the SFR evolution of UV-luminous galaxies selected at fixed number density (Papovich et al., 2011). Finally, Pacifici et al. (2012) introduced a state-of-the-art SED fitting procedure with realistic, hierarchical mass-assembly histories and showed that declining $\tau$-model histories do not well represent galaxies even at $z < 2$.

Although galaxies at $z > 3$ likely have star formation histories that increase monotonically with time, we found it was impractical to use such models as the derived results are less physical. Our full justification for fitting individual galaxies with a constant star formation history is provided in Appendix A.1. Briefly, the BC03 stellar populations currently only allow for star formation histories that rise *exponentially* with time using simple parameterizations. At late times, such histories increase their SFR much faster than supported by observations. In Appendix A.1, we show that our modeling of synthetic photometry for galaxies from semi-analytic models recovers the most accurate stellar masses and SFRs when we adopt *constant* star formation histories. We interpret this as due to the fact that the SFRs in the models are approximately constant over the past $\sim$100 Myr (see, e.g., Finlator et al., 2006), and not consistent with exponentially increasing SFRs. Therefore, we fix the fitting templates to have a constant star formation history in our analysis of the CANDELS data for the remainder of this chapter. In a future work, we will explore possible improvements in parameters using models with star formation histories that increase as a power law in time ($\Psi \sim t^{\gamma}$).

### *2.4.2 Nebular Emission*

This section presents our method of incorporating nebular emission. Nebular emission is important because many galaxies at high redshift are observed to have intense star formation and high equivalent widths (EW) from emission lines (Erb et al., 2010; van der Wel et al., 2011; Atek et al., 2011; Brammer et al., 2013). Such strong nebular emission is able to enhance broadband flux by up to a factor of $\sim 2-3$ in IRAC 3.6 and 4.5 $\mu$m bands (Shim et al., 2011). Previous studies have shown that the flux excess from high EW emission lines causes a systematic decrement in stellar mass and SFR inferred from SED fitting (Schaerer & de Barros, 2009, 2010; Ono et al., 2010; Finkelstein et al., 2011; de Barros et al., 2014; Reddy et al., 2012b; Stark et al., 2013).

#### *2.4.2.1 Nebular Lines*

The strength of a given emission line is dependent on the properties of both the gas cloud and the incident ionizing source. These properties include metallicity, ionization parameter, electron density, and number of ionizing photons. Inoue (2011) explored these parameters and the resulting strength of nebular emission in the regime of high-redshift galaxies by utilizing CLOUDY 08.00(Ferland et al., 1998), which we use in our incorporation method.

After modeling a wide parameter space of seven metallicities, five ionization parameters and five Hydrogen densities, Inoue (2011) reports 119 sets of metallicity-dependent emission line strength relative to H$\beta$. These line ratios, ranging from 1216 Å to 1 $\mu$m, are in close agreement with empirical metal line ratios (Anders & Fritze-v. Alvensleben, 2003; Maiolino et al., 2008). We use the Inoue (2011) line ratios and include Paschen and Bracket series lines from Osterbrock & Ferland (2006) and Storey & Hummer (1995). Following Inoue (2011), we relate the H$\beta$ line luminosity

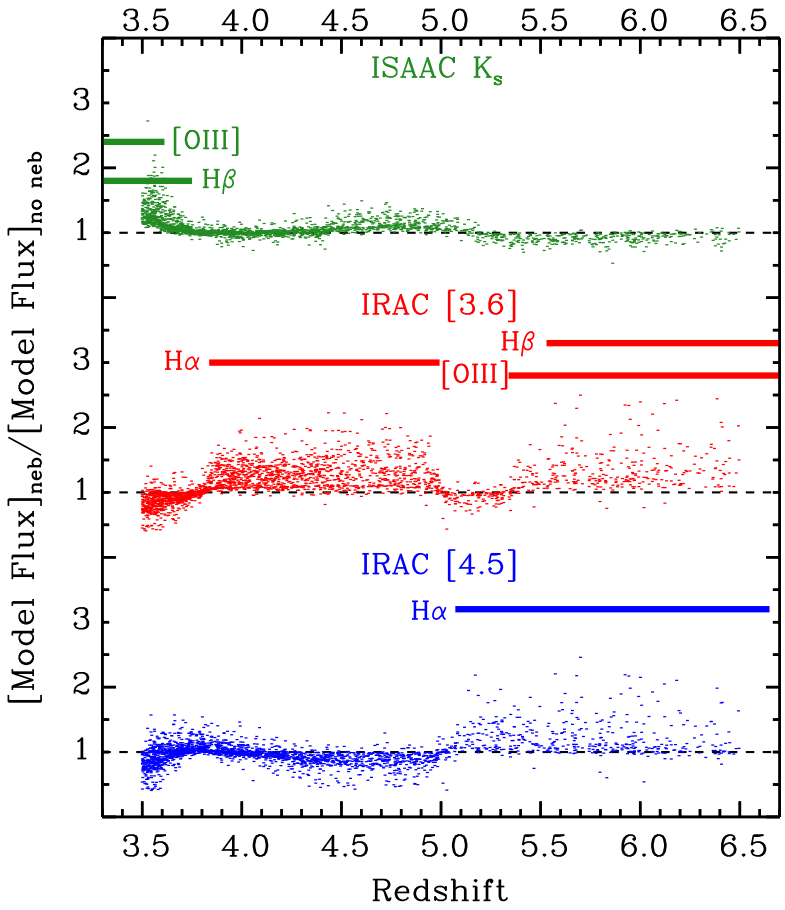


Figure 2.3: Flux Excess from Nebular Emission.
Best-fit SED model fluxes with and without emission lines are shown as ratios for ISAAC $K_s$, IRAC 3.6, and IRAC 4.5 bands as a function of redshift. Horizontal lines describe the redshift at which a strong emission is in the bandpass. The effect of adding emission lines is an increase to the model fluxes by as much as a factor of 2–3, especially in case of strong emission lines, such as [O III] or H$\alpha$.

to the incident number of Lyman-continuum photons as

$$\mathrm{L_{H\beta}} \;=\; 4.78 \times 10^{-13} \frac{1 - f_{\mathrm{esc}}}{1 + 0.6 f_{\mathrm{esc}}} \mathrm{N_{LyC}} \; [\mathrm{erg\ s^{-1}}], \tag{2.1}$$

where $f_{\mathrm{esc}}$ is the fraction of ionizing Lyman continuum (LyC) photons escaping the galaxy into the IGM and $\mathrm{N_{LyC}}$ is the production rate of Hydrogen-ionizing photons (see also Osterbrock & Ferland, 2006; Ono et al., 2010). The number of ionizing Lyman-continuum photons, $N_{\mathrm{LyC}}$, depends on the age of the stellar population, and we take $N_{\mathrm{LyC}}$ from each BC03 SPS model for each age. It follows that $1 - f_{\mathrm{esc}}$ is the fraction of LyC photons that ionize gas within the galaxy, which then produce the emission lines. The additional factor in the denominator of equation 2.1 comes from a ratio of recombination coefficients (see Inoue, 2011). Here, we equate the metallicity of the nebular gas to the metallicity of the SPS template (set as $Z = 20\%\ Z_{\odot}$ for all models, see above). Following the results of Erb et al. (2006b), we attenuate both nebular and stellar emission in the same manner (see § 2.4.3 for details on attenuation).

The escape fraction has been measured to be low, i.e., $f_{\mathrm{esc}} \approx 0$ at low redshift $z \sim$1 (see Malkan et al., 2003; Siana et al., 2007, 2010; Bridge et al., 2010). At $z \gtrsim 4$, the IGM imparts a large optical depth to ionizing photons, making it difficult to constrain $f_{\mathrm{esc}}$. Nestor et al. (2011) used $z \sim 3$ Lyman Break Galaxies to study the high-redshift escape fraction, finding it to be consistent with $f_{\mathrm{esc}} \approx 0.1$. Finkelstein et al. (2012a) concluded that if galaxies are the main contributors to reionization, then the escape fraction must be $f_{\mathrm{esc}} < 0.34$, or $f_{\mathrm{esc}} < 0.13$ ($2\sigma$) at $z \sim 6$ if the luminosity function extends to fainter galaxies than those observed, in order for the inferred ionization from galaxies to be consistent with the ionization background inferred from quasar spectra (Bolton & Haehnelt, 2007). In addition, Jones et al.

(2013b) reinforced this claim by finding the covering fraction of neutral hydrogen in $z \sim 4$ galaxies to be lower by 25% compared to $z \sim 2$-3. From these results, it seems reasonable to assume a low, but non-zero, escape fraction at high redshift.

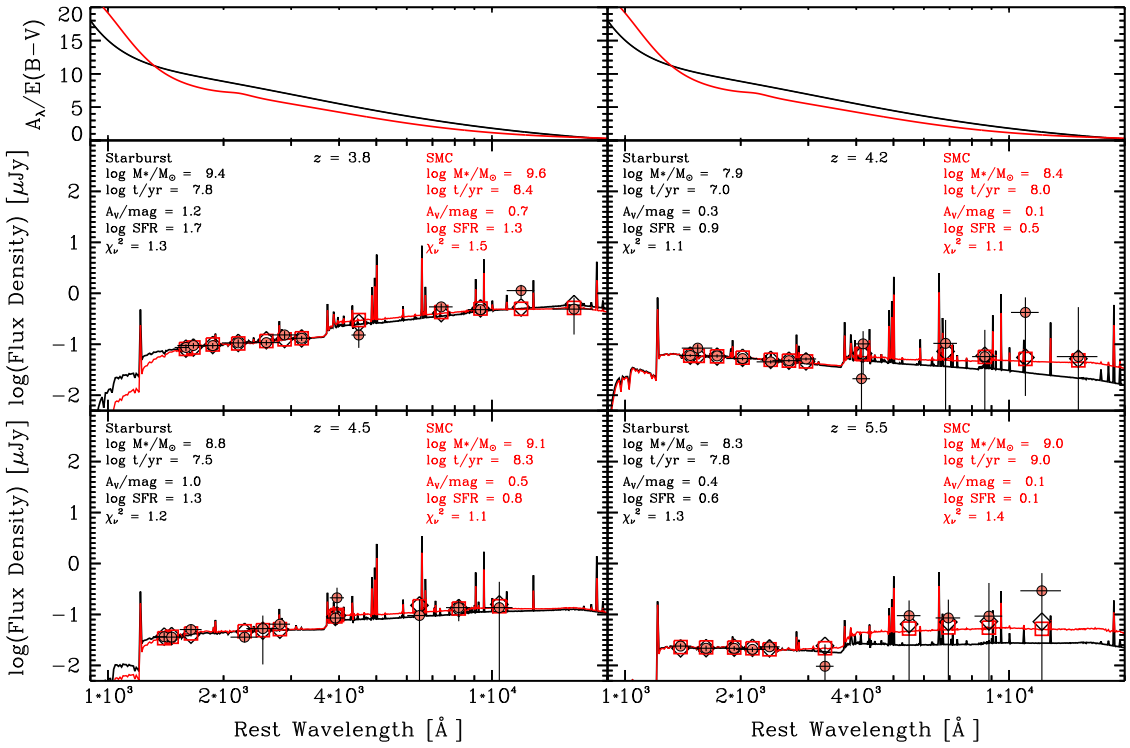


Figure 2.4: Examples of SEDs Assuming Different Dust Laws.

Four example galaxies with the largest differences in the SFR derived from the best-fit models using SMC and starburst attenuations. For each galaxy, the best-fit SEDs are shown for SMC (red) and starburst (black) attenuations. Circles are the observed photometry and squares (diamonds) are the fluxes of the best-fit SED with SMC (starburst) attenuation assumed. The legends indicate the derived properties when assuming each attenuation. All objects were fit assuming a constant star formation history with nebular emission lines. Objects may have similarly shaped SEDs, but the difference in $A_V$ drives the change in the inferred parameters. In all cases, the $\chi^2$ values are equal or exhibit no preference for the SMC or starburst attenuations.

Here we consider two limiting cases. The first has $f_{\rm esc} = 1$, for which all LyC photons escape the galaxy, preventing the creation of nebular emission and reverting the spectrum to the output of the SPS model. The second case has $f_{\rm esc} = 0$, for which all LyC photons are absorbed and their energy is converted into the nebular emission spectrum. These two cases span the range of possibilities and allow us to study the effects of nebular emission on the inferred physical parameters. Nevertheless, given current constraints of $f_{\rm esc} \sim 0.1$ (see above), we expect the $f_{\rm esc} = 0$ case will provide a more physical model for galaxies in our sample.

To illustrate the effect of nebular emission, Figure 2.2 displays four examples that include the best-fit SED models with and without nebular emission lines for galaxies. Depending on the redshift, emission from H$\alpha$ and/or [O III] will enhance the IRAC flux and can lead to highly different model-parameter values. The effect of nebular emission lines on the inferred stellar mass has a simple, qualitative explanation: the flux excess to the optical bands from nebular emission mimics a strong Balmer break that is typical for massive, older stellar populations. In this sense, when it is assumed that all of the observed broadband flux is produced by stars when much of it is produced by nebular emission, the inferred stellar mass will be over-estimated.

Similarly, Figure 2.3 illustrates how the specific emission lines ([O III], H$\beta$ , and H$\alpha$ ) affect the bandpass-averaged flux densities for the observed $K_s$ and IRAC [3.6] and [4.5] bands from the best-fit SED models. The inclusion of [O III], H$\alpha$, and H$\beta$ lines raise the flux of these bands by up to a factor of $\sim$2. In Appendix A.2, we explore how the effects of nebular emission lines change the best-fit stellar masses and SFRs. However, as we show below, these changes are largely mitigated using our Bayesian formalism.

#### *2.4.2.2 Nebular Continuum*

Evolutionary synthesis modeling suggests that nebular continuum emission can impact broadband photometry (Leitherer & Heckman, 1995; Mollá et al., 2009; Raiter et al., 2010). In addition, recent observational evidence has discovered the presence of strong nebular continuum in star-forming galaxies (Reines et al., 2010). The inverse Balmer and Paschen breaks (Balmer and Paschen "jumps"), may contribute additional flux red-ward of rest-frame optical wavelengths (Guseva et al., 2006). We currently omit these effects, as the strongest nebular continuum is present at wavelengths redder than rest-frame 8 $\mu$m (observed-frame $36-60$ $\mu$m for the redshift range investigated here), where the objects in this chapter are not well observed (see Zackrisson et al., 2008).

### *2.4.3 Dust Attenuation Prescriptions*

Recent work has suggested that the typically assumed Calzetti et al. (2000) attenuation prescription for star-forming galaxies is not ubiquitous (Reddy et al., 2012b; Oesch et al., 2013; Chevallard et al., 2013; Kriek & Conroy, 2013). The slope of the attenuation curve or presence of the UV dust bump at 2175 Å may be dependent on the galaxy type, geometry, metallicity, or inclination. However, galaxies at $z > 4$ currently lack sufficient observations to quantify these effects, so some attenuation prescription must be assumed. This chapter aims to test the effects of changing the type of assumed attenuation in order to gauge its impact on our broadband SED fitting procedure. In this subsection, we describe the two different attenuation prescriptions used in this chapter: the Calzetti et al. (2000) attenuation prescription ("starburst"-like attenuation, hereafter), and the Pei (1992) attenuation prescription derived for the SMC ("SMC"-like attenuation, hereafter).

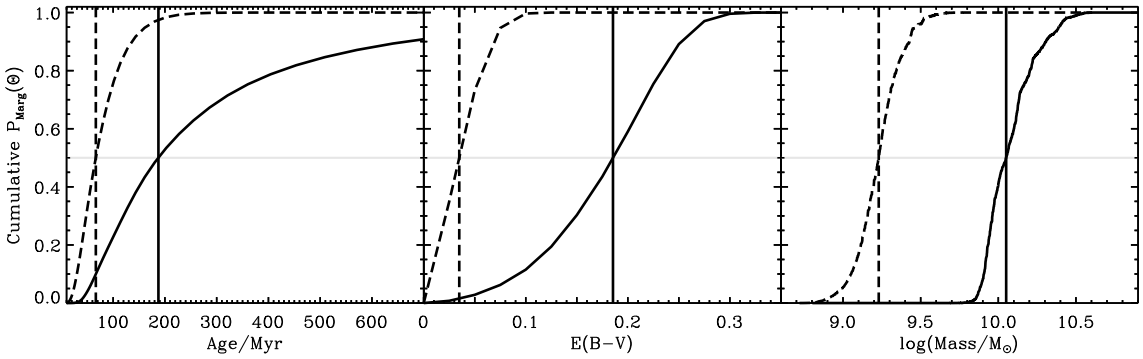


Figure 2.5: Examples of Marginalized Posteriors.
Examples of the posterior cumulative probability densities on a given model parameter value, $\Theta$, for a galaxy with higher extinction (solid lines) and one with lower extinction (dashed lines), with $z_{\rm spec} = 4.142$ and 3.791, respectively. The posteriors in age are often broad, as it is the least constrained parameter. The posteriors in stellar mass are typically narrower. Throughout, we assign the medians of each parameter's posterior (taken as the 50th percentile, shown as vertical lines) as the accepted value, with the 68% confidence range as the region that spans the 16th to 84th percentiles.

Figure 2.4 shows four example best-fit SEDs of objects that emphasize the difference in SFRs for best-fit models using the SMC and starburst dust prescriptions. The starburst attenuation has a much "grayer" wavelength dependence in the UV than the SMC-like attenuation. This means the SMC-like attenuation curve has a much stronger attenuation at rest-frame, far-UV wavelengths $\lambda \lesssim 1200$ Å, and a weaker attenuation across near-UV-to-near-infrared wavelengths $\lambda \gtrsim 1200$ Å, as shown in the top two panels of Figure 2.4. As stated above, bands shortward of Ly$\alpha$ are omitted in our procedure, so we do not fit where the difference between attenuation prescriptions is strongest.

We find no obvious preference in $\chi^2$ between the best-fit models for an SMC-like or starburst-like attenuation, and thus cannot as yet promote the use of one prescription

over the other from this data set. However, we argue that the SMC-like attenuation could be invoked as a physical prior to reconcile the unphysical, extremely young stellar population ages that result from assuming a starburst-like attenuation. This method is preferred over, for example, increasing the minimum allowed age in the models (e.g., from $\geq$ 10 Myr to $\geq$ 60 Myr), which will not remove the preference of the fit to choose the youngest available age. A similar line of reasoning is used by Tilvi et al. (2013) to argue for SMC-like attenuation over starburst-like attenuation. Nevertheless, as we will show in § 2.5.3, in our Bayesian formalism these differences arising from changes in the dust prescription are mitigated, and the dust attenuation prescription has negligible impact on the results here.

## 2.5 A Bayesian Approach to Determine Physical Parameters

This section describes our method to measure the posterior probability density for each object and shows how the likelihoods for each stellar population parameter were determined during the SED fitting. For the remainder of this chapter, we consider the fully marginalized posterior probability density functions to derive constraints on physical quantities such as stellar population age, galaxy attenuation (i.e., dust extinction), SFR, and stellar mass.

### *2.5.1 Probability Density Functions: Methods*

Given a set of data for an individual galaxy which is a function of flux densities, $\mathrm{D}(f_\nu)$, we derive the likelihood,

$$P(D|\Theta') \propto \exp(-\chi^2/2) \tag{2.2}$$

where $\chi^2$ is measured between the data, $D$, and a model in the usual way for a given set of model stellar population parameters, $\Theta' = (\Theta\{t_{\rm age}, \tau, A_{\rm V}\}, \mathrm{M}_\star)$. Note that the

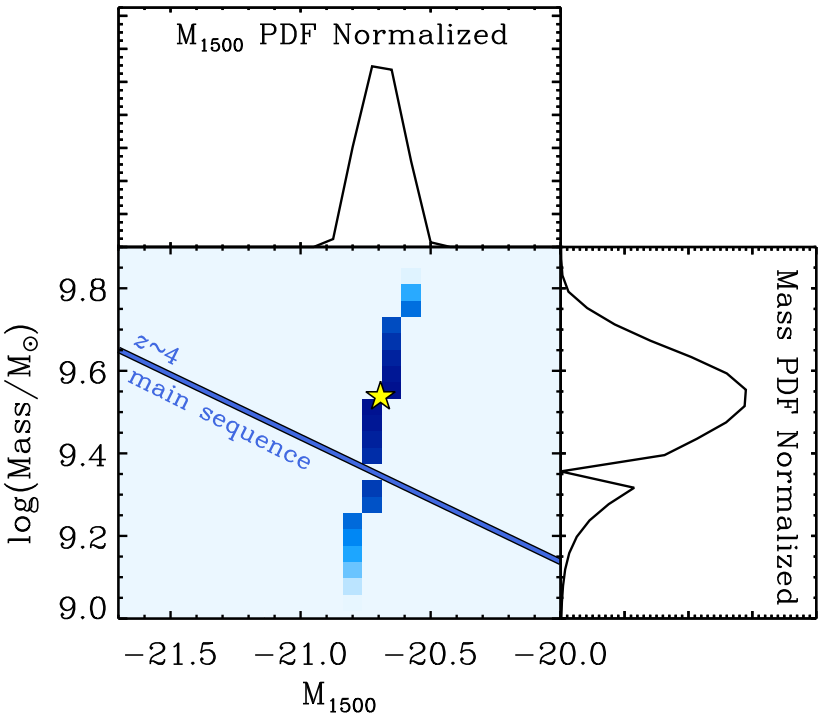


Figure 2.6: Example 2D Posterior in $M_{1500}$ and Stellar Mass.
An example of the posterior, joint probability density between stellar mass and $M_{1500}$ for a single object (where here $M_{1500}$ is the observed value derived from the model parameters analogous in the way for the stellar mass, and is uncorrected for dust attenuation). Darker blue regions show higher probability density, and the yellow star denotes the accepted (median) values. The lower left to upper right covariance is typical for most objects and results from covariances between the extinction and age parameters. It is noteworthy that the scatter in $M_{1500}$-$M_\star$ for a single object is roughly orthogonal to the direction of the $M_{1500}$-$M_\star$ "main sequence" as derived from the full sample (see Fig. 2.10). Therefore, this scatter in $M_{1500}$-$M_\star$ likely contributes to the scatter in the SFR–mass sequence discussed later.

likelihood in equation 2.2 is constructed based on linear fluxes. We then find the posterior probability density for any parameter given an observed set of data, $D$, and probability density using Bayes' theorem (see also, Moustakas et al., 2013),

$$P(\Theta'|D) = \ P(D|\Theta') \times p(\Theta')/\eta \tag{2.3}$$

where $\Theta'$ represents the fitted parameters $\Theta$ and $\mathrm{M}_\star$, and $\eta$ is a constant such that $P(\Theta'|D)$ will normalize to unity when integrated over all parameters (see Kauffmann et al., 2003). $p(\Theta')$ represents the priors on the model parameters, and is described further in Appendix A.3. As described in § 2.4 and Table 2.1, we have adopted a prior (quasi-logarithmic) on the age from 10 Myr to the age of the Universe for a galaxy's redshift, and we have adopted a prior (linear) that the attenuation is non-negative up to a maximum value. Further details on these priors and their effect on the fitting can be found in Appendix A.3.

We then derive posterior probability densities on individual parameters such as $t_{\mathrm{age}}$, $A_{\mathrm{UV}}$, etc. For example, the posterior on the age can be written as,

$$P(t_{\mathrm{age}}|D) \ = \int_{A_{\mathrm{UV}},\tau} P(t_{\mathrm{age}}, A_{\mathrm{UV}}, \tau|D) \ dA_{\mathrm{UV}} \ d\tau, \tag{2.4}$$

where the integration is a marginalization over "nuisance" parameters, dust attenuation, $A_{\mathrm{UV}}$, and possible star formation histories/$e$-folding timescales, $\tau$[4].

The stellar mass must be treated differently because it is effectively a scale factor in the fitting process. In order to derive its posterior probability density we must integrate over all parameters, $P(\mathrm{M}_\star|\mathrm{D}) \propto \int P(\mathrm{D}|\Theta') * p(\Theta') d\Theta$. The mean and variance of the stellar mass can be computed as the first and second moments of the

[4]Here, we ultimately set the star formation history to be constant (a single value of $\tau$) for the reasons discussed in the S 2.4.1 and Appendix A.3.

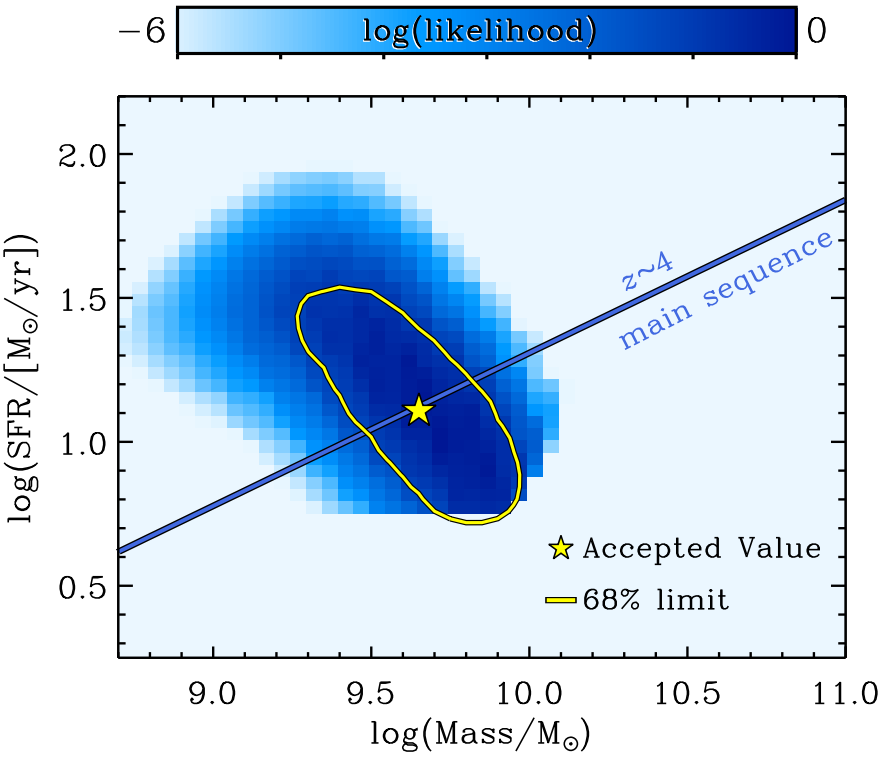


Figure 2.7: Example 2D Posterior in Stellar Mass and SFR.
An example of the posterior joint probability between the SFR and stellar mass for one object. Darker blue regions show higher probability density and the yellow star denotes the accepted (median) values. The range in SFR is driven nearly entirely by the posterior probability density for attenuation, as described in the text (see equation 2.5). The covariance in SFR and stellar mass is mostly orthogonal to the "main sequence" as derived from the full sample (see Fig. 2.11), which implies that the scatter in the SFR–$M_\star$ relation for individual galaxies translates to scatter in the SFR–$M_\star$ relation for the galaxy population.

posterior. Similarly, the median stellar mass is defined as the value of $M_\star$ such that the integral over the posterior from negative infinity to $M_\star$ is equal to 50%, while the 68% confidence range can be calculated by integrating the posterior from the 16th to 84th percentiles.

### *2.5.2 Probability Density Functions: Results*

We computed the posterior probability densities for all galaxies in our sample, including posteriors for the stellar mass, age, and attenuation, using the methods described above. Figure 2.5 shows examples of the cumulative posteriors on age, attenuation (or color excess, $E(B-V)$), and stellar mass for two galaxies in our sample: a relatively un-extincted and a relatively extincted galaxy. These objects are typical of those in the sample, where the posterior for age is typically broad, while that for the stellar mass is relatively tighter.

In our analysis below, we will consider the relation between stellar mass and UV magnitude, as well as stellar mass and SFR for our full galaxy sample. Here, we discuss the relation between stellar mass and these quantities for an individual object, as it is illustrative. Figure 2.6 shows a two-dimensional probability density function between stellar mass and UV absolute magnitude. Here we take the $M_{1500}$ from the conditional posterior on age and attenuation (similar to way we derive the posterior for stellar mass given the model parameters and data). Figure 2.6 also shows the posterior for $M_{1500}$ and stellar mass individually.

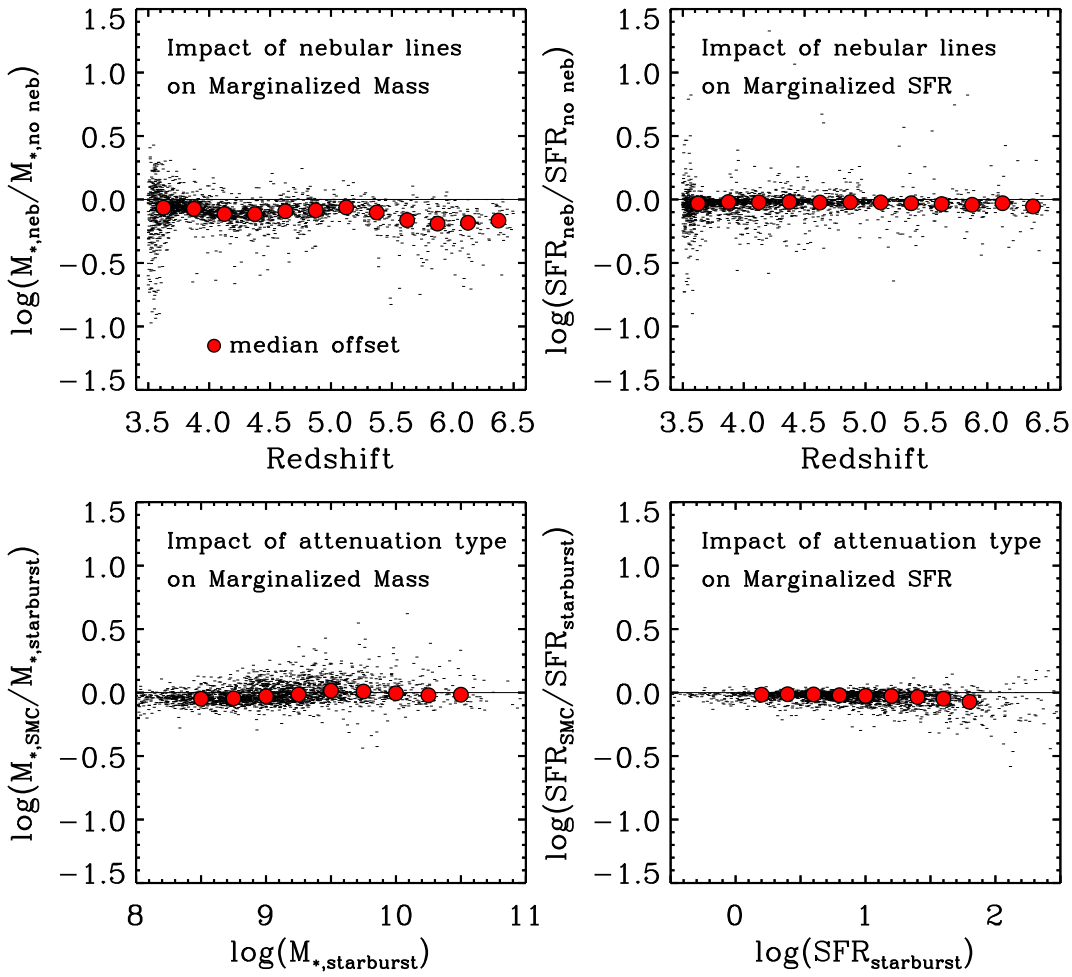


Figure 2.8: Impact of Nebular/Dust Treatment on Marginalized Values. The change in SFRs and stellar masses derived from the galaxy posteriors using different model assumptions. The top panels compare the SFRs and stellar masses derived using models that include and exclude nebular emission lines. The inclusion of nebular emission lines has minimal effect on the SFRs ($\lesssim 0.1$ dex), and the stellar masses have a slight decrease ($0.1 - 0.2$ dex) when nebular emission lines are included. The bottom panels compare SFRs and stellar masses derived using models with SMC-like and starburst-like dust attenuation. Here, varying the dust attenuation prescription has a negligible impact on the derived SFRs and stellar masses. These results can be directly compared to the results derived from best fits, which show much stronger differences in these quantities derived from these models (see Appendix A.2).

There is a weak covariance between $M_{1500}$ and $M_\star$, which results from the degeneracy in dust attenuation and age. A galaxy with a redder rest-frame UV continuum has near equal likelihood to a model with an older, less extincted stellar population as to a model with younger, higher extinction. The two models produce a joint posterior that is anticorrelated between $M_{1500}$ and stellar mass. The figure also shows the "main sequence" of the $M_{1500}$–$M_\star$ relation as derived from the full sample (see Fig. 2.10). The joint posterior is approximately orthogonal to the main sequence, which implies that the likelihood scatter in each galaxy's $M_{1500}$–$M_\star$ plane will lead directly to scatter in the main sequence of the sample. We return to this point in the discussion of the SFR-$M_\star$ relation below.

We derive the SFR from the model parameters in the following manner. We first determine the rest-frame UV luminosity at 1500 Å. At these redshifts, a large sample of detections red-ward of the rest-frame optical are unavailable, which can cause age and attenuation inferred from SED fitting to be degenerate quantities. These degeneracies can bias the $M_{1500}$ inferred from the model parameters, especially if limited to best-fit values (see the discussion above and Appendix A.2). For this reason, we choose the closest observed band to rest-frame 1500 Å as a more observationally motivated value of $M_{1500}$ because the broad-band photometry well samples the rest-frame UV portion of the SED. Galaxies have relatively blue rest-frame UV colors, so any corrections between the band closest to 1500 Å and the interpolated magnitude at 1500 Å are small (in the "extreme" examples of Figure 2.4 the differences are $<$ 0.1 mag). Furthermore, our tests show that none of our conclusions depend strongly on the manner we use to obtain $M_{1500}$.

The 1500 Å luminosity is corrected for dust attenuation using the median from the posterior of the attenuation at 1500 Å, or $A_{\rm UV}$. The dust-corrected UV luminosity is converted to the $\rm SFR_{UV}$ using the ratio $\kappa(t, \tau) = \rm SFR_{UV}/L_{1500}$. This is similar to the

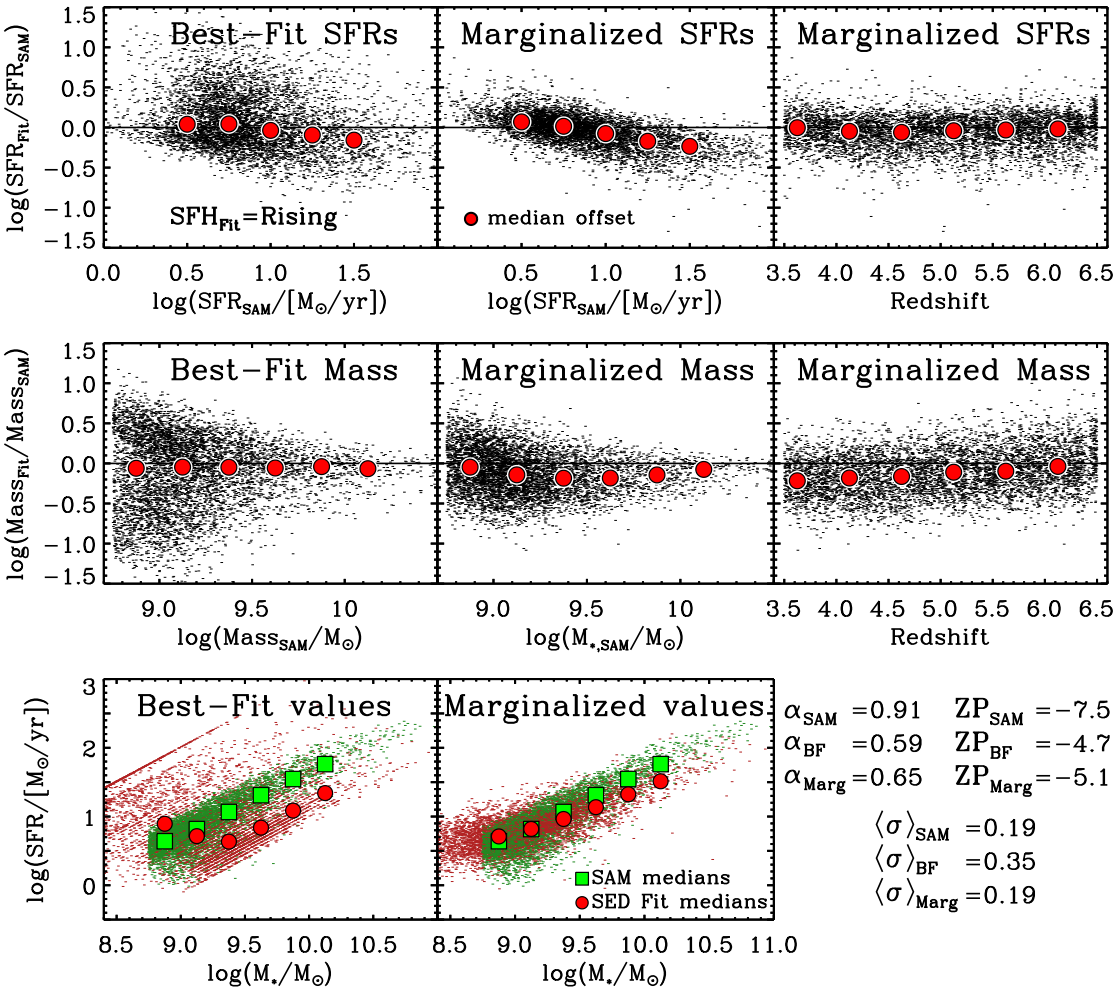


Figure 2.9: Testing Our Results with Semi-Analytic Models.
Tests of the derived SFRs and stellar masses from the posteriors of our SED fitting to synthetic photometry of mock catalogs from the SAM of Somerville et al. The top panels show the log difference of measured-to-true SFRs. The derived SFRs show a weak trend in that our fits overestimate the SFRs of low-SFR objects and underestimate the SFRs of high-SFR objects. The middle panels show the ratio of the measured-to-true stellar masses. The scatter in the derived stellar masses from their true values likely arises from our simple prescription for the star formation histories (similar offsets are observed by Lee et al. (2010)). The bottom panels show that our derived SFRs and stellar masses recover the SFR–mass relation in the models, though with a more shallow slope. The legend to the lower right indicates the slope, zero point, and scatter of the SFR–mass relation for the SAMs and those recovered using best-fit values or our preferred marginalized values. The main point of the figure is that the bayesian method does better at recovering both the SFRs and stellar masses and the SF main sequence.

conversion given by Kennicutt (1998), but we account for variations in $\mathrm{SFR_{UV}}/L_{1500}$ owing to the age ($t$) and star formation history ($\tau$) of the stellar population (see, Reddy et al., 2012b). For each object, we use the median stellar population age from the posterior to calculate $\mathrm{SFR_{UV}}/L_{1500}$. However, we note that because most of these median ages from posteriors are >100 Myr for the galaxies in our sample and we have assumed constant star formation histories, in most cases $\kappa(t, \tau)$ is very similar to that of Kennicutt (1998).

We summarize the derivation of our $\mathrm{SFR_{UV}}$ mathematically as follows.

$$\mathrm{SFR_{UV}} = f_{\mathrm{CB}} \cdot \frac{4\pi D_L^2}{1+z} \cdot 10^{0.4\ A_{\mathrm{UV}}} \cdot \kappa(t, \tau) \tag{2.5}$$

where $f_{\mathrm{CB}}$ is the flux of the closest band to rest-frame 1500 Å, $D_L$ is the luminosity distance, $A_{\mathrm{UV}}$ is the median, marginalized attenuation at 1500 Å, and $\kappa$ is the modified Kennicutt (1998) conversion that depends on age ($t_{\mathrm{age}}$) and star formation history ($\tau$).

The differences between the SFRs derived using equation 2.5 and other common methods are described in Appendix A.2. In summary, methods that derive the SFR using the best-fit or direct UV luminosity slope exhibit higher scatter when compared to the marginalized SFR method from this chapter. This scatter stems from degeneracies between the young, dusty and old, dust-free solutions of a given SED, and photometric uncertainties (which affect the accuracy of measuring the UV spectral slope). We find the results of our method more robust as it reproduces SFRs from SAMs (see § 2.5.4), and our method is relatively unaffected by model variations such as extinction prescription and/or nebular emission lines.

Figure 2.7 shows the SFR–stellar mass joint posterior for one object from our sample. As with the $\mathrm{M_{1500}}$–$\mathrm{M_\star}$ example, the covariance is roughly orthogonal to

the star formation main-sequence, but there is more scatter because of the range in dust attenuation (and, to a lesser extent, the stellar population age). The errors on the measured (extrinsic, or attenuated) $M_{1500}$ are relatively small as they stem from photometric errors only, whereas the SFR depends on the UV luminosity corrected by the UV extinction, $A_{UV}$.

SED models with higher $A_{UV}$ have higher stellar-mass–to–light ratios (and therefore higher stellar masses at fixed UV luminosity). This induces some correlation in the SFR–stellar mass plane for each object. However, the covariance is mostly orthogonal to the expected direction of the SFR–stellar mass correlation, which implies that it contributes mostly to the scatter of the SFR–stellar mass relation and less to the correlation itself. In our analysis we take this covariance into account using Monte Carlo simulations (see § 2.6.2.1).

### *2.5.3 Impact of SED Fitting Assumptions on Marginalized Values*

Here we discuss our SED model assumptions and their impact on derived quantities such as SFR and stellar mass using our Bayesian method. In Appendix A.2, we show that these model choices have a significantly stronger impact on best-fit results, while the results using medians derived from posteriors are relatively unaffected.

The panels of Figure 2.8 show that the SFRs and stellar masses derived from the posteriors for the galaxies in our sample are rather insensitive to the choice of dust-attenuation prescription or the presence/exclusion of nebular emission (where we compare the results with $f_{esc}$=0 or 1). In general, varying the assumed dust attenuation prescription has a negligible impact on the derived SFRs and stellar masses (differences are <0.1 dex over the redshift range of our sample). Similarly, including emission lines has minimal effect on the SFRs ($\lesssim$ 0.1 dex).

There is some evidence that the stellar masses are reduced slightly when the

models include nebular emission lines. This is in the same direction but weaker in magnitude as seen in comparisons of the best-fit models (e.g., see Appendix A.2). However, the effect is only a slight decrease of $< 0.25$ dex, and is typically less than the measurement errors on mass derived from the posteriors. Therefore, the inclusion of nebular emission does not strongly impact the SFRs or stellar masses. For this reason, we have neglected exploring nebular emission over the full range of $f_{\rm esc}$ values in our analysis, and instead report results assuming $f_{\rm esc} = 0$ (all ionizing radiation is absorbed and produces emission lines).

The results from Figure 2.8 can be directly compared to the results derived from best-fits, which show stronger differences in these quantities when switching between the above model assumptions (see Appendix A.2). In contrast to using best-fit values, the Bayesian method uses the likelihood of all the models, and so even if there is a "highest likelihood" solution of low age, there are many good solutions with larger ages, and when marginalized, the latter dominate the posterior.

#### *2.5.4 Tests of Derived SFR and Stellar Masses Using Semi-Analytic Models*

We tested the ability of our SED fitting procedure to reproduce accurately the SFRs and stellar masses in mock galaxy catalogs. We used synthetic galaxy photometry in the CANDELS bandpasses derived from the Somerville et al. SAM discussed in § 2.3.4.1. The advantage of using synthetic catalogs from a SAM is that the models include realistic (and complex) star formation histories, as well as more sophisticated treatments of extinction (e.g., Charlot & Fall, 2000). Therefore, the mock catalog from the SAM acts as a realistic observation where many of the model parameters (star formation history, extinction prescription) are known, and are distinct from the simpler models used in SED fitting to fit to the galaxy photometry. Comparing to the SAMs therefore provides a powerful test of our method to recover physical stellar

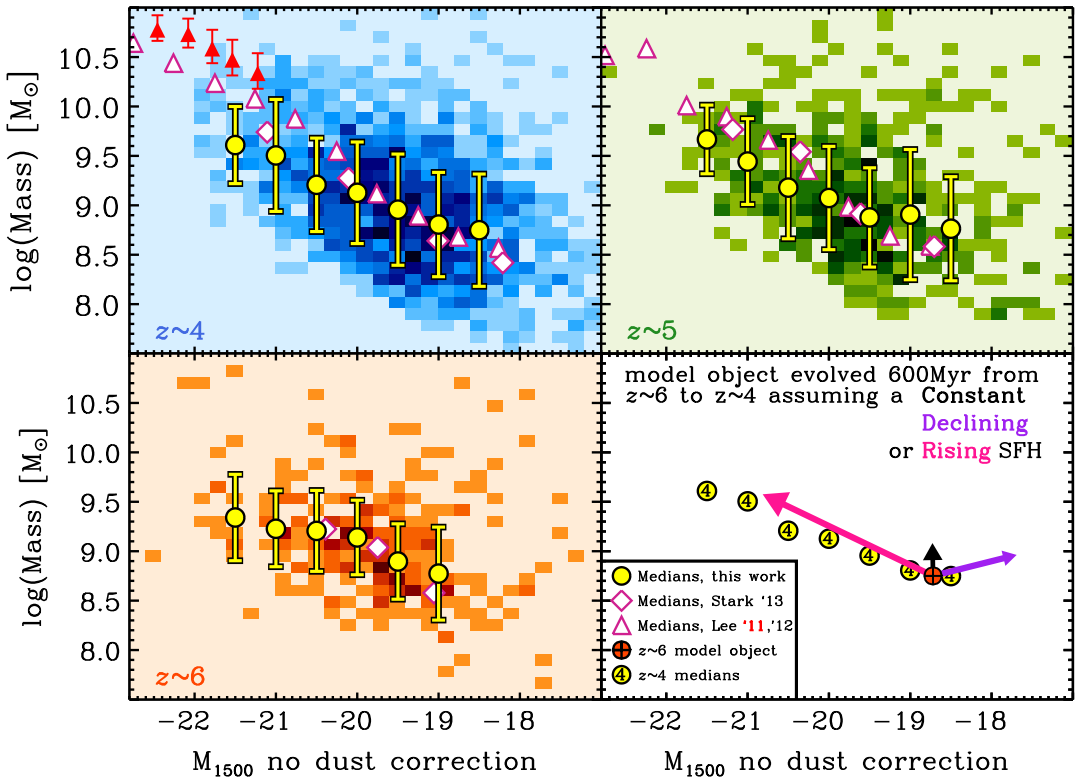


Figure 2.10: The Relation Between Stellar Mass and $M_{1500}$.
The closest band to rest-frame UV magnitude ($M_{1500}$) versus stellar mass. Darker-shaded regions indicate a higher number of individual objects in bins of stellar mass and $M_{1500}$. Yellow circles are the medians of stellar mass in a given $M_{1500}$ bin and error bars are the $\sigma_{\rm MAD}$ confidence range (analogous to the 68% confidence, $\sigma$, if the error distribution were Gaussian, see § 2.3.2). Red triangles, white triangles, and white diamonds are medians from Lee et al. (2011), Lee et al. (2012), and Stark et al. (2013) respectively. *Bottom right:* For reference, this cartoon shows the strength and direction of galaxy evolution over 590 Myr from $z \sim 6$ to $z \sim 4$ under an assumed star formation history. This plot implies that there is a weak relation between UV magnitude and stellar mass in place up to $z \sim 6$ with significant scatter, and that rising star formation histories offer a simple explanation of how galaxies may evolve along this relation.

Table 2.2: $M_{1500}$ – Stellar Mass Relation Median Values.

| $z \sim 4$ | | | | | | | |
|---|---|---|---|---|---|---|---|
| $M_{1500}$ | -21.5 | -21.0 | -20.5 | -20.0 | -19.5 | -19.0 | -18.5 |
| log(Median Mass/$M_\odot$) | 9.61 | 9.50 | 9.21 | 9.13 | 8.96 | 8.81 | 8.75 |
| $\sigma_{\rm MAD}$[5] | 0.39 | 0.57 | 0.47 | 0.51 | 0.56 | 0.53 | 0.57 |
| $z \sim 5$ | | | | | | | |
| $M_{1500}$ | -21.5 | -21.0 | -20.5 | -20.0 | -19.5 | -19.0 | -18.5 |
| log(Median Mass/$M_\odot$) | 9.67 | 9.44 | 9.18 | 9.07 | 8.88 | 8.91 | 8.76 |
| $\sigma_{\rm MAD}$ | 0.35 | 0.43 | 0.52 | 0.52 | 0.50 | 0.66 | 0.53 |
| $z \sim 6$ | | | | | | | |
| $M_{1500}$ | -21.5 | -21.0 | -20.5 | -20.0 | -19.5 | -19.0 | -18.5 |
| log(Median Mass/$M_\odot$) | 9.34 | 9.23 | 9.21 | 9.14 | 8.90 | 8.77 | — |
| $\sigma_{\rm MAD}$ | 0.44 | 0.38 | 0.41 | 0.38 | 0.38 | 0.47 | — |

population parameters, even when the physical details are unknown, such as the case of our observed galaxies. A similar but more comprehensive study was conducted among many CANDELS team members which compared the estimated and expected parameters from galaxies measured using SED fits (see Mobasher et al., in prep.).

The mock catalog from the SAM was filtered to a sample of 6000 simulated galaxies, evenly distributed across the mass and redshift range of our CANDELS sample. We took the synthetic photometry from the models and randomly perturbed them according to a Gaussian error distribution with a similar $\sigma$ as the CANDELS data at a given band and magnitude. This process accounts for any systematic errors in creating the mock catalogs, and we process these fluxes the same way we process the data, even when fluxes are perturbed to negative values. These fluxes were used as input to the same SED-fitting procedure we applied to the real CANDELS

samples. The masses and SFRs in the SAM were scaled to a Salpeter IMF, to match our procedure. We also fit to templates that exclude the effects of nebular emission (using $f_{\rm esc} = 1$) because the SAMs also exclude nebular effects. For the test here, we show only the case where we fix the star formation history to be constant. Our tests (discussed in Appendix A.1) show that we recover the most accurate SFRs and stellar masses using constant star formation histories. Appendix A.1 discusses how including additional star formation histories affects the SFRs and stellar masses.

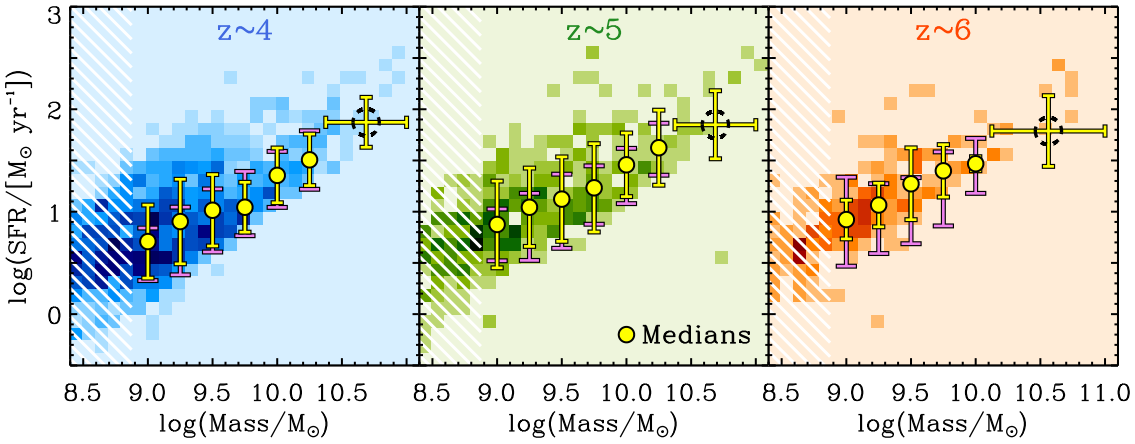


Figure 2.11: The Relation Between SFR and Stellar Mass.
The SFR–stellar mass relation for the CANDELS galaxy samples. The darker-shaded regions indicate a higher number of individual objects in bins of stellar mass and SFR. Yellow circles are medians in bins of mass and yellow error bars are their $\sigma_{\rm MAD}$ confidence range (see Table 2.3). The median SFR of a wider, high-mass bin is also shown by the dashed black circle. The white hatched regions mark the limit above which completeness effects become negligible. We measure a slope of ∼0.6 (see Table 2.4), with no evidence for evolution over the redshift range $z$ ∼6 to 4. The purple error bars show the 68% range of errors from the Monte Carlo simulations described in § 2.6.2.1.

Figure 2.9 compares the "true" stellar masses and SFRs from the SAM with those

derived from using either the "best-fit" values or our method of taking the median, marginalized value from the posterior. This figure shows that taking advantage of the whole posterior with marginalized values produces less scatter in the recovering the "true" SAM values. This is because the maximum likelihood can be more sensitive to template assumptions than the median posterior values, as shown in Figure 2.8 and discussed in Appendix A.2. We note that there is a weak systematic where the fits slightly overestimate objects with low SFRs and slightly underestimate objects with high SFRs. The effect is mild, ranging by $\pm 0.25$ dex. This systematic could be due to differences in the extinction prescription and assumed star formation history between models used in the fit and those in the SAM.

The bottom panel of Figure 2.9 shows that the offsets in stellar mass and SFRs conspire to reproduce the accurate SFR–mass relation as expected from the SAMs. The parameters derived from our fits better reproduce the zero point, scatter, and slope of the relation than when using best-fit values. We also find no appreciable difference in the ability to recover the SFR–stellar mass relation across redshift. Our ability to test the success of our procedure, however, is limited to the maximal level of stochasticity in the star formation histories of the SAMs and we have not tested our procedure to observe its sensitivity to very bursty star formation histories. Nevertheless, these tests give us confidence that even in the presence of realistic photometric errors, we are able to derive a SFR–stellar mass relation from high-redshift galaxies in the CANDELS data that reproduces the intrinsic relation within these $\sim 0.25$ dex uncertainties in SFR or stellar mass.

## 2.6 Evolution of SFR and Stellar Mass at $3.5 < z < 6.5$

This section describes the relations between the observed rest-frame UV magnitude, $M_{1500}$, and stellar mass, and the SFR and stellar mass of galaxies in our

Table 2.3: SFR – Stellar Mass Relation Median Values.

$z \sim 4$

| $\log(M_\star/M_\odot)$ | 9.00 | 9.25 | 9.50 | 9.75 | 10.00 | 10.25 | $> 10.375$[6] |
|---|---|---|---|---|---|---|---|
| $\log(\text{Median SFR}/M_\odot\ \text{yr}^{-1})$ | 0.71 | 0.90 | 1.01 | 1.04 | 1.35 | 1.51 | 1.87 |
| $\sigma_{\text{MAD}}$[7] | 0.36 | 0.41 | 0.35 | 0.24 | 0.27 | 0.25 | 0.24 |
| Monte Carlo $\sigma$[8] | 0.26 | 0.33 | 0.31 | 0.31 | 0.27 | 0.29 | — |

$z \sim 5$

| $\log(M_\star/M_\odot)$ | 9.00 | 9.25 | 9.50 | 9.75 | 10.00 | 10.25 | $> 10.375$ |
|---|---|---|---|---|---|---|---|
| $\log(\text{Median SFR}/M_\odot\ \text{yr}^{-1})$ | 0.88 | 1.04 | 1.12 | 1.23 | 1.46 | 1.62 | 1.85 |
| $\sigma_{\text{MAD}}$ | 0.42 | 0.38 | 0.41 | 0.43 | 0.31 | 0.37 | 0.33 |
| Monte Carlo $\sigma$ | 0.25 | 0.33 | 0.36 | 0.28 | 0.27 | 0.25 | — |

$z \sim 6$

| $\log(M_\star/M_\odot)$ | 9.00 | 9.25 | 9.50 | 9.75 | 10.00 | $> 10.125$ | — |
|---|---|---|---|---|---|---|---|
| $\log(\text{Median SFR}/M_\odot\ \text{yr}^{-1})$ | 0.92 | 1.07 | 1.27 | 1.40 | 1.47 | 1.79 | — |
| $\sigma_{\text{MAD}}$ | 0.19 | 0.21 | 0.35 | 0.26 | 0.07 | 0.35 | — |
| Monte Carlo $\sigma$ | 0.43 | 0.34 | 0.32 | 0.36 | 0.27 | — | — |

CANDELS sample from $z = 3.5$ to 6.5. All SFRs and stellar masses are derived from the posteriors from the SED fits.

### *2.6.1 $M_{1500}$–Stellar Mass Relation*

The panels of Figure 2.10 show the relation between the observed magnitude of the band closest to 1500 Å at the redshift of the galaxy (the rest-frame UV magnitude) and stellar mass at each redshift as two-dimensional histograms for our CANDELS sample. The median and $\sigma$ of stellar mass in each bin of $M_{1500}$ are given in Table 2.2. Here we show the observed UV absolute magnitude with no dust corrections in order to easily compare against previous studies (Stark et al., 2009, 2013; Lee et al., 2011, 2012). As discussed above, quantities used in this figure are median stellar masses derived from the marginalized PDF of each object (see § 2.5 for details).

We find a correlation between UV absolute magnitude and stellar mass, though this relation retains significant scatter. Recent evidence has suggested a relation with significant scatter between $M_{1500}$ and stellar mass at high redshift, $z \gtrsim 2$ (Reddy et al., 2006; Daddi et al., 2007; Stark et al., 2009; González et al., 2011; Reddy et al., 2012b; Schaerer et al., 2013; Stark et al., 2013). The $M_{1500}$–stellar mass trend in this chapter is weaker than the literature because we use an $H_{160}$-band selected catalog, which is closer to stellar mass than optically selected samples, as were used in the previous works listed above. This means that at fixed UV luminosity (or SFR) we are less sensitive to blue sources, which have higher mass-to-light ratios. Therefore, below our limiting stellar mass ($10^9/M_\odot$) we may be missing the bluer sources, as seen in Figure 2.10. At bright magnitudes (SFRs) our results agree with previous studies (that usually used $z_{850}$-band selected catalogs). It is at fainter magnitudes where our sources have fewer low-mass objects compared to the literature. Our

results are also consistent with an independent analysis of the CANDELS catalogs, which used the same $H_{160}$-band selection (Duncan et al., 2014).

Regardless of the median relation, we consider the large scatter in $M_{1500}$ at fixed stellar mass to mean one or both of the following. First, it could mean gas accretion is low such that galaxies undergo recurrent and stochastic star formation that leads to a range of $M_{1500}$ at a fixed stellar mass (Lee et al., 2006, 2011). Second, galaxies at a fixed redshift and fixed stellar mass could exhibit a range of $A_{\rm UV}$ attenuations. In the second scenario, the observed scatter in the plane of $M_{1500}$–$M_\star$ would be largely diminished once we apply corrections for dust attenuation. As discussed in the next subsection, the simulations favor the latter scenario.

The bottom right panel of Figure 2.10 illustrates an evolutionary cartoon depicting a model z$\sim$ 6 object of a given mass that is evolved forward $\approx$ 600 Myr to $z \sim 4$. This is done by assuming an initial stellar mass ($10^8$ $M_\odot$), age ($\sim$ 500 Myr, the average marginalized age of our entire sample), and zero dust ($A_{\rm UV}$= 0). The strength and direction of three different star formation histories with the Bruzual & Charlot (2003) SPS code are shown: a constant SFR, a declining SFR (where $\Psi \sim \exp(-t/\tau)$, with $\tau = 1$ Gyr), or a rising SFR (where $\Psi \sim t^\gamma$ using our results derived below from § 2.7.2). As illustrated in Figure 2.10, only a rising star formation history naturally evolves galaxies along the median relation between stellar mass and $M_{1500}$. Though this simple explanation does well to explain the UV-faint to UV-bright evolution, it offers little insight to the fate of the UV-bright galaxies at later epochs. It remains to be seen if some population of massive, UV-bright galaxies at $z \sim 6$ quench their SFR such that we are missing a population of massive UV-faint galaxies at $z \sim 4$.

### *2.6.2 SFR–Stellar Mass Relation*

Figure 2.11 shows the relation between the (dust-corrected) SFR and the stellar mass, where both parameters are derived from the fully marginalized probability density functions. Table 2.3 shows the median and $\sigma$ scatter of log SFR in bins of stellar mass from Figure 2.11. We measure a tight SFR–stellar mass relation (a "main sequence") for galaxies with $\log M_\star/\mathrm{M}_\odot > 9$, the mass completeness limit (e.g., Duncan et al., 2014). We explore how our SED fitting process could contribute to the correlation between SFR and stellar mass in Appendix A.3. This main-sequence in the SFR–mass relation has received much attention in the literature, and its existence implies that stellar mass and star formation both scale with the star formation history (Stark et al., 2009; González et al., 2010; Papovich et al., 2011). If true, then it follows that the gas accretion onto dark-matter halos at higher redshift is smooth when averaged over large timescales and stellar mass growth at high redshift is not driven by mergers (Cattaneo et al., 2011; Finlator et al., 2011). Our results support this picture.

We fit a linear relation to the SFR–stellar mass relation as

$$\log(\mathrm{SFR}/\mathrm{M}_\odot\ \mathrm{yr}^{-1}) = a\ \log(M_\star/\mathrm{M}_\odot) + b \tag{2.6}$$

where $a$ is the slope of the relation and $b$ is a zero point. The fitted values for $a$ and $b$ are given in Table 2.4. We also show the fitted values for $b$ when the slope is fixed to be $a = 1$, since the slope and intercept are often degenerate. We find that the slope and normalization in the SFR–mass relation shows no indication for evolution, with slopes of $a = 0.54 \pm 0.16$ at $z \sim 6$ and $0.70 \pm 0.21$ at $z \sim 4$. Furthermore, the scatter in SFR at fixed stellar mass shows no evidence for evolution, with a range of $\sigma(\log \mathrm{SFR}/\mathrm{M}_\odot\mathrm{yr}^{-1}) = 0.2 - 0.4$ dex from the median.

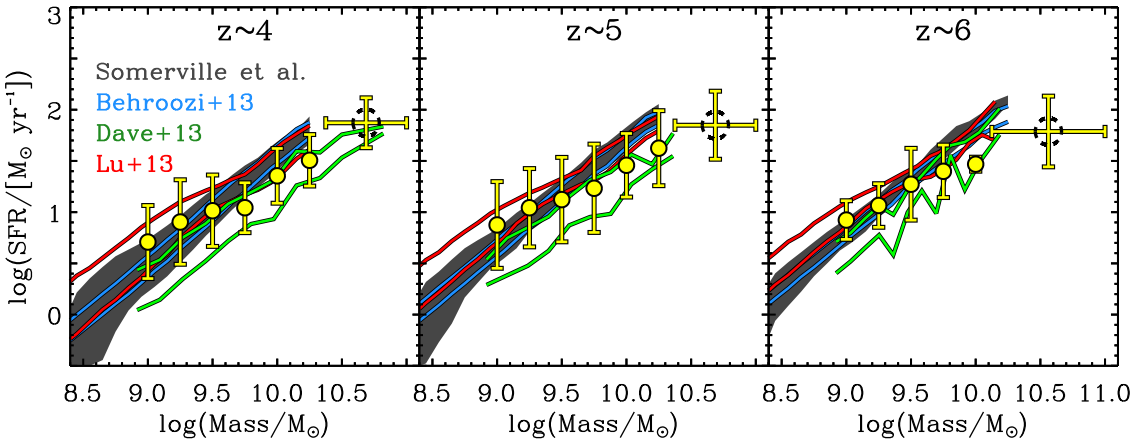


Figure 2.12: Comparison of SFR and Stellar Mass Relation to Models. The SFR–stellar mass relation predicted from the models. Each set of lines or shaded swatch shows the $\pm\sigma$-range of galaxies from each model as given in the inset. The yellow points and errors bars show the measured relation for the CANDELS samples and are identical to the points in Figure 2.11. The zero point, scatter and slope of the SFR–stellar mass relation from the models is consistent with the measured values over this redshift range.

We must consider the possibility that the scatter in SFR at fixed mass is higher, and we are simply missing galaxies with low SFR due to incompleteness. We consider this unlikely because even if star formation ceased in some fraction of the galaxies, the galaxies would require $0.5 - 1$ Gyr to have their SFR drop below a detectable threshold in the WFC3 IR data. These timescales are comparable to the period of time spanned by our subsamples (i.e. the lookback time between $z = 4.5$ and 3.5 is only 480 Myr), so it seems unlikely galaxies would "instantly" move from the observed SFR–mass sequence to undetectable values. For example, if such low-SFR objects existed at $z = 4$ their progenitors should be seen at $z = 5$ and 6 as they are fading, inducing a larger scatter in SFR–stellar mass. This work finds no evidence for such a population in our sample. Parenthetically, we note that some studies report

Table 2.4: SFR–Stellar Mass Best-Fit Parameters.

$z \sim 4$

| | Slope $a$[9] | Zero Point $b$ | $b$ when $a \equiv 1$ | $\langle\sigma_{\rm MAD}\rangle$ [10] | $\chi^2$ [11] |
|---|---|---|---|---|---|
| This work | 0.70 ± 0.21 | -5.7 ± 2.1 | -8.64 ± 0.11 | 0.35 (0.31)[12] | 0.38 |
| Somerville et al. | 1.1 ± 0.13 | -9.0 ± 1.3 | -8.47 ± 0.05 | 0.18 | 0.06 |
| Behroozi et al. | 1.1 ± 0.07 | -9.2 ± 0.7 | -8.47 ± 0.03 | 0.10 | 0.17 |
| Lu et al. | 0.80 ± 0.11 | -6.5 ± 1.1 | -8.45 ± 0.04 | 0.14 | 0.44 |
| Davé et al. | 0.80 ± 0.05 | -6.8 ± 0.6 | -8.95 ± 0.03 | 0.16 | 2.1 |

$z \sim 5$

| | Slope $a$ | Zero Point $b$ | $b$ when $a \equiv 1$ | $\langle\sigma_{\rm MAD}\rangle$ | $\chi^2$ |
|---|---|---|---|---|---|
| This work | 0.59 ± 0.26 | -4.4 ± 2.6 | -8.49 ± 0.14 | 0.41 (0.29)[d] | 0.05 |
| Somerville et al. | 1.0 ± 0.09 | -8.6 ± 0.9 | -8.29 ± 0.03 | 0.13 | 0.07 |
| Behroozi et al. | 1.0 ± 0.05 | -8.6 ± 0.5 | -8.32 ± 0.02 | 0.07 | 0.35 |
| Lu et al. | 0.79 ± 0.07 | -6.3 ± 0.7 | -8.29 ± 0.02 | 0.10 | 0.78 |
| Davé et al. | 0.80 ± 0.07 | -6.7 ± 0.7 | -8.72 ± 0.02 | 0.15 | 1.5 |

$z \sim 6$

| | Slope $a$ | Zero Point $b$ | $b$ fwhen $a \equiv 1$ | $\langle\sigma_{\rm MAD}\rangle$ | $\chi^2$ |
|---|---|---|---|---|---|
| This work | 0.54 ± 0.16 | -3.9 ± 1.6 | -8.45 ± 0.06 | 0.21 (0.34)[d] | 0.10 |
| Somerville et al. | 1.0 ± 0.06 | -8.5 ± 0.6 | -8.16 ± 0.02 | 0.10 | 0.47 |
| Behroozi et al. | 0.96 ± 0.05 | -7.8 ± 0.5 | -8.21 ± 0.02 | 0.07 | 0.81 |
| Lu et al. | 0.77 ± 0.07 | -6.0 ± 0.7 | -8.15 ± 0.02 | 0.10 | 1.3 |
| Davé et al. | 1.1 ± 0.10 | -9.6 ± 0.9 | -8.29 ± 0.03 | 0.15 | 6.7 |

evidence for massive, $\log M_\star/\mathrm{M}_\odot > 10.6$ dex, quiescent galaxies at $z \sim 3-4$, but this population lies at stellar masses above those in our sample (Straatman et al., 2014; Muzzin et al., 2013; Spitler et al., 2014).

We note that our SFR–stellar mass relation is tighter than our $\mathrm{M}_{1500}$–stellar mass relation (Fig. 2.10), and we find that this can be explained by a correlation between stellar mass and our derived dust attenuation (there is no correlation between derived attenuation and $\mathrm{M}_{1500}$). For example, objects at masses of $10^{8.5}$, $10^{9.5}$, and $10^{10.5}$ $\mathrm{M}_\odot$ have median marginalized $E(B-V)$ values of 0.05±0.03, 0.13±0.07, and 0.32±0.18 respectively. This relation accounts for the differences in the scatter seen in Figures 2.10 and 2.11.

#### *2.6.2.1 Constraints on the Intrinsic Scatter in the SFR–Mass Relation*

Before comparing against models, it is necessary to understand how much of the scatter in the SFR–mass relation is intrinsic to the galaxy population and how much is a result of observational errors in SFR and stellar mass. To a simple approximation, the observed scatter (yellow in Fig. 2.11) is a combination of the intrinsic (true) scatter and the measurement errors added in quadrature,

$$\sigma_{\mathrm{observed}} = (\sigma^2_{\mathrm{intrinsic}} + \sigma^2_{\mathrm{errors}})^{1/2}. \tag{2.7}$$

The SFR–mass joint probability density is broad, with covariance between the SFR and stellar mass (e.g., Fig. 2.7). Because we calculate the posterior probability density functions for both the stellar mass and SFR for galaxies in our samples, we are able to estimate how correlations in these parameters contribute to the scatter and slope of the SFR and stellar mass relation. Here we use a Monte Carlo simulation to estimate $\sigma_{\mathrm{errors}}$, and to determine how these errors affect the slope of the SFR–stellar mass relation.

We set up the Monte Carlo as follows. As discussed above, the SFR and stellar mass posteriors are covariant because both involve the dust attenuation, $A_{\rm UV}$, where models with higher $A_{\rm UV}$ have higher SFR from dust corrections, and higher mass-to-light ratios, which produce higher stellar masses. For each galaxy in each subsample at $z = 4$, 5 and 6, we randomly sample the galaxy's posterior density function of $A_{\rm UV}$ to find a new UV attenuation, $A_{{\rm UV},i}$. We then compute the conditional posterior for the stellar mass, $P({\rm M}_\star|A_{UV,i})$. Next, we derive the SFR from equation 2.5 and the medians of SFR in bins of stellar mass are re-calculated. This process is repeated $10^4$ times for each galaxy to generate $10^4$ new realizations of our galaxy sample. We then calculate at each stellar mass the median SFR and compute the $\sigma_{\rm MAD}$ from the distribution of medians. The scatter in log SFR from this Monte Carlo is shown in Figure 2.11 and Table 2.3.

The $\sigma_{\rm MAD}$ scatter in the SFR from the Monte Carlo simulations is comparable to the observed SFR scatter, $\sigma_{\rm observed}$, in most bins of mass and redshift. The scatter in the SFRs at fixed stellar mass from the Monte Carlo are shown in Figure 2.11 and given in Table 2.3. We make the approximation that $\sigma_{\rm errors} = \sigma_{\rm MAD}$ from the Monte Carlo. We subtract these in quadrature from the observed SFR scatter to estimate the intrinsic scatter in SFR at fixed mass using equation 2.7. We find that the average intrinsic scatter in SFR across the mass bins to be $\sigma = 0.26 \pm 0.04, 0.23 \pm 0.10$, and $0.34 \pm 0.11$ at $z \sim 4, 5$, and 6, respectively. In some instances, the measurement errors from the Monte Carlo accounts for more scatter than the observed scatter, in which case there is no meaningful constraint on the intrinsic scatter. In this case, we take the Monte Carlo measurement scatter alone as a conservative limit on the intrinsic scatter (as *some* of the errors on the derived quantities must arise from the intrinsic scatter). This has implications for the gas accretion rate that we discuss below in § 2.7.1.

The above test ignores the effects of our photometric redshift uncertainties since redshift is a fixed parameter during the fitting process. We constructed the following test to determine the effects of redshift uncertainties on SFR and stellar mass. We randomly selected 100 objects from each redshift sample and performed a Monte Carlo on their redshift uncertainty. In the Monte Carlo, each object's redshift was re-assigned according to a Gaussian error distribution with a sigma equal to the object's 68% photometric redshift uncertainty. Then, we derived the stellar masses and SFRs in the same manner as with the data, fixing the redshifts to be the new redshift values. We calculated the medians in the SFR–stellar mass relation, as in as in Figure 2.11, for each of $10^4$ realizations of this process. Finally, we found the median and $\sigma$ of SFR in each stellar mass bin from the distribution of SFR medians that each Monte Carlo realization produced.

Redshift errors produce a higher median log SFR of $<$0.1 dex per stellar mass bin, and the redshift errors can contribute as much as $\sim$0.1 dex to the scatter in every stellar mass bin (usually it is much smaller, contributing $<$0.03 dex for 50% of the stellar mass bins). Therefore the redshift uncertainties do not significantly contribute to the error budget of the SFR–stellar mass relation.

We cannot rule out the possibility that a population of dusty, low-SFR galaxies are missing from our sample, which would attribute more scatter to the SFR–stellar mass relation. Indeed, some recent studies find evidence that such a population may exist at high redshift, at least at high stellar masses (Spitler et al., 2014; Man et al., 2014). Furthermore, at low stellar masses, our sample may be biased toward objects experiencing recent "bursts" of star formation (Schreiber et al., 2014). A deep investigation with ALMA is needed for further confirmation (Schaerer et al., 2014). However, our redshift range limits the data to rest-frame UV-to-optical wavelengths, and we defer the search for such a population for future work.

#### *2.6.2.2 Comparison to the SFR–Stellar Mass Relation in Models*

This subsection compares the results of the SFR–stellar mass relation in the previous section to results of recent SAM (Somerville et al., Lu et al.) semi-empirical dark matter abundance matching (Behroozi et al., 2013b), and hydrodynamic (Davé et al., 2013) simulations. Each of these simulations were briefly summarized in section 2.3.4 and are collectively referred to as "the models".

Figure 2.12 shows the scatter in the SFR–stellar mass relation for each of the models as compared to the observed median and scatter in the SFR at fixed stellar mass (with data and errors bars identical to those in Figure 2.11). For each model, the median and scatter in the SFR at fixed mass was computed in the same way as the data (with all models converted to a Salpeter (1955) IMF, as assumed in this chapter).

The SFR–mass relations from each model are in general agreement with each other and imply a tight relation between SFR and stellar mass exists for galaxies at high redshift. The SFR–mass relations from the models are also very similar to the observed relation derived from the data. Though some models predict a steeper slope of near unity ($a \simeq 1$), higher than measured in this work ($a \simeq 0.6$), the difference is negligible as it is within the errors. The observed offset in the zero point between the models and observations is likewise insignificant as the zero point is strongly anticorrelated with the slope in the linear fits of this work. In addition, from Figure 2.9 it was shown that the recovered SFRs from tests with the mock data tended to under- (over-) estimate the SFR of model galaxies with high (low) SFRs. No attempt was made to correct this for systematic. Therefore the similar offsets seen in Figure 2.12 between the high-SFR objects may imply that the data and SAMs are in even closer agreement.

As listed in Table 2.4, the scatter in the SFR at fixed mass is typically $0.1 - 0.2$ dex in the models, whereas the limits on the intrinsic scatter from the data are $\sigma(\log \mathrm{SFR}) < 0.2 - 0.3$ dex (see S 2.6.2.1). Therefore, both the observations and models support the conclusion that the SFR in galaxies at $3.5 < z < 6.5$ at fixed mass (for $\log M_\star/\mathrm{M}_\odot > 9$ dex) scales nearly linearly with increasing stellar mass and does not vary by more than a factor of order 2. We explore the implication this has for the net gas accretion rate below in § 2.7.1.

## 2.7 Discussion

### *2.7.1 Implications of the SFR–Stellar Mass Relation*

The fact that there is a tight SFR–stellar mass relation implies that the SFR scales almost linearly with stellar mass for the galaxies in our sample at $3.5 < z < 6.5$. Because the SFR is (to a coarse approximation) the time derivative of the stellar mass, this implies that the SFR is an increasing function with time. We explore this further below in § 2.7.2. Furthermore, the tightness of the scatter indicates that there is little variation in the SFR at fixed stellar mass. One caveat is that the SFRs are based on the galaxies' UV luminosity. Therefore, the SFRs that we measure are the "time-averaged" over the time it takes for the UV luminosity in galaxies to respond to changes in their instantaneous SFR. For the UV luminosity this timescale is approximately 30-100 Myr (e.g., Salim et al., 2009). Recent simulations have shown that the scatter is highly sensitive to the timescale of the SFR indicator (Hopkins et al., 2014; Domínguez et al., 2014). Therefore, the tightness in the SFR–mass relation of this work is conditional on the timescale associated with UV SFRs. With that in mind, the scatter observed in this work implies that galaxies at fixed mass in our sample have similar star formation histories when averaged over this timescale.

The scatter in the SFR–mass relation has important implications for net interplay

between gas accretion into halos and galaxy feedback and outflows at these redshifts. The gas-accretion rate is a crucial piece of physics in galaxy formation models, and measures of the scatter in the SFR–mass relation are therefore an important test to constrain simulations and SAMs. As discussed above, the SFR is expected to track the net accretion rate/outflow rate of baryonic gas into the galaxies' dark-matter halos (Kereš et al., 2005; Dekel et al., 2009; Bouché et al., 2010; Lu et al., 2014a). Because the SFR–mass relation is tight, it then follows that the gas accretion rate has little variation ($\sigma \sim 0.2-0.3$ dex, or a factor of $< 2$) at fixed stellar mass. Therefore, this favors a relatively smooth gas accretion process for galaxies at $3.5 < z < 6.5$, at least above $\log M_\star/\mathrm{M}_\odot > 9$ dex.

### *2.7.2 Evolution of the SFR*

As discussed above, a tight, linear relation between SFR and stellar mass implies an SFR that increases with time. In this section, we study the SFR history directly to see if it is consistent with the observed SFR–stellar mass relation. This is achieved by tracking the evolution of the progenitors of $z = 4$ galaxies by selecting galaxies at different redshifts based on their number density.

Many studies have shown that a constant (comoving) number-density selection can trace the progenitor and descendant evolution both to relatively low and high redshifts (e.g., van Dokkum et al., 2010; Papovich et al., 2011; Lundgren et al., 2014; Leja et al., 2013b; Patel et al., 2013; Tal et al., 2014). In addition, recent studies have suggested using an evolving number-density selection to better track the progenitor populations of galaxies (e.g., Leja et al., 2013a; Behroozi et al., 2013a). Here, we use the parameterization of Behroozi et al. (2013a), who provide simple functions to track the number density evolution of the progenitors of galaxies.

This number density evolution is used to select the progenitors of galaxies in our

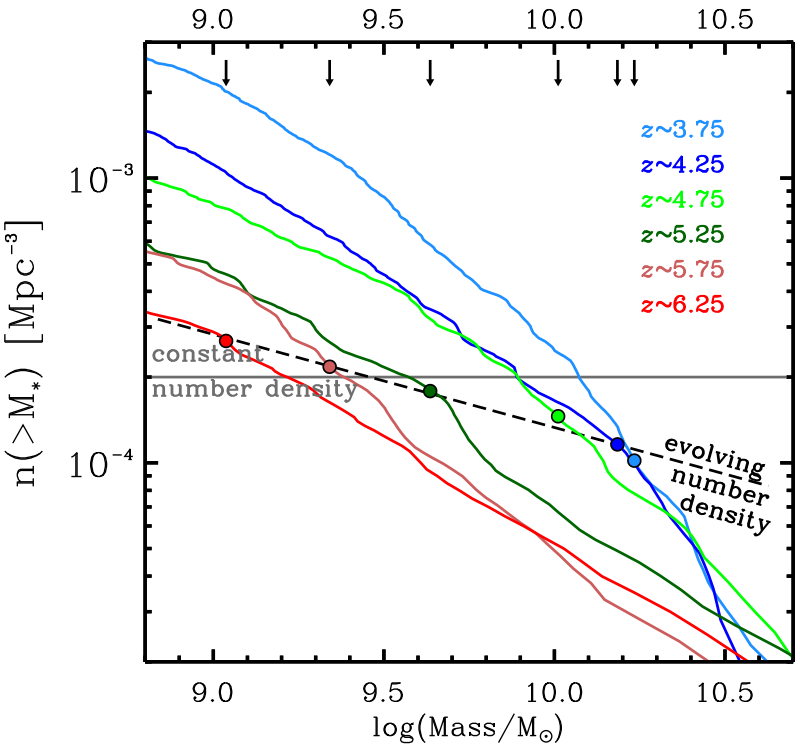


Figure 2.13: Cumulative Stellar Mass Functions.
Cumulative stellar mass functions in bins of redshift. No corrections have been applied for completeness, but Duncan et al. (2014) show these corrections are negligible for $\log M_\star/\mathrm{M}_\odot > 9$ dex. The arrows and circles indicate the stellar mass evolution of the progenitors of galaxies with an evolving number density with $\log n(> M_\star)/\mathrm{Mpc}^{-3} = -4$ at $z = 3.5$ using the evolution parameterized by Behroozi et al. (2013a). We measure the SFR evolution of these galaxies. As we discuss below, we would have inferred a very similar evolution in SFR for galaxies selected at constant number density, with $\log n(> M_\star)/\mathrm{Mpc}^{-3} = -3.7$, at all redshifts.

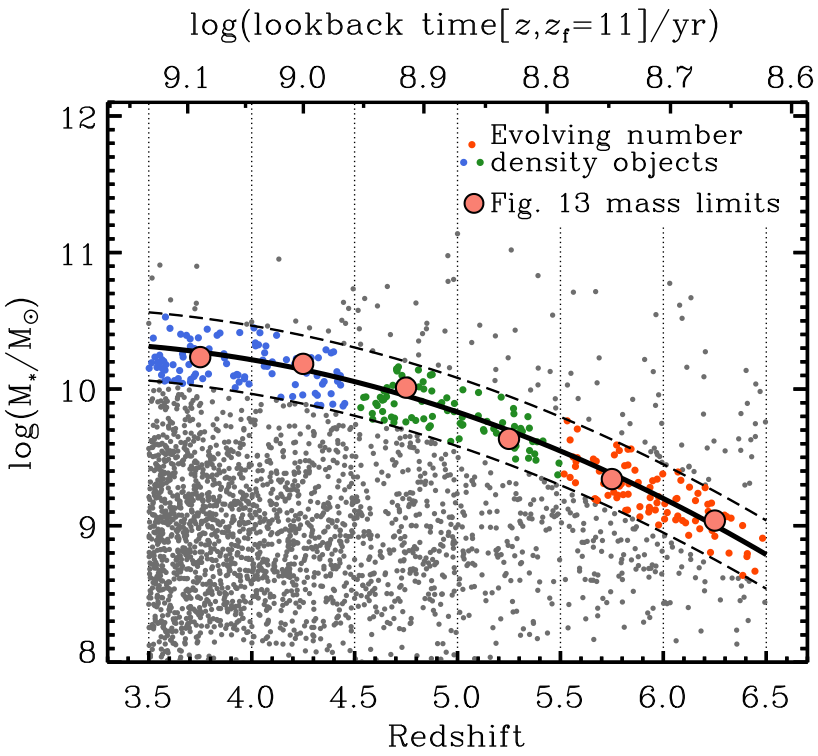


Figure 2.14: Tracking Galaxy Evolution by Number Density.
The selection of galaxies according to the Behroozi et al. (2013a) evolving number density of $\log n(> M_\star)/\mathrm{Mpc}^{-3} = -4$ at $z = 3.5$. The large salmon-colored circles show the median stellar mass evolution, and the dashed lines illustrate our sample selection of $\pm 0.25$ dex in stellar mass about these median values. We select all galaxies within these lines, and use them to derive the star formation history.

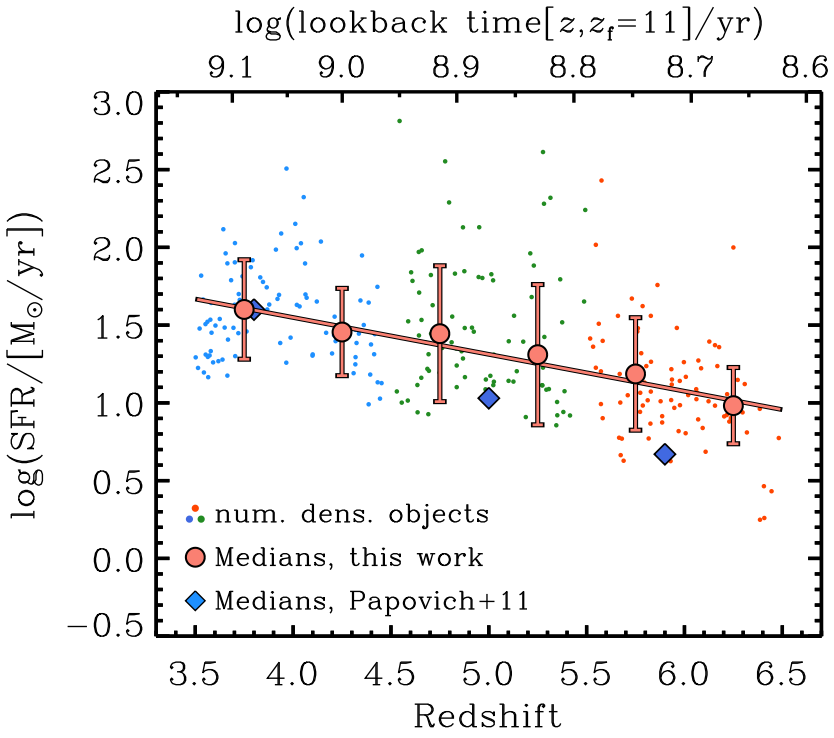


Figure 2.15: The SFR History.
The SFR history (the SFR as a function of redshift) for galaxies selected by their (evolving) number density to track the evolution in the progenitors of galaxies at $z = 3.5$ with $\log n/\mathrm{Mpc}^{-3} = -4$. The galaxies from each redshift subsample $z = 4$, 5, and 6 are indicated as blue, green, and orange points respectively. The larger salmon-colored circles and error bars show the median SFR and $\sigma_{\mathrm{MAD}}$ in bins of $\Delta z = 0.5$. An average rising star formation history is derived for this redshift range that can be represented by a power law $\Psi = t^{\gamma}$ where $\gamma = 1.4 \pm 0.1$. This evolution is somewhat shallower than that found by Papovich et al. (2011), but consistent within the error budget.

sample. Figure 2.13 shows the cumulative stellar mass functions for the galaxies in our $3.5 < z < 6.5$ CANDLES samples in bins of redshift. The results of Duncan et al. (2014) show that the objects in this field are complete for masses greater than $\log M_\star/\mathrm{M}_\odot = 8.55$, 8.85, and 8.85 dex at $z \sim 4$, 5 and 6 respectively. We assume a survey area of 170 arcmin$^2$ as described by Koekemoer et al. (2011) and the co-moving volume is calculated at each redshift assuming an uniform depth across each field. These cumulative functions are used to determine the stellar mass at which the galaxies of that redshift range achieve a given evolving number density as described by Behroozi et al. (2013a). As indicated in the figure, we take the galaxies with stellar mass $\log M_\star/\mathrm{M}_\odot = 10.2$ dex at $z = 3.75$, which have a number density of $\log n/\mathrm{Mpc}^{-3} = -4$, and identify the galaxies at higher redshift that have a stellar mass that corresponds to the appropriate (de-evolved) number density at that redshift.

Figure 2.14 illustrates our criteria to select objects according to an evolving number density. We use the Figure 2.13 stellar mass limits to find a best-fit curve across $3.5 < z < 6.5$. Then, we select objects from our data that are $\pm$ 0.25 dex in stellar mass about this relation. For the remainder of this chapter, we refer to these objects as "evolving number density–selected". We will later compare these briefly to objects selected at "constant number density" as such samples have received attention in the recent literature.

Figure 2.15 shows the average SFR as a function of redshift for the evolving number density–selected galaxies. The SFR clearly increases as a function of time (decreasing redshift). We fit this evolution with a power law, $\Psi(t) \sim (t/\tau)^\gamma$ where $\gamma = 1.4 \pm 0.1$ and $\tau = 92 \pm 14$ Myr. If our sample is incomplete at low stellar masses ($\log M_\star/\mathrm{M}_\odot < 9.5$ dex), then this would influence the measured power, $\gamma$. Based on Figure 2.13, the lower-mass objects will suffer greater incompleteness for objects

of low SFR. This could mean that the intrinsic power-law slope is steeper than the one we measure here. We also note that we observe little difference between this evolution and that derived from using a constant-number density-selection.

Lastly, we can explore whether the SFR evolution derived above produces an average SFR–mass relation as measured from the data. We took the SFR history derived above and compute the resulting stellar mass and SFR for a stellar population starting at $z = 6$ and evolving to $z = 4$ using the BC03 SPS models (see discussion in § 2.6.1 and bottom right panel of Figure 2.10). We plot the resulting SFR–mass relation in Figure 2.16 along with the medians derived above in Figure 2.11. Formally, the star formation history derived here corresponds to a galaxy with stellar mass $\log M_\star/\mathrm{M}_\odot = 10.2$ dex at $z = 3.75$. Looking only at that point, the SFR–mass relation inferred from the SFR history matches the SFR–mass relation at $z \sim 4$ remarkably well. (This is not circular because the stellar mass evolution is measured from the SFR evolution and *not* from the data itself.)

### *2.7.3 Evolution of the sSFR*

Lastly, we use our derived SFRs and stellar masses to study the evolution of the sSFR. We first explore the evolution with redshift at fixed stellar mass as this has received attention in the literature (even though it is clear that galaxies with such high SFRs will not remain at the same stellar mass over this redshift range). We then consider the evolution in sSFR for the evolving number density-selected sample described above, as this will better track the evolution in galaxy progenitors across this redshift range.

Figure 2.17 shows the evolution of the sSFR for objects selected with constant stellar mass: within $\pm 0.5$ dex of $\log M_\star/\mathrm{M}_\odot = 9$. The sSFR for objects at this stellar mass increases with increasing redshift, with high scatter. This evolution is

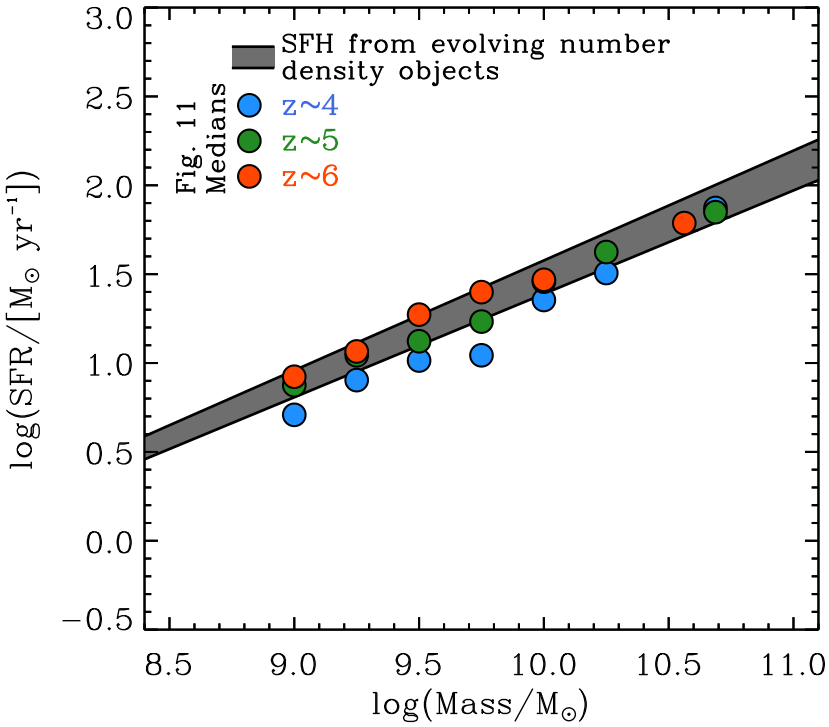


Figure 2.16: A Rising SFH on the Relation Between SFR and Stellar Mass. The median values of SFR and stellar mass relation from Figure 2.11 are shown, color coded by redshift. The gray region line is not a fit to the points, but is instead the implied relation (with errors) using the measured SFR history (from Fig. 2.15) derived by integrating that SFR history with the Bruzual & Charlot SPS models. For the $z = 4$ galaxies with $\log M_\star/\mathrm{M}_\odot = 10.2$ dex there is good agreement between the observed SFR–mass relation and the implied value from the SFR history. This is reassuring as the derived star formation history corresponds to the progenitors of galaxies of this mass at this redshift. At lower stellar masses, the SFR–mass relation implied from the derived star formation history underproduces the SFR, but we attribute this to the fact that the SFR history of lower-mass galaxies evolves less steeply with time.

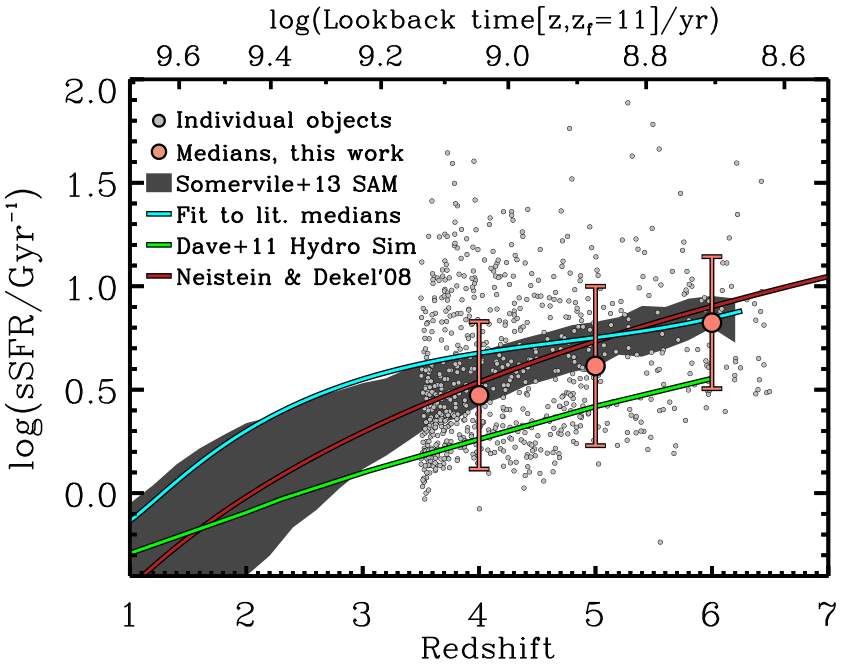


Figure 2.17: The Evolution of sSFR at Constant Stellar Mass.
The evolution of the sSFR as a function of redshift for galaxies selected with constant stellar mass ($\pm 0.5$ dex of $\log M_\star/\mathrm{M}_\odot = 9$ dex). Grey points represent individual objects, while salmon-colored circles are medians in $\Delta z = 0.5$ bins of redshift. The cyan curve shows a fit to the literature medians across all redshift. We find that at constant stellar mass, the sSFR gradually decreases over our redshift range. The other lines and shaded region correspond to model predictions as listed in the legend. The zero point and rate of evolution between the models and data are similar.

consistent with hydrodynamic simulations (Davé et al., 2011b), SAMs (Somerville et al., Lu et al.), and other recent observational results from the literature (Stark et al., 2013; González et al., 2014).

Figure 2.18 shows that the sSFR increases with redshift when galaxies are selected with an evolving number density. The evolution of the simple cosmological accretion models[13] where sSFR$\sim\ (1+z)^{\phi=2.5}$ (e.g., Neistein & Dekel, 2008) is consistent with the sSFR evolution found in this work (Fig. 2.18), which has $\phi = 3.4 \pm 2.5$ from

[13]Note the Neistein & Dekel (2008) model has a halo-mass dependence and tracks cosmological accretion, not a number density–selected evolution.

$z$=3.5 to $z$=6.5. There is a weak difference between the evolution of the evolving number density-selected sample and the sample at constant mass in Figure 2.17; the sSFR evolution for the evolving number density–selection is shifted to lower values as a function of redshift. This is basically a confirmation of the fact that the SFR–mass relation produces an sSFR that is nearly independent with stellar mass: sSFR = SFR / $M \sim M^{a-1}$, where sSFR $\sim M^{-(\approx 0.4)}$ using our results in Table 2.4. This implies that samples selected at constant stellar mass or an evolving stellar mass (from a number density selection) return only slightly different sSFR values because the sSFR is a slowly changing function with stellar mass, as recently found by Kelson (2014). Consequently, this permits mass-independent modeling of the specific accretion rate, and therefore the sSFR (see Dekel & Mandelker, 2014, for a detailed discussion).

One way to explain the slight offset of the observed sSFR to lower values than the predictions from the SAMs is that some feedback mechanism may be present to hinder SFR from tracing halo or stellar mass growth. Gabor & Bournaud (2014) recently showed that cold streams of gas can increase the velocity dispersion in star-forming disks. They show that at $z > 3$ this increased turbulence causes the gas-mass to stay higher, but reduces the SFR / gas-mass by a factor of two. Assuming gas-mass traces the baryonic-mass in galaxies at $z > 3$, then this could explain why the observed median sSFRs of this work are lower by about a factor of order two compared to other models.

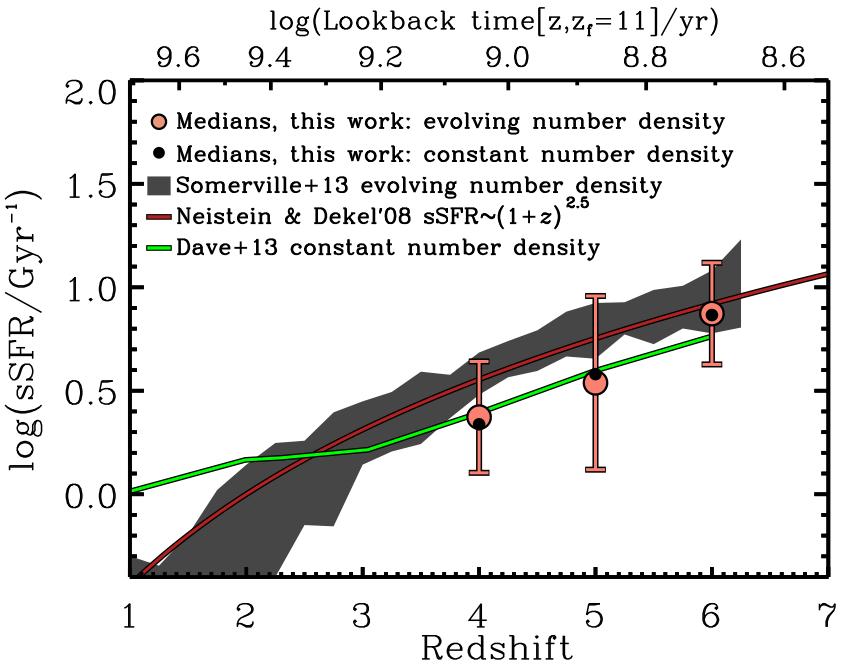


Figure 2.18: The Evolution of sSFR Selected by Number Density.
The evolution of the sSFR as a function of redshift for galaxies selected by their evolving number density to track the progenitors of galaxies at $z = 3.5$ with $\log n/\mathrm{Mpc}^{-3} = -4$. The larger salmon-colored circles and error bars show the medians of log sSFR in bins of redshift. The other lines and shaded region correspond to model predictions as listed in the legend.

# 3. BREAKING THE CURVE WITH CANDELS: A BAYESIAN APPROACH TO REVEAL THE NON-UNIVERSALITY OF THE DUST-ATTENUATION LAW AT HIGH REDSHIFT*

## 3.1 Synopsis

Dust attenuation affects nearly all observational aspects of galaxy evolution, yet very little is known about the form of the dust-attenuation law in the distant Universe. In this chapter, we model the spectral energy distributions (SEDs) of galaxies at $z \sim 1.5$–3 from CANDELS with rest-frame UV to near-IR imaging under different assumptions about the dust law, and compare the amount of inferred attenuated light with the observed infrared (IR) luminosities. Some individual galaxies show strong Bayesian evidence in preference of one dust law over another, and this preference agrees with their observed location on the plane of infrared excess ($IRX$, $L_{\rm TIR}/L_{\rm UV}$) and UV slope ($\beta$). We generalize the shape of the dust law with an empirical model, $A_{\lambda,\delta} = E(B-V)\ k_\lambda\ (\lambda/\lambda_V)^\delta$ where $k_\lambda$ is the dust law of Calzetti et al. (2000), and show that there exists a correlation between the color excess $E(B-V)$ and tilt $\delta$ with $\delta = (0.62 \pm 0.05)\log(E(B-V))+(0.26 \pm 0.02)$. Galaxies with high color excess have a shallower, starburst-like law, and those with low color excess have a steeper, SMC-like law. Surprisingly, the galaxies in our sample show no correlation between the shape of the dust law and stellar mass, star-formation rate, or $\beta$. The change in the dust law with color excess is consistent with a model where attenuation is caused by scattering, a mixed star-dust geometry, and/or trends with stellar pop-

*Reprinted with permission from "Breaking the Curve with CANDELS: A Bayesian Approach to Reveal the Non-Universality of the Dust-Attenuation Law at High Redshift" by Salmon et al., 2016. The Astrophysical Journal, Copyright 2016 by Brett Salmon.

ulation age, metallicity, and dust grain size. This rest-frame UV-to-near-IR method shows potential to constrain the dust law at even higher ($z > 3$) redshifts.

## 3.2 Background Information

Our knowledge of star-formation rates (SFRs) among the majority of $z > 4$ galaxies is, except in rare cases, limited to observations in the rest-frame ultraviolet (UV) where the effects of the dust attenuation are most severe and lead to large systematics. Galaxy surveys at the highest redshifts are predominantly limited to studying the rest-frame ultraviolet (UV)-to-near infrared (NIR) spectral energy distribution (SED). The dust attenuation at this critical portion of the SED cannot be dismissed even at $z = 7 - 8$, considering the mounting observations of high-redshift dusty star-forming galaxies, sub-millimeter galaxies, and quasars (Wang et al., 2008; Casey et al., 2014a; Mancuso et al., 2016). In addition, while there is no shortage of observations and simulations that offer potential mechanisms for dust production in the early universe (Todini & Ferrara, 2001; Gall et al., 2011a,b,c; Ventura et al., 2014), it is still uncertain how, and to what degree, these mechanisms influence the wavelength-dependence of attenuation at high redshift.

The nuances of dust geometry, extinction, and scattering from the interstellar medium (ISM) and star-forming regions are often conveniently packaged into a "recipe" of reddening (Calzetti, 1997), parameterized by a wavelength-dependent curve of the total-to-selective extinction (Witt & Gordon, 2000, and references therein),

$$k_\lambda = A_\lambda / E(B-V) \text{ and } R_\mathrm{V} = A_\mathrm{V} / E(B-V) \ , \tag{3.1}$$

where $A_\lambda$ is the total extinction in magnitudes at wavelength $\lambda$ and $E(B-V)$ is the color excess of selective extinction. We emphasize the distinction that dust "extinction" accounts for the absorption and scattering of light out of the line of

sight, whereas "attenuation" also accounts for the spatial scattering of light into the line of sight for extended sources such as galaxies. We refer to both extinction and attenuation models as "dust laws" for brevity. Successful empirical and analytic dust laws have been used for decades as a necessary *a priori* assumption when inferring fundamental physical properties of distant galaxies (Meurer et al., 1999; Papovich et al., 2001).

Dust laws are already known to be non-universal across all galaxy types from derivations of the Small and Large Magellanic Cloud (SMC and LMC) and Milky Way dust laws, as well as dust attenuation in $z$<1 galaxies (Conroy & Gunn, 2010). For example, Kriek & Conroy (2013) have shown that the form of the dust law can vary significantly at $z$ <2 as a function of galaxy type, and in some cases it differs strongly from the conventionally assumed Calzetti et al. (2000) prescription, derived from local UV-luminous starbursts. The conditions that produce these unique dust laws are complex. They depend on the covering factor, the dust grain size (which is dependent on the observed composition and metallicity), and line-of-sight geometry and can therefore change when galaxies are viewed at different orientations (Witt & Gordon, 2000; Chevallard et al., 2013) or stellar population ages (Charlot & Fall, 2000).

Changes to the observed star-dust geometry, that is, the relative geometry between stars and dust grains, produce different dust laws even for galaxies of a similar type. For example, observations of the infrared excess ($IRX \equiv L_{\rm TIR}/L_{\rm UV}$) and the UV slope ($\beta$, where $f_\lambda \propto \lambda^\beta$ over 1268< $\lambda$ <2580 Å Calzetti et al., 1994) have shown that star-forming galaxies bracket a range of attenuation types from starburst to SMC-like attenuations (Buat et al., 2011, 2012; Muñoz-Mateos et al., 2009; Overzier et al., 2011). The position of galaxies on the $IRX - \beta$ plane suggests that a single dust-attenuation prescription is incapable of explaining all observations (Burgarella

et al., 2005; Seibert et al., 2005; Papovich et al., 2006; Boquien et al., 2009; Casey et al., 2014b).

Although star-forming galaxies have a variety of attenuation scenarios, it is possible to infer their dust geometries by correlating their inferred dust laws with physical properties. For example, Reddy et al. (2015) studied a sample of $z \sim 2$ galaxies and found that the differences in attenuation between gas and stars are correlated with the galaxy's observed specific SFR (sSFR $\equiv$ SFR/$M_\star$), potentially a byproduct of the visibility of star-forming birth clouds. If the dust law is dependent on star-formation activity, then it may be different at earlier epochs ($z > 2$). This follows intuition because the intensity of star-formation and ionization conditions, which directly influence the attenuation conditions, have been shown to evolve with redshift (Madau & Dickinson, 2014; Steidel et al., 2014; Casey et al., 2014b; Shimakawa et al., 2015; Shapley et al., 2015; Sanders et al., 2015). These attenuation conditions are regulated by the formation, destruction, and spatial distribution of dust grains, and this cycle is one of the most poorly quantified processes in galaxies. One reason to seek evidence for the dust law is to place constraints on the observed dust grain size, which can be used to infer limits on dust production by SNe and AGB stars, especially given the maximum stellar population ages at the redshifts of distant galaxies.

While the dust law gives clues to the underlying grain size distribution in a broad sense (Gordon et al., 2000), it is difficult to connect the current grain sizes to their production sources due to their complex history of growth, destruction, and recycling over short timescales (Jones et al., 2013a). In addition, the dust production sources themselves, such as supernovae (SNe), asymptotic giant branch (AGB) stars, or Population III stars have changed in relative strength over cosmic timescales (Morgan & Edmunds, 2003; Nozawa et al., 2003). Contraints on the dust law can be used to infer the observed dust grain sizes, which is helpful when modeling the evolution

of dust grain production and evolution (e.g., in high-redshift quasars Nozawa et al., 2015). A better understanding of these mechanisms would help to constrain metal buildup and galactic feedback (Gall et al., 2011a; Davé et al., 2011a).

In addition, both the scale and the shape of the dust law affect the interpretation of galaxy SFRs, the evolution of the SFR density, and the evolution of the intergalactic medium (IGM) opacity. For example, Smit et al. (2014) showed that the measured $z \sim 7$ sSFR changes by nearly an order of magnitude depending on the assumed prescription of dust attenuation. It is clear that new methods must be developed to determine the shape of the dust law in the distant universe.

Our goal in this chapter is to provide evidence for the dust law at high redshifts using the information from galaxies' rest-frame UV-to-NIR SEDs. We use a Bayesian formalism that marginalizes over stellar population parameters from models of the galaxy SEDs (Salmon et al., 2015). This allows us to measure evidence in favor of one dust law over another for individual galaxies. We show that the favored dust laws are consistent with the galaxies' locations on the $IRX - \beta$ diagram for a sample of galaxies at $1.5 < z < 3.0$ with mid-IR imaging, where we can verify that the predicted attenuation agrees with the $IRX$.

This chapter is organized as follows. § 4.3 outlines our photometric and IR data, redshifts, and sample selection, as well as our calculations of IR luminosities and $\beta$. § 3.4 describes the framework of our SED-fitting procedure, including the stellar population models and dust laws. § 3.5 defines the use of Bayes factors as our selection method, and § 3.6 defines our parameterization of the dust law. § 3.7 shows the main results of the paper, where we use our Bayesian technique to quantify the evidence that star-forming galaxies at $z\sim$1–2 have a given dust law, using CANDELS *Hubble Space Telescope* (*HST*) and *Spitzer* data spanning the rest-frame UV-to-NIR SED. We then show that the UV color and thermal IR emission (measured from mid-

IR data) of these galaxies match the properties of their predicted dust law. § 3.8 discusses the implications and physical origins of our results, as well as comparisons to previous work and dust theory. Finally, § 5.2 summarizes our main conclusions. We assume concordance cosmology such that $H_0 = 70$ km s$^{-1}$ Mpc$^{-1}$, $\Omega_{\mathrm{M},0} = 0.3$ and $\Omega_{\Lambda,0} = 0.7$.

## 3.3 Data, Redshifts, and Sample Selection

### *3.3.1 Photometry: CANDELS GOODS Multi-Wavelength Data*

This chapter takes advantage of the multi-wavelength photometry from the GOODS North and South Fields (Giavalisco et al., 2004), the CANDELS survey (Grogin et al., 2011; Koekemoer et al., 2011), the WFC3 Early Release Science program (ERS Windhorst et al., 2011), and the Hubble Ultra Deep Field (HUDF Beckwith et al., 2006; Ellis et al., 2013; Koekemoer et al., 2013; Illingworth et al., 2013). We define magnitudes measured by *HST* passbands with the ACS F435W, F606W, F775W, F814W and F850LP as $B_{435}$, $V_{606}$, $i_{775}$, $I_{814}$, and $z_{850}$ and with the WFC3 F098M, F105W, F125W, F140W, and F160W as $Y_{098}$, $Y_{105}$, $J_{125}$, $JH_{140}$, and $H_{160}$, respectively. Similarly, bandpasses acquired from ground-based observations include the VLT/ISAAC $K_s$ and VLT/HAWK-I $K_s$ bands. We refer to Guo et al. (2013) for more details on the GOODS-S dataset, and Barro et al. (in prep.) for the GOODS-N dataset.

As applied by Salmon et al. (2015), we include an additional uncertainty, defined to be 10% of the flux density per passband of each object. This accounts for any systematic uncertainty such as flat-field variations, PSF and aperture mismatching, and local background subtraction. The exact value was chosen from series of recovery tests to semi-analytic models applied by Salmon et al. (2015). Including this additional uncertainty also helps to avoid situations where a given model SED band serendipitously finds a perfect match to an observed low-uncertainty band, creating

a biased posterior around local maxima. The additional uncertainty was added in quadrature to the measured uncertainties.

### *3.3.2 IR Photometry: Spitzer and Herschel*

We utilize imaging in the IRAC 3.6 and 4.5 $\mu$m bands from the *Spitzer* Extended Deep Survey (Ashby et al., 2013) to measure the rest-frame NIR of the galaxy SED. As described by Guo et al. (2011), the IRAC catalog uses the *HST* WFC3 high-resolution imaging as a template and matches to the lower-resolution images using TFIT (Laidler et al., 2007) to measure the photometry.

In order to verify the dust-attenuation law derived from the rest UV-to-NIR data, we require a measure of the rest UV-to-optical light reprocessed by dust and reemitted in the far-IR. Conventionally, the important quantities are the ratio of the observed IR-to-UV luminosities, $L(IR)/L(UV)$, which measures the amount of reprocessed light, and the UV-spectral slope, $\beta$, which measures the shape of the dust-attenuation curve (e.g., Meurer et al., 1999; Charlot & Fall, 2000; Gordon et al., 2000; Noll et al., 2009; Reddy et al., 2010). We used MIPS 24 $\mu$m measurements from the GOODS-*Herschel* program (Elbaz et al., 2011), where the GOODS IRAC 3.6 $\mu$m data were used as prior positions to determine the MIPS 24 $\mu$m source positions. Then, PSF-fitting source extraction was performed to obtain 24 $\mu$m fluxes, which we require to be $> 3\sigma$ detections for our sample. While we also examined galaxies with *Herschel* PACS and SPIRE 100 to 250 $\mu$m photometry, these data were ultimately not included because they had no effect on the results (see Appendix B.2).

### *3.3.3 Redshifts*

To minimize uncertainties in SED-fitting owing to redshift errors, we selected objects that have the highest quality spectroscopic redshifts. The spectroscopic redshifts are a compilation (Nimish Hathi & Mark Dickinson, private communication)

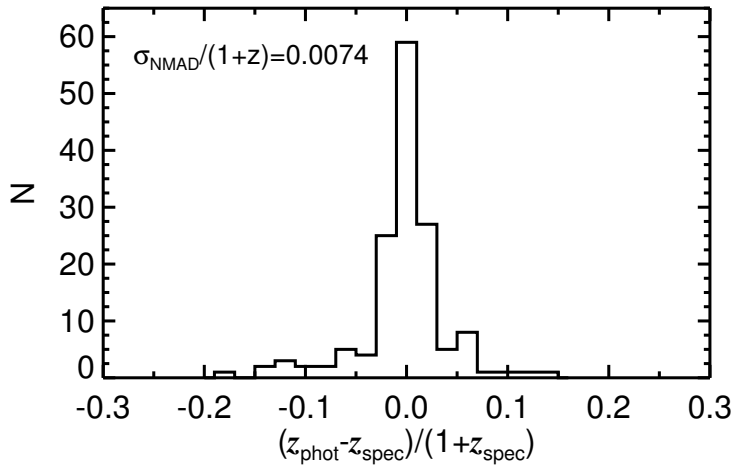


Figure 3.1: Redshift Accuracy of $z \sim 2$ Sample.
The photometric redshift accuracy for galaxies that are in both the phot-$z$ and spec-$z$ samples. The $\sigma_{\rm NMAD}$ gives the 68% scatter of the distribution.

from several published and unpublished studies of galaxies in GOODS-S (Mignoli et al., 2005; Vanzella et al., 2008; Balestra et al., 2010; Popesso et al., 2009; Doherty et al., 2005; Kriek et al., 2008; Fadda et al., 2010, Weiner et al. (unpublished)) and GOODS-N (Reddy et al., 2006; Daddi et al., 2009). We define the sample of galaxies with high-quality redshifts as the "spec-$z$" sample, but later we consider the full sample with photometric redshifts, which we call the "phot-$z$" sample.

The primary goal of this chapter is to determine the ubiquity of the dust-attenuation law at the peak of cosmic SFR density. When deriving properties of distant galaxies, we must naturally consider how our results are dependent on the assumed redshift of each galaxy. This can be done in two ways. First, we explore how our results depend on redshift accuracy by testing how our results vary if we use photometric redshifts for galaxies rather than their spectroscopic redshifts. Second, we determine how the results of the spec-$z$ sample differ from a larger sample of galaxies with photometric redshifts. The former test addresses how photometric redshift accuracy in general

affects the methods and results, while the latter test addresses if the photometric redshift accuracy within a larger sample is sufficient to reproduce the spectroscopic-redshift results. In addition, a photometric-redshift sample can reveal biases in the spec-$z$ sample because the latter is likely biased towards the brighter, bluer galaxies.

We used photometric redshifts that were derived following the methods by Dahlen et al. (2013), who developed a hierarchal Bayesian technique to convolve the efforts of eleven photometric redshift investigators in the CANDELS team. The photometric-redshift estimates of GOODS-S are taken from Santini et al. (2015) and those of GOODS-N are taken from Dahlen et al. (2015 in prep.). The GOODS-N photometric-redshift estimates also take advantage of SHARDS-grism narrow-band data. We take the photometric redshift as the median from the combined full $P(z)$ distributions of nine GOODS-N and six GOODS-S photometric-redshift investigators.

Figure 3.1 shows the accuracy of the photometric redshifts when compared to galaxies with known spectroscopic redshifts. We estimate the photometric-redshift accuracy from the normalized median absolute deviation (Brammer et al., 2008) which gives a 68% scatter of the distribution of $\sigma_{\rm NMAD}/(1+z) = 0.0074$. In addition, 94% of the sample has a quality of $|z_{\rm phot} - z_{\rm spec}|/(1 + z_{\rm spec}) < 0.1$. This gives us confidence that the redshifts of the phot-$z$ sample are well determined.

### *3.3.4 Sample Selection*

We limited the sample to $z > 1.5$, such that the ACS $B_{435}$ band still samples the rest-frame far-UV (FUV, $\sim$1500 Å), which is a crucial portion of the SED when distinguishing between dust laws. § 3.7.1 discusses the consequences of a galaxy not having a band close to the FUV, due to the redshift or available photometry. We also required a $z < 3$ limit because the IR-selection of sources at higher redshift

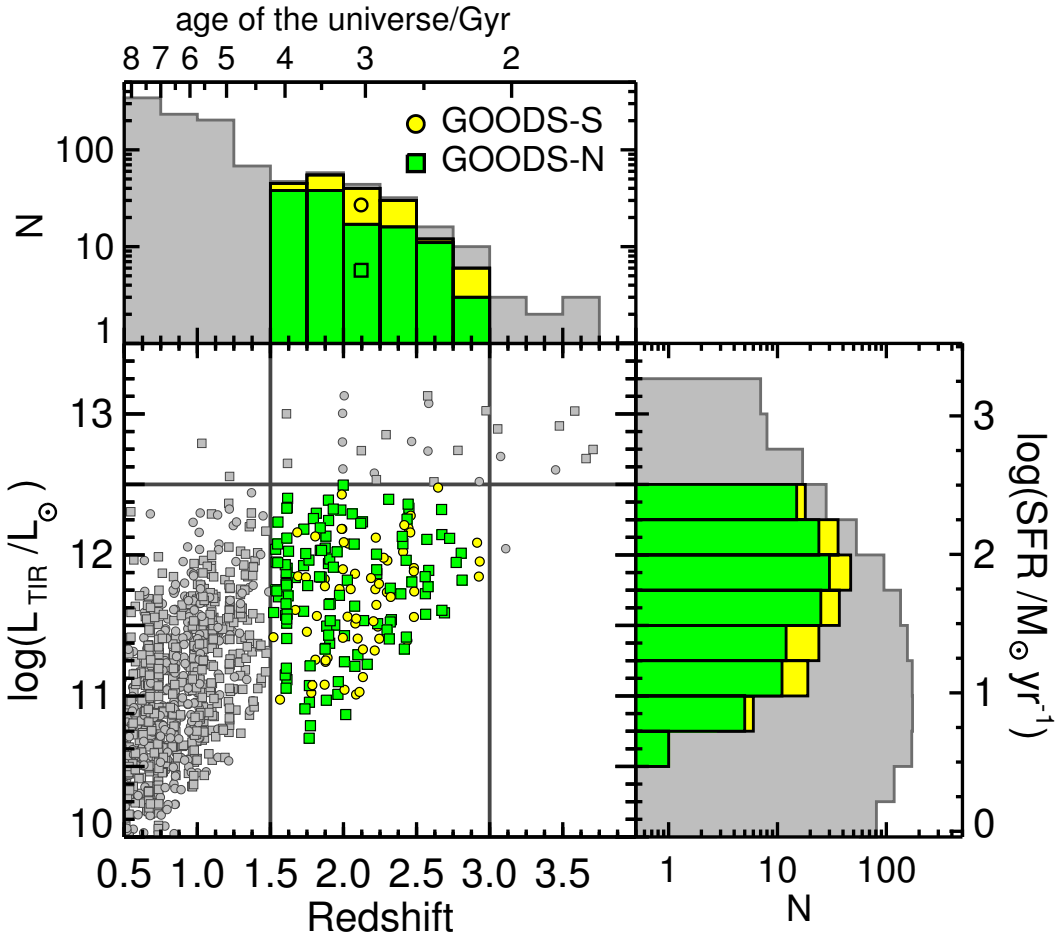


Figure 3.2: Total Infrared Luminosities.
The log of total IR Luminosity ($L_{\rm TIR}$), which was determined using a redshift-dependent conversion from $L_{24}$ $\mu$m, as a function of redshift. Galaxies in our sample lie in GOODS-N (yellow) and GOODS-S (green) and were restricted to log $L_{\rm TIR}<$ 12.5 and $1.5 < z_{\rm spec} < 3.0$. The adjacent histograms compare the logarithmic distributions of our sample to the parent sample. For reference, the top and right axes show the age of the universe and the SFR respectively.

correspond to objects with very bright IR luminosities (log $L_{\rm TIR}/{\rm L}_{\odot}>$ 12.5), where the frequency of objects dominated by AGN emission increases to $\sim$ 60% (Nardini et al., 2010). In addition, the upper redshift limit was chosen to avoid significant redshift evolution within the sample.

Applying the redshift range of $1.5 < z < 3.0$ and requiring 24 $\mu$m detections ($S/N > 3$) to the sample produces an initial sample of 65 (554) GOODS-N and 123 (552) GOODS-S spec-$z$ (phot-$z$) selected galaxies. A small number ($<$ 5% of the spec-$z$ sample and $<$ 2% of the phot-$z$) of objects were identified on or near bright stars and diffraction spikes, as well as at the edges of the image (Guo et al., 2013) and were removed from all samples.

We further identified galaxies that imply the presence of an active galactic nucleus (AGN) from their IR or radio data (Padovani et al., 2011; Donley et al., 2012) or if they have known X-ray detections (Xue et al., 2011). This selection removes 6 (52) GOODS-N and 31 (108) GOODS-S sources in the spectroscopic (phot-$z$) spec-$z$ sample. Our final sample contains 56 (485) GOODS-N and 88 (432) GOODS-S galaxies in the fiducial spec-$z$ (phot-$z$) sample.

### *3.3.5 Calculation of Total Infrared Luminosities*

One method to calculate the total infrared luminosity ($L_{\rm TIR}$) involves fitting broadband flux densities to a suite of look-up tables that were derived from templates of local IR luminous galaxies (Elbaz et al., 2011; Dale et al., 2001; Dale & Helou, 2002; Rieke et al., 2009). However, recent work has shown that template-fitting can overestimate $L_{\rm TIR}$ especially when the observed bands do not well sample the dusty SED (see Papovich et al., 2007; Overzier et al., 2011). At the redshifts of our sample, 46% of our galaxies lack detections redward of 24 $\mu$m (i.e., *Herschel* PACS or SPIRE).

Detailed studies have shown that the rest-frame mid-IR emission is an excellent estimator for $L_{\rm TIR}$ for both local and high-redshift ($z < 2.8$) galaxies once it has been properly calibrated (Wuyts et al., 2008; Rujopakarn et al., 2013, R13 hereafter). This conversion was developed using the fact that the average IR SEDs of galaxies are governed by their IR surface densities (Rujopakarn et al., 2011), allowing bolometric corrections to account for high-redshift polyaromatic hydrocarbon (PAH) emission. For the galaxies in our range of redshift and luminosity, R13 showed that the scatter in $L_{\rm TIR}$ derived from the 24 $\mu$m emission is very tight, only 0.06 dex (see R13, their Figure 2). Therefore, we adopted the relation from R13 (their equation 3) to derive $L_{\rm TIR}$ for the galaxies in this chapter using their observed 24 $\mu$m emission and redshifts.

The adopted 24 $\mu$m conversion was developed under several relevant assumptions: it applies to $z \sim 2$ galaxies that lie on the SFR-stellar mass main sequence (most galaxies in our sample are on the main sequence), the galaxies are not hyperluminous ($L_{\rm TIR} < 10^{13} L_{\odot}$), and the log $L_{\rm TIR}$ surface density scales linearly with log $L_{\rm TIR}$. These assumptions become important for compact starburst galaxies and ULIRGs ($L_{\rm TIR}/{\rm L}_{\odot} > 10^{12}$). Nevertheless, these objects are rare, and fewer than 25% of galaxies have $L_{\rm TIR}/{\rm L}_{\odot} > 10^{12}$ in both the phot- and spec-$z$ samples. This fraction of the sample are not the galaxies that drive the results of this chapter.

As a further check, 54% of the galaxies in our spec-$z$ sample have *Herschel* PACS and/or SPIRE data. The comparison using this data to calculate $L_{\rm TIR}$ can be found in Appendix B.2, but in short, the results of this chapter are unaffected by using fits to *Herschel* data instead of the 24 $\mu$m conversion to calculate $L_{\rm TIR}$.

The distribution of $L_{\rm TIR}$ is shown in Figure 3.2 as a function of redshift for all 24 $\mu$m-detected sources with spectroscopic redshifts, including those within our redshift range. For reference, we also show the SFRs corresponding to a given $L_{\rm TIR}$

following conversions equation 8 of R13 which is similar to the Kennicutt (1998) conversion with factors applied appropriate for a Salpeter (1955) IMF. This figure shows that galaxies in our sample have IR luminosities ranging from $5 \times 10^{10}$ to $3 \times 10^{12}$ $L_{\odot}$, consistent with luminosities of LIRGs.

### *3.3.6 Calculation of the UV Luminosity*

We derive the observed UV luminosity, $L_{\rm UV}$, that is, the UV luminosity uncorrected for dust attenuation as follows. $L_{\rm UV}$ was determined by taking the average luminosity of the best-fit SED in a 100 Å bandwidth centered at 1500 Å. There is little dependence on the choice of SED models, such as the choice of dust law or SFH, in determing $L_{\rm UV}$. Similar results are also found when approximating $L_{\rm UV}$ as the luminosity of the observed band closest to rest-frame 1500 Å.

### *3.3.7 Calculation of the UV Spectral Slope $\beta$*

The rest-frame UV slope is an important observational tool due to its relative ease of measurement for the highest redshift galaxies (even to $z \sim 10$, see Wilkins et al., 2015) and its sensitivity to stellar population age, metallicity, and attenuation by dust. Moreover, $\beta$ has often been used to estimate the dust attenuation by extrapolating its well-known local correlation with infrared excess (Meurer et al., 1995, 1999). Studies of the origins of the scatter in the $IRX - \beta$ relation show that it depends on metallicity, stellar population age, star-formation history, spatial disassociation of UV and IR components, and the shape of the underlying dust-attenuation curve, including the presence of the 2175 Å absorption feature (Gordon et al., 2000; Buat et al., 2005, 2010; Reddy et al., 2006; Muñoz-Mateos et al., 2009; Boquien et al., 2012). This raises concerns about generalizing the $IRX - \beta$ relation to higher redshifts (e.g. see the discussion by Casey et al., 2014b).

Historically, the methods used to calculate $\beta$ have been entirely dependent on

the available dataset. In the absence of UV continuum spectroscopy (the original method to determine $\beta$, Calzetti et al., 1994), we must calculate $\beta$ from the UV colors provided by broadband photometry. Specifically, we calculated $\beta$ from the best-fit SED following the methods of Finkelstein et al. (2012b). We favor this method over a power-law fit to the observed photometric bands for the following reasons.

First, we ran simple tests on the stellar population models to recover the input $\beta$ with a power-law fit to the bands with central wavelengths between rest-frame $1200 < \lambda < 3000$ Å. The true $\beta$ is determined from stellar population models by Kinney et al. (1996), using the spectral windows defined by Calzetti et al. (1994) after applying a range of $E(B-V)$. This method produced a systematic offset at all redshifts such that $\beta_{\rm true} = \beta_{\rm phot} - 0.1$, and at some redshifts the recovery is off as much as $\Delta\beta = -0.5$.

Second, Finkelstein et al. (2012b) saw a similar offset and scatter in recovering $\beta$ from a single color or power-law fit. They promoted calculating $\beta$ by using UV-to-optical photometry to find the best-fit SED and using the UV spectral windows of Calzetti et al. (1994) to determine $\beta$. Their simulations reported a better recovery of $\beta_{\rm true}$ with no clear systematics and a scatter of $\Delta\beta = \pm 0.1$ for galaxies at $z = 4$. We therefore used the best-fit model to calculate $\beta$, assuming a constant SFH and a starburst (Calzetti et al., 2000) dust law (see Appendix B.3 which shows that the results are not sensitive to changing the derivation of $\beta$ to be a power-law fit to the photometry in the rest-frame UV).

Table 3.1: SED Fitting Parameters

| Parameter | Quantity | Prior | Relevant Sections |
|---|---|---|---|
| Redshift | fixed | spectroscopic redshifts, $1.5 \leq z_{\rm spec} \leq 3.0$ | § 3.3.3 § 3.7.2 |
| | fixed | photometric redshifts, $1.5 \leq z_{\rm phot} \leq 3.0$ | § 3.3.3 § 3.7.3 |
| Age | 100 | 10 Myr to $t_{\rm max}$ [1] | – |
| Metallicity | 5 | $Z = 0.02, 0.2, 0.4, 1.0, 2.5\ Z_{\odot}$ | – |
| $E(B-V)$ [2] | 85 | Linear, $-0.6 < E(B-V) < 1.5$, $\Delta E(B-V) = 0.025$ | § 3.4.3 |
| Attenuation prescription | fixed | starburst (Calzetti et al., 2000) or SMC92 (Pei, 1992) | § 3.4.3 § 3.7.2.2 |
| | 11[3] | $-0.6 < \delta < +0.4$, in steps of $\Delta\delta = 0.1$ | § 3.6 § 3.7.3.2 |
| $f_{\rm esc}$ | fixed | 0 | – |
| Star formation history [4] | fixed | 100 Gyr (constant) | § 3.4.2 |
| | 10 | $\pm\tau$ = 0.1, 0.3, 1, 3, 10 Gyr | § 3.4.2 |

One may be concerned that the adopted method makes $\beta$ sensitive to the assumed dust law of the SED models. However, the best-fit SED will always provide a close match to the UV colors so long as the assumed dust law does not have any extreme features such as the excess of absorption at 2175 Å or the almost broken power-law rise in the far UV of the Pei (1992) extinction curve. We found similar results when calculating $\beta$ from the best-fit SED when we allow the shape of the dust law to vary as a new parameter in § 3.6.

## 3.4 Modeling Stellar Populations

The bulk of the methods and procedures of the SED fitting are described by Salmon et al. (2015), which we summarize here including recent changes. The SED fitting is Bayesian in nature, offering a mechanism to determine the conditional probability for each desired physical property of the galaxy.

### *3.4.1 Bayesian Methods*

Using Bayes' theorem,

$$P(\Theta'|D) = P(D|\Theta')\ P(\Theta')/P(D), \tag{3.2}$$

we determine the posterior, $P(\Theta'|D)$, with parameters $\Theta' = (\Theta\{t_{\rm age}, E(B-V), Z\}, {\rm M}_\star)$ and data, $D$, under the *a priori* probability of the parameters or simply the "prior", $P(\Theta')$. The likelihood, $P(D|\Theta')$, is determined in the usual way using $\chi^2$ statistics (i.e., equation 2 of Salmon et al., 2015). The unconditional marginal likelihood of the data, $P(D)$, often referred to as the Bayesian evidence[5], normalizes the posterior such that the integrated posterior across all parameters is equal to unity (Jeffreys,

[5]The Bayesian evidence is occasionally denoted by $Z$. We adopt the formal definition, $P(D)$, to avoid confusion with the conventional astronomical symbol of metallicity.

1961; Heckerman, 1995; Newton et al., 1996):

$$\text{Bayesian evidence} \equiv P(D) = \int_{\Theta} P(D|\Theta)\ P(\Theta)\ \mathrm{d}\Theta. \tag{3.3}$$

Calculating the unconditional marginal likelihood is a way to eliminate the parameters $\Theta$ from the posterior (in equation 3.2) through integration, leaving us with the probability of seeing the data $D$ given all possible $\Theta$ (Kass & Raftery, 1995). The importance of the marginal likelihood will be discussed further in § 3.5.

Posteriors on individual parameters can be determined by marginalizing over nuisance parameters. The strength of this Bayesian approach is that the marginal probability of a given parameter is conditional to the probability from the nuisance parameters. For example, the posterior on $E(B-V)$ is conditional to the probability contribution from all stellar population ages, metallicities, and star-formation histories. This approach is an alternative to using parameter results taken from the best-fit (minimum $\chi^2$) model SED because it relies on posterior integration instead of likelihood maximization. The disadvantage of the latter is that small differences in $\chi^2$ or an underrepresentation of measurement uncertainties can result in best-fit models that are sporadic across the parameter space, making results highly dependent on the SED template assumptions (see Figures 20 and 21 of Salmon et al., 2015). We therefore favor using the median of each parameter's marginalized posterior over results determined from the best-fit model, as supported by recent literature (Song et al., 2015; Tanaka, 2015; Smith & Hayward, 2015).

### *3.4.2 Stellar Population Models*

Table 3.1 shows the ranges, quantity of values considered, and priors of the SED fitting parameters. Each combination of age, metallicity, and $E(B-V)$ produces an SED shape and associated $\chi^2$. The parameter space was constructed following

the listed priors on each parameter. We used Bruzual & Charlot (2003) stellar population synthesis models with the addition of nebular emission lines assuming an ionizing continuum escape fraction of $f_{\rm esc}$=0 (Salmon et al., 2015). We assumed a Salpeter (1955) initial mass function and H I absorption from line-of-sight IGM clouds according to Meiksin (2006). The Meiksin (2006) IGM attenuation model includes higher order Lyman transitions. Nevertheless, the assumption of IGM attenuation has minimal effect on the results because few galaxies have photometry covering wavelengths blueward of 1216 Å.

The range of $E(B-V)$ extends below zero for two reasons. First, consider the example where a Gaussian-shaped posterior for parameter $x$ peaks at $x = 0$, but all probability at $x < 0$ is set to zero. The $x$ corresponding to the median probability of such a posterior would be biased to $x > 0$, an artifact of the choice of parameter space. This was pointed out by Noll et al. (2009), who showed a bias to Bayesian estimates of certain parameters, especially parameters such as $E(B-V)$ whose posterior often peaks at the edge of the parameter space. Second, negative values of $E(B-V)$ are not necessarily unphysical. There are some, albeit rare, situations where isotropic scattering by dust in face-on galaxies can produce an enhancement of optical light (i.e., $A_{\rm V} < 0$ Chevallard et al., 2013).

We also considered how our results are dependent on the assumed shape of the star-formation history. The star-formation history is known to be a poorly constrained parameter in the fitting process (e.g. Papovich et al., 2001; Noll et al., 2009; Reddy et al., 2012a; Buat et al., 2012; Mitchell et al., 2013). While it is not the motivation of this chapter to accurately fit the star-formation history for individual galaxies, assuming a fixed history may reduce flexibility in the parameter space and overstate the perceived evidence between different dust laws. We therefore considered three scenarios of the star-formation history (SFH): constant, rising, and declining

exponentially with cosmic time, with ranges for the latter two cases described in Table 3.1. We take the assumption of a constant history as our fiducial model, and we show in Appendix B.4 that our main results are unchanged if we instead adopt rising or declining star-formation histories.

The stellar mass was treated differently than the individual parameters $\Theta$. It is effectively a normalization of the SED, given the mass-to-light ratio associated with the SED shape, hence the distinction in § 3.4.1 between $\Theta$, which represents the parameters that actually drive the goodness of fit, and $\Theta'$, which is those parameters and their associated stellar mass. In this manner, the posterior in stellar mass was determined by integrating the posterior rank-ordered by stellar mass to achieve a cumulative probability distribution in stellar mass such that the median is defined where the cumulative probability is equal to 50%.

### *3.4.3 Known Dust Attenuation Curves*

The dust law was fixed during the fitting process (along with the redshift, escape fraction, and star-formation history), although we individually considered a variety of commonly used dust laws. The curves of these dust laws are shown in Figure 3.3 and include those of the empirically derived attenuation for local starburst galaxies (Calzetti et al., 2000), the Milky Way extinction (which showcases the strong 2175 Å dust absorption feature, Gordon et al., 2003), an empirically derived attenuation for $z \sim 2$ star-forming galaxies ("MOSDEF", Reddy et al., 2015), and two interpretations of the SMC extinction: SMC92 (Pei, 1992) and SMC03 (Gordon et al., 2003), hereafter.

In Figure 3.4, several dust attenuation and extinction laws from Figure 3.3 are shown on the plane of infrared excess, $IRX$, and UV slope, $\beta$. Each dust law's $IRX - \beta$ relation represents the predicted location of a variety of stellar populations

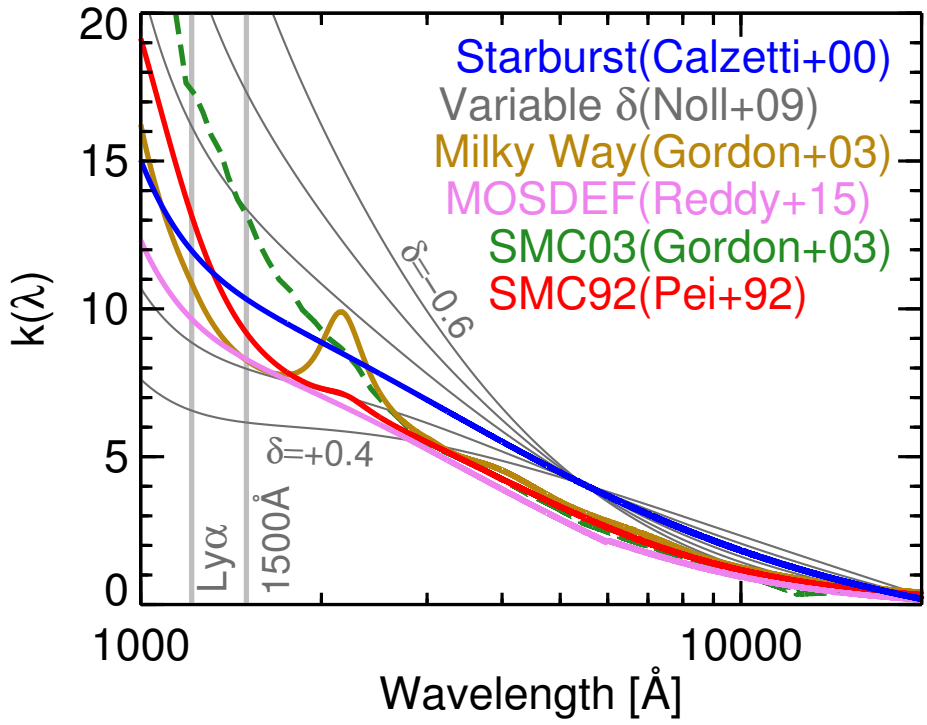


Figure 3.3: Common Dust Laws.
A variety of common dust laws shown by their total-to-selective extinction or attenuation as a function of wavelength. The Pei (1992) derivation of the SMC extinction (red, SMC92) will be used in this work to compare to the starburst prescription derived by Calzetti et al. (2000) (blue). Other dust laws are also shown including the MOSDEF (pink) attenuation curve derived from $z \sim 2$ galaxies (Reddy et al., 2015), and the Milky Way (gold) and SMC (SM03, green, dashed) extinction curves derived by Gordon et al. (2003). In addition, we consider power-law deviations to the starburst curve (equation 3.7) to be more ($+\delta$) or less ($-\delta$) grey. The wavelengths of 1500 Å and the Lyman $\alpha$ emission line are shown for reference.

that have been reddened according to their given dust-attenuation or dust-extinction curve. Creating these relations requires several assumptions about the intrinsic stellar populations, which manifest as an increase in the relation's width. First, we obtained a library of BC03 stellar populations with a range of ages (50 Myr to 1 Gyr), star-formation histories (SFR$\sim e^{t/\tau}$, where 1 Gyr $< \tau <$ 100 Gyr), and metallicities ( 0.02 $Z_{\odot} < Z <$ 2.5 $Z_{\odot}$). Then, we subtracted the dust attenuated SED from the intrinsic SED and integrated the residual across all wavelengths to obtain an estimate of the bolometric IR luminosity for these models. We made the approximation that the calculated IR luminosity of each model is representative of $L_{\rm TIR}$, under the assumption that all attenuated UV-to-NIR light is completely reprocessed to produce the total IR luminosity. $L_{\rm UV}$ and $\beta$ for these models were calculated using the same methods as used on the best-fit SEDs of the data (in § 3.3.6 and § 3.3.7, respectively).

From this framework, each dust model in Figure 3.4 has a width in the $IRX - \beta$ plane which is a product of the range in the stellar population parameters (age, metallicity, star-formation history), which affects both $IRX$ and $\beta$ and produce the scatter illustrated by the colored swath. The left edge represents younger, low-metallicity, and maximally blue stellar populations, while the right edge extends towards older, metal-rich, and intrinsically red stellar populations. With increasing steps of $E(B-V)$ (moving up each $IRX - \beta$ relation), a steeper dust law will redden the SED faster and therefore produce less $IRX$ at a given $\beta$ when compared to greyer, starburst-like dust laws (Siana et al., 2009). In addition, the presence of a 2175 Å dust absorption feature, such as is found in the Milky Way dust law, will produce a significant excess of IR emission without significantly contributing to the reddening (although this depends on the manner in which $\beta$ is determined, see Kriek & Conroy, 2013). These $IRX - \beta$ relations provide an observational basis with which to distinguish between dust-attenuation curves.

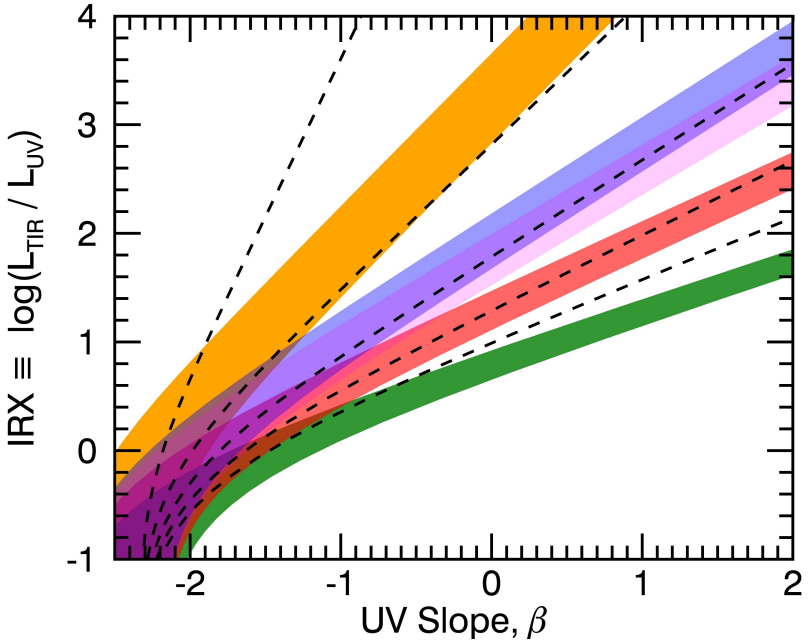


Figure 3.4: Dust Laws on $IRX - \beta$.
The predicted locations of galaxies with different dust laws on the plane of the UV slope $\beta$ and infrared excess ($L_{\rm TIR}/L_{\rm UV}$). The colored swaths correspond to the same dust laws as in Figure 3.3, clockwise from top left: Milky Way, starburst, MOSDEF, SMC92, and SMC03. The width of each $IRX - \beta$ relation accounts for the scatter in the intrinsic $\beta$ from the effects of stellar population age (50 Myr to 1 Gyr), SFH (SFR$\sim e^{-t/\tau}$, with 1 Gyr $< \tau <$ 100 Gyr), and metallicity (0.02 $Z_\odot < Z <$ 2.5 $Z_\odot$). The dashed lines show the relations according to the parameterized dust law (see § 3.6) with (clockwise from left) $\delta$ = +0.4, +0.2, 0.0, -0.2 -0.4.

## 3.5 Distinguishing Between Dust Laws with Bayes Factors

Determining the shape of the dust-attenuation curve from broadband data is nontrivial. Broadband SED fitting is fraught with parameter degeneracies, a product of several physical mechanisms that conspire to produce similar SED shapes (e.g. stellar population age, metallicity, star-formation history, and dust attenuation; e.g. Papovich et al., 2001, 2011; Lee et al., 2010, 2011; Walcher et al., 2011; Pacifici et al., 2012; Pforr et al., 2012, 2013; Mitchell et al., 2013). As mentioned in § 3.4, these degeneracies spawn biases in simple $\chi^2$ likelihood-ratio tests because best-fit models are more sensitive to SED template assumptions such as the inclusion of nebular emission lines, changing the assumed dust curve and/or the degeneracies within the parameters themselves (Tilvi et al., 2013; Salmon et al., 2015).

To distinguish between dust laws, we should consider all parameters, $\Theta$, as nuisance parameters, such that the fully marginalized parameter space contains probability contribution from all $\Theta$. We are then left to quantify the difference between the fully marginalized posteriors under their respective assumptions of non-parametric dust laws. In order to achieve this, we consider the posterior in Bayes theorem (equation 3.2) as being further conditional to a model assumption exterior to the fitting process (in this case, the assumed dust-attenuation curve, $k_\lambda$). Then we may determine the odds that the hypothesis of one dust-attenuation curve is correct over another. The ratio of a posterior assuming dust-attenuation curve $k_\lambda^1$ and a posterior assuming dust-attenuation curve $k_\lambda^2$ is therefore given by,

$$\begin{gathered}\frac{P(\Theta', k_\lambda^1|D)}{P(\Theta', k_\lambda^2|D)} = \frac{P(D|\Theta', k_\lambda^1)}{P(D|\Theta', k_\lambda^2)} \times \frac{P(\Theta'|k_\lambda^1)}{P(\Theta'|k_\lambda^2)}, \\ \text{or} \quad \text{posterior odds} = \text{Bayes factor} \times \text{prior odds}.\end{gathered} \tag{3.4}$$

The term in the middle is referred to as the Bayes factor (Jeffreys, 1935, 1961;

Kass & Raftery, 1995). In practice, we may write the Bayes factor as a ratio of the marginal likelihood (see Sutton & Abrams (2001) for a similar definition). Combining the definition in equation 3.3 with the conditions in equation 3.4, we obtain the plausibility that one dust-attenuation curve is more likely given another, marginalized over all parameters:

$$\text{Bayes factor} \equiv \ B_{12} = \frac{P(D|k_\lambda^1)}{P(D|k_\lambda^2)} \tag{3.5}$$

Kass & Raftery (1995) offered descriptive statements for Bayes factors in order to denominate several standard tiers of scientific evidence. These were defined using twice the natural logarithm of the Bayes factor, which we will call the Bayes-factor evidence, $\zeta$:

$$\begin{aligned} \text{Bayes}-\text{factor evidence} \equiv \ \zeta &= 2 \cdot \ln B_{12} \\ \zeta &= 2 \cdot \ln \frac{\int_\Theta P(D|\Theta', k_\lambda^1)\ P(\Theta'|k_\lambda^1)\ \mathrm{d}\Theta}{\int_\Theta P(D|\Theta', k_\lambda^2)\ P(\Theta'|k_\lambda^2)\ \mathrm{d}\Theta}. \end{aligned} \tag{3.6}$$

We adopt the significance criteria of Kass & Raftery (1995), who define the evidence to be "very strong" ($\zeta >$10), "strong" ($6 < \zeta <$ 10), or "positive" ($2 < \zeta <$ 6) towards $k_\lambda^1$ (and equivalent negative values for evidence towards $k_\lambda^2$). Intuitively, because the Bayesian evidence $P(D)$ is proportional to the integral over the likelihood (equation 3.3), a model that produces a better fit to the data (low $\chi^2$) will yield a higher $P(D)$, making $|\zeta|$ larger in the case that one dust law is more likely than another.

Throughout this paper, we refer to galaxies with high $|\zeta|$ as having strong Bayes-factor evidence towards a given dust law. However, we caution that Bayes factors do not necessarily mandate which of two models is correct but instead describe the evidence against the opposing model. For example, a galaxy with very strong

evidence towards model 2 (e.g. $\zeta \approx -20$ according to equation 3.6), promotes the *null hypothesis* that model 1 is correct. Formally, it does not say the model 2 is the correct model, but promotes the rejection of model 1 (and vice versa). In the next section, we address this subtlety with a direct parameterization of the dust-attenuation curve in order to confirm if the Bayes-factor evidence is indeed pointing towards the appopriate dust prescription.

## 3.6 Parameterizing the Dust Law

While it is instructive to search for the evidence that galaxies have one of the empirically or physically motivated dust laws from § 3.4.3, there is no guarantee that these dust laws apply to all galaxies, particularly at high-redshifts. We therefore adopted an alternative model for the dust attenuation, where we parameterize the dust law in the SED-fitting process. The parameterization allows a smooth transition between the different dust laws. Following Kriek & Conroy (2013), we allowed the dust-attenuation curve to vary as a tilt from the starburst curve of Calzetti et al. (2000) similar to the parameterization provided by Noll et al. (2009). This paramaterized dust law, which is a purely analytical interpretation of how the dust-attenuation curve may be adjusted is:

$$A_{\lambda,\delta} \equiv \; E(B-V)\; k_{\lambda}^{\mathrm{SB}} \; (\lambda/\lambda_{\mathrm{V}})^{\delta} \tag{3.7}$$

This definition returns the starburst attenuation curve, $k_{\lambda}^{\mathrm{SB}}$, when $\delta = 0$, a steeper, stronger attenuation in the FUV when $\delta < 0$, or a flatter, greyer attenuation across UV-to-NIR wavelengths when $\delta > 0$. Examples of these dust laws are shown in Figure 3.3. We chose a parameter space with a range $-0.6 < \delta < +0.4$ in steps of $\Delta\delta$=0.1 (see Table 3.1). This range brackets the range of dust laws observed in the literature. In comparison, SMC92 is slightly steeper than the starburst curve across

UV-to-NIR wavelengths, similar to $\delta \approx -0.1$, but is much steeper at $\lambda \lesssim 1500\mathring{A}$, similar to $\delta \approx -0.5$.

Given the set of dust laws, we can marginalize over all other parameters $\Theta$ to obtain the posterior on $\delta$ for each galaxy. This process is the same as the marginalization in equation 3.3, where we marginalize over all $\Theta$ to obtain the full marginal likelihood, except that we have added an additional parameter $\delta$. In some cases $\delta$ may be poorly constrained, and the posterior will be very broad. This is to be expected, as there is similarly a population of galaxies for which the Bayes factor is unable to return significant evidence. The results of fitting to $\delta$ are described in § 3.7.2.2 and 3.7.3.2.

Equation 3.7 assumes there is no additional contribution from the 2175 Å absorption feature, which is a hallmark of the Milky Way dust-attenuation curve (Gordon et al., 2003) and is likely caused by absorption from polycyclic aromatic hydrocarbons. Although there is evidence of the 2175 Å feature in high-redshift quasars (Noterdaeme et al., 2009), gamma ray burst host galaxies (Elíasdóttir et al., 2009), and star-forming galaxies (Noll et al., 2007; Buat et al., 2011), its strength and prevalence in distant galaxy populations remains uncertain (Buat et al., 2012). As we discuss below (§ 3.7.3.2), we tested for indications of the 2175Å feature in the dust law and found no substantive evidence for it based on our model fits to the broadband data. We therefore did not include the 2175Å feature in our modeling. Introducing it would add another parameter to the dust law (see Kriek & Conroy, 2013).

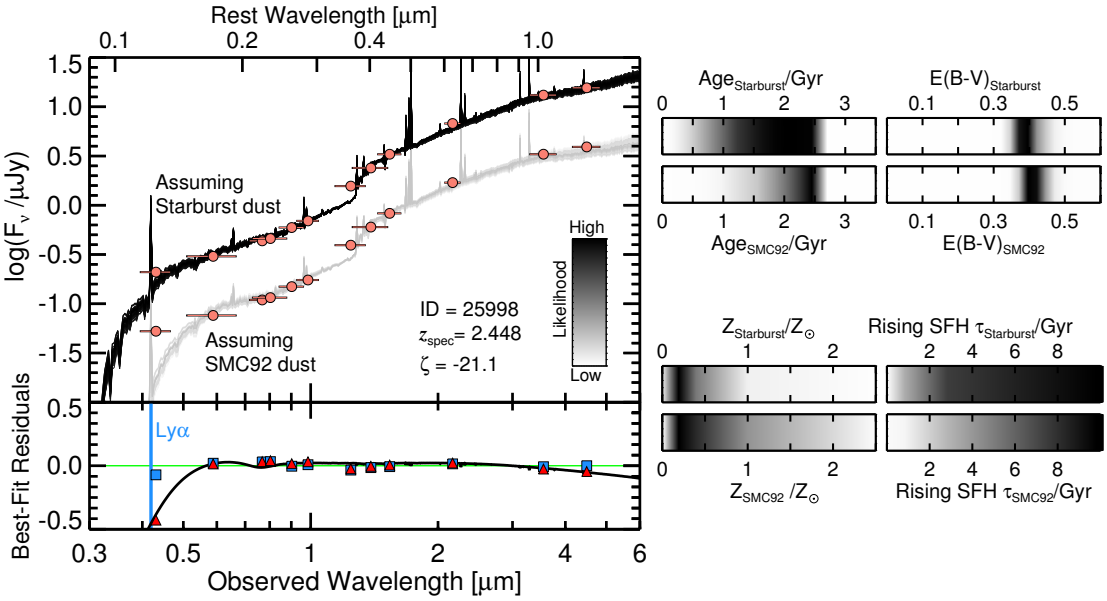


Figure 3.5: Example SEDs That Favor a Starburst Dust Law.
The SED of a galaxy in our spec-$z$ sample with strong Bayes-factor evidence ($\zeta = -21$) towards a starburst-like attenuation. The salmon-colored photometric data points are shown twice, with the second set offset by 0.6 dex for clarity. The 50 most likely SEDs are shown, scaled in opacity such that darker curves represent higher likelihood up to the best-fit model, under an assumed starburst (upper) or SMC92 (lower) dust law. The black curve in the lower panel shows the log-difference residual of the best-fit SED under each dust assumption, and the average residual of the data and the 50 best-fit starburst (SMC92) model fluxes in blue squares (red triangles). The residual of the best-fit SEDs are shown in the lower panel. The bars to the right show the marginalized posteriors of individual parameters, with darker regions denoting higher likelihood. For galaxies with very red SEDs across rest-frame $\lambda = 0.2 - 2$ $\mu$m (the inferred $E(B-V)$ is high) the UV-steep SMC92 dust law is incapable of producing high-likelihood models that match both the $B_{435} - V_{606}$ color and the red rest-frame NIR color. This leads to the large difference in Bayesian evidence and the low Bayes-factor evidence, $\zeta$.

## 3.7 The Non-Universality of Dust Laws at $z \sim 2$

### *3.7.1 Relevant Spectral Features*

Figure 3.5 shows the SED of a single galaxy in the spec-$z$ sample that has strong Bayes-factor evidence promoting a starburst dust-attenuation law. The SED features that drive the differences in likelihood between the two dust assumptions are subtle. In general, the rest-frame UV flux (1200 Å $\lesssim \lambda \lesssim$ 1400 Å), which at the redshift range of this chapter is either the $B_{435}$ or $V_{606}$ filter, catches the wavelength where the dust laws differ the most. For galaxies like the example in Figure 3.5, the rest-frame optical-to-NIR SED suggests a highly attenuated stellar population (high $E(B-V)$), yet the flux from the rest-frame FUV band is brighter than the prediction when assuming SMC92 dust. This results in a lower likelihood for SMC92 models compared to models that assume starburst dust. This is true even when accounting for the contribution from Ly$\alpha$ emission in the models or variations to the assumed star-formation history. The likelihood difference, when marginalized over all parameters, is reflected in the Bayes-factor evidence.

Figure 3.6 shows the SED of a single galaxy in the spec-$z$ sample that has strong Bayes-factor evidence promoting an SMC92 dust-extinction law. For this galaxy, the rest-frame optical-to-NIR SED suggests a stellar population with relatively low levels of attenuation (low $E(B-V)$). However, there is a subtle decrease in the rest-frame FUV emission, which the starburst attenuation has difficulty matching simultaneously with the rest of the SED, resulting in less overall likelihood as compared to the SMC92 assumption. Again, this likelihood difference is reflected in the Bayes-factor evidence.

One potential alternative explanation for the shape of these SEDs is a two-component stellar population: a young burst of star formation producing O- and

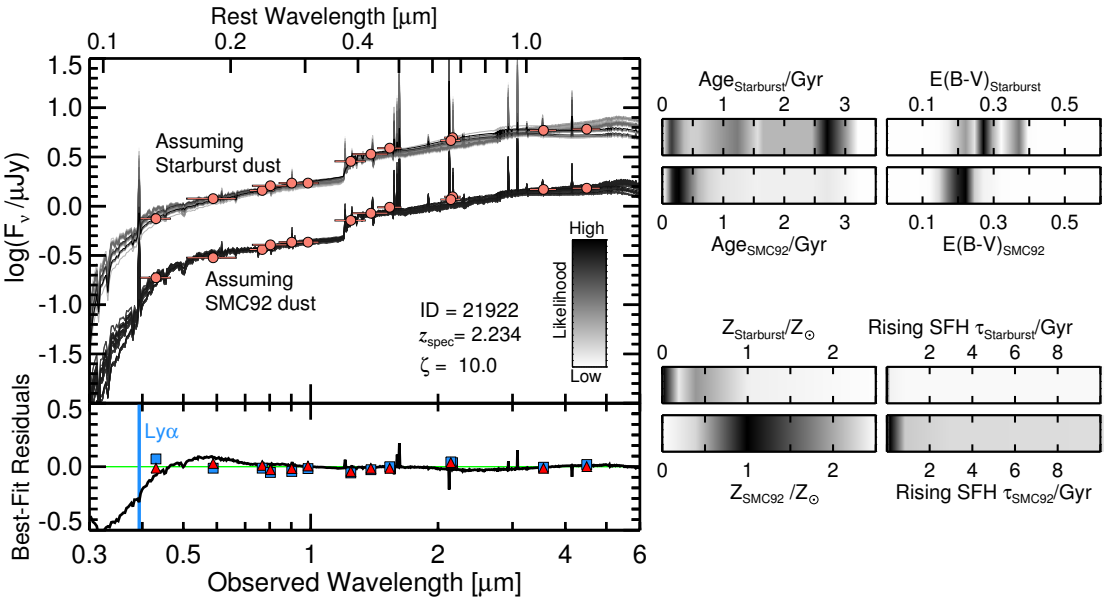


Figure 3.6: Example SEDs That Favor an SMC Dust Law.
The SED of a galaxy that has strong Bayes-factor evidence ($\zeta = 10$) towards an SMC92-like dust-attenuation law. The data are shown twice for fits under each dust assumption, offset by 0.6 dex for clarity. The results between assuming starburst and SMC92 attenuations are subtle; when most of the SED (rest-frame $\lambda = 0.2 - 2\ \mu$m) suggests relatively low values of $E(B-V)$, the assumpition of a starburst law does not produce as many models with significant likelihood as the SMC92 law capable of reproducing both the red $B_{435} - V_{606}$ color and the rest-frame NIR color. The resulting difference in likelihood is reflected in the Bayes-factor evidence, $\zeta$.

B-type stars that dominate the rest-frame UV and an already present intermediate-age population that dominates the rest-frame optical-to-NIR SED. As shown in the single-parameter likelihood distributions of Figures 3.5 and 3.6, the exponential star-formation history is a poorly constrained parameter with this dataset. Folding in additional SFH parameters will require data with a higher wavelength resolution of the SED in order to overcome its degeneracies with age, metallicity, and the tilt and scale of dust attenuation.

### *3.7.2 Results from the Spectroscopic Redshift Sample*

#### *3.7.2.1 Bayes Factors on the $IRX - \beta$ Relation: spec-z sample*

Figure 3.7 shows the selection of Bayes-factor evidence for individual galaxies as a function of stellar mass. As expected, most galaxies lack enough evidence from their broadband data alone to distinguish their underlying dust law. However, there are examples of galaxies that display strong evidence towards having an SMC-like or starburst-like attenuation. Figure 3.7 also shows the plane of $IRX - \beta$, where the total infrared luminosities were calculated as described in § 3.3.5 and $\beta$ in § 3.3.7. As noted in Figures 3.5 and 3.6, the band closest to the Ly$\alpha$ is the most sensitive to determining the evidence towards a given dust law because it is at the wavelength where the dust prescriptions differ the most.

The Bayes-factor evidence for different dust laws among is consistent with the galaxies' positions in the $IRX - \beta$ plane. The Bayes-factor evidence was derived from the rest UV-to-NIR photometry and shows that some galaxies have very strong evidence against the starburst law or SMC92 law. Those same galaxies have $IRX - \beta$ measurements consistent with the Bayes-factor evidence. This is significant because the $L_{\rm TIR}$ data provide an independent measure of the dust law.

Though the results of Figure 3.7 seemingly identify galaxies with two types of underlying dust scenarios, we must recognize the possibility that neither dust-attenuation curve is appropriate, even for some of the objects with the strongest evidence. In the next section, we pursue this possibility using the methods described in § 3.6 to parameterize the dust-attenuation curve as a new variable in the fitting process.

#### *3.7.2.2 Fitting the Curve of the Dust Law: spec-z sample*

Figure 3.8 shows the results of fitting to the parameterized dust-attenuation curve (equation 3.7). The selection of galaxies with strong evidence towards a starburst-like dust-attenuation curve agrees with the results from fitting to the dust-attenuation curve directly. Similarly, SMC-like galaxies are better described by a steeper dust-attenuation curve ($\delta < -0.2$), albeit at varying degrees. The galaxies selected to have strong evidence towards an SMC92 dust law exhibit a marked steepness in their fitted dust-attenuation curve that contrasts with a starburst dust law.

In § 3.5, we mentioned how the Bayes factor is formally promoting the *null hypothesis* of the opposing model. For example, the Bayesian evidence formally does not favor model 1, but provides evidence against the competing model 2 compared to model 1. However, taken together, the results in Figure 3.8 imply that galaxies with negative $\delta$ really do have steeper attenuation curves like that of the SMC92. In this case, we may consider the evidence towards the null hypothesis of the opposing dust law as being the same as positive evidence for the hypothesis of the dust law itself.

One of the main results of this chapter is seen in Figure 3.9: there is a strong relation between $E(B-V)$ and $\delta$. Figure 3.9 shows the derived values of $E(B-V)$ and $\delta$ for galaxies with high Bayes-factor evidence. Because both axes are derived quanties with associated posteriors, we combine the posteriors into a two-dimensional posterior for the whole sample. In both cases, a clear trend emerges such that galaxies with steeper, SMC-like dust laws also have lower levels of attenuation, whereas galaxies with high attenuation have greyer, starburst-like dust laws. This correlation agrees with the $IRX-\beta$ relation in Figure 3.4; galaxies with low $IRX$ are expected

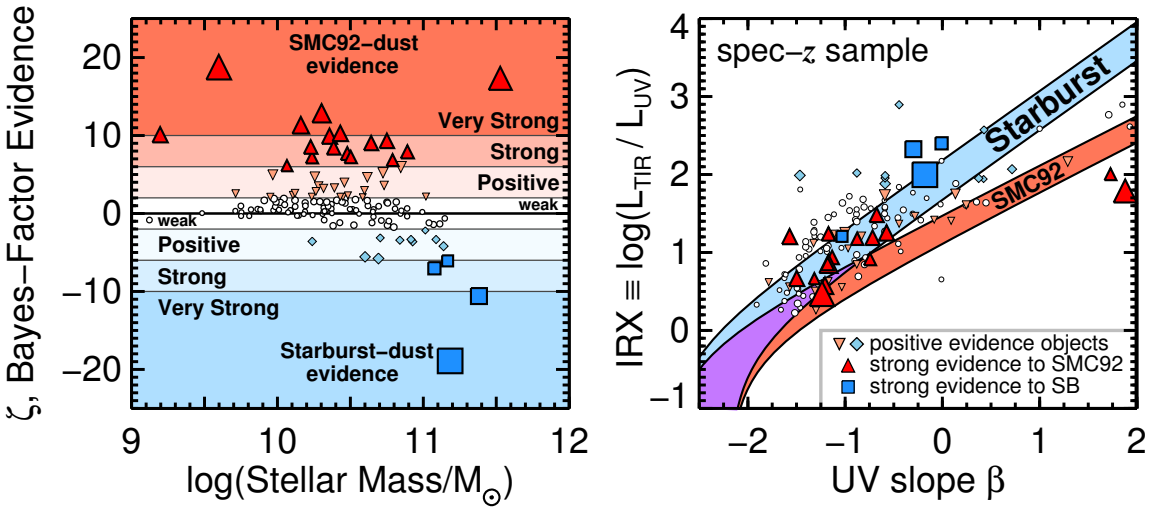


Figure 3.7: Bayes-Factor Evidence on $IRX - \beta$.
Left: The Bayes-factor evidence as a function of stellar mass for galaxies in the spec-$z$ sample with $1.5 \leq z \leq 2.5$ and MIPS 24$\mu$m detections of S/N>3. Darker shaded regions indicate levels of increasing evidence and are used to select objects that show strong preference between SMC92 (red triangles) or starburst (blue squares) dust curves. No mid-IR information was used in the left figure; these values were achieved by modeling rest-frame UV-to-NIR fluxes only. Right: Measured IR excess versus UV slope to test results inferred from the UV/NIR SED. Prediction curves from stellar population models for SMC92 (red) and starburst (blue) dust laws are shown. Objects selected by the strength of their Bayes-factor evidence follow the curve of their predicted dust-attenuation curve with some scatter. The independent measurements of the $IRX - \beta$ relation supports the Bayesian evidence from the modeling of the UV/NIR SED: galaxies with (very-)strong Bayes-factor evidence follow the correct $IRX - \beta$ relation.

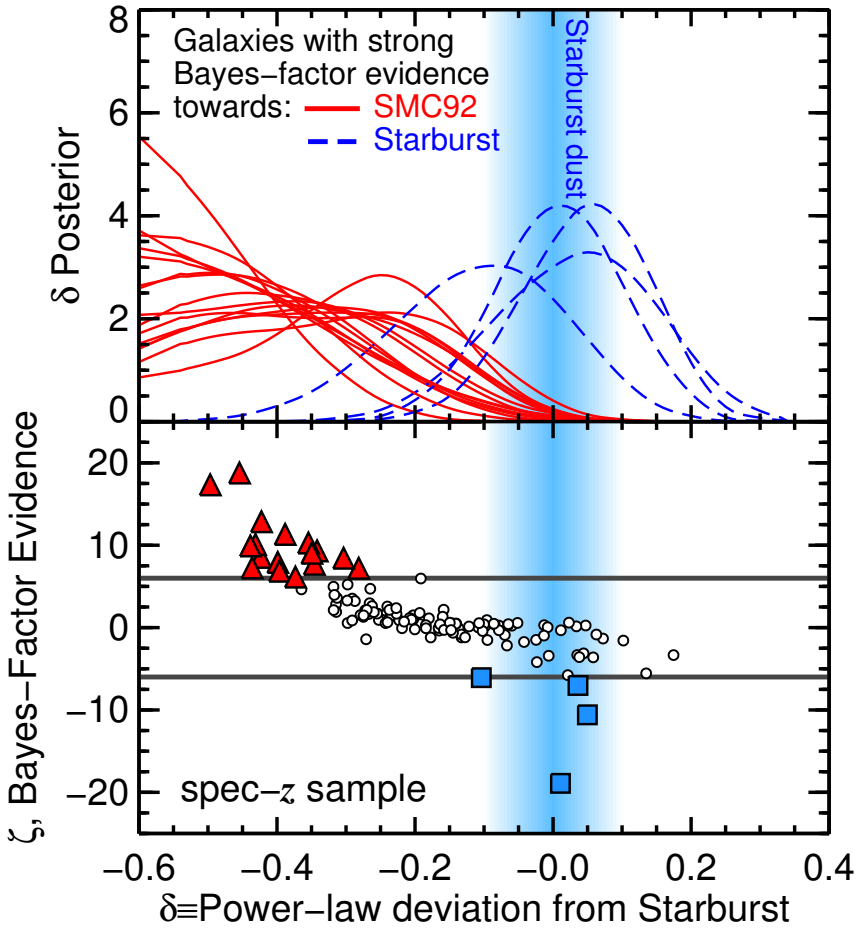


Figure 3.8: Posteriors of the Parameterized Dust Law, $\delta$.
Top: The posterior probability of the fitted parameter $\delta$, the power-law deviation from a starburst (Calzetti et al., 2000) dust-attenuation curve, for galaxies in the spec-$z$ sample and a broadband filter near Ly$\alpha$. Each curve represents a galaxy that was selected in Figure 3.7 as having strong Bayes-factor evidence towards an SMC-like (red, solid) or a starburst-like (blue, dashed) dust-attenuation curve. The width of the blue hazed region shows the typical 1-$\sigma$ uncertainty in the median value of $\delta$, centered on $\delta = 0$ where a galaxy would have a starburst dust-attenuation curve. Bottom: The evidence from the Bayes factors between the SMC92 and starburst dust laws as a function of the $\delta$ posterior median. Symbols shapes and colors are the same as Figure 3.7. The Bayes factors of galaxies with strong evidence broadly agree with the median $\delta$, as would be expected.

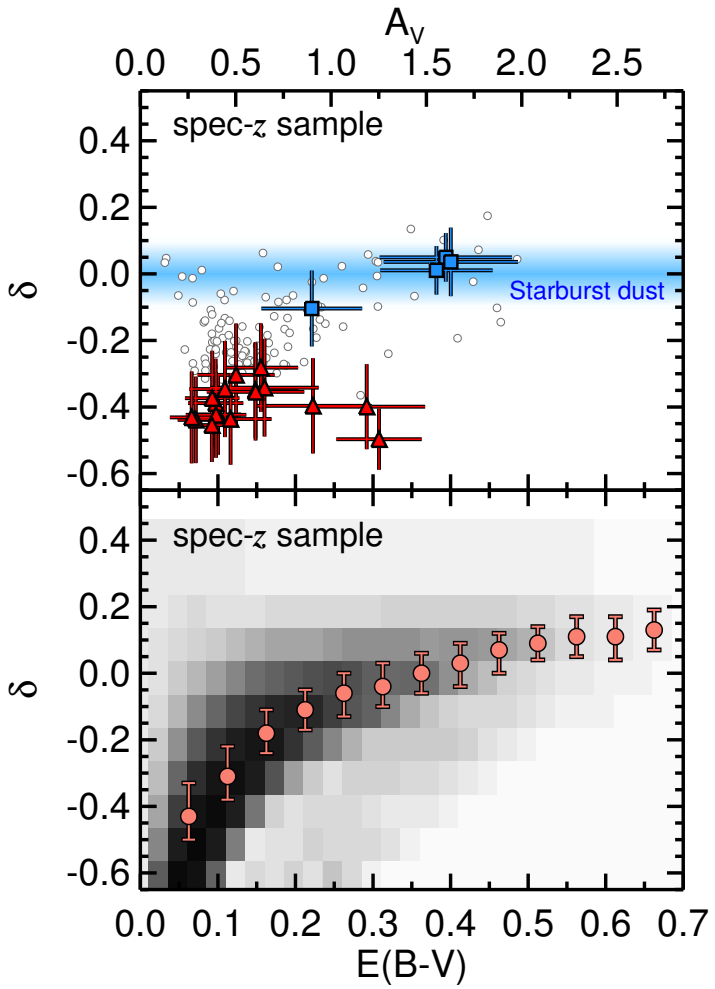


Figure 3.9: The Relation Between $\delta$ and $E(B-V)$ in the Spec-$z$ Sample. Top: The median of the posterior on the tilt of the dust-attenuation curve, $\delta$, as a function of the median color excess, $E(B-V)$, for galaxies in the spec-$z$ sample. Red triangles and blue squares are galaxies with strong Bayes-factor evidence towards SMC-like and starburst-like dust laws, respectively. Galaxies with low Bayes-factor evidence are shown as open white circles. For reference, a blue haze is shown where $\delta$ represents a starburst attenuation, where the width represents typical 1-$\sigma$ uncertainties on the posteriors of $\delta$. Bottom: The joint probability between the $\delta$ and $E(B-V)$ posteriors. Medians in bins of $E(B-V)$ and their 68% limits are shown as salmon-colored points and error bars respectively. The spec-$z$ sample suggests a relation between the scale of dust attenuation and the tilt of the dust law, such that galaxies with higher attenuation have a flatter (or grey) starburst-like dust law, and galaxies with relatively lower attenuation have a steeper, SMC-like dust law.

to have steeper dust laws.

### *3.7.3 Results from the Photometric Redshift Sample*

#### *3.7.3.1 Bayes Factors on the $IRX - \beta$ Relation: phot-z sample*

Figure 3.10 shows the $IRX - \beta$ plot for the phot-$z$ sample (see § 3.3.3). The phot-$z$ sample includes galaxies from the spec-$z$ sample but with their redshifts assigned to their photometric-redshift value. Figure 3.10 also shows the results from directly substituting the photometric redshifts for the spec-$z$ sample, in order to explore how photometric-redshift accuracy can affect the main results. The calculation of the UV slope is also sensitive to the photometric-redshift uncertainty because the bands used to find the slope may differ for large changes in redshift (see the details on the calculation of $\beta$ in § 3.7.2.1). It is plausible that galaxies in the spec-$z$ sample have better photometric-redshift accuracies than those for the full phot-$z$ sample. However, we assume that the selection bias to the right panel of Figure 3.10 is negligible because the trends of Bayes-factor evidence on the $IRX - \beta$ plane are the same for the phot-$z$ sample.

Figure 3.10 shows that the phot-$z$ sample of this work is able to reproduce the main result derived for the spec-$z$ sample. In most cases, the Bayes-factor evidence promotes the same dust law that the observations suggest, based on their location in the $IRX - \beta$ plane. However, there is significant scatter on an individual galaxy basis, especially for the galaxies that seemingly promote an SMC92 attenuation (or discredit the starburst attenation). This is to be expected; it is unlikely that all galaxies divide into two specific types of dust laws. For example, the SMC92-favored galaxies may have a range of attenuations that are, in different ways, steeper than the starburst dust law.

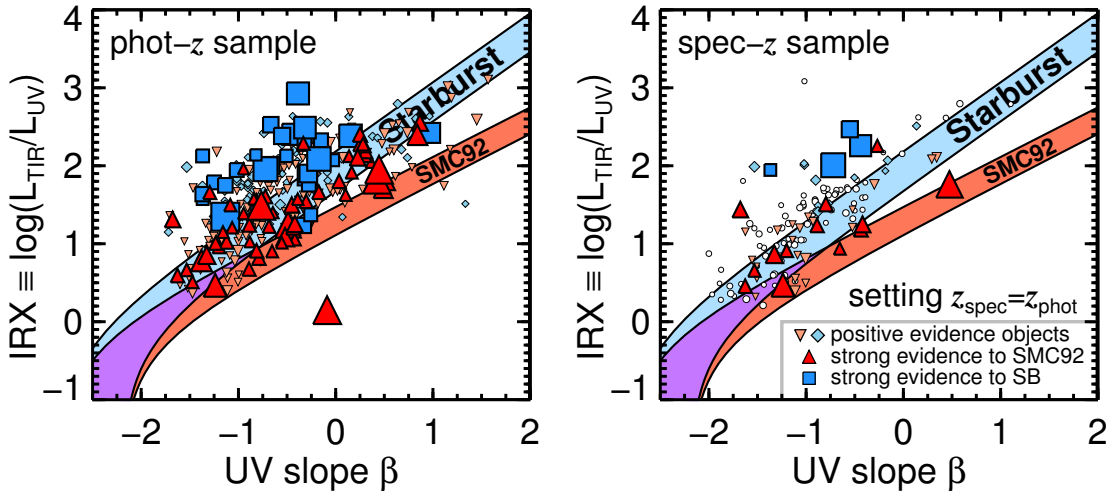


Figure 3.10: Bayes Factors on $IRX - \beta$ with the Phot-$z$ Sample.
Left: The measured IR excesss versus UV slope for the phot-$z$ sample (see § 3.3.3). For clarity, only galaxies with positive and strong Bayes-factor evidence are shown, with the symbol size scaling with the evidence. Curves show the predicted location of a variety of stellar populations according to an SMC92 or starburst dust-attenuation law. This panel shows that the galaxies in the phot-$z$ sample selected by the strength of their Bayes-factor evidence follow the curve of their predicted dust-attenuation law with some scatter Right: The same as the right panel of Figure 3.7 (galaxies from the spec-$z$ sample), but with $\beta$ and the Bayes-factor evidence recalculated when the photometric redshift is used for the spec-$z$ sample. This panel shows that the selection methods and Bayes-factor evidence can overcome the errors from photometric-redshift estimates to predict galaxy dust laws, verified by their position in the $IRX - \beta$ plane.

#### *3.7.3.2 Fitting the Curve of the Dust Law: phot-z sample*

Figure 3.11 shows the Bayes-factor evidence of the galaxies in the phot-$z$ sample as a function of their $\delta$ posterior median. The median tilt of the dust-attenuation curve, marginalized over all combinations of stellar population age, metallicity, and $E(B-V)$, agrees with the trends suggested by the Bayes-factor evidence. Galaxies with high SMC92 evidence tend to allocate their likelihood around steeper tilts to the attenuation law ($\delta < -0.2$), and galaxies with high starburst evidence allocate towards shallower tilts to the attenuation law ($\delta > 0$).

Figure 3.11 again shows that the results of the phot-$z$ sample are an extension of the results from the spec-$z$ sample (Figure 3.9). This figure shows that the steepness of the dust-attenuation curve correlates with the galaxy's attenuation optical depth, as parameterized by the color excess. Galaxies that seem to scatter away from the main trend have poor wavelength coverage of rest-UV wavelengths and have relatively broad posteriors in $E(B-V)$ and $\delta$.

Figure 3.11 also shows the posterior joint probability between $\delta$ and $E(B-V)$ for all galaxies in the phot-$z$ sample. In this depiction, the galaxies with poor constraints on $\delta$ or $E(B-V)$, which appear as outliers according to their median posteriors, get suppressed relative to the trend of the whole sample. The distribution shows a probability covariance such that galaxies with low attenuation optical depths have steeper dust laws and are well-fit by the relation

$$\delta = (0.62 \pm 0.05)\log(E(B-V)) + 0.26 \pm 0.02 \tag{3.8}$$

We tested for the effect of the 2175Å dust feature by refitting all the galaxies but excluding any band with a central rest-frame wavelength within ±250 Å of this

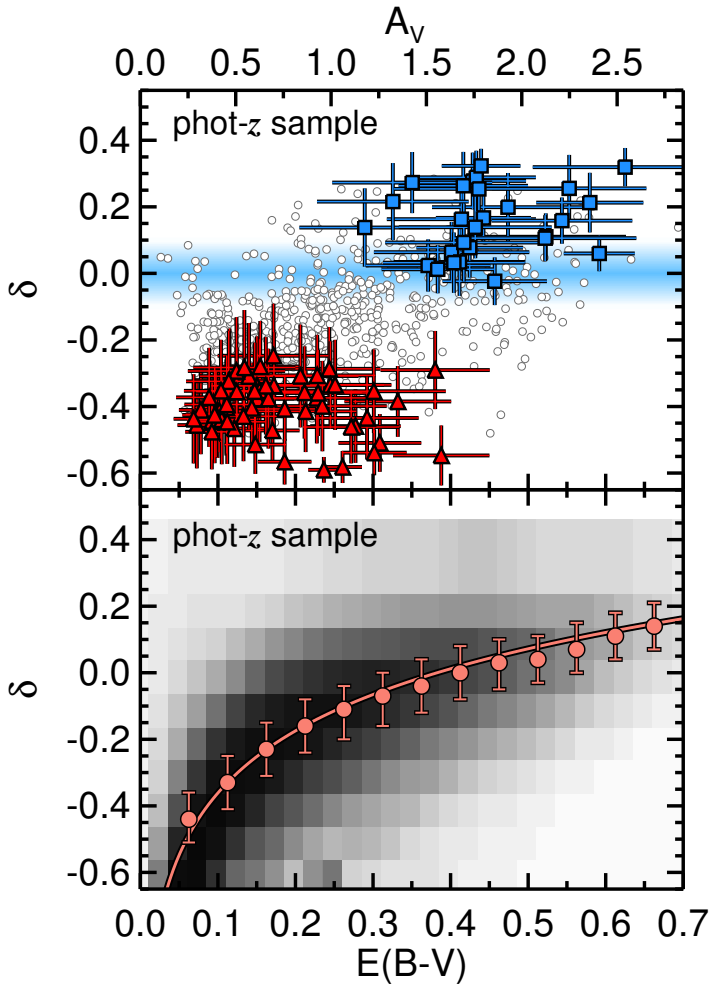


Figure 3.11: The Relation Between $\delta$ and $E(B-V)$ in the Phot-$z$ Sample. The same as Figure 3.9 but for the phot-$z$ sample. Top: The medians of the $\delta$ and $E(B-V)$ posteriors are shown as grey circles, with strong Bayes-factor-evidence galaxies highlighted as red triangles (SMC92-like) and blue squares (starburst-like). For reference, a blue haze is shown where $\delta$ represents a starburst attenuation, given typical uncertainties in $\delta$. Bottom: The joint probability between the $\delta$ and $E(B-V)$ posteriors. The salmon-colored circles show the $\delta$ at median likelihood in bins of $E(B-V)$ and error bars represent their 68 % range in likelihood. The solid line represents a fit to the medians following equation 4.1.

feature. This excludes at most one band for each galaxy. The relation in Figure 3.11 was unchanged, implying that the dust feature does not affect our results.

## 3.8 Discussion

### *3.8.1 Origins of the Relation Between $E(B-V)$ and $\delta$*

The parameter $\delta$ applies a spectral tilt to the attenuation law that pivots about the central wavelength of the $V$ band. Unlike the original definition by Noll et al. (2009), our parameterization allows the total-to-selective attenuation at the $V$ band, $R_{\rm V}$, to change. This is because $R_{\rm V}$ is inversely proportional to the slope of the dust law around $\lambda = \lambda_{\rm V}$, which means that low $\delta$ implies low $R_{\rm V}$. This is physically motivated by the fact that different dust laws have different $R_V$. For example, $R_V = 2.95$ for the SMC dust law (Pei, 1992) and $R_V = 4.05$ for the starburst dust law (Calzetti et al., 2000). Therefore, while the relation of Figure 3.11 displays a correlation between $\delta$ and $E(B-V)$, it could be interpreted as a correlation between $R_{\rm V}$ and $E(B-V)$. Intriguingly, this result may be the consequence of dust physics in galaxies. The value of $R_{\rm V}$ has been linked to the average dust grain size (Gordon et al., 2000), with smaller grains being associated with smaller $R_{\rm V}$. However, even if the result in Figure 3.11 was linked to a change in dust grain size, it would still be difficult to comment on the dust production sources, given the short timescale for dust grain evolution (Jones et al., 2013a).

While there is some covariance between $\delta$ and $E(B-V)$ in the posteriors from the model fits, this does not drive the observed correlation between them. The covariance between the parameters can be understood as follows. Imagine an SED well represented by some $\delta$ and then applying a very small increase in $\delta$ towards a flatter dust curve, keeping other parameters fixed. This would produce less attenuation to UV bands, and the models respond by applying more likelihood to higher

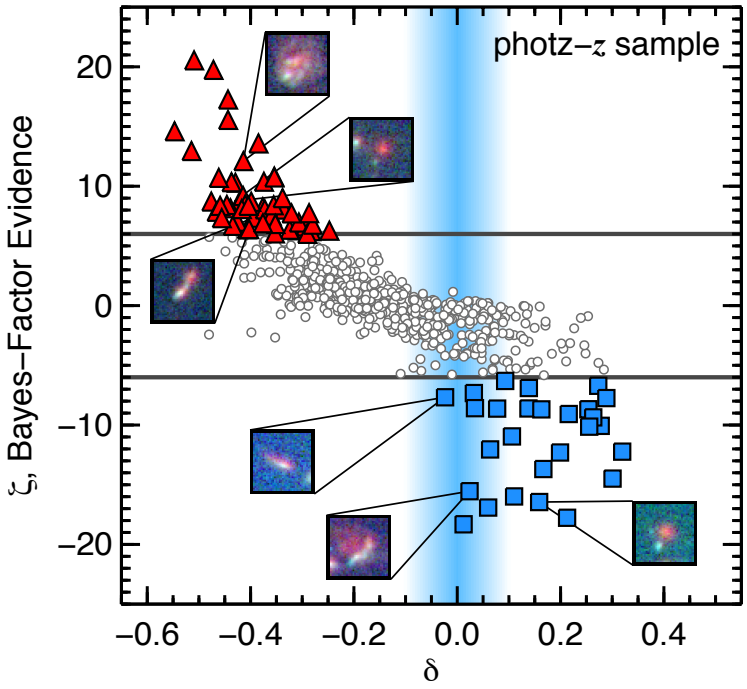


Figure 3.12: Lack of Correlation with Morphologies.
Top: Bayes-factor evidence versus $\delta$ for the phot-$z$ sample. Galaxies with strong Bayes-factor evidence are highlighted as red triangles (SMC92-like) and blue squares (starburst-like). Example RGB image stamps ($H_{160}$, $V_{606}$, and $B_{435}$, respectively) of galaxies from both subsamples are shown as insets. This figure demonstrates that there are no distinct morphological trends with $\delta$ or Bayes-factor evidence.

values of $E(B-V)$ in order to attenuate the UV. While this is a known parameter degeneracy that is unavoidable with the current data set, we explore a variety of tests in Appendix B.1 to confirm that the relation in Figure 3.11 is real despite the influence of covariance. In addition, Figure 3.7 serves as independent, observational confirmation that the tilt of the dust law correlates with the amount of attenuation.

### *3.8.2 Physical Origins of Non-Universal Attenuation*

The ways that dust grain type, size, and distribution affect the observed UV-to-NIR attenuation are enigmatic. There are many physically motivated explanations

for how the relationship between stellar emission and the scattering and absorption by dust manifest to an observed attenuation (Witt & Gordon, 2000). One possible explanation for the change in observed attenuation for different galaxies is their orientation. There is evidence that galaxy inclination correlates with the strength of Ly$\alpha$ emission, such that we observe less Ly$\alpha$ equivalent width for more edge-on galaxies (Charlot & Fall, 1993; Laursen & Sommer-Larsen, 2007; Yajima et al., 2012; Verhamme et al., 2012; U et al., 2015). Resonant scattering and absorption by dust are likely the primary impediments to the escape of UV light from star-forming regions, which were predicted by Charlot & Fall (1993) to be exacerbated in edge-on galaxies. This qualitatively agrees with radiative transfer simulations that show an increasing attenuation optical depth with galaxy inclination (Chevallard et al., 2013). Therefore, based on physical models, one expects that galaxies with "greyer" dust laws and larger overall attenuation should have higher inclinations, on average.

However, we find no correlation with the scale or shape of attenuation and the axis ratios in either the phot-$z$ or spec-$z$ samples. Figure 3.12 shows the selection of galaxies in the phot-$z$ sample with strong Bayes-factor evidence. The inset image stamps are a few examples that show similar morphologies among SMC92-like and starburst-like galaxies. Compact red, large axis ratio, and clumpy extended galaxies are found in both samples. A more detailed study with a wider mass range may be needed to find correlations with inclination, axis ratio, or sérsic index. Alternatively, it may be that neither *HST* or *Spitzer* provides the wavelength coverage with high enough angular resolution to discern the trends between attenuation and morphology. Future observations with *JWST* (with an angular resolution seven times higher than *Spitzer* at similar wavelengths) may be needed to offer spatial insight on the morphology of warm dust regions.

Even if galaxy orientation/inclination correlates with the strength of attenuation,

it may not be the fundamental cause of non-universal shapes to the dust-attenuation law. For example, Chevallard et al. (2013) predicted the relation between $\delta$ and attenuation optical depth at all orientations, assuming only Milky-Way type dust grains. Their model predicted a relationship between the shape of the extinction law (here parameterized by $\delta$) and the dust-attenuation optical depth. We consider this relationship in two scenarios: small and large dust-attenuation optical depths, $\tau$, where the optical depth is related to the color excess by $\tau_\lambda = 0.92\ k_\lambda\ E(B-V)$.

In the low-attenuation scenario, the steep curve of the dust law is likely a product of dust scattering, specifically the asymmetry parameter of the scattering phase function and its dependence with wavelength. The asymmetry parameter, $g_\lambda$, describes the degree of scattering in the forward direction Mann et al. (2009). Dust is more forward scattering at UV wavelengths, such that $g_\lambda$ approaches unity, and more isotropic at optical-to-IR wavelengths, such that $g_\lambda$ approaches zero (Gordon et al., 1994; Witt & Gordon, 2000; Draine, 2003). This means that in the small-optical-depth regime, red light will tend to scatter isotropically and escape the galaxy, while blue light will tend to forward scatter until absorption. Therefore, relatively more optical-to-IR light and less UV light escapes the galaxy, resulting in a steepening of the curve of dust-attenuation ($\delta < 0$). This only applies at small optical depths where light has a chance to scatter out of the galaxy before absorption. Also in the low-attenuation scenario, dust is more transparent and scattering is less frequent, so the scattering asymmetry parameter may not be the only source of a steeper dust law. Galaxies with smaller dust optical depths may have steeper dust laws because they produce less scattering into the line of sight, causing the galaxy's dust-attenuation law to appear more like a dust-extinction law. In that case, the effects of dust grain size become more pronounced. For example, the steepness of the SMC extinction law has been attributed to its observed underabundance of carbon, which implies

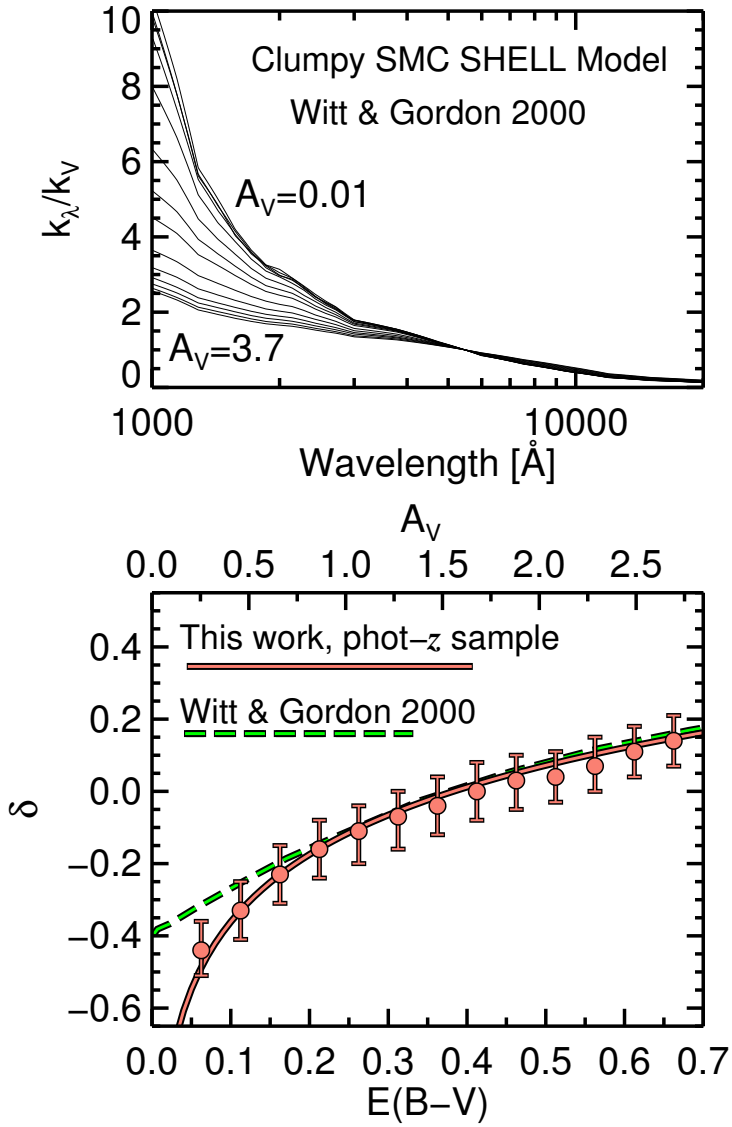


Figure 3.13: Comparison with Dust Theory.
Top: attenuation curves from the radiative transfer calculations by Witt & Gordon (2000) assuming SMC-like dust grains, a clumpy density distribution, and a spherical shell geometry. Bottom: The relation between $E(B-V)$ and $\delta$ from Figure 3.11. The salmon-colored circles show the $\delta$ at median likelihood in bins of $E(B-V)$ and error bars represent their 68 % range in likelihood. The solid line represents a fit to the medians following equation 4.1. The dashed green line represents radiative transfer predictions from the above dust-attenuation models.

fewer heavy-element graphite grains than smaller silicate interstellar grains (Prevot et al., 1984). This picture is consistent with the trend of finding galaxies with more SMC-like dust at very high redshifts (e.g. $z > 5$ by Capak et al., 2015), where the metallicity of galaxies, in a broad sense, is expected to be lower (Madau & Dickinson, 2014). The low $\delta$ for small $E(B-V)$ in this work can, at least in part, be attributed to lower $R_{\rm V}$. Thus, the relation between $E(B-V)$ and $\delta$ could be a product of underlying relations in grain size, averaged over the surface brightness of the galaxy.

In the regime of large attenuation optical depths, attenuation becomes ubiquitous with wavelength. The flatter curve of the dust-attenuation law resulting from high attenuation is consistent with the picture proposed by Charlot & Fall (2000) whereby galaxies have a mixed distribution of stars and dust. In this case, any escaping UV light must come from regions of small optical depth, which corresponds to UV light at the outer "skin" of the mixed distribution (Calzetti, 2001). Conversely, redder light will come from deeper physical locations within the region. The resulting attenuation function is grey, or flatter with wavelength, which translates to $\delta \geq 0$.

### *3.8.3 Comparison with Dust Theory*

Figure 3.8.2 shows the predictions from radiative transfer calculations by Witt & Gordon (2000). In general, the curves of dust-attenuation become greyer at increasing optical depths for models assuming SMC-like dust grains, a clumpy density distribution, and a spherical shell geometry. We determined $\delta$ for each curve using the definition in equation 3.7 and compared its evolution with $E(B-V)$ to the results of Figure 3.11. The steepest curves in Figure 3.8.2 are poorly represented by the $\delta$ parameterization (their curvature is higher than a power-law can reproduce), which explains the disagreement between $E(B-V)$ and $\delta$ at the low end. The radiative transfer relations at high and low optical depths are consistent with the observed

correlation between $E(B-V)$ and $\delta$ found in this work.

Although the agreement in Figure 3.8.2 seems obvious given the prevalent predictions of dust theory (Bruzual et al., 1988; Witt et al., 1992; Gordon et al., 2001; Charlot & Fall, 2000), radiative transfer simulations (Witt & Gordon, 2000; Gordon et al., 2000; Chevallard et al., 2013), and observations of local nebular regions (Draine & Li, 2001; Draine, 2003), this is the first time the trend has been found from only UV-to-NIR broadband photometry of distant galaxies. Indeed, investigating origins of the relation between $E(B-V)$ and $\delta$ elucidates provocative explanations, as a result of similar correlations in stellar population age, metallicity, and dust grain size from dust theory.

### *3.8.4 Comparisons with Recent Literature*

Several studies have noted populations of galaxies that lie off of the nominal Meurer et al. (1999) $IRX-\beta$ relation, suggesting galaxies with younger ages have steeper, SMC-like dust laws (Siana et al., 2009; Reddy et al., 2006, 2010, 2012a; Buat et al., 2012; Sklias et al., 2014). Other recent studies find galaxies at high redshift harbor dust laws that, at least in large subsets of their samples, agree with the assumption of a starburst dust law (Scoville et al., 2015; de Barros et al., 2015; Zeimann et al., 2015; Kriek & Conroy, 2013). Our results suggest that these studies are not in conflict but provide clues to the overall non-universality of how dust attenuates light in star-forming galaxies. For example, the studies that find evidence for starburst-like dust laws do so with galaxies selected by their strong nebular emission lines (e.g. H$\alpha$ and H$\beta$), by recent star-formation activity (strong CIV absorption), and/or by SEDs with appreciable reddening, allowing the underlying dust law to be tested. A common thread to these starburst-dust galaxies is their large dust-attenuation optical depths, assuming galaxies with strong nebular features also have high levels of

stellar attenuation by dust, averaged over the whole galaxy as foreground screen (see Penner et al., 2015, for a discussion on alternatives to the foreground screen).

The trend with $\delta$ and $E(B-V)$ (or with $IRX$) was also found by Buat et al. (2012) and Kriek & Conroy (2013). The latter authors attributed the change in $\delta$ to a change in the strength of H$\alpha$ equivalent width. The difference in this study is that the evolution of $\delta$ is determined for individual galaxies based on rest-frame UV-to-NIR broadband photometry, suggesting that the methods can be used at even higher redshifts.

### *3.8.5 Implications for SED-Derived Properties of Galaxies*

The determination that individual galaxies at $z \sim 2$ have different dust laws has several implications for determinations of distant galaxy evolution. At relatively low $E(B-V)$ ($\approx 0.1$), this manifests as a factor of $\approx$2 underprediction in the 1500 Å luminosity dust correction ($10^{0.4k_\lambda E(B-V)}$) and therefore UV SFR compared to the $\delta = 0$ starburst assumption. Higher SFRs for SMC92-like galaxies agrees with the determination of stellar population ages: galaxies with an SMC92-like attenuation, are on average half the age of galaxies with a starburst-like attenuation, consistent with the results of previous studies (Siana et al., 2009; Reddy et al., 2010). At $E(B-V)$>0.6, UV luminosity dust corrections are overestimated by a factor of $2-5$ compared to the starburst-dust assumption at fixed $E(B-V)$.

The dust law also has implications for studies that use the rest-frame colors to infer dust attenuation in star-forming galaxies. The rest-frame $UVJ$ diagram is a particularly helpful visualization used to break the degeneracy between old stellar population ages and reddening due to dust (Wuyts et al., 2007; Williams et al., 2009). Star-forming galaxies move along the $UVJ$ diagram in an identifiable relation, where the redder colors are to increasing levels of attenuation by dust (Price et al.,

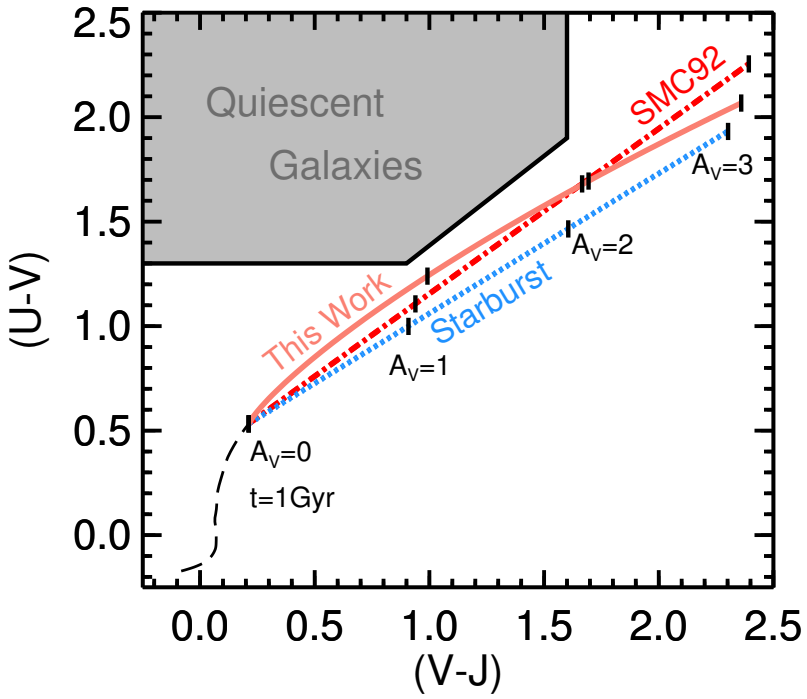


Figure 3.14: Dust Laws on the UVJ Diagram.
Tracks of dust attenuation under different dust laws on the $UVJ$ diagram. The dashed black line follows the age of a stellar population with a constant star-formation history from $t = 0.02$ Gyr to $t = 1$ Gyr. The colored lines show how the rest-frame $UVJ$ colors of the $t = 1$ Gyr stellar population change with increasing levels of attenuation ($0 < A_V < 3$) following a starburst-like dust law (blue, dotted), an SMC92-like dust law (red, dot-dashed), and a dust law that follows equation 4.1 (salmon, solid).

2014; Forrest et al., 2016, Fang et al. 2016 (in prep.)) Figure 3.8.4 shows how the rest-frame $UVJ$ colors change with attenuation under different assumed dust laws. The dust law derived in this work may induce slight differences to the positions of star-forming galaxies, but these will be degenerate with star-formation histories and age/metallicity variations. In addition, the dust law would not significantly influence the selection between star-forming and quiescent galaxies.

Lastly, the relationship between $\delta$ and $E(B-V)$ does not translate to a relationship between the UV spectral slope $\beta$ and the dust law. At fixed $\beta$ there is high scatter in $IRX$ (see Figures 3.7 and 3.10). Even at relative modest UV slopes, $-1 < \beta < 0$, the scatter in $L_{\rm TIR}/L_{\rm UV}$ is more than 1 dex depending on the assumption of the dust attenuation law (Buat et al., 2012). This may have a substantive impact on the interpretation of the intrinsic UV luminosity function if the dust-corrections to the observed UV lumonsity densities assume a unique relationship between $M_{\rm UV}$ and $\beta$.

# 4. THE SFR FUNCTION FROM 4< $Z$ <8 AND THE NON-UNIVERSALITY OF THE HIGH-REDSHIFT DUST LAW

## 4.1 Synopsis

The ubiquity of the dust-attenuation law and the existence of highly dust-obscured galaxies at very high redshifts is not well understood, yet their presence has broad implications for galaxy assembly and evolution physics. In this chapter, we use *HST* CANDELS and *Spitzer* photometry to derive star-formation rates (SFRs) of galaxies over $4 < z < 8$. First, I calculated the first estimates of the shape of the dust-attenuation law in $z > 4$ galaxies and used it to account for the missing ultraviolet (UV) light reprocessed into the far infrared ($\lambda_{\rm rest} > 8$ $\mu$m). I then used the number densities and SFRs of individual galaxies to construct a SFR function that shows a clear excess at the high end. These higher SFRs are due to UV-faint galaxies with modest attenuation that are otherwise missed by early work where a single dust correction is applied at fixed (observed) UV magnitude. The number densities at high SFR found in this work agree with the expectation from the time evolution of the observed stellar mass function, as well as the number densities of the few dusty star-forming galaxies already observed at $z < 4$.

## 4.2 Background Information

The number densities of galaxies as a function of rest ultraviolet (UV) luminosity (Bouwens et al., 2015; Finkelstein et al., 2015), stellar mass (Grazian et al., 2015; Song et al., 2015), and star-formation rate (SFR; Smit et al., 2012) have shown that these distributions change in scale and shape from $z\sim8$ to present. These functions help constrain which mechanisms influence the growth of galaxies, such as mergers, cosmological accretion, and the feedback processes that can suppress star formation

and gas accretion (Somerville & Davé, 2015). Constraining these processes requires either assumptions from theory (e.g., sub-grid physics or how dark matter follows baryonic matter) or from observations (e.g., how stellar masses are derived from SEDs or the strength of the corrections for dust attenuation used to infer the intrinsic SFR).

The SFR function (SFRF) offers one of the most direct observations for cosmological models to constrain star-formation and feedback processes, yet it is poorly understood at high redshift. The biggest challenge is to convolve the UV luminosity function (UVLF) with dust attenuation. One way is to assume the UV slope ($\beta$, where $f_\lambda \propto \lambda^\beta$ over 1268$<\lambda<$2580 Å; Calzetti et al., 1994) relates directly to the UV attenuation using the relationship of infrared excess ($L_{\rm IR}/L_{\rm UV}$) and $\beta$ (the $IRX-\beta$ relation; Meurer et al., 1999). Some studies extrapolate further by assuming the UV luminosity itself correlates with $\beta$, and therefore there exists a unique relation between UV luminosity and UV attenuation. (Smit et al., 2012; Mashian et al., 2016). However, the scatter in these relationships is large and misrepresents the variations in the intrinsic $\beta$ due to a range of stellar population ages and metallicities (Reddy et al., 2012b), and the scatter in $IRX$ due to the non-universality of the dust law (Buat et al., 2012; Salmon et al., 2016). In this chapter, I use the results and methods developed in Chapters 2 and 3 to improve estimates of the $z > 4$ dust law and SFRF.

## 4.3 Data, Redshifts, and Sample Selection

### *4.3.1 Photometry: CANDELS Multi-wavelength Data*

In the absence of rest-frame far-infrared data ($\lambda_{\rm rest} > 8\mu$m) for $z > 3$ galaxies, we must infer the dust-obscured component of star formation using careful modeling of the UV-to-optical SED. To do this, we take advantage of the deep multi-wavelength observations from several *Hubble* (*HST*) and *Spitzer Space Telescope* surveys. The

deepest imaging comes from surveys of the *Hubble Ultra Deep Field* (HUDF): the original optical imaging with the Advanced Camera for Surveys (ACS; Beckwith et al., 2006), the near-infrared imaging with the Wide Field Camera 3 (WFC3) for the HUDF09 surveys (PI Illingworth; Bouwens et al., 2010; Oesch et al., 2010), and WFC3 imaging of the recent UDF12 surveys (PI Ellis; Ellis et al., 2013; Koekemoer et al., 2013). The full list of *HST* passbands are the ACS F435W, F606W, F775W and F850LP and the WFC3 F105W, F125W, F140W, and F160W. We respectively define the magnitudes of each of these ACS bands as $B_{435}$, $V_{606}$, $i_{775}$, and $z_{850}$ and the WFC3 bands as $Y_{105}$, $J_{125}$, $JH_{140}$, and $H_{160}$.

In addition to the deep data from the HUDF, we take advantage of data from the now completed Cosmic Assembly Near-infrared Deep Extragalactic Legacy Survey (CANDELS, PIs Faber and Ferguson; Grogin et al., 2011; Koekemoer et al., 2011). CANDELS produced 902 orbits over five fields, including deep imaging covering half of the GOODS-N and -S legacy fields (Giavalisco et al., 2004) and wide imaging covering the rest of the GOODS-N field and the southern $\sim$25% of the GOODS-S field.

We additionally include data from the Frontier Fields program (PI Lotz) using the parallel fields of galaxy clusters Abell 2744 and MACS J0416.1-2403. This program provides imaging in the the $B_{435}$, $V_{606}$, $I_{814}$, $Y_{105}$, $J_{125}$, $JH_{140}$, and $H_{160}$ bands. We use the data reduction applied by (Finkelstein et al., 2015, F15 hereafter) and refer to their work for further details on the point-spread function matching, source extraction, aperture corrections, Galactic extinction, and visual inspection.

Following the work in Chapters 2 and 3 (from Salmon et al. (2015) and Salmon et al. (2016), S15 and S16 hereafter), we adopt additional photometric uncertainties to account for any systematics that may occur from flat-field variations, PSF and aperture mismatching, and local background subtraction. We arrived at the 10%

value from a series of recovery tests by S15 where semi-analytic models were used as inputs. This additional uncertainty was added in quadrature to the measured uncertainties.

### *4.3.2 Photometric Redshifts*

Photometric surveys are an excellent way to build large samples of galaxies at high redshift, provided the redshift estimates are robust. This can be done by either a color selection that keys off of the strength of the Lyman break or by simultaneously fitting all observed fluxes to a series of templates in order to derive a photometric redshift. The latter technique is advantageous in that a redshift probability distribution function is derived for each galaxy, offering improved estimates of the redshift uncertainty. We adopt the photometric redshift technique of F15 which we briefly summarize.

Photometric redshifts were derived using the fitting code EAZY (Brammer et al., 2008). All available fluxes were used as inputs to match to PÈGASE stellar population templates which include the effects of nebular emission lines (Fioc & Rocca-Volmerange, 1997). The default prescription for the attenuation by the Intergalactic Medium (IGM) was used (Madau, 1995). While magnitude priors can be optionally included, we chose to omit this function because the priors at the bright end of the luminosity function are not yet well defined.

## 4.4 Sample Selection

We begin with the base photometric redshift sample selection used by F15 to place galaxies in their appropriate $\Delta z$=1 redshift samples. In short, the full redshift probability distributions ($P(z)$) output from EAZY were used to quantify the confidence in and around the redshift of highest likelihood, omitting galaxies with too high likelihood at lower redshift solutions, as well as magnitude limits to avoid

stellar contamination.

One way in which redshift selection of this work differs from F15 is in the probability limit of low redshift solutions. F15 requires that the integral from $z = 0$ to $z_{\rm sample} - 1$ must encompass less than 50% of the total $P(z)$ distribution (i.e., $\int P(z > 6)\ dz > 0.5$ for a galaxy in the $z = 7$ sample). After inspecting several SEDs that fit this criteria, we instead choose a more stringent limit 35%. We also clarify the integration to be $\int P(z > z_{\rm phot})\ dz > 0.35$ where we have substituted the sample redshift for $z_{\rm phot}$, the accepted photometric redshift of the galaxy. This new limit affects a small sample of mostly UV-faint galaxies with moderate levels of reddening. Therefore, the already faint UV luminosities would not impact the determinations of the UVLF because of the already high number densities of the faint end slope. These galaxies are, however, much more significant to the shape of the SFR function, especially at the high end.

The goal of this chapter is to both determine the best estimates for SFRs by improving constraints on the $z > 4$ dust law, and applying those SFRs to derive the SFR functions. Each of these science goals necessitate different sample selections, which we describe in the following subsections.

### *4.4.1 Galaxy Samples for Analysis of the Dust Law*

I showed in Chapter 3 that the dust-attenuation law some individual galaxies at $z \sim 2$ can be determined through a Bayesian analysis of their SEDs. This method used photometric data from the rest-UV to near-infrared SEDs, and was supported by the observed total infrared luminosities. Importantly, not all galaxies will produce a reliable estimate of the underlying dust law. In order to infer the dust law at $z > 4$ we must make a careful sample selection such that the galaxies have data both in the rest far-UV ($1216 < \lambda_{\rm rest} < 1500$ Å), where the differences between dust laws become

the most pronounced, and in the optical, so we can infer the degree of reddening, marginalized over all probability from all possible stellar population ages.

We therefore enforce the following additional selection criteria, besides those used for the redshift selection, and refer to these galaxies as being in the "dust-law sample." Galaxies must have at least $N_{\rm bands}$ >4, an SED fit with $\chi^2_\nu$ <2 (below the 2-$\sigma$ scatter of the $\chi^2$ distribution), and 3-$\sigma$ detections in both *Spitzer* channels 1 and 2 (3.5 and 4.5 $\mu$m). We must also omit galaxies that appear to have very little dust attenuation as that makes it difficult, or even irrelevant, to distinguish between dust laws. I pointed out this caveat in S16, where we found that the estimates of the dust law become unreliable at $E(B-V)< 0.1$. Although it is difficult to estimate the strength of attenuation *a priori*, especially for galaxies that have relatively broad $E(B-V)$ posteriors, we exclude galaxies with a median $E(B-V)< 0.1$ when analyzing the results.

In addition, we limit our analysis of the high-$z$ dust law to $4 < z < 6$ because there are few galaxies (8 in total) that match the above criteria in the $z > 6$ redshift samples. The number of galaxies in the final dust-law sample are shown in Table 4.1. There are fewer galaxies in the $z = 4$ than the $z = 5$ sample because because we require at least one photometric datum between 1250–1500 Å, and it is not until $z > 4.2$ that the $i_{775}$ band is redshifted into this wavelength region.

### *4.4.2 Galaxy Samples for Derivation of the SFR Function*

Calculating the SFR number density requires a more inclusive sample than the dust-law sample. We therefore take special caution to avoid galaxies that are misidentified as having high dust content. In this subsection we outline the sample selection for the galaxies used to determine the SFR functions. We refer to these galaxies as the "SFR-function sample."

Table 4.1: Dust Law and SFRF Samples.

$4 < z < 6$ Dust-Law Sample

| | $z = 4$ | $z = 5$ | $z = 6$ |
|---|---|---|---|
| N | 86 | 136 | 51 |

$4 < z < 8$ SFR Function Sample

| | $z = 4$ | $z = 5$ | $z = 6$ | $z = 7$ | $z = 8$ |
|---|---|---|---|---|---|
| N | 3372 | 1374 | 484 | 146 | 24 |

A visual inspection of galaxies SEDs revealed some very red galaxies with high SFRs but a poor $\chi^2$ from spurious photometry. We therefore remove galaxies with log SFR/$M_\odot$>1 that have best-fit $\chi^2$ values above the 2-$\sigma$ scatter of the distribution. During the SED-fitting process, we fit to all bands redder than $\lambda_{\rm rest} = 1216$Å. We also remove galaxies with fewer than four detected bands in the $z = 4$, $z = 5$, $z = 6$, and $z = 7$ samples (and fewer than three bands in the $z = 8$ sample). This avoids galaxies that have little to no constraint on their reddening or stellar population age. The total number of galaxies in each redshift sample are presented in Table 4.1.

## 4.5 SED Fitting and SFRs

We adopt our SED fitting methods developed in S15 and S16 to derive likelihoods of the stellar population ages, color excess $E(B-V)$, metallicity, and dust law for each galaxy. As defined in S16, the shape of the dust law is a fitted parameter defined as $A_{\lambda,\delta} = E(B-V)\ k_\lambda\ (\lambda/\lambda_V)^\delta$ where $k_\lambda$ is the dust law of Calzetti et al. (2000) (for examples of this parameterization, see also Noll et al., 2009; Buat et al., 2012; Zeimann et al., 2015). By this formalism, $\delta$ is a power-law deviation from a starburst dust law. Lower $\delta$ produce a steeper dust law that attenuates more strongly in the far-

$UV$ and higher $\delta$ produce a flatter, "grayer" dust law that attenuates wavelengths more uniformly. It is difficult to place any meaningful constraints on the stellar population metallicity with broadband photometry. However, the additional colors by including metallicity as a parameter improve the determination of $\delta$.

These four parameters define the distribution of likelihood. The posterior in stellar mass is inferred from each linear combination of these parameters (stellar mass is effectively a scale factor in the fitting process). The posteriors on individual parameters are calculated by marginalizing over all other parameters (also called "nuisance parameters"). For example, the posterior of stellar population age reflects the contributed likelihood from all other parameters $\Theta = \{E(B-V), Z, \delta\}$.

In S15 I showed that the SFR derived from the best-fit SED was more sensitive to the stellar population template assumptions such as the inclusion of nebular emission or the exact star-formation history. This was found in both the data as well as in the recovered parameter values compared to their true values for galaxies from a semi-analytic model (SAM Somerville et al., 2012). Importantly, I concluded that SFRs based on the observed rest-UV luminosity with a dust correction from the $E(B-V)$ posterior produced the least scatter between the true SAM value and the recovered value, and was less sensitive to assumptions from the SED-fitting templates.

In S16 I found a relationship between $E(B-V)$ and the tilt to the dust law $\delta$,

$$\delta = (0.62 \pm 0.05) \log(E(B-V)) + 0.26 \pm 0.02. \tag{4.1}$$

With this relation in hand, the median of the $E(B-V)$ posterior can be used to determine the appropriate dust law, and therefore the most appropriate dust correction. In addition, I used the median stellar population age to calibrate the conversion from the UV luminosity to a SFR. The conversion is similar to that of Kennicutt

(1998), with the ages accounting for variations between the stellar population age and star formation history (see the Appendix of Reddy et al., 2012b)

The determination of the SFR can be summarized as

$$\mathrm{SFR_{UV}} = f_{\mathrm{CB}} \cdot \frac{4\pi D_L^2}{1+z} \cdot 10^{0.4\ A_{\mathrm{UV}}} \cdot \kappa(t) \tag{4.2}$$

where $f_{\mathrm{CB}}$ is the flux of the band closest to rest-frame 1500 Å, $D_L$ is the luminosity distance, $A_{\mathrm{UV}}$ is the median, marginalized attenuation at 1500 Å using the S16 relation between $E(B-V)$ and $\delta$, and $\kappa$ is the modified Kennicutt (1998) conversion that depends on the median stellar population age ($t_{\mathrm{age}}$) assuming a constant star-formation history.

## 4.6 Results

### *4.6.1 The Evolution of the High-Redshift Dust Law*

Figure 4.1 summarizes the results of the dust law sample. Similar to the relation found at lower redshifts ($z < 3$) we find a relationship between the tilt of the dust law and the color excess. The relation appears to steepen at higher redshifts, although this is likely due to galaxies becoming less dusty in general, making the shape of the dust law more difficult to constrain but also less pertinent.

Importantly, Figure 4.1 supports the picture that galaxies come with a range of dust-attenuation scenarios, with a steeper dust law (low $\delta$) being the most appropriate at these redshifts. There has already been some anecdotal evidence that galaxies at $z > 4$ have a dust law similar to the extinction law of the SMC (Tilvi et al., 2013; Oesch et al., 2013). Figure 4.1 supports those claims, while also showing that the most obscured galaxies still exhibit starburst-like dust laws. In general, as galaxies become less dusty at $z > 3$, low-$E(B-V)$ galaxies will follow this relation and dis-

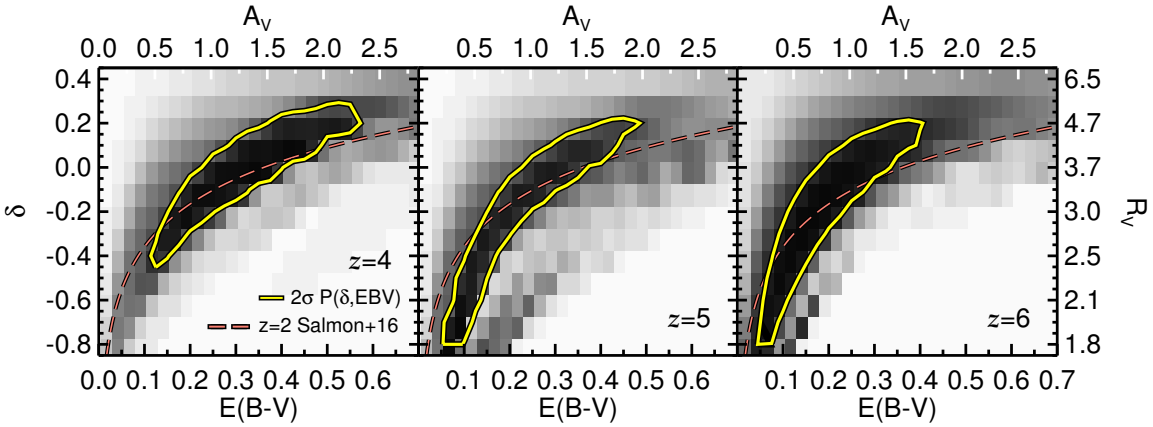


Figure 4.1: The Evolution of the Dust Law from $z = 6$ to $z = 4$.
The evolution of the dust law from $z = 6$ to $z = 4$. $\delta$ is a power-law tilt to the starburst dust-attenuation law of Calzetti et al. (2000), such that more negative $\delta$ produce a steeper, SMC-like dust law, and more positive produce a flatter, grayer attenuation. Darker regions correspond to areas of higher likelihood in $E(B-V)$ and $\delta$. The yellow contours indicate where the likelihood of $E(B-V)$ and $\delta$ is equal to twice the standard deviation of the sample. The dashed, salmon-colored line shows the relation found at $z \sim 2$ from S16.

play steeper dust laws (the SMC has $\delta \approx -0.3$ to $-0.5$, depending on the model; Pei, 1992; Gordon et al., 2003).

Figures 4.2 and 4.3 show the galaxies from the dust-law sample on the plane of SFR and stellar mass. Most galaxies in the sample are on the main sequence of star-forming galaxies. Higher mass (and therefore higher SFR) galaxies have a higher level of dust attenuation $E(B-V)$, similar to the trend seen at other redshifts (Whitaker et al., 2012).

However, the trend between the median $\delta$ and mass or $\delta$ and SFR is either weak or nonexistent. This is partly because the median values of $\delta$ have wide errors for individual galaxies at these redshifts, whereas the likelihood of the entire sample indicates a strong relationship between $E(B-V)$ and $\delta$. A similar trend is not seen

between $\delta$ and stellar mass nor SFR, reinforcing that the shape of the dust law is best connected to the strength of dust attenuation.

We refrain from relying on the derivations of $\delta$ in our determinations of individual galaxy SFRs in the SFR-function sample (see equation 4.2), because the constraints on $\delta$ are poor for individual galaxies, especially those with low reddening. This motivated our careful restrictions on the selection of the dust-law sample. Instead, we take Figure 4.1 as evidence that the relation between $\delta$ and $E(B-V)$ found at $z \sim 2$ by S16 is still present at these redshifts, and for this reason we use the S16 relation when applying dust corrections to the SFR. Support from future rest-frame far-infrared detections will be able to confirm the functional form of the $\delta$ and $E(B-V)$ relation at $z > 4$ This will be possible following the steady buildup of far-infrared detections with *ALMA*.

### *4.6.2 The Evolution of the SFR Function*

The distribution function of SFR is very similar to that of the UVLF, with the primary differences being the treatment of dust attenuation and assumptions of star-formation history. We take advantage of the robust completeness simulations used by F15 to create the $z > 4$ UVLFs. These simulations calculated the effective volume for galaxies of a given UV magnitude, redshift, size, and UV color (parameterized by the UV slope, $\beta$; Calzetti et al., 1994). The simulations were run for each of the subfields used in this study (see F15 for details).

Each galaxy in our SFRF sample was assigned an effective volume based on its observed field and four parameters: its UV magnitude, redshift, size, and UV color. The number density for each field in each bin of $\Delta(\log \mathrm{SFR}/\mathrm{M}_\odot\ \mathrm{yr}^{-1})$=0.5 dex was calculated as:

$$\phi_{i_{\mathrm{SFR}},\ j_{\mathrm{Field}}} = \sum_{n=1}^{n=N_{i,j}} \frac{1}{\Delta \log \mathrm{SFR}\ V_{\mathrm{eff}\ i,j}(n)} \tag{4.3}$$

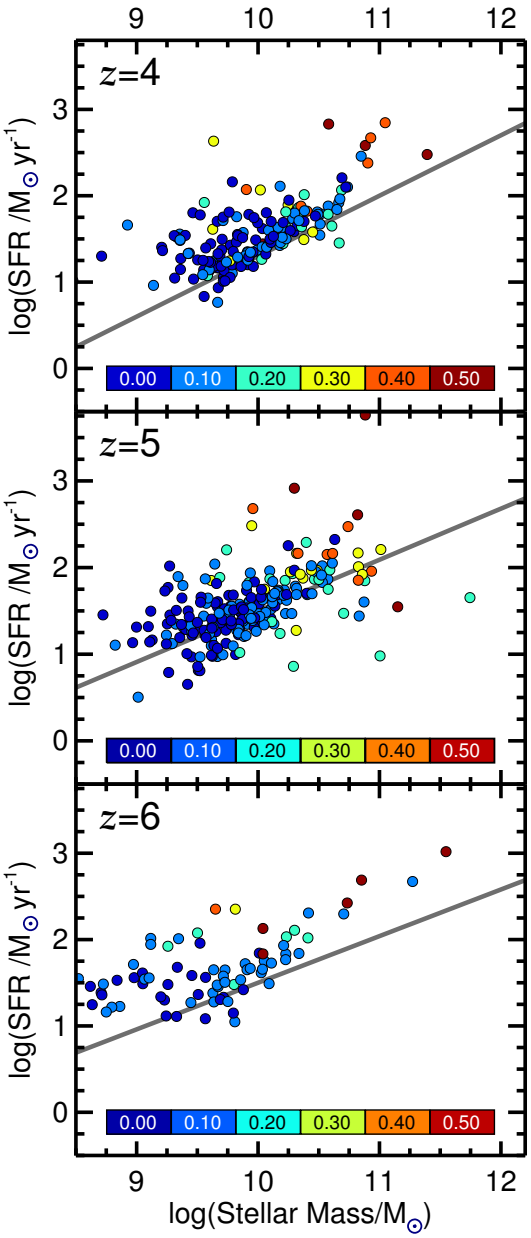


Figure 4.2: $E(B-V)$ on the SFR and Stellar Mass Relation.
The relation between SFR and stellar mass for galaxies in the $z_{\rm phot}$ =4, 5, and 6 samples used to explore the dust law. The symbols are color-coded by their median values of $E(B-V)$, as indicated by the color bar. The grey lines represent the main sequence of star-forming galaxies at each redshift by S16. Galaxies tend to have higher amounts of $E(B-V)$ at higher stellar mass and SFRs along the main sequence.

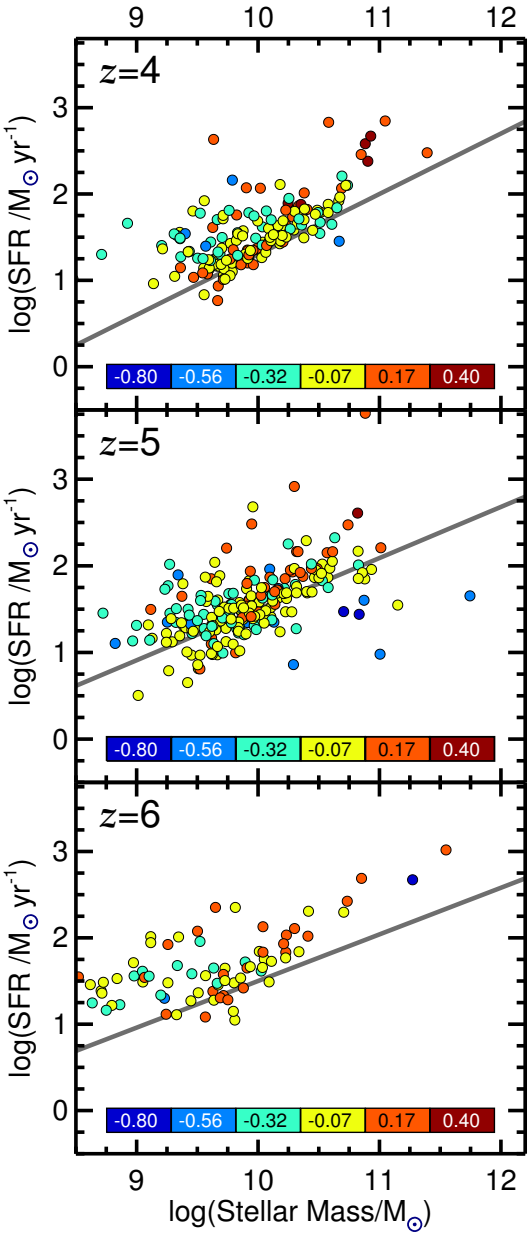


Figure 4.3: $\delta$ on the SFR and Stellar Mass Relation.
The relation between SFR and stellar mass for galaxies in the $z_{\rm phot}$ =4, 5, and 6 samples used to explore the dust law. The grey lines represent the main sequence of star-forming galaxies at each redshift by S16. The symbols are color-coded by their median values of their dust law $\delta$, as indicated by the color bar. There is no obvious relationship between the median values of $\delta$ and stellar mass or SFR at all redshifts.

where $N_{\rm i,j}$ is the number of galaxies in a given bin of SFR $i$ and field $j$, and $V_{\rm eff\ }{}_{i,j}(n)$ is the effective volume for each object based on the above four parameters. The final number density for each SFR bin was calculated by a weighted sum based on the number of objects in each field:

$$\phi_{i_{\rm SFR}} = \sum_{j=1}^{j=N_{\rm Fields}} \frac{N_{i,j}\ \phi_{i,j}}{N_{i,j}} \tag{4.4}$$

where again $N_{\rm i,j}$ is the number of galaxies in a given field and bin of SFR.

Figure 4.4 shows the resulting SFR function at from $z = 8$ to $z = 4$ and its comparison to the literature. Formally, galaxies are complete to UV magnitudes of $M_{\rm UV} < -18$ which corresponds to a minimum SFR $/{\rm M}_\odot\ {\rm yr}^{-1} \approx -0.1$ to 0.0 depending on the stellar population age. However this completeness limit does not exactly translate to a limit in SFR, as individual galaxies scatter between bins. The drop in number density at the low SFR end is likely due to either incompleteness, underestimated volume corrections, or our more stringent $P(z)$ sample selection than F15. At the high SFR end, there is a clear excess in number density at redshifts $4< z <6$. The same excess at high SFR is observed when allowing galaxies to fractionally contribute to multiple SFR bins according to their $E(B-V)$ posterior, and that approach does not affect the results of this work.

## 4.7 Discussion

### *4.7.1 On the Differences in Results in the Literature*

All current observations of the SFR of galaxies at $z > 4$ rely on UV data, and therefore require some assumptions in order to correct for the attenuation by dust. Smit et al. (2012) and Mashian et al. (2016) used the correlation between $M_{\rm UV}$ and $\beta$ in bins of UV magnitude to assign a fixed UV attenuation at a given UV magnitude

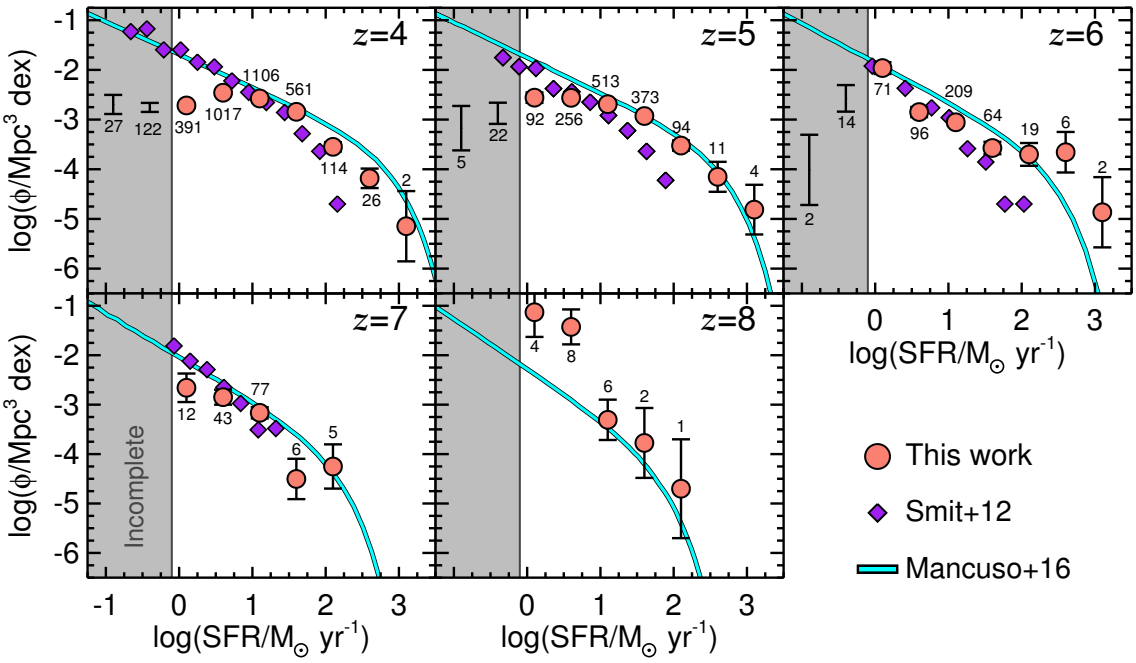


Figure 4.4: The SFR Function of Galaxies from $z_{\rm phot} = 6$ to $z_{\rm phot} = 4$. Salmon-colored circles indicate the number density in bins of SFR, the above/below numbers indicate the number of galaxies used in each bin, and the grey region indicates the SFRs below which we are dominated by effects from incompleteness. The purple diamonds is the SFRF from Smit et al. (2012), which used $\beta$ to determine dust corrections and therefore the SFRs. The cyan curve is an estimate for the intrinsic SFRF from the continuity equation by Mancuso et al. (2016).

(Bouwens et al., 2012). Then, they used the expected IRX-$\beta$ relation to convert the UV attenuation to a dust-corrected SFR. This method poses a difficulty for galaxy evolution models because it under-predicts the amount of star formation required to match the observed stellar mass functions (Duncan et al., 2014; Grazian et al., 2015; Song et al., 2015) and disagrees with predictions of the SFRF derived from the continuity equation (Mancuso et al., 2016).

The divergent observational pictures of the SFR function can be sourced to the relation between $M_{\rm UV}$ and $\beta$. Figure 4.5 shows the relation at $z = 5$ for individual objects in this sample, with the median values and $\sigma_{\rm NMAD}$ scatter reported in Table 4.2. Some studies find an average trend such that UV bright galaxies (presumably more massive) have redder UV colors (presumably more attenuated by dust). However, the individual objects exhibit a high scatter in this relation, showing a non-negligible amount of red galaxies at all UV magnitudes. In fact, the recent *ALMA* survey of the HUDF has shown that the sources detected in the rest-frame far-infrared, due to their significant dust content, have a range of UV magnitudes (Dunlop et al., 2016). One would then expect a SFR function computed in this work using individual galaxies will produce a greater volume of dust corrections than if one assumes dust corrections using an $M_{\rm UV} - \beta$ relation, regardless of which IRX-$\beta$ relation is used.

### *4.7.2 Implications for SFR Efficiency*

The SFR function can give insight into the star-formation histories of massive galaxies. A challenge for cosmological models is the balance between merging and *in-situ* processes to regulate star-formation. In the past, this has been done by comparing the observed stellar masses to the predicted abundances from the growth of dark matter halos (abundance matching; Vale & Ostriker, 2004; Shankar et al.,

Table 4.2: $M_{\rm UV} - \beta$ Relation at $z = 5$

| $M_{\rm UV}$ | -21.0 | -20.5 | -20.0 | -19.5 | -19.0 | -18.5 |
|---|---|---|---|---|---|---|
| median $\beta$ | -1.79 | -1.83 | -1.93 | -1.91 | -1.85 | -1.74 |
| $\sigma_{\rm NMAD}$ | 0.44 | 0.47 | 0.64 | 0.73 | 0.85 | 0.78 |

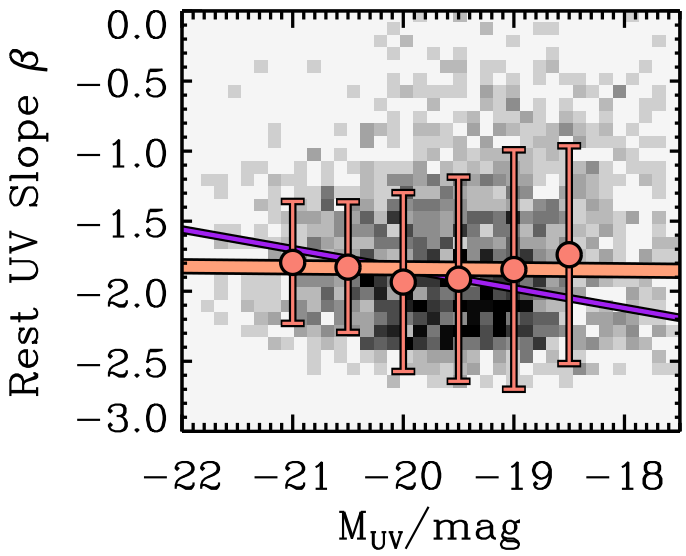


Figure 4.5: The Relation Between UV Magnitude and $\beta$ at $z = 5$.
The relation between the rest-frame UV magnitude $M_{1500}$ and the UV slope $\beta$ at $z = 5$. Darker regions correspond to bins of $M_{1500}$ and $\beta$ with more galaxies. The salmon-colored circles, error bars, and lines represent the median $\beta$ in bins of $M_{1500}$, their $\sigma_{\rm NMAD}$ scatter, and their best-fitting slope, respectively. The purple line presents the $M_{1500} - \beta$ relation by Bouwens et al. (2012).

2006; Moster et al., 2013). A similar technique can be done with the SFR function, allowing one to compare the relationship between halo mass and stellar mass, as well as halo mass and SFR. If there is no evolution with halo mass, this hints to a star-formation that is not regulated by gas accretion on cosmological timescales (assuming cosmological gas accretion follows dark matter halo accretion), but instead is regulated by *in-situ* processes (Mancuso et al., 2016).

In addition, (Steinhardt et al., 2015) pointed out that the observed abundances of SFR meant that galaxies had to have formed impossibly early in the universe in order to match the abundances of stellar mass. This problem is circumvented with the SFR function of this work. The higher number densities at the high SFR end is fully consistent with the observed stellar mass functions (Song et al., 2015), it agrees with the current sparse infrared number densities of high-$z$ sources (Riechers et al., 2014; Cooray et al., 2014), and it connects smoothly with the observed distribution of IR-detected sources at $z < 3$ (Aversa et al., 2015).

Finally, the SFR function of this work is in broad agreement with the recent predictions of the intrinsic SFR function implied by Mancuso et al. (2016). They used an approach using the continuity equation to estimate the number density of SFR at these high redshifts. In short, their method assumes analytical continuity of the SFR function such that the assumedly dust-free $z = 8$ SFRF evolves continuously to into the observed SFR function at $z < 3$ (where there is infrared data to give a more reliable handle to high SFRs).

# 5. SUMMARY AND CONCLUSIONS

In this thesis, I have contributed to the body of knowledge on the properties of galaxies in the very distant universe. I studied the star-formation activity and history of these galaxies, and addressed several outstanding questions in the field: (1) Does the relation between SFR and stellar mass in star-forming galaxies extend to $z > 4$, or do galaxies become bursty? (2) Does the sSFR level off at $z > 3$? (3) What is the functional form of the SFR history at these redshifts? (4) Is the dust-attenuation law universal for all star-forming galaxies at high redshift? and (5) Is there a number density excess at high SFRs across $4 < z < 6$, as implied by the evolution of the stellar mass function? These questions were the focus of this thesis, and I summarize below the results of each chapter.

## 5.1 The Relation Between SFR and Stellar Mass at High Redshift

First, in Chapter 2 I used a photometric-redshift sample selected from the CANDELS GOODS-S field to study the average population of galaxies across the redshift range $3.5 < z < 6.5$. I presented a Bayesian SED fitting procedure that takes advantage of the full posterior to determine the physical properties (stellar mass, SFR) of each galaxy. This method incorporated effects of nebular emission lines and different dust attenuations, although I showed that the effects of these different models are largely mitigated when the parameters are derived from posterior probability densities. This method was shown to have several advantageous over using best-fit parameter values from SED fits, including the fact that our method well-recovered the stellar masses and SFRs from a SAM mock catalog.

I found that from $3.5 < z < 6.5$ the star-forming galaxies in CANDELS follow a nearly unevolving correlation between SFR and stellar mass, parameterized as SFR

$\sim \mathrm{M}^{a}$ with $a = 0.54 \pm 0.16$ at $z \sim 6$ and $0.70 \pm 0.21$ at $z \sim 4$. The observed scatter in the SFR–stellar mass relation is small for galaxies with $\log M_{\star}/\mathrm{M}_{\odot} > 9$ dex at all redshifts, at least on timescales associated with UV SFRs. This evolution requires a star formation history that increases with decreasing redshift (on average, the SFRs of individual galaxies rise with time). I note that the redshift range of this study limits the data to cover rest-frame UV-to-optical wavelengths, and we defer the search for an underlying dust obscured population for future work.

The low scatter in the SFR and stellar mass relation implies interesting physics. Comparing the observed log SFR scatter at fixed stellar mass with the scatter due to measurement uncertainties, the true intrinsic scatter is as much as $\sigma(\log \mathrm{SFR}) = 0.2-0.3$ dex at all masses and redshifts. Assuming that the SFR is tied to the net gas inflow rate (including gas accretion and feedback), then the scatter in the gas inflow rate for star-forming galaxies over our stellar mass and redshift range is equally smooth, $\sigma(\log \dot{\mathrm{M}}_{\mathrm{gas}}) < 0.2 - 0.3$ dex, at least when averaged over the timescale of UV SFRs ($\sim 100$ Myr).

I also measured the evolution in the SFR for galaxies from $z = 6.5$ to 3.5 using an evolving number density selection to measure the evolution in galaxy progenitors that accounts for mergers between halos and variations in halo growth factors. For galaxies with $\log M_{\star}/\mathrm{M}_{\odot} = 10.2$ dex at $z = 4$, the star formation history follows $\Psi/\mathrm{M}_{\odot}\ \mathrm{yr}^{-1} = (t/\tau)^{\gamma}$ with $\gamma = 1.4 \pm 0.1$ and $\tau = 92 \pm 14$ Myr from $z = 6.5$ to $z = 3.5$. I further showed that this star formation history reproduces the measured SFR–mass relation for galaxies at this mass and redshift.

Finally, I showed that the sSFR gradually increases with increasing redshift from $z = 4$ to $z = 6$, with only small qualitative differences if galaxies are selected at fixed stellar mass or by using an evolving number density. Broadly, the evolution in the sSFR is consistent with the theory of cosmological gas accretion where the SFR fol-

lows the net gas accretion rate. This means that the sSFR plateau is likely unphysical and is ruled out with more advanced methods of stellar population modeling.

## 5.2 The Non-Universality of the $z = 2$ Extragalactic Dust Law

Next, in Chapter 2 I investigated the shape of the dust-attenuation law in star-forming galaxies at $z \sim 2$ in the CANDELS GOODS-N and GOODS-S deep fields. I applied a Bayesian SED-fitting technique to galaxies with spectroscopic and photometric redshifts, and determined the evidence for their underlying dust law and its correlation with other galaxy physical properties. The results from this chapter can be summarized as follows.

I found that IR-luminous galaxies at $z \sim 2$ can be characterized by a range of dust laws bounded between two opposing types: (1) A starburst-like (Calzetti et al., 2000) attenuation that is greyer (flatter) across UV-to-NIR wavelengths and (2) a dust law that steepens towards the rest-frame FUV like the curve of the SMC extinction law (Pei, 1992). These two dust laws have been the basis of many comparisons in the literature and served as a starting point in our search for statistical evidence between dust laws in individual galaxies.

Next, I developed a Bayesian method to infer the dust law of a sample of galaxies at $z \sim 2$ using their rest-frame UV-to-NIR photometry. The Bayes-factor evidence of individual galaxies suggested a dust law that was supported by their position along the $IRX - \beta$ relations. This result gives credibility that a Bayesian analysis of rest-frame UV-to-NIR fluxes is capable of broadly distinguishing between dust laws that are grey or steep in the rest-frame FUV.

Furthermore, I found that the steepness of the dust law, parameterized by a $\delta$ power-law deviation from the starburst dust law, is correlated with their color excess, $E(B-V)$, for IR-bright galaxies at $z \sim 2$. Galaxies with lower levels of dust

attenuation have dust laws that are steeper in the rest-frame FUV, following

$\delta = (0.62 \pm 0.05) \log(E(B-V)) + (0.26 \pm 0.02)$

The relation between $E(B-V)$ and $\delta$ is also supported by predictions from radiative transfer. The agreement with dust theory offers possible interpretations for the relation and its origins from different dust production mechanisms. For example, the change in the shape of the dust law may be a result of star-dust geometry, properties of dust grains, and/or stellar population age, emphasizing the non-universality of the dust law in star-forming galaxies.

## 5.3 The Dust Law and SFR Functions at $z > 4$

Finally, in Chapter 4 I used the methods developed throughout this thesis to place constraints on the number density of galaxies as a function of SFR, a useful tool for theoretical models. First, I sought to confirm if the relation from Chapter 3 between the shape of the dust law and the strength of dust attenuation in galaxies persisted in galaxies at redshifts $z > 4$. I applied the methods developed in Chapter 3 and placed the first ever observational constraints on the dust law at very high redshifts ($4 < z < 6$). Then, I then selected a robust sample of galaxies from $z = 8$ to $z = 4$ and constructed a SFR functions at those redshifts. The conclusions from this chapter are as follows.

I fond that galaxies at $4 < z < 6$ follow a relation between the strength of their attenuation (parameterized by their color excess $E(B-V)$) and the tilt of their dust law (parameterized by a power-law tilt $\delta$ from the Calzetti et al., 2000, starburst dust law). This relationship is similar to what is found at $z < 2$ by Salmon et al. (2016), albeit shifted to lower $E(B-V)$ for galaxies at these redshifts. This suggests that the relation between the dust law and $E(B-V)$ found at $z \sim 2$ from Chapter 3 can be used to derive SFRs at these redshifts.

In addition, I found no obvious relationship between $\delta$ and SFR nor stellar mass, implying that the color excess is the parameter that best correlates with the change in shape of the dust law. Fits to the dust law using $\delta$ are only reliable for a subset of our $z > 4$ samples, and we therefore adopt the relationship between $\delta$ and $E(B-V)$ from Chapter 3 when deriving the SFR.

Next, I derive the number density of galaxies as a function of SFR from the volume corrections to individual galaxies following Finkelstein et al. (2015). I constructed the number densities of galaxies at each redshift and each bin of log SFR by summing the number densities of individual galaxies. This method is therefore more sensitive to highly reddened galaxies at all UV luminosities. I found that there is a clear excess of number density at the high SFR end when accounting for the dust attenuation of individual galaxies.

Finally, I noted that the SFR function of this work is qualitatively consistent with evolution of the massive end of current observed stellar mass functions. It also agrees with number densities of the to-date few sources detected in the infrared at $z > 4$. Comparing to results in the literature, this implies that the SFR function of this thesis connects smoothly with the observed distribution of IR-detected sources at $z < 3$.

## 5.4 Future Work

Much of the work presented in this thesis involved the construction of improved techniques to model the SEDs of distant galaxies. The implications for these methods are far reaching, and naturally extend into studies of dust grain physics, nebular emission, and galaxy evolution in the very high redshift universe. In this section, I discuss the how the results and conclusions of this dissertation lead into other promising studies of galaxy evolution.

### *5.4.1 The Physics of Dust in the Distant Universe*

Understanding dust grain properties and how their origins coincide with metal buildup, stellar winds, and supernovae (SNe) remains elusive for local galaxies and star-forming regions, let alone in the distant universe. Several "recipes for reddening" attempt to package the geometric effects of extinction and scattering into a single, wavelength-dependent prescription for extragalactic dust-attenuation, often called a "dust law" (Calzetti et al., 2000). The dust law affects nearly all aspects of galaxy evolution, because it is usually assumed *a priori* when deriving physical properties of galaxies (Papovich et al., 2001). Correlating the shape of the dust law with galaxy observables would improve dust-corrections to ultra-violet (UV) SFRs and give clues about the properties of dust grains and the mechanisms that produce them.

With a sample of galaxies at $z_{\rm spec}\sim2$, I showed in Chapter 2 that a Bayesian modeling of individual galaxies' rest-UV-to-near-infrared (IR) photometry can produce evidence between different dust laws. This method was specifically designed to be applicable to even higher redshifts ($z > 4$). However, we can modify this method to conduct a more detailed exploration of the dust law around $z = 1 - 2$.

For example, Figure 5.1 shows a galaxy from Chapter 2 with rest-UV colors indicative of a starburst (ie., Calzetti et al., 2000) dust law. However we could also include the GTC/SHARDS (Gran Telescopio Canarias/Survey for High-$z$ Absorption Red and Dead Sources) medium bands (PI Pérez-González Pérez-González et al., 2013) which provide an even finer sampling of the rest-UV. This data can better constrain the shape of the dust law and even produce evidence for the enigmatic 2175Å dust absorption feature, whose presence is poorly constrained in distant galaxies. The Bayesian methods required for this project have already been developed in Chapter and the SHARDS data is provided through collaboration with CANDELS

team members.

### *5.4.2 Using ALMA to Find Dusty Star-Forming Galaxies at High Redshift*

Mounting observational evidence of submillimeter galaxies suggest the presence of obscured starbursts even out to $z>5$ (Capak et al., 2011; Riechers et al., 2013; Casey et al., 2014b). These galaxies are invisible to rest-frame UV-selected samples and give credence to the higher number densities of galaxies at high SFR found in Chapter 4. While these galaxies are extreme cases, they question our assumptions of dust prevalence in the early universe. The so-called 'dust budget crisis' (Morgan & Edmunds, 2003) is the recognition that the usual suspects of dust production, namely low-intermediate mass stars, are incapable of explaining the large dust masses observed so early in the universe (Rowlands et al., 2014). If rapid mechanisms of dust formation exist at high redshift (e.g. from asymptotic giant branch stars, SNe, or grain growth in the interstellar medium), then this has implications for galaxy evolution models that otherwise assume little-to-no dust (e.g., the intrinsic rest-UV luminosity function, SFR density, and SFR function).

A significant quantity of dust at high redshift would also affect our interpretation of reionization. Dust readily absorbs and scatters UV ionizing radiation which is difficult to disentangle from IGM attenuation on a galaxy-to-galaxy basis. (Finkelstein et al., 2012b) show that the redder UV colors ($\beta$, $f_\lambda \propto \lambda^\beta$) of the most massive galaxies at $4<z<8$ imply their deep gravitational potentials are able to retain their dust. Conversely, low-mass galaxies become bluer with increasing redshift, suggesting dust in those galaxies is either not produced or blown away at earlier times. However, the connection between $\beta$ and dust content is uncertain, given the scatter between $\beta$ and optical depth from factors such as star-formation history, metallicity, and star-dust geometry (Reddy et al., 2015).

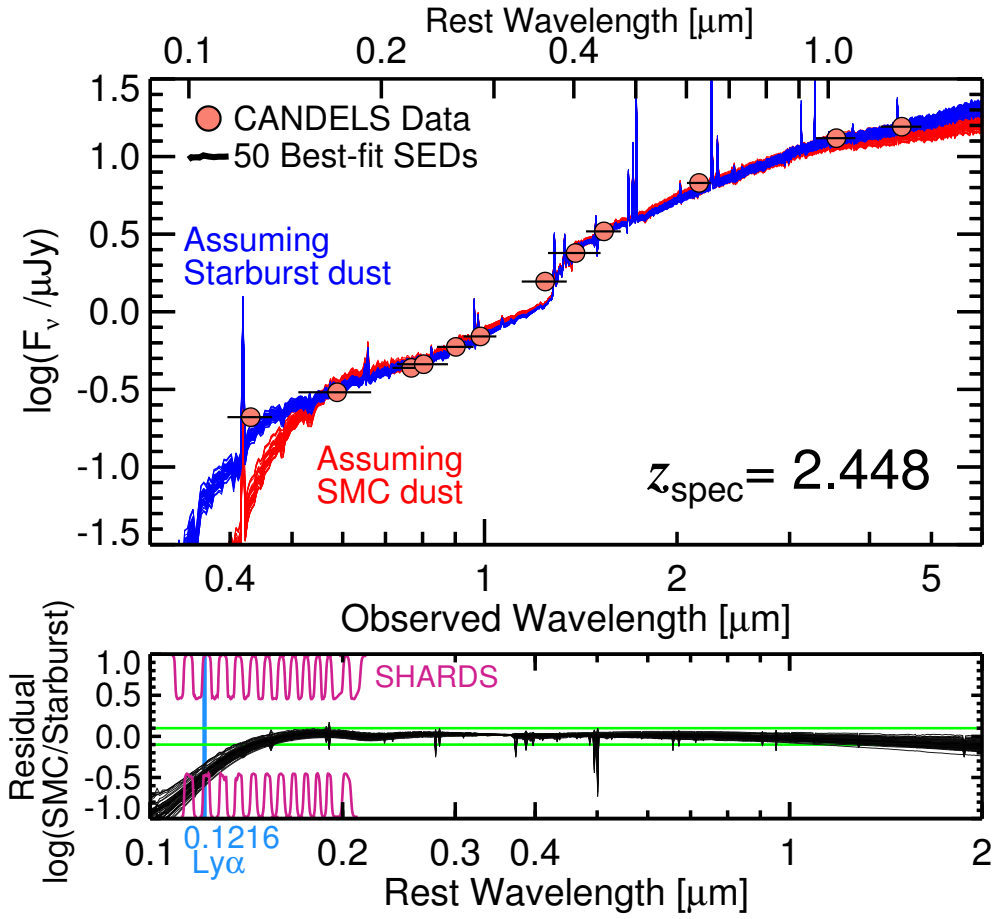


Figure 5.1: Better Determinations of the Dust Law Using SHARDS. Example of fitting stellar populations to a galaxy SED under two assumptions of the underlying dust law. For reddened galaxies, the color of the two bands in the rest-UV can help constrain the dust law. Bottom: residuals of the SEDs show that SHARDS medium bands can better sample the rest-UV at $z\sim3$.

The uncertainty in dust corrections present two different interpretations of the distribution of SFRs, which leads to different constraints on cosmological models. One promising resolution that is an outcome of this thesis is the prospect of follow observations with *ALMA*. Figure 5.2 shows the SEDs of galaxies that have high attenuation, and detectable thermal emission from dust. In an *ALMA* proposal I led (submitted in Cycle 4), we target these objects to confirm their high SFRs. Their predicted dust continuum measurements at 850 $\mu$m are bright enough to be measured in a matter of minutes. Continuum detections of these galaxies would confirm the large SFRs and extinctions, while non-detections would allow us to place meaningful priors on the model fits and dust attenuation law.

In addition, larger far-IR and sub-mm searches for galaxies at $z > 4$ will build the science case for future *JWST* NIRCam and MIRI proposals. At $z$>9, NIRCam and MIRI provide analogous wavelength coverage to $z\sim$2 galaxies by *HST* and *Spitzer*. At these early ages of the universe we can begin to place meaningful priors on the lack of dust and/or evolved stellar populations.

### *5.4.3 The Correlation of Nebular Emission with Galaxy Properties*

A now obvious challenge for studying galaxies within the neutral era ($z$>7) of the intergalactic medium (IGM) is the paucity of photons at wavelengths less than the rest-frame Lyman-$\alpha$ transition (Ly$\alpha$). We know the strength of Ly$\alpha$ (ie., equivalent width, EW) decreases with increasing redshift (Tilvi et al., 2013), but it is important to disentangle the effects of galaxy evolution, dust attenuation, and IGM attenuation before correlating this observation directly to an evolution in the covering fraction of line-of-site neutral hydrogen.

For example, we know that with increasing redshift (above $z\sim$2), galaxies generally decrease in SFR (their star-formation histories rise with cosmic time Papovich

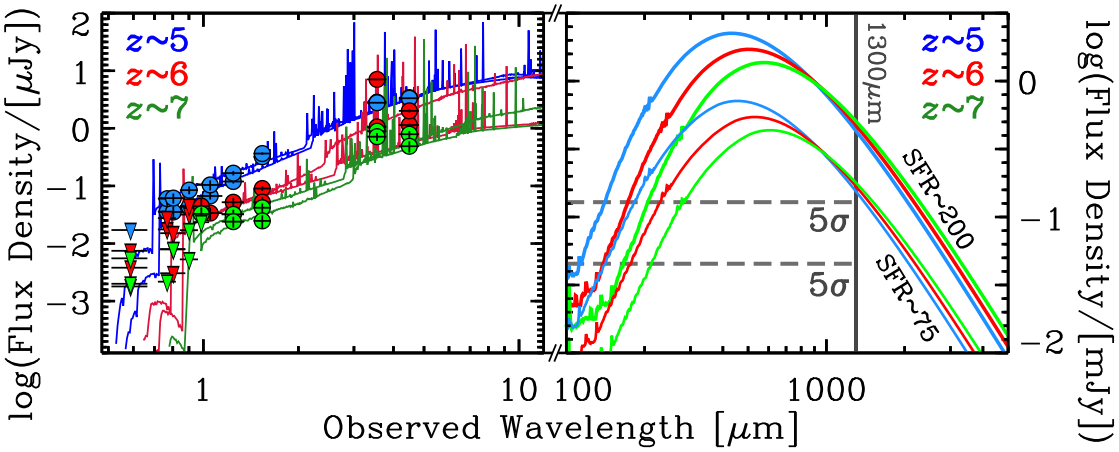


Figure 5.2: *ALMA* Can Reveal Dusty Galaxies at Very High Redshifts. Example best-fit SEDs of objects in each bin of $z$∼5, 6, and 7. *Right:* The predicted FIR SEDs (Rieke et al. 2009) assuming two SFR scenarios: the SED-derived SFRs of ∼200 $M_\odot$/yr or the conservative 5%-tile of $P$(SFR) of ∼75 $M_\odot$/yr. Dashed lines show the 5-$\sigma$ limits for each SFR.

et al., 2011; Salmon et al., 2015) and become bluer (potentially from a decrease in dust content, (Finkelstein et al., 2012b). From relationships of Ly$\alpha$ and galaxy physical properties, we should expect Ly$\alpha$ to decrease at higher redshifts from galaxy evolution alone (Kornei et al., 2010). While the plummet in Ly$\alpha$ EW at $z \sim 7$ is likely due, in part, to increased IGM opacity, it remains to be seen how much should be disentangled from normal galaxy evolution.

One promising future study is to perform a closer inspection of the evolution of Ly$\alpha$ and study how its strength evolves with galaxy properties, using existing CANDELS multi-wavelength data and supporting ground-based spectroscopy. No study to date has modeled both the strength of Ly$\alpha$ and the stellar continuum SED in a fully Bayesian framework. The work presented in this dissertation incorporating nebular emission to galaxy SEDs and modeling high-redshift galaxies is highly relevant to address the drop of Ly$\alpha$ EW into the era of reionization.

### *5.4.4 A Bayesian Approach to the SFRF*

Even a handful of dust-obscured star-forming galaxies would significantly validate the bright end of the $z > 4$ SFRF. Finding the true shape of the SFRF requires followup observations from *ALMA* and *Herschel*, which will naturally follow from the results of this dissertation. Measuring the bright end of the high-$z$ SFRF would not only constrain feedback in galaxy simulations, but the abundances the first dusty star-forming galaxies can help to place meaningful upper limits on dust grain growth and/or dust production mechanisms.

Furthermore, Bayesian methods have already been developed to infer the luminosity function (Schmidt et al., 2014) and can be adopted to create a fully Bayesian SFRF. This will be especially relevant with RELICS (Reionization Lensing Cluster Survey) which will produce the first constraints to the $z > 9$ luminosity functions (and therefore extending the evolution of the SFR function studies in this thesis). These promising datasets will pave the way for selecting the most distant galaxies in the universe, a necessity for fundamental *JWST* science into the epoch of reionization.

# REFERENCES


Anders, P., & Fritze-v. Alvensleben, U. 2003, A&A, 401, 1063

Ashby, M. L. N., Willner, S. P., Fazio, G. G., et al. 2013, ApJ, 769, 80

Atek, H., Siana, B., Scarlata, C., et al. 2011, ApJ, 743, 121

Aversa, R., Lapi, A., de Zotti, G., Shankar, F., & Danese, L. 2015, ApJ, 810, 74

Balestra, I., Mainieri, V., Popesso, P., et al. 2010, A&A, 512, A12

Banerji, M., Glazebrook, K., Blake, C., et al. 2013, MNRAS, 431, 2209

Becker, R. H., Fan, X., White, R. L., et al. 2001, AJ, 122, 2850

Beckwith, S. V. W., Stiavelli, M., Koekemoer, A. M., et al. 2006, AJ, 132, 1729

Beers, T. C., Flynn, K., & Gebhardt, K. 1990, AJ, 100, 32

Behroozi, P. S., Conroy, C., & Wechsler, R. H. 2010, ApJ, 717, 379

Behroozi, P. S., Marchesini, D., Wechsler, R. H., et al. 2013a, ApJL, 777, L10

Behroozi, P. S., Wechsler, R. H., & Conroy, C. 2013b, ApJ, 770, 57

Behroozi, P. S., Wechsler, R. H., & Wu, H.-Y. 2013c, ApJ, 762, 109

Behroozi, P. S., Wechsler, R. H., Wu, H.-Y., et al. 2013d, ApJ, 763, 18

Bell, E. F. 2002, ApJ, 577, 150

Bell, E. F., & de Jong, R. S. 2001, ApJ, 550, 212

Bell, E. F., McIntosh, D. H., Katz, N., & Weinberg, M. D. 2003, ApJS, 149, 289

Birnboim, Y., & Dekel, A. 2003, MNRAS, 345, 349

Bolton, J. S., & Haehnelt, M. G. 2007, MNRAS, 382, 325

Bolzonella, M., Miralles, J.-M., & Pelló, R. 2000, A&A, 363, 476

Boquien, M., Calzetti, D., Kennicutt, R., et al. 2009, ApJ, 706, 553

Boquien, M., Buat, V., Boselli, A., et al. 2012, A&A, 539, A145

Bouché, N., Dekel, A., Genzel, R., et al. 2010, ApJ, 718, 1001

Bouwens, R. J., Illingworth, G. D., González, V., et al. 2010, ApJ, 725, 1587

Bouwens, R. J., Illingworth, G. D., Oesch, P. A., et al. 2012, ApJ, 754, 83

—. 2015, ApJ, 803, 34

Brammer, G. B., van Dokkum, P. G., & Coppi, P. 2008, ApJ, 686, 1503

Brammer, G. B., van Dokkum, P. G., Illingworth, G. D., et al. 2013, ApJL, 765, L2

Bridge, C. R., Teplitz, H. I., Siana, B., et al. 2010, ApJ, 720, 465

Bruzual, G., & Charlot, S. 2003, MNRAS, 344, 1000

Bruzual, G., Magris, G., & Calvet, N. 1988, ApJ, 333, 673

Buat, V., Iglesias-Páramo, J., Seibert, M., et al. 2005, ApJL, 619, L51

Buat, V., Giovannoli, E., Burgarella, D., et al. 2010, MNRAS, 409, L1

Buat, V., Giovannoli, E., Heinis, S., et al. 2011, A&A, 533, A93

Buat, V., Noll, S., Burgarella, D., et al. 2012, A&A, 545, A141

Buat, V., Heinis, S., Boquien, M., et al. 2014, A&A, 561, A39

Burgarella, D., Buat, V., & Iglesias-Páramo, J. 2005, MNRAS, 360, 1413

Calzetti, D. 1997, in American Institute of Physics Conference Series, Vol. 408, American Institute of Physics Conference Series, ed. W. H. Waller, 403–412

Calzetti, D. 2001, PASP, 113, 1449

Calzetti, D., Armus, L., Bohlin, R. C., et al. 2000, ApJ, 533, 682

Calzetti, D., Kinney, A. L., & Storchi-Bergmann, T. 1994, ApJ, 429, 582

Calzetti, D., Wu, S.-Y., Hong, S., et al. 2010, ApJ, 714, 1256

Capak, P., Mobasher, B., Scoville, N. Z., et al. 2011, ApJ, 730, 68

Capak, P. L., Carilli, C., Jones, G., et al. 2015, Nature, 522, 455

Casey, C. M., Narayanan, D., & Cooray, A. 2014a, PhR, 541, 45

Casey, C. M., Scoville, N. Z., Sanders, D. B., et al. 2014b, ApJ, 796, 95

Cattaneo, A., Mamon, G. A., Warnick, K., & Knebe, A. 2011, A&A, 533, A5

Ceverino, D., Dekel, A., & Bournaud, F. 2010, MNRAS, 404, 2151

Chabrier, G. 2003, PASP, 115, 763

Charlot, S., & Fall, S. M. 1993, ApJ, 415, 580

—. 2000, ApJ, 539, 718

Chevallard, J., Charlot, S., Wandelt, B., & Wild, V. 2013, MNRAS, 432, 2061

Colless, M., Dalton, G., Maddox, S., et al. 2001, MNRAS, 328, 1039

Conroy, C., & Gunn, J. E. 2010, ApJ, 712, 833

Conroy, C., Gunn, J. E., & White, M. 2009, ApJ, 699, 486

Cooray, A., Calanog, J., Wardlow, J. L., et al. 2014, ApJ, 790, 40

Curtis-Lake, E., McLure, R. J., Dunlop, J. S., et al. 2013, MNRAS, 429, 302

Daddi, E., Dickinson, M., Morrison, G., et al. 2007, ApJ, 670, 156

Daddi, E., Dannerbauer, H., Stern, D., et al. 2009, ApJ, 694, 1517

Dahlen, T., Mobasher, B., Faber, S. M., et al. 2013, ApJ, 775, 93

Dale, D. A., & Helou, G. 2002, ApJ, 576, 159

Dale, D. A., Helou, G., Contursi, A., Silbermann, N. A., & Kolhatkar, S. 2001, ApJ, 549, 215

Davé, R. 2008, MNRAS, 385, 147

Davé, R., Finlator, K., & Oppenheimer, B. D. 2011a, MNRAS, 416, 1354

Davé, R., Katz, N., Oppenheimer, B. D., Kollmeier, J. A., & Weinberg, D. H. 2013, MNRAS, 434, 2645

Davé, R., Oppenheimer, B. D., & Finlator, K. 2011b, MNRAS, 415, 11

de Barros, S., Reddy, N., & Shivaei, I. 2015, ArXiv 1509.05055

de Barros, S., Schaerer, D., & Stark, D. P. 2014, A&A, 563, A81

Dekel, A., & Birnboim, Y. 2006, MNRAS, 368, 2

Dekel, A., & Mandelker, N. 2014, MNRAS, 444, 2071

Dekel, A., Birnboim, Y., Engel, G., et al. 2009, Nature, 457, 451

Dickinson, M. 1998, in The Hubble Deep Field, ed. M. Livio, S. M. Fall, & P. Madau

(New York: Cambridge Univ. Press), 219

Doherty, M., Bunker, A. J., Ellis, R. S., & McCarthy, P. J. 2005, MNRAS, 361, 525

Domínguez, A., Siana, B., Brooks, A. M., et al. 2014, ArXiv 1408.5788

Donley, J. L., Koekemoer, A. M., Brusa, M., et al. 2012, ApJ, 748, 142

Draine, B. T. 2003, ApJ, 598, 1017

Draine, B. T., & Li, A. 2001, ApJ, 551, 807

Drory, N., Bender, R., & Hopp, U. 2004, ApJL, 616, L103

Duncan, K., Conselice, C. J., Mortlock, A., et al. 2014, MNRAS, 444, 2960

Dunkley, J., Komatsu, E., Nolta, M. R., et al. 2009, ApJS, 180, 306

Dunlop, J. S., McLure, R. J., Biggs, A. D., et al. 2016, ArXiv 1606.00227

Dunne, L., Ivison, R. J., Maddox, S., et al. 2009, MNRAS, 394, 3

Dutton, A. A., van den Bosch, F. C., & Dekel, A. 2010, MNRAS, 405, 1690

Elbaz, D., Dickinson, M., Hwang, H. S., et al. 2011, A&A, 533, A119

Elíasdóttir, Á., Fynbo, J. P. U., Hjorth, J., et al. 2009, ApJ, 697, 1725

Ellis, R. S., McLure, R. J., Dunlop, J. S., et al. 2013, ApJL, 763, L7

Erb, D. K., Pettini, M., Shapley, A. E., et al. 2010, ApJ, 719, 1168

Erb, D. K., Shapley, A. E., Pettini, M., et al. 2006a, ApJ, 644, 813

Erb, D. K., Steidel, C. C., Shapley, A. E., et al. 2006b, ApJ, 647, 128

Eyles, L. P., Bunker, A. J., Ellis, R. S., et al. 2007, MNRAS, 374, 910

Fadda, D., Yan, L., Lagache, G., et al. 2010, ApJ, 719, 425

Fan, X., Strauss, M. A., Schneider, D. P., et al. 2001, AJ, 121, 54

Fan, X., Strauss, M. A., Becker, R. H., et al. 2006, AJ, 132, 117

Faucher-Giguère, C.-A., & Kereš, D. 2011, MNRAS, 412, L118

Ferland, G. J., Korista, K. T., Verner, D. A., et al. 1998, PASP, 110, 761

Finkelstein, S. L., Hill, G. J., Gebhardt, K., et al. 2011, ApJ, 729, 140

Finkelstein, S. L., Papovich, C., Ryan, R. E., et al. 2012a, ApJ, 758, 93

Finkelstein, S. L., Papovich, C., Salmon, B., et al. 2012b, ApJ, 756, 164

Finkelstein, S. L., Ryan, Jr., R. E., Papovich, C., et al. 2015, ApJ, 810, 71

Finlator, K., Davé, R., & Oppenheimer, B. D. 2007, MNRAS, 376, 1861

Finlator, K., Davé, R., Papovich, C., & Hernquist, L. 2006, ApJ, 639, 672

Finlator, K., Oppenheimer, B. D., & Davé, R. 2011, MNRAS, 410, 1703

Fioc, M., & Rocca-Volmerange, B. 1997, A&A, 326, 950

Fontana, A., Pozzetti, L., Donnarumma, I., et al. 2004, A&A, 424, 23

Forbes, J. C., Krumholz, M. R., Burkert, A., & Dekel, A. 2014, MNRAS, 443, 168

Forrest, B., Tran, K.-V. H., Tomczak, A. R., et al. 2016, ApJL, 818, L26

Förster Schreiber, N. M., van Dokkum, P. G., Franx, M., et al. 2004, ApJ, 616, 40

Freedman, W. L., Madore, B. F., Mould, J. R., et al. 1994, Nature, 371, 757

Gabor, J. M., & Bournaud, F. 2014, MNRAS, 437, L56

Gall, C., Andersen, A. C., & Hjorth, J. 2011a, A&A, 528, A13

—. 2011b, A&A, 528, A14

Gall, C., Hjorth, J., & Andersen, A. C. 2011c, A&A Rv, 19, 43

Giavalisco, M. 2002, ARA&A, 40, 579

Giavalisco, M., Ferguson, H. C., Koekemoer, A. M., et al. 2004, ApJL, 600, L93

González, V., Bouwens, R., Illingworth, G., et al. 2014, ApJ, 781, 34

González, V., Labbé, I., Bouwens, R. J., et al. 2011, ApJL, 735, L34

—. 2010, ApJ, 713, 115

Gordon, K. D., Clayton, G. C., Misselt, K. A., Landolt, A. U., & Wolff, M. J. 2003, ApJ, 594, 279

Gordon, K. D., Clayton, G. C., Witt, A. N., & Misselt, K. A. 2000, ApJ, 533, 236

Gordon, K. D., Misselt, K. A., Witt, A. N., & Clayton, G. C. 2001, ApJ, 551, 269

Gordon, K. D., Witt, A. N., Carruthers, G. R., Christensen, S. A., & Dohne, B. C. 1994, ApJ, 432, 641

Grazian, A., Fontana, A., Santini, P., et al. 2015, A&A, 575, A96

Grogin, N. A., Kocevski, D. D., Faber, S. M., et al. 2011, ApJS, 197, 35

Gunn, J. E., & Peterson, B. A. 1965, ApJ, 142, 1633

Guo, Q., White, S., Boylan-Kolchin, M., et al. 2011, MNRAS, 413, 101

Guo, Y., Ferguson, H. C., Giavalisco, M., et al. 2013, ApJS, 207, 24

Guseva, N. G., Izotov, Y. I., & Thuan, T. X. 2006, ApJ, 644, 890

Heckerman, D. 1995, A Tutorial on Learning with Bayesian Networks, Tech. Rep. MSR-TR-95-06, Learning in Graphical Models, Cambridge, MA, USA

Hopkins, P. F., Kereš, D., Oñorbe, J., et al. 2014, MNRAS, 445, 581

Hubble, E. P. 1926, ApJ, 64

Huchra, J., Davis, M., Latham, D., & Tonry, J. 1983, ApJS, 52, 89

Ilbert, O., Salvato, M., Le Floc'h, E., et al. 2010, ApJ, 709, 644

Illingworth, G. D., Magee, D., Oesch, P. A., et al. 2013, ApJS, 209, 6

Inoue, A. K. 2011, MNRAS, 415, 2920

Jarosik, N., Bennett, C. L., Dunkley, J., et al. 2011, ApJS, 192, 14

Jeffreys, H. 1935, JRSS, 98, 39

—. 1961, Theory of Probability, 3rd edn. (Oxford, England: Oxford)

Jones, A. P., Fanciullo, L., Köhler, M., et al. 2013a, A&A, 558, A62

Jones, T. A., Ellis, R. S., Schenker, M. A., & Stark, D. P. 2013b, ApJ, 779, 52

Kass, R. E., & Raftery, A. E. 1995, JASA, 90, 773

Katz, N., Keres, D., Dave, R., & Weinberg, D. H. 2003, in Astrophysics and Space Science Library, Vol. 281, The IGM/Galaxy Connection. The Distribution of Baryons at z=0, ed. J. L. Rosenberg & M. E. Putman (Dordrecht:Kluwer: Astrophysics and Space Science Library), 185

Katz, N., Weinberg, D. H., & Hernquist, L. 1996, ApJS, 105, 19

Kauffmann, G., Heckman, T. M., White, S. D. M., et al. 2003, MNRAS, 341, 33

Kelson, D. D. 2014, ArXiv 1406.5191

Kennicutt, Jr., R. C. 1998, ARA&A, 36, 189

Kennicutt, Jr., R. C., Hao, C.-N., Calzetti, D., et al. 2009, ApJ, 703, 1672

Kereš, D., Katz, N., Weinberg, D. H., & Davé, R. 2005, MNRAS, 363, 2

Kinney, A. L., Calzetti, D., Bohlin, R. C., et al. 1996, ApJ, 467, 38

Klypin, A. A., Trujillo-Gomez, S., & Primack, J. 2011, ApJ, 740, 102

Koekemoer, A. M., Faber, S. M., Ferguson, H. C., et al. 2011, ApJS, 197, 36

Koekemoer, A. M., Ellis, R. S., McLure, R. J., et al. 2013, ApJS, 209, 3

Komatsu, E., Dunkley, J., Nolta, M. R., et al. 2009, ApJS, 180, 330

Kormendy, J., & Bender, R. 1996, ApJL, 464, L119

Kornei, K. A., Shapley, A. E., Erb, D. K., et al. 2010, ApJ, 711, 693

Kriek, M., & Conroy, C. 2013, ApJL, 775, L16

Kriek, M., van Dokkum, P. G., Franx, M., et al. 2008, ApJ, 677, 219

Kriek, M., Labbé, I., Conroy, C., et al. 2010, ApJL, 722, L64

Krumholz, M. R., & Dekel, A. 2012, ApJ, 753, 16

Krumholz, M. R., Dekel, A., & McKee, C. F. 2012, ApJ, 745, 69

Labbé, I., Bouwens, R., Illingworth, G. D., & Franx, M. 2006, ApJL, 649, L67

Labbé, I., González, V., Bouwens, R. J., et al. 2010, ApJL, 716, L103

Laidler, V. G., Papovich, C., Grogin, N. A., et al. 2007, PASP, 119, 1325

Laursen, P., & Sommer-Larsen, J. 2007, ApJL, 657, L69

Lee, K.-S., Giavalisco, M., Conroy, C., et al. 2009, ApJ, 695, 368

Lee, K.-S., Giavalisco, M., Gnedin, O. Y., et al. 2006, ApJ, 642, 63

Lee, K.-S., Dey, A., Reddy, N., et al. 2011, ApJ, 733, 99

Lee, K.-S., Ferguson, H. C., Wiklind, T., et al. 2012, ApJ, 752, 66

Lee, S.-K., Ferguson, H. C., Somerville, R. S., Wiklind, T., & Giavalisco, M. 2010, ApJ, 725, 1644

Leitherer, C., & Heckman, T. M. 1995, ApJS, 96, 9

Leja, J., van Dokkum, P., & Franx, M. 2013a, ApJ, 766, 33

Leja, J., van Dokkum, P. G., Momcheva, I., et al. 2013b, ApJL, 778, L24

Lu, Y., Mo, H. J., Lu, Z., Katz, N., & Weinberg, M. D. 2014a, MNRAS, 443, 1252

Lu, Y., Wechsler, R. H., Somerville, R. S., et al. 2014b, ApJ, 795, 123

Lundgren, B. F., van Dokkum, P., Franx, M., et al. 2014, ApJ, 780, 34

Lynds, R. 1971, ApJL, 164, L73

Madau, P. 1995, ApJ, 441, 18

Madau, P., & Dickinson, M. 2014, ARA&A, 52, 415

Madau, P., Pozzetti, L., & Dickinson, M. 1998, ApJ, 498, 106

Magdis, G. E., Rigopoulou, D., Huang, J.-S., & Fazio, G. G. 2010, MNRAS, 401, 1521

Maiolino, R., Nagao, T., Grazian, A., et al. 2008, A&A, 488, 463

Malkan, M., Webb, W., & Konopacky, Q. 2003, ApJ, 598, 878

Man, A. W. S., Greve, T. R., Toft, S., et al. 2014, ArXiv 1411.2870

Mancuso, C., Lapi, A., Shi, J., et al. 2016, ArXiv 1604.02507

Mann, I., Nakamura, A. M., & Mukai, T., eds. 2009, Lecture Notes in Physics, Berlin Springer Verlag, Vol. 758, Small Bodies in Planetary Systems

Mannucci, F., Cresci, G., Maiolino, R., et al. 2009, MNRAS, 398, 1915

Maraston, C. 2005, MNRAS, 362, 799

Maraston, C., Pforr, J., Renzini, A., et al. 2010, MNRAS, 407, 830

Marchesini, D., van Dokkum, P. G., Förster Schreiber, N. M., et al. 2009, ApJ, 701, 1765

Mashian, N., Oesch, P. A., & Loeb, A. 2016, MNRAS, 455, 2101

McDonald, P., Seljak, U., Burles, S., et al. 2006, ApJS, 163, 80

Meiksin, A. 2006, MNRAS, 365, 807

Melbourne, J., Williams, B. F., Dalcanton, J. J., et al. 2012, ApJ, 748, 47

Meurer, G. R., Heckman, T. M., & Calzetti, D. 1999, ApJ, 521, 64

Meurer, G. R., Heckman, T. M., Leitherer, C., et al. 1995, AJ, 110, 2665

Michałowski, M. J., Dunlop, J. S., Cirasuolo, M., et al. 2012, A&A, 541, A85

Mignoli, M., Cimatti, A., Zamorani, G., et al. 2005, A&A, 437, 883

Mitchell, P. D., Lacey, C. G., Baugh, C. M., & Cole, S. 2013, MNRAS, 435, 87

Mobasher, B., , & . in prep., ApJ

Mollá, M., García-Vargas, M. L., & Bressan, A. 2009, MNRAS, 398, 451

Morgan, H. L., & Edmunds, M. G. 2003, MNRAS, 343, 427

Moster, B. P., Naab, T., & White, S. D. M. 2013, MNRAS, 428, 3121

Moustakas, J., Coil, A. L., Aird, J., et al. 2013, ApJ, 767, 50

Muñoz-Mateos, J. C., Gil de Paz, A., Boissier, S., et al. 2009, ApJ, 701, 1965

Murali, C., Katz, N., Hernquist, L., Weinberg, D. H., & Davé, R. 2002, ApJ, 571, 1

Muzzin, A., Marchesini, D., Stefanon, M., et al. 2013, ApJ, 777, 18

Nardini, E., Risaliti, G., Watabe, Y., Salvati, M., & Sani, E. 2010, MNRAS, 405, 2505

Neistein, E., & Dekel, A. 2008, MNRAS, 383, 615

Neistein, E., & Weinmann, S. M. 2010, MNRAS, 405, 2717

Nestor, D. B., Shapley, A. E., Steidel, C. C., & Siana, B. 2011, ApJ, 736, 18

Newton, M. A., Czado, C., & Chappell, R. 1996, JASA, 91, 142

Noeske, K. G., Weiner, B. J., Faber, S. M., et al. 2007, ApJL, 660, L43

Noll, S., Pierini, D., Pannella, M., & Savaglio, S. 2007, A&A, 472, 455

Noll, S., Pierini, D., Cimatti, A., et al. 2009, A&A, 499, 69

Noterdaeme, P., Ledoux, C., Srianand, R., Petitjean, P., & Lopez, S. 2009, A&A, 503, 765

Nozawa, T., Asano, R. S., Hirashita, H., & Takeuchi, T. T. 2015, MNRAS, 447, L16

Nozawa, T., Kozasa, T., Umeda, H., Maeda, K., & Nomoto, K. 2003, ApJ, 598, 785

Oesch, P. A., Bouwens, R. J., Illingworth, G. D., et al. 2010, ApJL, 709, L16

Oesch, P. A., Labbé, I., Bouwens, R. J., et al. 2013, ApJ, 772, 136

Oke, J. B., & Gunn, J. E. 1983, ApJ, 266, 713

Oliver, S., Frost, M., Farrah, D., et al. 2010, MNRAS, 405, 2279

Ono, Y., Ouchi, M., Shimasaku, K., et al. 2010, ApJ, 724, 1524

Oppenheimer, B. D., & Davé, R. 2008, MNRAS, 387, 577

Osterbrock, D. E., & Ferland, G. J. 2006, Astrophysics of Gaseous Nebulae and Active Galactic Nuclei (Sausalito, CA: University Science Books)

Overzier, R. A., Heckman, T. M., Wang, J., et al. 2011, ApJL, 726, L7

Pacifici, C., Charlot, S., Blaizot, J., & Brinchmann, J. 2012, MNRAS, 421, 2002

Padovani, P., Miller, N., Kellermann, K. I., et al. 2011, ApJ, 740, 20

Pannella, M., Carilli, C. L., Daddi, E., et al. 2009, ApJL, 698, L116

Papovich, C., Dickinson, M., & Ferguson, H. C. 2001, ApJ, 559, 620

Papovich, C., Finkelstein, S. L., Ferguson, H. C., Lotz, J. M., & Giavalisco, M. 2011, MNRAS, 412, 1123

Papovich, C., Moustakas, L. A., Dickinson, M., et al. 2006, ApJ, 640, 92

Papovich, C., Rudnick, G., Le Floc'h, E., et al. 2007, ApJ, 668, 45

Patel, S. G., van Dokkum, P. G., Franx, M., et al. 2013, ApJ, 766, 15

Pei, Y. C. 1992, ApJ, 395, 130

Penner, K., Dickinson, M., Weiner, B., et al. 2015, ArXiv 1507.00728

Pérez-González, P. G., Cava, A., Barro, G., et al. 2013, ApJ, 762, 46

Pforr, J., Maraston, C., & Tonini, C. 2012, MNRAS, 422, 3285

—. 2013, MNRAS, 435, 1389

Popesso, P., Dickinson, M., Nonino, M., et al. 2009, A&A, 494, 443

Prevot, M. L., Lequeux, J., Prevot, L., Maurice, E., & Rocca-Volmerange, B. 1984,

A&A, 132, 389

Price, S. H., Kriek, M., Brammer, G. B., et al. 2014, ApJ, 788, 86

Raiter, A., Schaerer, D., & Fosbury, R. A. E. 2010, A&A, 523, A64

Reddy, N., Dickinson, M., Elbaz, D., et al. 2012a, ApJ, 744, 154

Reddy, N. A., Erb, D. K., Pettini, M., Steidel, C. C., & Shapley, A. E. 2010, ApJ, 712, 1070

Reddy, N. A., Pettini, M., Steidel, C. C., et al. 2012b, ApJ, 754, 25

Reddy, N. A., Steidel, C. C., Fadda, D., et al. 2006, ApJ, 644, 792

Reddy, N. A., Kriek, M., Shapley, A. E., et al. 2015, ApJ, 806, 259

Reines, A. E., Nidever, D. L., Whelan, D. G., & Johnson, K. E. 2010, ApJ, 708, 26

Renzini, A. 2009, MNRAS, 398, L58

Richards, G. T., Strauss, M. A., Fan, X., et al. 2006, AJ, 131, 2766

Riechers, D. A., Bradford, C. M., Clements, D. L., et al. 2013, Nature, 496, 329

Riechers, D. A., Carilli, C. L., Capak, P. L., et al. 2014, ApJ, 796, 84

Rieke, G. H., Alonso-Herrero, A., Weiner, B. J., et al. 2009, ApJ, 692, 556

Robertson, B. E., Furlanetto, S. R., Schneider, E., et al. 2013, ApJ, 768, 71

Rodighiero, G., Cimatti, A., Gruppioni, C., et al. 2010, A&A, 518, L25

Rowlands, K., Gomez, H. L., Dunne, L., et al. 2014, MNRAS, 441, 1040

Rudnick, G., Rix, H.-W., Franx, M., et al. 2003, ApJ, 599, 847

Rujopakarn, W., Rieke, G. H., Eisenstein, D. J., & Juneau, S. 2011, ApJ, 726, 93

Rujopakarn, W., Rieke, G. H., Weiner, B. J., et al. 2013, ApJ, 767, 73

Salim, S., Dickinson, M., Michael Rich, R., et al. 2009, ApJ, 700, 161

Salmon, B., Papovich, C., Finkelstein, S. L., et al. 2015, ApJ, 799, 183

Salmon, B., Papovich, C., Long, J., et al. 2016, ArXiv 1512.05396

Salpeter, E. E. 1955, ApJ, 121, 161

Sancisi, R., Fraternali, F., Oosterloo, T., & van der Hulst, T. 2008, A&A Rv, 15,

Sandage, A. 1961, The Hubble Atlas of Galaxies (Carnegie Institute of Washington)

Sanders, R. L., Shapley, A. E., Kriek, M., et al. 2015, ArXiv 1509.03636

Santini, P., Ferguson, H. C., Fontana, A., et al. 2015, ApJ, 801, 97

Sawicki, M. 2012, MNRAS, 421, 2187

Sawicki, M., & Yee, H. K. C. 1998, AJ, 115, 1329

Schaerer, D., Boone, F., Zamojski, M., et al. 2014, ArXiv 1407.5793

Schaerer, D., & de Barros, S. 2009, A&A, 502, 423

—. 2010, A&A, 515, A73

Schaerer, D., de Barros, S., & Sklias, P. 2013, A&A, 549, A4

Schaye, J., Dalla Vecchia, C., Booth, C. M., et al. 2010, MNRAS, 402, 1536

Schmidt, K. B., Treu, T., Trenti, M., et al. 2014, ApJ, 786, 57

Schreiber, C., Pannella, M., Elbaz, D., et al. 2014, ArXiv 1409.5433

Scoville, N., Faisst, A., Capak, P., et al. 2015, ApJ, 800, 108

Seibert, M., Martin, D. C., Heckman, T. M., et al. 2005, ApJL, 619, L55

Shankar, F., Lapi, A., Salucci, P., De Zotti, G., & Danese, L. 2006, ApJ, 643, 14

Shapley, A. E., Steidel, C. C., Adelberger, K. L., et al. 2001, ApJ, 562, 95

Shapley, A. E., Steidel, C. C., Erb, D. K., et al. 2005, ApJ, 626, 698

Shapley, A. E., Reddy, N. A., Kriek, M., et al. 2015, ApJ, 801, 88

Shim, H., Chary, R.-R., Dickinson, M., et al. 2011, ApJ, 738, 69

Shimakawa, R., Kodama, T., Steidel, C. C., et al. 2015, MNRAS, 451, 1284

Siana, B., Teplitz, H. I., Colbert, J., et al. 2007, ApJ, 668, 62

Siana, B., Smail, I., Swinbank, A. M., et al. 2009, ApJ, 698, 1273

Siana, B., Teplitz, H. I., Ferguson, H. C., et al. 2010, ApJ, 723, 241

Sklias, P., Zamojski, M., Schaerer, D., et al. 2014, A&A, 561, A149

Smit, R., Bouwens, R. J., Franx, M., et al. 2012, ApJ, 756, 14

Smit, R., Bouwens, R. J., Labbé, I., et al. 2014, ApJ, 784, 58

Smith, D. J. B., & Hayward, C. C. 2015, ArXiv 1507.07554

Somerville, R. S., & Davé, R. 2015, ARA&A, 53, 51

Somerville, R. S., Gilmore, R. C., Primack, J. R., & Domínguez, A. 2012, MNRAS, 423, 1992

Somerville, R. S., Hopkins, P. F., Cox, T. J., Robertson, B. E., & Hernquist, L. 2008, MNRAS, 391, 481

Song, M., Finkelstein, S. L., Gebhardt, K., et al. 2014, ApJ, 791, 3

Song, M., Finkelstein, S. L., Ashby, M. L. N., et al. 2015, ArXiv 1507.05636

Speagle, J. S., Steinhardt, C. L., Capak, P. L., & Silverman, J. D. 2014, ApJS, 214, 15

Spitler, L. R., Straatman, C. M. S., Labbé, I., et al. 2014, ApJL, 787, L36

Springel, V., & Hernquist, L. 2003, MNRAS, 339, 289

Springel, V., White, S. D. M., Jenkins, A., et al. 2005, Nature, 435, 629

Stark, D. P., Ellis, R. S., Bunker, A., et al. 2009, ApJ, 697, 1493

Stark, D. P., Schenker, M. A., Ellis, R., et al. 2013, ApJ, 763, 129

Steidel, C. C., Adelberger, K. L., Giavalisco, M., Dickinson, M., & Pettini, M. 1999, ApJ, 519, 1

Steidel, C. C., & Hamilton, D. 1993, AJ, 105, 2017

Steidel, C. C., Shapley, A. E., Pettini, M., et al. 2004, ApJ, 604, 534

Steidel, C. C., Rudie, G. C., Strom, A. L., et al. 2014, ApJ, 795, 165

Steinhardt, C. L., Capak, P., Masters, D., & Speagle, J. S. 2015, ArXiv 150601377

Steinhardt, C. L., Speagle, J. S., Capak, P., et al. 2014, ApJL, 791, L25

Stewart, K. R., Kaufmann, T., Bullock, J. S., et al. 2011, ApJ, 738, 39

Storey, P. J., & Hummer, D. G. 1995, MNRAS, 272, 41

Straatman, C. M. S., Labbé, I., Spitler, L. R., et al. 2014, ApJL, 783, L14

Strauss, M. A., Weinberg, D. H., Lupton, R. H., et al. 2002, AJ, 124, 1810

Sutton, A. J., & Abrams, K. R. 2001, SMMR, 10, 277

Tal, T., Dekel, A., Oesch, P., et al. 2014, ApJ, 789, 164

Tanaka, M. 2015, ApJ, 801, 20

Tilvi, V., Papovich, C., Tran, K.-V. H., et al. 2013, ApJ, 768, 56

Tinsley, B. M. 1980, FCPh, 5, 287

Todini, P., & Ferrara, A. 2001, MNRAS, 325, 726

U, V., Hemmati, S., Darvish, B., et al. 2015, ApJ, 815, 57

Vale, A., & Ostriker, J. P. 2004, MNRAS, 353, 189

van der Wel, A., Straughn, A. N., Rix, H.-W., et al. 2011, ApJ, 742, 111

van Dokkum, P. G., Whitaker, K. E., Brammer, G., et al. 2010, ApJ, 709, 1018

Vanzella, E., Cristiani, S., Dickinson, M., et al. 2008, A&A, 478, 83

Ventura, P., Dell'Agli, F., Schneider, R., et al. 2014, MNRAS, 439, 977

Verhamme, A., Dubois, Y., Blaizot, J., et al. 2012, A&A, 546, A111

Verma, A., Lehnert, M. D., Förster Schreiber, N. M., Bremer, M. N., & Douglas, L. 2007, MNRAS, 377, 1024

Walcher, J., Groves, B., Budavári, T., & Dale, D. 2011, Ap&SS, 331, 1

Wang, R., Carilli, C. L., Wagg, J., et al. 2008, ApJ, 687, 848

Weinmann, S. M., Neistein, E., & Dekel, A. 2011, MNRAS, 417, 2737

Whitaker, K. E., van Dokkum, P. G., Brammer, G., & Franx, M. 2012, ApJL, 754, L29

Wiersma, R. P. C., Schaye, J., & Smith, B. D. 2009, MNRAS, 393, 99

Wilkins, S. M., Bouwens, R. J., Oesch, P. A., et al. 2015, ArXiv 1510.01514

Williams, R. J., Quadri, R. F., Franx, M., van Dokkum, P., & Labbé, I. 2009, ApJ, 691, 1879

Windhorst, R. A., Cohen, S. H., Hathi, N. P., et al. 2011, ApJS, 193, 27

Witt, A. N., & Gordon, K. D. 2000, ApJ, 528, 799

Witt, A. N., Petersohn, J. K., Bohlin, R. C., et al. 1992, ApJL, 395, L5

Wuyts, S., Franx, M., Cox, T. J., et al. 2009, ApJ, 696, 348

Wuyts, S., Labbé, I., Schreiber, N. M. F., et al. 2008, ApJ, 682, 985

Wuyts, S., Labbé, I., Franx, M., et al. 2007, ApJ, 655, 51

Wuyts, S., Förster Schreiber, N. M., van der Wel, A., et al. 2011a, ApJ, 742, 96

Wuyts, S., Förster Schreiber, N. M., Lutz, D., et al. 2011b, ApJ, 738, 106

Wyithe, J. S. B., Loeb, A., & Oesch, P. A. 2014, MNRAS, 439, 1326

Xue, Y. Q., Luo, B., Brandt, W. N., et al. 2011, ApJS, 195, 10

Yajima, H., Li, Y., Zhu, Q., et al. 2012, ApJ, 754, 118

Yan, H., Dickinson, M., Giavalisco, M., et al. 2006, ApJ, 651, 24

Zackrisson, E., Bergvall, N., & Leitet, E. 2008, ApJL, 676, L9

Zackrisson, E., Bergvall, N., Olofsson, K., & Siebert, A. 2001, A&A, 375, 814

Zeimann, G. R., Ciardullo, R., Gronwall, C., et al. 2015, ApJ, 814, 162

Zibetti, S., Gallazzi, A., Charlot, S., Pierini, D., & Pasquali, A. 2013, MNRAS, 428, 1479

# APPENDIX A

# APPENDICES OF SECTION 2

## A.1 Changing the Assumed Star Formation History

The SFRs and stellar masses used in this work are derived using SPS models with constant SFRs. In contrast, one of the main results of this work is that the high-redshift galaxies experience SFRs that increase monotonically with time, $\Psi \propto t^{1.4\pm0.1}$. Naively, it would seem these statements are in conflict. Here we discuss how the star formation history affects the model interpretation, and we offer justification for the use of models with constant SFRs.

First, we tested SED fits with our Bayesian formalism that marginalize over a range of star formation histories, including those that rise with time, with $e$-folding times, $\tau$ = 50, 100, 300 Myr, and 100 Gyr (the long $e$-folding time approximates a constant SFR and keeps all the models handled identically in normalization by the BC03 software), where the star formation history is then defined as $\Psi \sim \exp^{t/\tau}$. We then use our Bayesian formalism to derive model parameters using the synthetic photometry from the galaxy mock catalog using the Somerville et al. SAM.

Figure A.1 shows the SFRs and stellar masses measured from the synthetic photometry compared to the true model values using this large range of model parameters. This figure can be compared directly to Figure 2.9 above, which used models assuming only a constant star formation history. In comparison, the model parameters derived using the suite of histories that include rising SFRs produce stellar masses that are skewed low and SFRs that are skewed high compare to the true values. This appears to be unphysical.

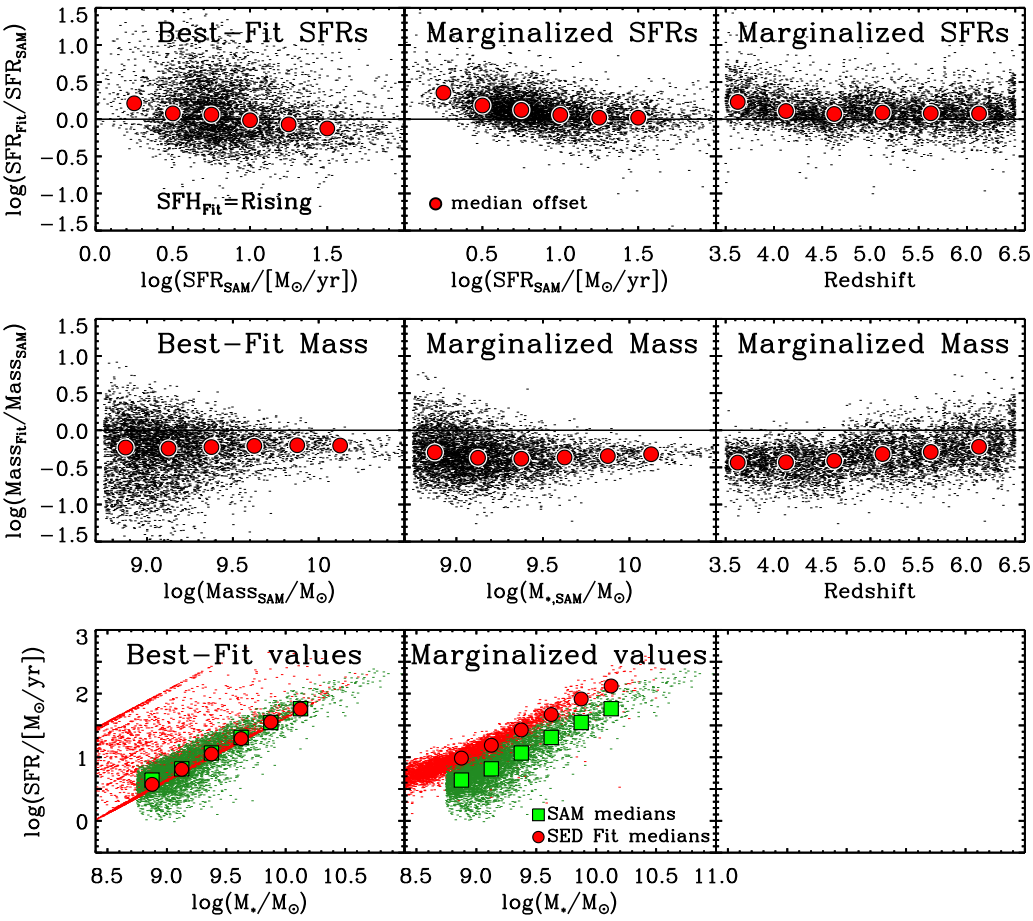


Figure A.1: Changing the Assumed Star-Formation History

Results of SED fitting to synthetic photometry of recent SAM mock catalogs (Somerville et al)., now fitting to templates with exponentially rising star formation histories (similar to Fig. 2.9). The top panels show the log difference of measured-to-true SFRs. The derived SFRs are systematically higher than the true values, with high scatter. The middle panels show the ratio of the measured-to-true stellar masses. The stellar masses are systematically lower. The bottom panels show that the derived SFRs and stellar masses do not well recover the SFR–mass relation in the models when using exponentially rising star formation histories.

In hindsight, the reason for this is the following. In the BC03 models, the star formation history parameterization uses $e$-folding timescales (motivated by the exponentially decreasing models pioneered by Tinsley (1980)) and therefore the SFRs

rise *exponentially* in time. Therefore, older stellar populations have unphysically increasing SFRs. At these late times, the models increase much faster than supported by observations (e.g., Papovich et al., 2001) or seen in simulations (e.g., Finlator et al., 2006). As a result, models with exponentially increasing SFRs must underproduce the stellar mass and overproduce the SFR to match the observed SED of galaxies. In contrast, the star formation histories of galaxies in our redshift range and in simulations can be approximately accurately as constant when averaged over the past $\sim$ 100 Myr, which includes the recently formed stars that dominate the luminosity-weighted age (see, e.g., Finlator et al., 2006). As a result, we do not consider the assumption of a constant star formation history to be a significant factor on the conclusions of this work. We note parenthetically that this is only true for the galaxies observed in this work because they are all heavily star-forming with high sSFRs; quiescent galaxies would require declining star formation histories.

Furthermore, our tests (discussed above in § 2.5.4 and Figure 2.9) show that SED fits using models with constant star formation reproduce accurately the SFRs and stellar masses from the models. Therefore, this work fixes the star formation history in fitting templates to be constant during the analysis of the CANDELS data. As the conclusions show, the galaxy populations require a star formation history with a rising SFR, but this evolution is slow and monotonic, $\Psi \propto t^{\gamma}$ (where $\gamma = 1.4 \pm 0.1$ from § 2.7.2 and Figure 2.15), which is not currently supported in a simple parameterization in the BC03 models. Nevertheless, in a future work, we will explore possible improvements in parameters using models with star formation histories that increase as a power law in time, as well as other more complex star formation histories.

## A.2 Stellar Population Synthesis Fitting: Comparing Best-Fit Results

We compare between using the best-fit results from SED fitting procedures to using our Bayesian formalism to derive parameters from their posterior probability densities. In each subsection, we observe the offsets under different fitting template assumptions, including the effect of nebular emission lines and dust-attenuation prescription.

### *A.2.1 Effect of Including Nebular Emission*

The effects of including effects of nebular emission to the stellar templates are largely mitigated when using our Bayesian formalism (see Figure 2.8). In contrast, the nebular emission lines can strongly affect stellar masses and SFRs derived from best-fit model parameters. Figure A.2 shows that in the redshift range of our galaxy sample, the presence (or absence) of an emission line in the ISAAC $K_s$, [3.6], and [4.5] bandpasses results in best-fit models that typically have lower SFRs and stellar masses by up to 0.5 dex (factor of 3). This is because a galaxy with a redder rest-frame UV-optical color requires either an older stellar population or heavier dust attenuation, with higher $M_\star/L$ ratios. Models where emission lines are present in the redder passbands reproduce the redder rest-frame UV-optical colors with lower stellar masses and SFRs. The effects of nebular emission are strongest in the redshift range that strong emission lines are present (see Fig. 2.3). The median decrease is up 0.3 dex (factor of 2) in both SFR and stellar mass for $5.5 < z < 6.5$. As discussed in the literature, this can affect the interpretation of the galaxies (Schaerer & de Barros, 2009, 2010; Schaerer et al., 2013; Ono et al., 2010; Finkelstein et al., 2011; Curtis-Lake et al., 2013; de Barros et al., 2014; Reddy et al., 2012b; Stark et al., 2013; Tilvi et al., 2013).

It is worth noting that strength of the nebular emission lines is highly uncertain for

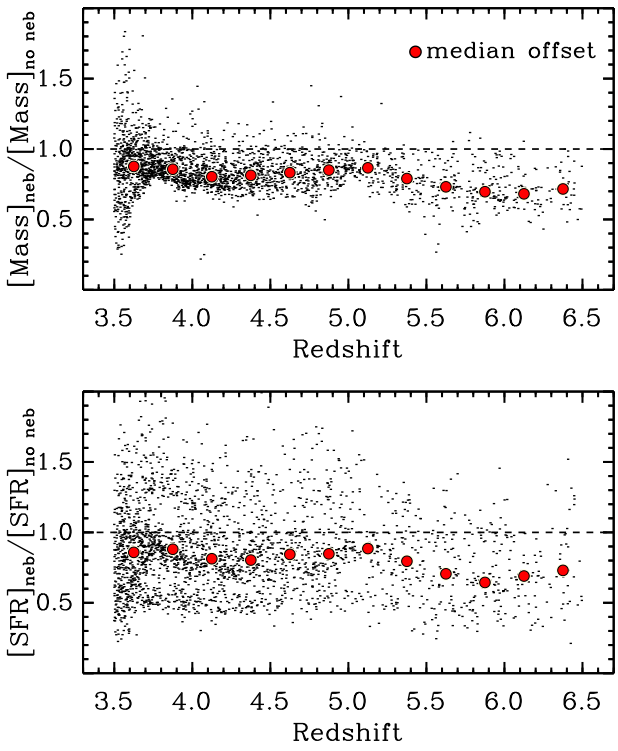


Figure A.2: Influence of Nebular Emission on Stellar Mass

*Top:* The ratio of the best-fit stellar masses from model fits that include the effects of nebular emission lines (e.g., $f_{\rm esc} = 0$) and exclude emission lines (e.g., $f_{\rm esc} = 1$) for the objects in our CANDELS sample. Black points show the ratio of the best-fit values as a function of redshift, and the large red points show the medians in bins of redshift. *Bottom:* Ratio of best-fit SFRs from model fits with and without nebular emission lines. For galaxies with redshifts that place strong emission lines in one or more of the bandpasses (see Fig. 2.3), the best-fit SFRs and stellar masses can be reduced by up to 0.5 dex (factor of 3), with a median of 0.3 dex (factor of 2). In contrast, our Bayesian formalism finds that including nebular emission has only a small effect on the derived stellar masses and SFRs (Fig. 2.8).

several reasons. One clear reason is that the model must use some escape fraction of ionizing photons, which is allowed to range between $0 \leq f_{\rm esc} \leq 1$. Another uncertainty is that in our parameterization, the strength of line emission is tied to the age of the model stellar population, and age is less constrained in SED fitting (see, e.g., Papovich et al. (2001) and Fig. 2.5 above). Fits to galaxies using models with a starburst-like attenuation prescription (Calzetti et al., 2000) produce age distributions skewed heavily to the low ages (in some cases unphysically low as the ages are much less than a dynamical time, (e.g., Yan et al., 2006; Eyles et al., 2007; Schaerer & de Barros, 2009; de Barros et al., 2014; Reddy et al., 2012b)). Both the escape fraction and inferred ages are poorly known quantities which cause the effect of nebular emission lines to likewise be poorly constrained, (see also, Verma et al., 2007; Oesch et al., 2013). For these reasons it is advantageous to use SED fitting that is not strongly influenced by the presence or absence of such lines. As we show above (§ 2.5.3 and Fig. 2.8), our Bayesian formalism is less affected by nebular emission lines in the models. Therefore, for the analysis in this paper we adopt models with $f_{\rm esc} = 0$. In a future work, we will consider fully marginalizing over a range of escape fraction, although it seems unlikely to change the conclusions here.

### *A.2.2 Dependence on Attenuation Prescription*

Figure A.3 shows the effects of the dust attenuation prescription on the stellar masses and SFRs from the best-fit models. The choice of dust attenuation prescription has a weak effect on stellar mass, where models using the SMC-like attenuation prescription have lower stellar masses by $\sim$0.1 dex in the median compared to the starburst-like dust attenuation (although the spread is larger, up to $\pm$0.2 dex).

The choice of dust attenuation prescription has a much stronger effect on the SFRs derived from best-fit models. Figure A.3 shows that there is a strong trend in

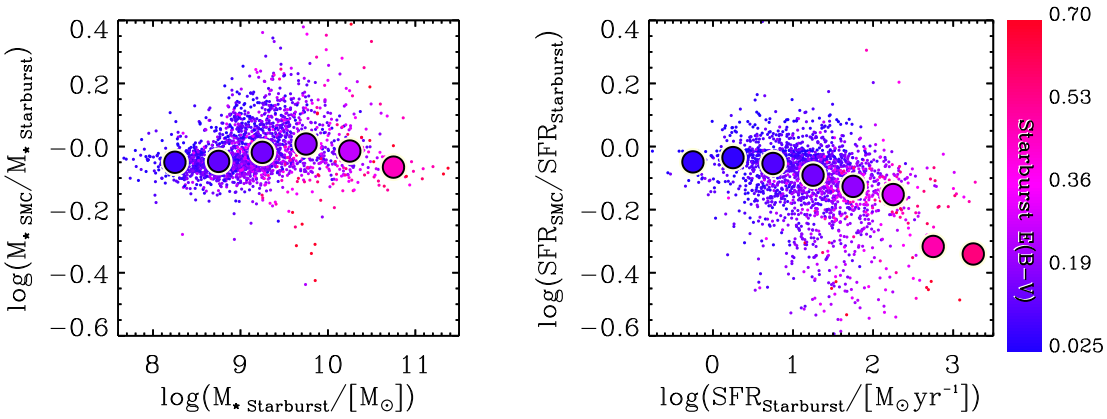


Figure A.3: The Affects of Changing the Dust Law on Stellar Mass and SFR *Left:*The ratio of stellar masses from best-fit models that assume SMC-like attenuation to those that assume a starburst-like attenuation as a function of best-fit mass. Small points show individual galaxies, where the color denotes the attenuation from the best-fit model assuming starburst-like dust. The large points show medians in bins of $d \log M_\star/\mathrm{M}_\odot = 0.5$ dex. (We have excluded showing objects with best-fit models that have zero reddening, $A_{\mathrm{UV}}$=0, as these lie on the unity line.) At lower masses, the extinction prescription has little effect on the best-fit masses. At higher masses, $\log M_\star/\mathrm{M}_\odot > 10$ dex, there is weak trend in that the best-fit models with SMC-like dust have lower stellar masses ($\sim$0.1 dex at $\log M_\star/\mathrm{M}_\odot \gtrsim 10.8$ dex). This is likely related to the fact that higher-mass galaxies appear to have higher reddening (so presumably lower mass, dusty galaxies would also have the same trend in mass). *Right:* Ratio of the SFRs for the same best-fit models. Here there is a strong trend in SFRs from the best-fit models: as the SFR increases, there the models with starburst-like dust have significantly higher SFRs, by up to a 0.5 dex, with a median of $\sim$0.3 dex (factor of 2). Clearly the choice of dust attenuation prescription affects the interpretation of galaxy SFRs in the best-fit models. Nevertheless, as we show above in Figure 2.8, in our Bayesian formalism these differences are mitigated, and the dust attenuation prescription has negligible impact on the results here.

SFRs from the best-fit models: as the SFR increases, the models with starburst-like dust have significantly higher SFRs, by up to a 0.5 dex, with a median of ∼0.3 dex (factor of 2) compared to the best-fit solutions using an SMC-like dust. This is due to a combination of effects. First, there are high degeneracies between the inferred attenuation and age that arise from broadband SED fitting (discussed in the previous Appendix subsection). The assumed SFR depends on the stellar population age, especially at lower ages, where this leads to much higher ratios of in the SFR/$L_{1500}$ ratio (see Appendix of Reddy et al., 2012b) compared to the value typically assumed in the Kennicutt (1998) relation which assumes ages greater than $10^8$ yr.

Dust extinction and age are degenerate (negatively covariant) in the SED modeling and models with starburst dust typically have lower best-fit ages (Papovich et al. 2001). Therefore, the effects of higher dust attenuation and higher SFR/$L_{1500}$ ratio both contribute to a larger SFR for the case of starburst-like dust. The differences between starburst-like and SMC-like dust models are highest for models with highest SFRs, as shown in Figure A.3. For objects with the highest SFR, the difference between the two prescriptions can be as high as $\sim$ 0.7 dex. Therefore, for best-fit models *an assumed SMC-like attenuation causes starburst-attenuation-derived young, dusty, and high-SFR objects to be older, less dusty, and with lower SFR.* This also reinforces the result of nebular emission in the Appendix above that simple template assumptions can significantly impact the best-fit SFR. Nevertheless, as we show above in Figure 2.8, in our Bayesian formalism these differences are mitigated, and the dust attenuation prescription has negligible impact on the results here.

For these reasons, this work assumed an SMC-like attenuation for all objects in our sample. If we otherwise had very reliable age estimates we might assume, as by Reddy et al. (2012b), an "age"-dependent attenuation prescription, such that

younger galaxies have SMC and older have starburst attenuation. However, the effects of nebular emission and assumed attenuation are strongest when adopting best-fit values. In contrast, we mitigate these effects by using the results from our Bayesian analysis, where the effects of changing dust attenuation prescription are minimized (see § 2.5).

### *A.2.3 Difference of Marginalized SFR Compared to Traditional Methods*

The method used in the work to derive UV SFRs for high redshift galaxies is different from the typical methods found in the literature. The common methods include using a dust correction based on the UV spectral slope, $f_\lambda \sim \lambda^\beta$, (Meurer et al., 1999; Madau et al., 1998; Kennicutt, 1998) and using the instantaneous SFR from the best-fit stellar population model. As shown in Figure A.4, both of these alternative methods show high scatter when compared to the marginalized SFR from the method of this work.

The large scatter in Figure A.4 is due to the fact that the scale of SFR is predominantly dependent on the treatment of the dust correction to UV luminosity, which is an unconstrained quantity in traditional SED fitting methods at high redshift. The Bayesian approach has the advantage in producing realistic ages, thereby reducing degeneracies with dust corrections. The median age for the SAM mock catalogs is $\log(t_{\rm age})= 8.48 \pm 0.22$ dex which resembles the distribution of marginalized ages found in this work for observed galaxies, $\log(t_{\rm age})= 8.73 \pm 0.14$ dex. Conversely, the distribution of best-fit ages is typically very dissimilar from SAM and simulation predictions. This is because best-fits typically find lowest $\chi^2$ at the extreme end of parameter space (youngest ages, highest extinction). As a result, the median best-fit ages are lower with higher scatter $\log(t_{\rm age})= 8.06 \pm 0.94$ dex. This scatter results from the degeneracies between the young, dusty and old, dust-free solutions of a

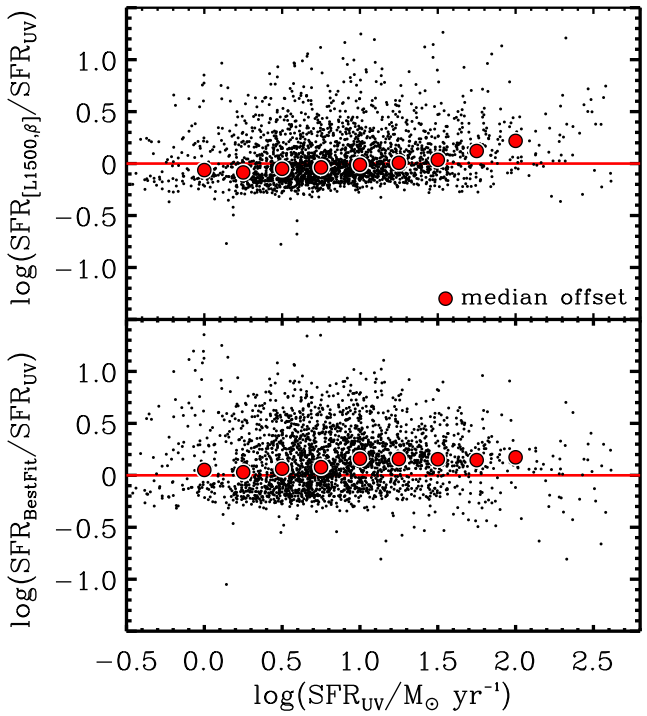


Figure A.4: Other SFR Methods

A comparison between different methods to compute the SFR. The abscissa shows our adopted method, which uses the SFR from the attenuated luminosity of the photometric measurement closest to rest-frame 1500 Å, corrected for dust attenuation using the median $A_{\rm UV}$ from the marginalized posterior PDF (see Equation 2.5). The ordinate of the top panel compares our SFR to the SFR derived from the UV luminosity at $L_{1500}$ and the UV slope, $\beta$, to correct for dust attenuation. The ordinate of the bottom panel compares our SFR toe the SFR from the best-fit stellar population model. In both cases the alternative SFRs show a large scatter, which can lead to significant biases. We favor using our method because our method reproduces the SFRs from the SAMs (see § 2.5.4 and Fig. 2.9), reducing some of this bias.

given SED, and photometric uncertainties (which affect the accuracy of measuring the UV spectral slope, $\beta$) thus producing a wide range of acceptable SFRs.

In summary, when marginalizing over other nuisance parameters, the posterior on age returns more physical ages on the order of ∼350–750 Myr, reducing degeneracies in the derived dust corrections and thereby reducing the uncertainty in SFR. In addition, the method used in this work reproduces SFRs from semi-analytic models (see § 2.5.4), and is relatively unaffected by model variations such as extinction prescription and/or nebular emission lines. This is additional evidence to favor the Bayesian approach to derive physical properties.

## A.3 Derivation of Prior

Here we describe the prior used in our SED fitting procedure and discuss tests to validate its use. The prior used in equation 2.3 was chosen to allow for an analytic derivation to the posterior probability densities that is straight-forward to calculate for each of the stellar population parameters, i.e., $p(t_{\rm age}|D)$. Our prior-likelihood pair is therefore more easily computable (time efficient) and does not require more sophisticated methods such as a Markov Chain Monte Carlo. Our "fiducial" prior, which is used for the results of this work, is can be expressed as a sum over $i$ bands as,

$$p(\Theta') \;=\; \left(\sum_{i=1}^{n} f_{\Theta}^{2}(\lambda_i)/\sigma_i^2\right)^{1/2} \tag{A.1}$$

where $\Theta'$ represents the entire set of parameters, $\Theta' \;= (\Theta\{t_{\rm age}, \tau, A_{\rm UV}\}, {\rm M}_{\star})$, and $f_{\Theta}$ is the model flux, unscaled by stellar mass. We express $\Theta$ as a separate parameter set from stellar mass because the prior in equation A.1 is dependent on the fluxes of the gridded set of models, and independent of mass.

This prior is "flat" with respect to stellar mass, but spans the range of masses

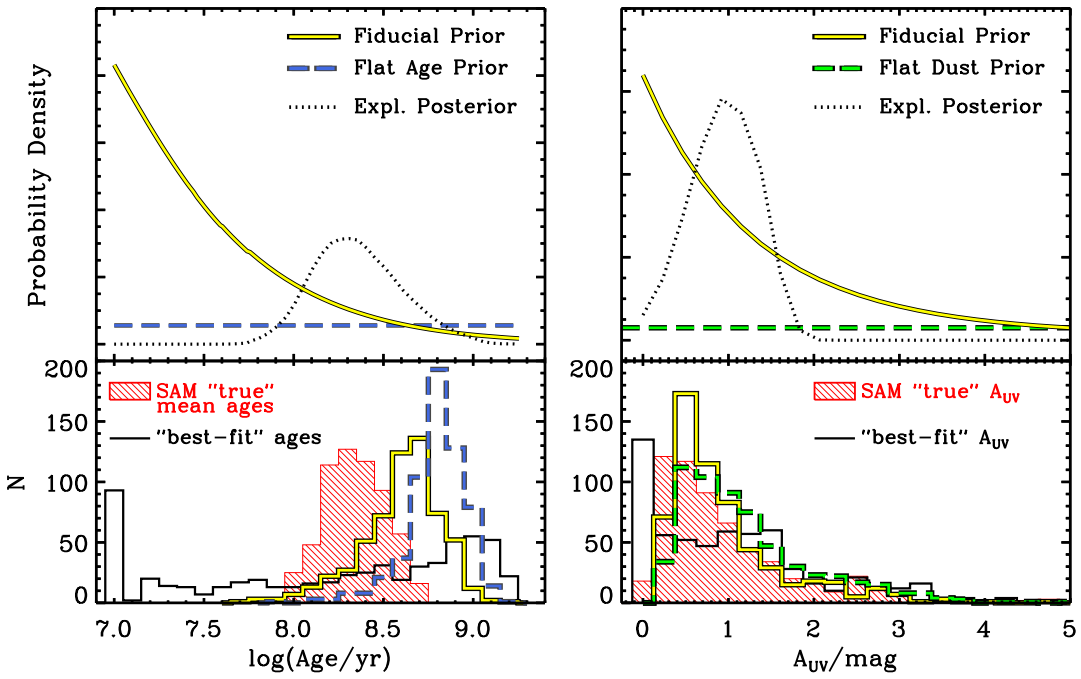


Figure A.5: The Shape of the Assumed Priors

*Top:* the shapes of priors as a function of log(age) (left) and UV attenuation (right). Our "fiducial" prior is what we adopt for the results of this work, while the flat priors are tests to study how the choice of prior affects the results. The dotted lines show the posterior of a given parameter for a single, example object assuming our fiducial prior. *Bottom* histograms of the inferred stellar population ages for a sample of 600 control objects from the Somerville et al. SAM. The red distribution is the "true" distribution from the SAM, while the yellow (solid, fiducial) and blue (dashed, flat) lines show the recovered distribution after fitting to the SAM fluxes assuming different priors. The thin black line shows the recovered values assuming the maximum likelihood solution, or "best-fit". This figure emphasizes that best-fit solutions do not well recover the distribution of input ages and attenuations, and that our fiducial prior is preferred over a flat prior to recover stellar ages.

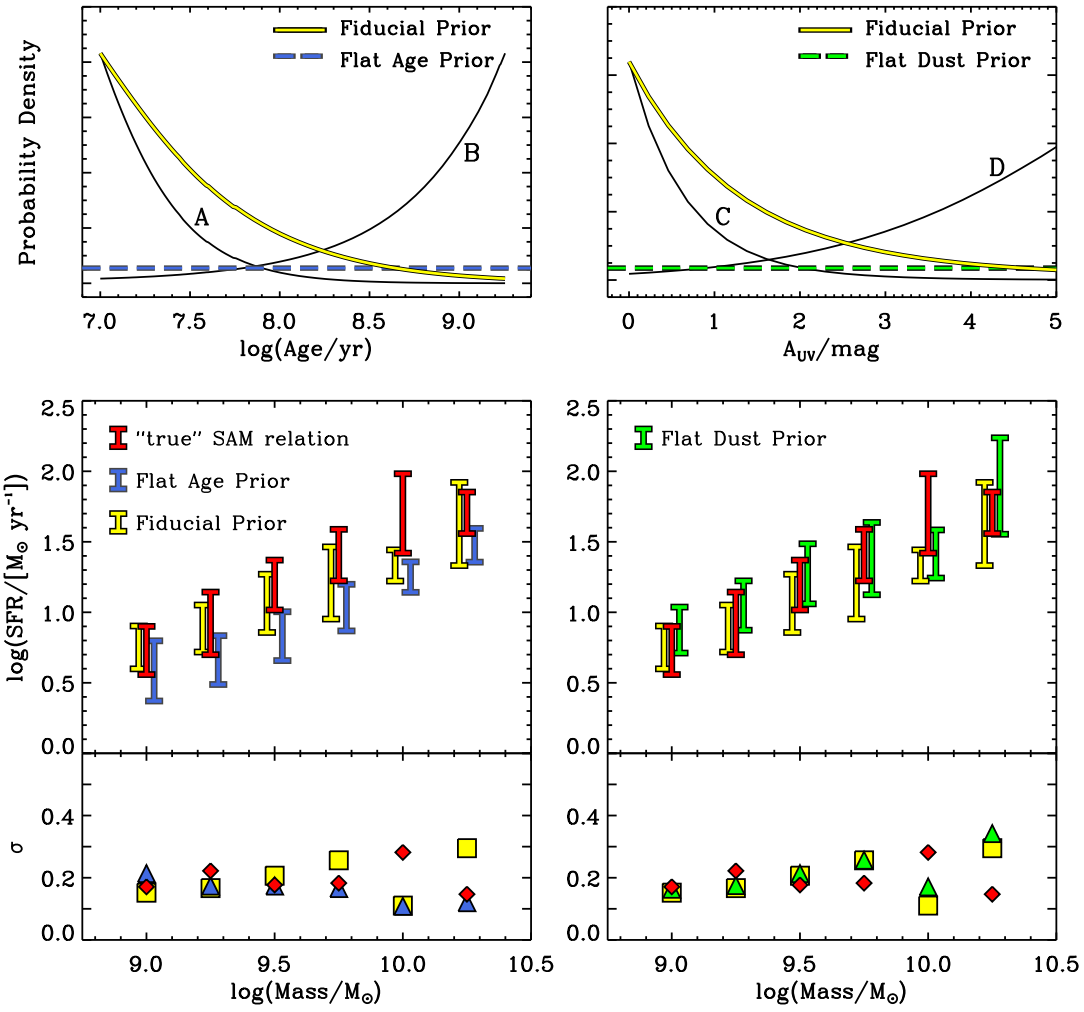


Figure A.6: Changing the Assumed Prior

*Top:* the same as the top of Fig. A.5, shown for reference. Four additional test priors labeled A–D are shown and referred to in the text. *Middle* The slope and $\sigma$ scatter of the SFR–stellar mass relation for a sample of 600 control objects from the Somerville et al. SAM. The red is the "true" scatter from the SAM, while the yellow (solid, fiducial) and blue (dashed, flat) is the scatter after fitting to the SAM fluxes assuming different priors on age (left) and attenuation (right). *Bottom:* the $\sigma$ scatter of SFR in each stellar mass bin. Squares and triangles represent the scatter assuming our fiducial prior or a flat prior, respectively, while the diamonds represent the scatter of the input objects. This figure shows the recovery of the SFR–stellar mass relation under different priors, and that our fiducial prior is preferred over flat priors to recover the input SFR–stellar mass relation.

that the stellar population models can produce for a given set of data. Formally, the prior does depend on the other model parameters and the photometric uncertainties that are used to construct the stellar population synthesis models (age, dust, and star formation history). This is because the models are constructed using a discretized grid of stellar population parameters and a normalization that gives the mass. Since the prior is dependent on the fluxes of the gridded set of model parameters but not stellar mass, we distinguish $\Theta$ and $M_\star$ separately in our equations. The shape of this fiducial prior is shown in the top panels of Figures A.5 and A.6.

In order to confirm that our posterior is constrained by the data and not dominated by the prior, we conducted several tests. First, we steadily increased the photometric uncertainties on the "mock" data from the SAM (lowered the S/N) and used that data as input to our procedure (a similar process as in S 2.5.4). This allows us to search for a characteristic S/N or stellar mass at which the SAM input values are poorly recovered, where here we adopt "poorly recovered" to mean systematically discrepant by a factor of 3 (0.5 dex) as compared to the input SAMs. We find that at S/N = 1 the recovered stellar masses of galaxies with $\log M_\star/M_\odot = 9.75$ are systematically higher by 0.5 dex. Such low S/N represents the scenario where the data have no power and the posterior reverts to the prior. Since all detected bands are typically of S/N $\gg$ 1, this test confirms that it is the likelihood computed from the data that is driving the shape of the posterior, and provides evidence that the conclusions of this work are not dominated by the prior.

In another test, we explored the effects of changing the assumed prior. We conducted this test on a control sample of 600 SAM objects that span the stellar masses and SFRs in the SAM for $z > 3.5$. We then observed how well we could recover the age and attenuation distributions of the SAM when we changed the assumed prior to be flat in age or flat in dust. Figure A.5 shows that using alternative priors shift

the distributions of each parameter, but the prior does not overwhelm the likelihood from the data. For example, the flat age prior pushes the recovered age distribution away from the input age distribution because the flat age prior assigns more weight to older solutions than the fiducial prior. For both priors, the age distributions are old compared to the "true" values from the SAMs, but this is possibly a result of the differences between our assumed (slowly varying) star formation histories and the "physical" ones from the SAM. We consider the agreement between the "true" ages and recovered ages to be good.

The attenuation distributions are much less sensitive to the choice of prior. Figure A.5 shows that there are only subtle differences between the distribution in $A_{\rm UV}$ using our fiducial prior compared to those when using a flat prior. The figure also shows an example ("Expl.") posterior for one object in the sample. This object shows that the probability density does not follow the prior. Moreover, this figure shows how either the fiducial or flat priors (for either parameter) do better at recovering the input distributions than the common method of taking the maximal likelihood, or "best-fit", model.

Finally, we test how the above priors impact the recovery of the slope and scatter of the SFR–stellar mass relation for the control sample of SAM objects. Figure A.6 shows the recovered $\sigma_{\rm MAD}$ scatter about the median SFR in bins of stellar mass, calculated in the same manner as in Figure 2.11, but assuming different priors. The flat age prior shifts the distribution to older ages, and this effect propagates to SFR–stellar mass relation, shifting the SFR distribution to lower values. The flat age prior produces an SFR–stellar mass relation that is tightened and lower in normalization. One reason we disfavor the flat age prior is that the scatter in the SFR–stellar mass relation is even tighter than for our fiducial prior, and therefore the results from the fiducial prior are more conservative. Switching to a flat dust-prior has little effect

on the slope and scatter in the SFR–stellar mass relation, given the scatter. We see similar effects on the results from the data when switching to these priors.

The top panels of Figure A.6 also show a suite of alternative priors (labeled A-D) that were applied to the SAM control sample. A prior younger than our fiducial, such as prior A, assigns more weight to the likelihood of high SFRs at a given mass. This creates a scenario where galaxies are preferred to be young, maximal starbursts, causing the SFR–stellar mass relation to be artificially higher in normalization by $\sim$0.25 dex than the input SAM relation with an inflated scatter ($\langle\sigma\rangle > 0.05$ dex) due to a wider range in mass-to-light ratios. Conversely, prior C and a "flat" age prior assign more weight to old age solutions than our fiducial prior. This results in a more narrow range of mass-to-light ratios, and therefore these priors produce a tighter SFR–stellar mass relation ($\langle\sigma\rangle \sim 0.16$ dex) with lower normalization (lower SFR at a given mass than the input SAMs by $\sim$0.4 dex). On the other hand, our fiducial prior assigns more weight to younger age solutions, therefore avoiding an artificial decrease in SFR–stellar mass scatter, while not being too strong such that the recovered SFRs from the SAM are overestimated. We also find our procedure to be robust against changes to the attenuation prior, and find little change to the normalization slope and scatter when assuming the fiducial, flat, C, and D priors.

In summary, our tests indicate that the SFR-mass scatter is insensitive to the prior on dust and mildly sensitive to the prior on age. However, we conclude that our fiducial prior in age best recovers the age distribution and the SFR-stellar mass scatter of the SAM control sample and is straightforward to implement. Other priors that better reproduce the age distribution or the slope or scatter in SFR-stellar mass have SFRs at a given mass that are significantly off in normalization from the input SAMs.

# APPENDIX B

# APPENDICES OF SECTION 3

## B.1 Testing the Relationship Between $E(B-V)$ and $\delta$

The main result of this paper is the relationship between the tilt of the dust law $\delta$ and the amount of attenuation as probed by the color excess, $E(B-V)$. While this relationship is qualtitatively and independently supported by the position of galaxies on the $IRX-\beta$ relation and their Bayes-factor evidence, it is prudent to consider if the covariance between $\delta$ and $E(B-V)$ contributes to the observed correlation (Figure 3.11). We addressed this concern with several tests below.

First, we defined a grid of $\delta$ and $E(B-V)$ that span the plane in Figure 3.11. Then, we calculated fluxes from our model SEDs for each value of $\delta$ and $E(B-V)$. The model flux at each bandpass was perturbed according to a Gaussian error distribution where sigma was defined as the average, flux-dependent signal-to-noise of the CANDELS data. We used those fluxes as inputs to our procedure and compared the derived values to the "true" values of $\delta$ and $E(B-V)$. We repeated this test fifteen times for five assumptions of the input SED stellar population age and three assumptions of metallicity.

We find that when the input stellar population age is less than a gigayear, we accurately recover all "true" $\delta$ and $E(B-V)$ across with no systematics or appreciable covariance and for all input metallicities. The covariance begins to appear when the galaxies are older than 1 Gyr, and the effect increases in strength at higher metallicities. In that case, the posterior distributions for $E(B-V)$ and $\delta$ are systematically shifted by $\sim$20% of their respective input values, where the covariance is

positive and moves models with higher $\delta$ to higher $E(B-V)$ and vice versa.

The results of the above test are unsurprising. Redder intrinsic SEDs will be fainter in the rest-UV, and by construction, the fainter model fluxes are assigned higher uncertainties. Older ages redden an SED in a similar manner as having high $E(B-V)$ and high $\delta$ or low $E(B-V)$ and low $\delta$ especially when uncertainties in the rest-UV are high. This causes a broadening in the posteriors of both $\delta$ and $E(B-V)$ in a way that is correlated, causing a covariance.

Second, we then asked if the distribution of galaxy ages in our sample is low enough such that the covariance does not significantly bias the relation between $E(B-V)$ and $\delta$. We addressed this with a similar test, where we fixed the age distribution of galaxies to be the same as the one we measure for the GOODS-S phot-$z$ sample. The input $E(B-V)$ was assigned to a random value, and the input $\delta$ follows one of three test relationships: $\delta$ is constant with $E(B-V)$, $\delta$ increases with $E(B-V)$, and $\delta$ decreases with $E(B-V)$. For the increasing $\delta$ case, we used the relationship from Witt & Gordon (2000) (shown in Figure 3.8.2) as the input. The input $\delta$ values were also given a small random scatter to simulate a more realistic relation and uncertainty in $\delta$.

We find that the input relation was well recovered for a sample similar to the phot-$z$ sample of GOODS-S with a realistic input age distribution. Figure B.1 summarizes the results of this final test. While the primary relation was recovered, the covariances conspire to recover the increasing-$\delta$ relation with less scatter and the decreasing-$\delta$ relation with more. In addition, at $E(B-V) \lesssim 0.1$ the attenuation is not strong enough to clearly distinguish between different dust laws. We conclude that (1) we are able to recover several types of relationships on the plane of Figure 3.11, and (2) there may be some bias at $E(B-V) \lesssim 0.1$, but because the attenuation is low regardless, the effect is small. At $E(B-V)$=0.05, the uncertainty of $\Delta(\delta)$=0.1

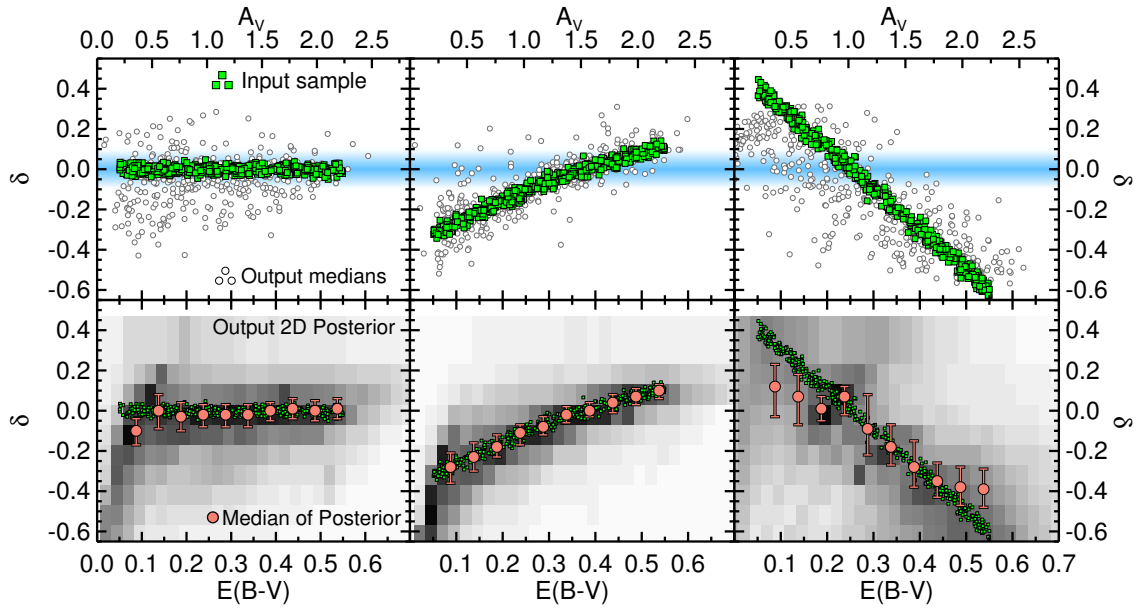


Figure B.1: Testing Different Relations Between $E(B-V)$ and $\delta$.
The tilt of the dust-attenuation curve, $\delta$, as a function of $E(B-V)$ for several input test samples to examine the robustness of the main relation in Figure 3.11. Green squares represent the input $E(B-V)$ and $\delta$ with a known model SED. The left panels show a model where delta is constant with $E(B-V)$, the right panels show a model where delta declines with $E(B-V)$, and the middle panel shows a model with the relation from Witt & Gordon (2000) (shown in Figure 3.8.2). The model fluxes are perturbed and assigned uncertainty according to the real errors in the data. The recovered median values of each $\delta$ and $E(B-V)$ posterior is shown as grey circles (top). The combined two-dimensional posterior for the whole input sample is shown in the lower panels, where shaded regions represent higher likelihood for the sample, salmon-colored circles show the $\delta$ at median likelihood in bins of $E(B-V)$, and error bars represent their 68 % range in likelihood.

changes the attenuation at 1500Å by only 10%. As supported by the observations in the $IRX - \beta$ relation, this test gives credence that the relation in Figure 3.11 is real and not an artifact of the SED-fitting procedure.

## B.2 Using Herschel to Calculate the Total Infrared Luminosities

The determinations of $L_{\rm TIR}$ used in this work come from conversions of 24 $\mu$m luminosity calibrated by R13. However, $\approx$ 40% of our sample have detections at longer wavelengths with *Herschel*, providing the opportunity to internally test our $L_{\rm TIR}$ measurements. We determined $L_{\rm TIR}$ by fitting several different suites of FIR SED templates to the observed MIPS 24 $\mu$mand/or *Herschel* PACS and SPIRE detections of galaxies in our spec-$z$ sample.

Figure B.2 shows several $L_{\rm TIR}$ calculations compared to our fiducial $L_{\rm TIR}$ determined from the 24 $\mu$m luminosity. We compared our adopted $L_{\rm TIR}$ with $L_{\rm TIR}$ values derived from fitting the full IR SED to Dale & Helou (2002) and Rieke et al. (2009) templates, as well as fitting to fluxes at 24$-$100 $\mu$m only. In addition, we compare the 24 $\mu$m conversion to $L_{\rm TIR}$ proposed by Wuyts et al. (2008, 2011a,b). The R13 calibration is very similar to that by Wuyts et al. calibrations. In all cases, the scatter in the derived $L_{\rm TIR}$ is within $\sigma_{\rm NMAD} \approx 0.2$ dex. This scatter is smaller than the correlations in $IRX - \beta$ found in our primary results, and therefore our approximation of 24 $\mu$m luminosity to $L_{\rm TIR}$ is reasonable.

One benefit to using the 24 $\mu$m flux to estimate $L_{\rm TIR}$ is that longer wavelength data, such as $> 70 - 160$ $\mu$m, could be affected more by the the heating of cold dust from old stars. Other studies have shown that the longer wavelength data show more scatter in the SFR calibration for this reason (see Rieke et al., 2009; Kennicutt et al., 2009). Regardless, this is likely not a significant factor in our sample (for example, dust heating from old stellar populations, which can lead to increased

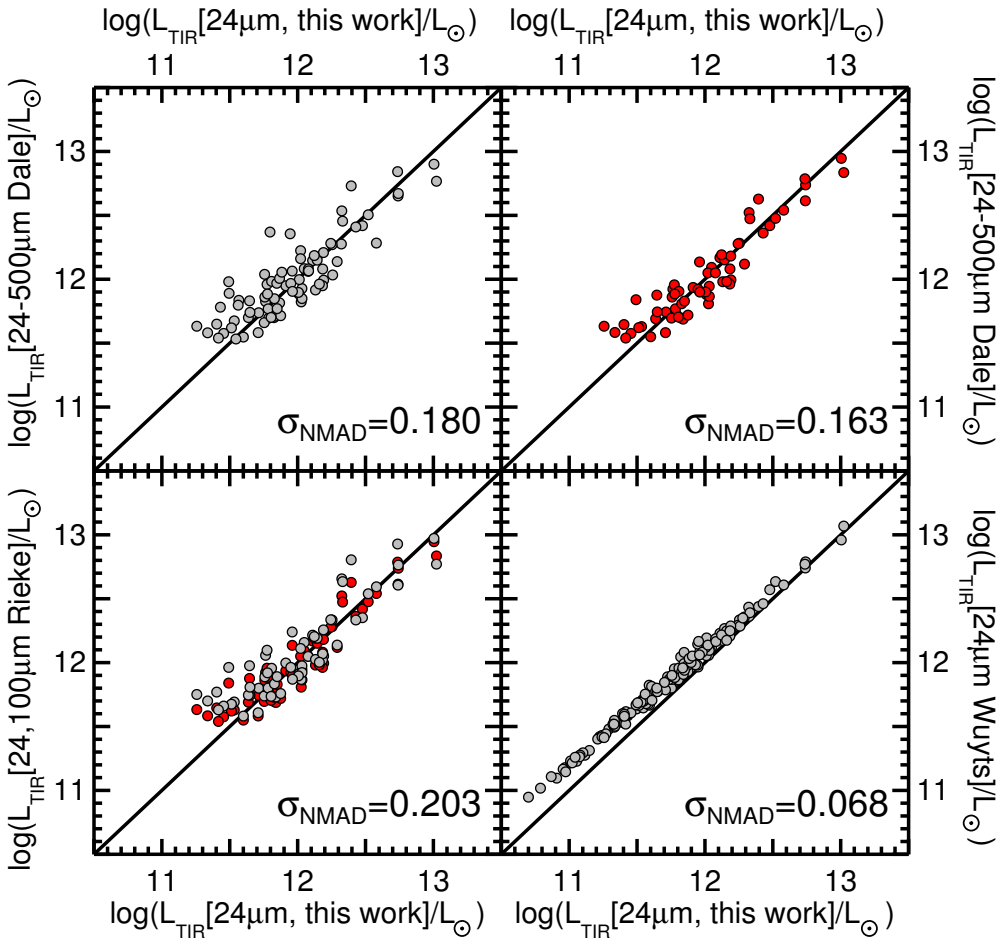


Figure B.16: $L_{\rm TIR}$ Comparison.
Galaxies in the spec-$z$ sample with *Herschel* PACS and/or SPIRE detections are shown with several determinations of $L_{\rm TIR}$ as a function of the fiducial 24 $\mu$m method. The top panels assume Dale & Helou (2002) fitting templates for all available FIR detections (top left) or 24 and 100 $\mu$m only (top right). The bottom left panel assumes Rieke et al. (2009) templates for 24 and 100 $\mu$m bands (grey), as well the Dale et al. assumption (red). The bottom right panel uses the 24 $\mu$m conversion to $L_{\rm TIR}$ from Wuyts et al. (2008).

scatter, is mostly important for lower-luminosity galaxies, and accounts for $< 10\%$ of the total IR luminosity for $L_{\rm TIR} > 10^{11}$ $L_{\odot}$ (Bell, 2002; Calzetti et al., 2010)) For these reasons the 24 $\mu$m calibration of R13 (and others in the literature) should be valid with a scatter of $\sim$0.2 dex. Lastly, we point out that any uncertainty from the $L_{\rm TIR}$ calibration affects only the discussion of the $IRX - \beta$ relation and not the derivation of the relation between $E(B-V)$ and $\delta$, which are based on the modeling of the UV-to-near-IR SED and is independent of the total IR luminosities.

## B.3 Changing the UV Slope, $\beta$

As described in § 3.3.7, we ran tests to recover the true $\beta$ when calculating $\beta$ from a power-law fit to the UV or when using the best-fit SED. For our data, the best-fit SED technique of Finkelstein et al. (2012b) reproduced the input $\beta$, while the power-law method produced some systematics that worsened at higher redshifts. Figure B.4 shows how the results of Figure 3.7 and Figure 3.10 would change when $\beta$ is calculated from a power-law fit to the observed UV bands. For both the spec-$z$ and phot-$z$ samples, the position of galaxies on $IRX - \beta$ broadly agrees with the favored dust law according to the Bayes-factor evidence, in some cases more than the fiducial plots. Importantly, small changes in $\beta$ do not change the clear divide in $IRX$ between galaxies with opposing levels of Bayes-factor evidence. For example, galaxies with evidence promoting a starburst-like dust law tend to have higher $IRX$ than those promoting an SMC-like dust law, at any given $\beta$. This provides evidence that the method is correctly identifying galaxies with opposing dust laws.

## B.4 Changing the Assumed Star-Formation History

For the primary results of this work, we used stellar population models that assume a constant star-formation history. However, we must consider if our choice of parameter space is missing models that could mimic the SED-fitting evidence

towards certain dust laws. In this appendix, we allow the $e$-folding timescale ($\tau$), the time interval over which the SFR is increased by a factor of $e$, to vary as a parameter. We consider SFRs that rise and decline with cosmic time with ranges described in Table 3.1. We also include the fits to rising histories in Figure 3.5 and Figure 3.6 to illustrate that the additional parameter does not create SED shapes that mimic the evidence towards different dust laws.

Figure B.18 shows how fitting the spec-$z$ sample with a range of star-formation histories affects the selection of galaxies based on their Bayes-factor evidence and how that selection propagates to the $IRX - \beta$ plane. While the distribution of Bayes-evidence shifts under the influence of a new parameter, there are still galaxies with convincing evidence between dust laws. In addition, no galaxy switches evidence from favoring the SMC92-like dust to favoring starburst-like dust or vice versa. We conclude that the evidence between dust laws is not an artifact of different star-formation histories, at least for simple rising and declining $\tau$-models.

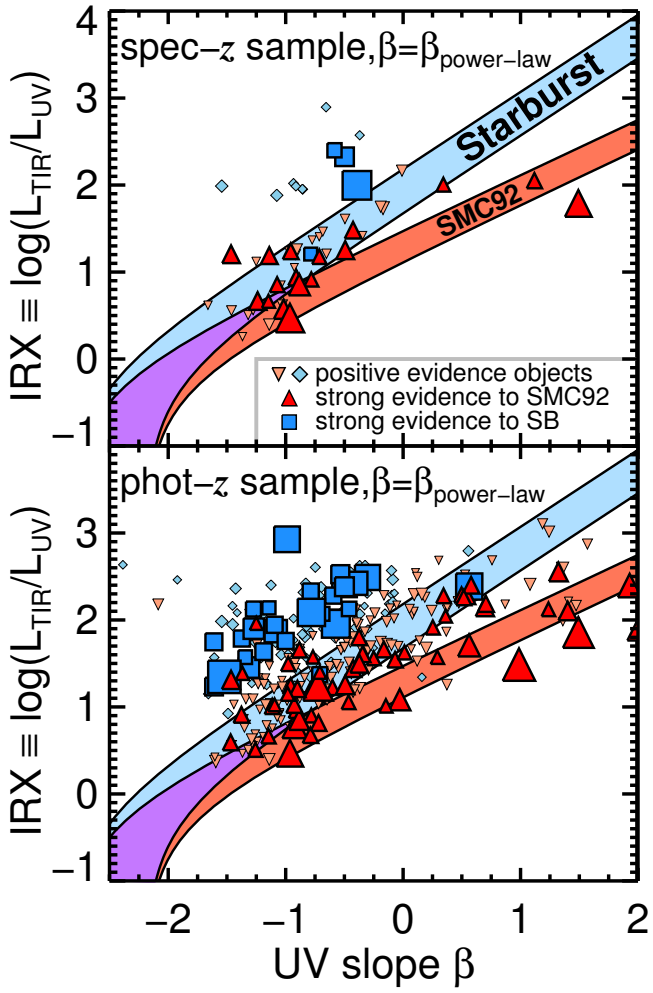


Figure B.17: The $IRX - \beta$ Relation After Changing $\beta$.
The $IRX - \beta$ relation for the spec-$z$ (top) and phot-$z$ (bottom) samples, where $\beta$ was derived from a power-law fit to the observed rest-UV fluxes.

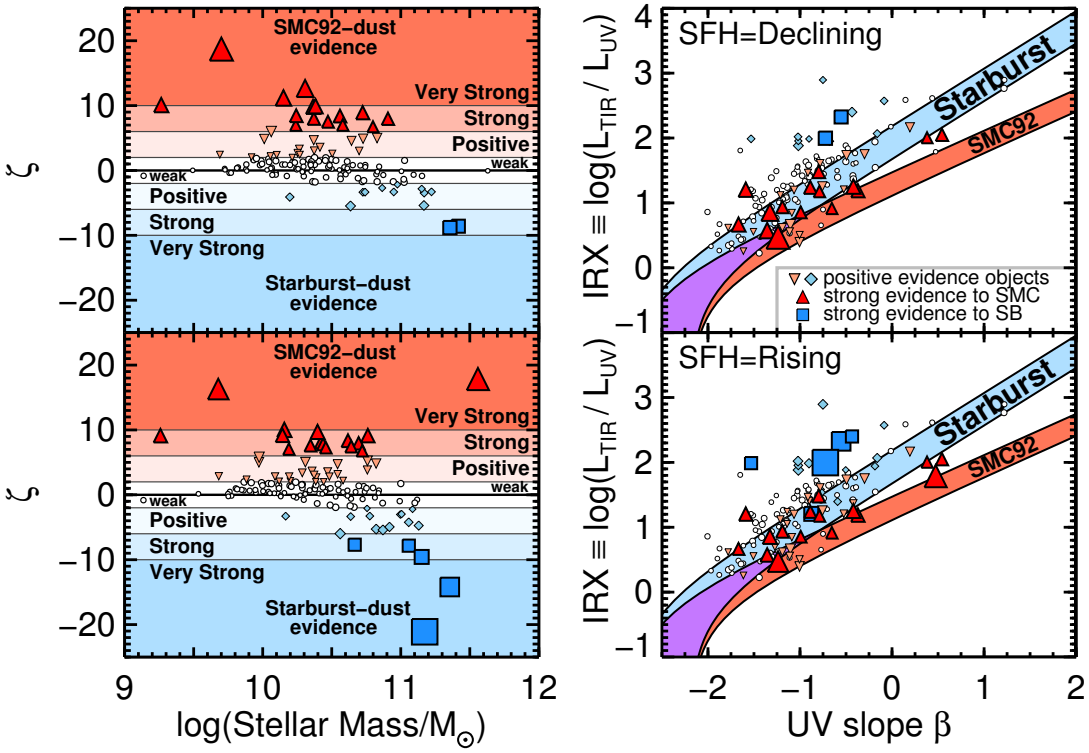


Figure B.18: The $IRX - \beta$ Relation Assuming Different SFHs.
Same as Fig. 3.7, but allowing the star formation history to vary as fitted parameter for star formation rates that decline (top) and rise (bottom) with time. Several colored tiers indicate the selection of galaxies to have strong Bayes-factor evidence towards an SMC92 (red triangles) or starburst (blue squares) dust law. Although the strength of evidence shifts when allowing the SFH to be free, galaxies only ever lose or gain favorance towards a single dust law; no galaxy changes the direction of its evidence.